UNIVERSITY OF CALIFORNIA

Los Angeles

Development of Terahertz Quantum-Cascade VECSELs

A dissertation submitted in partial satisfaction

of the requirements for the degree

Doctor of Philosophy in Electrical Engineering

by

Christopher Curwen

2019

ABSTRACT OF THE DISSERTATION

Development of Terahertz Quantum-Cascade VECSELs

by

Christopher Curwen
Doctor of Philosophy in Electrical Engineering
University of California, Los Angeles, 2019
Professor Benjamin S. Williams, Chair

Terahertz (THz) quantum-cascade lasers (QCLs) are an emerging semiconductor source of compact, high-power THz radiation. Though first realized more than 15 years ago, THz QCLs continue to suffer from poor beam quality and outcoupling efficiency due to the sub-wavelength nature of the semiconductor ridge-waveguides typically used. In this thesis, a new technique is discussed for obtaining high power and good beam quality from THz QCLs, the THz quantum-cascade external cavity surface emitting laser (QC-VECSEL). The concept of the QC-VECSEL is to use THz QC-gain material to design a millimete-scale reflective amplifying surface, or metasurface, for free space THz waves and incorporate it into a free-space THz resonant cavity to provide feedback to the amplification and form a laser. In this manner, the beam shape is determined by the external cavity, which supports fundamental Gaussian solutions. Further, the metasurface itself is composed of a subwavelength array (to prevent diffraction) of surface-coupled QC-elements whose properties, such as phase and polarization response, can be engineered on a unit cell basis allowing for a variety of unique experiments.

The power output power of the QC-VECSEL can be scaled by either increasing the size of the metasurface, or increasing the density (or fill factor) of QC-elements across the surface. In this work, large area metasurfaces with high fill-factor have been studied and demonstrated up to 1.35 W of peak output power for a QC-VECSEL operating at 3.4 THz at a heat sink

temperature of 4 K. A peak wall-plug efficiency of ∼2% is demonstrated, but observation of self lasing from the metasurface at high bias (when no external cavity is provided) in combination with a simultaneous roll-off in VECSEL output power suggests even higher efficiency can be achieved with improved suppression of self-lasing modes. The output beam is well fit to a Gaussian distribution with a 4° full-width half-maximum divergence angle.

In addition to power and beam quality, the QC-VECSEL opens the door to many interesting and unique studies via engineering of the metasurface properties and external cavity. Much of this thesis describes frequency tuning of QC-VECSELs based on broadband metasurfaces by varying the length of the external cavity. By making the external cavity extremely short (comparable to the operating wavelength), we are able to push all other external cavity modes outside of the gain bandwidth of the metasurface and demonstrate more than 20% fractional single-mode tuning around a center operating frequency of 3.5 THz. Because there are almost no diffraction losses at such a short cavity, the size of the metasurface could be reduced, allowing for continuous wave lasing with up to 20 milliwatts of output power at a heatsink temperature of 77 K, though the output power is highly variable as the reflectance of the output coupler has a strong frequency dependence. At the time of writing this, these are record performances in both frequency tuning and high-temperature continuous wave operation for lasers based on THz QC-gain material. The amount of tuning that be achieved with this approach is limited by the phase response of the metasurface, which squeezes the external cavity modes closer together in the spectral domain. Development of metasurfaces with lower electrical power consumption and higher conversion efficiency for the purpose of improving continuous wave performance. A sparse, patch-based metasurface with reduced power consumption is demonstrated, though the design was not optimal and only showed a 20% reduction in current draw compared to the previously demonstrated metasurfaces. Routes towards improving the performance are discussed.

The last subject discussed is the design of a mid-infrared (IR) QC-VECSEL. Due to the large metal losses at mid-IR frequencies compared to THz, the technique used to develop THz QC-VECSELs cannot be directly extended to the mid-IR. We propose a scheme based

on a diffraction grating to provide surface coupling of the QC-gain material. Progress on experimental realization is discussed, but lasing has not yet been observed.

The dissertation of Christopher Curwen is approved.

Tatsuo Itoh

Mona Jarrahi

Mark R. Morris

Benjamin S. Williams, Committee Chair

University of California, Los Angeles

2019

Table of Contents

List of Figures

Acknowledgments

I would like to thank my advisor, Benjamin Williams, for supporting and encouraging me through these years. He has always provided an excellent academic and professional example, and has taught me much about the world of science and engineering. I'm grateful for the opportunities Ben has offered me, and I look forward to pursuing a career in the field.

I would also like to thank my family. My parent's love and support has been the most important constant in my life and has allowed me to explore my opportunities and pursue this long and unpredictable career path. I have to thank my wife, Yi-Ping, for her companionship, and for keeping me grounded when I get too wrapped up in work. And I thank my brothers, Patrick and Nathan, for being great friends.

I wish to thank all of my labmates and collaborators over the years. Particularly, Luyao Xu and Phillip Hon, who helped contribute to the development of the first THz QC-VECESL; and Sudeep Khanal, Eilam Morag, and Mohammad Shahili, who have provided much support in the ongoing development of a mid-IR QC-VECSEL. Many thanks also to outside collaborators including John Reno at Sandia National Labratories, who provided the MBE growth for all of our samples, and our collaborators at JPL, Boris Karasik, Darren Hayton, and Jon Kawamura, who are helped to support our efforts to development of QCLs for remote sensing applications. Last, thanks to the rest of my labmates that have provided much discussion and collaboration over the years: Amir Tavallaee, Benjamin Burnett, Yue Shen, Parastou Mortazavian, Anthony Kim, Yu Wu, Daguan Chen, Nathan Atkinson, and Pranav Balgi.

I feel very lucky to work in a field that I enjoy and to be surrounded by good family, friends, and coworkers. I thank everyone who has helped me on the way and hope that I can someday return the favor.

Curriculum Vitae

2008 – 2012	B.S. in Electrical Engineering, Pennsylvania State University.
2012 – 2015	M.S. in Electrical Engineering, University of California, Los Angeles (UCLA).
2015 – present	Ph.D. Candidate in Electrical Engineering, University ofCalifornia, Los Angeles (UCLA)

Publications

Curwen, C. A., Reno, J. L., and Williams, B. S. "Broadband continuous single-mode tuning of a short-cavity quantum-cascade VECSEL." *Nature Photonics*, in press.

Curwen, C. A., Reno, J. L., and Williams, B. S. "Terahertz quantum cascade VECSEL with watt-level output power." *Applied Physics Letters*, 113(1):011104, 2018.

Xu, L. Y., Curwen, C. A., Chen, D. G., Reno, J. L., Itoh, T., and Williams, B. S. "Terahertz metasurface quantum-cascade VECSELs: theory and performance." *IEEE Journal of Selected Topics in Quantum Electronics*, 23(6):1200512, 2017.

Xu, L. Y., Curwen, C. A., Reno, J. L., Williams, B. S. "High performance terahertz metasurface quantum-cascade VECSEL with an intra-cryostat cavity." *Applied Physics Letters*, 111(10):101101, 2017.

Xu, L. Y., Chen, D. G., Curwen, C. A., Memarian, M., Reno, J. L., Itoh, T., and Williams, B. S. "Metasurface quantum-cascade laser with electrically switchable polarization." *Optica*, 4(4):468-475, 2017.

Xu, L. Y., Curwen, C. A., Hon, P. W. C., Chen, Q. S., Itoh, T., Williams, B. S. "Metasurface external cavity laser." *Applied Physics Letters*, 107(22):221105, 2015.

CHAPTER 1

Introduction

1.1 Terahertz technology

The terahertz (THz) portion of the electromagnetic spectrum is often defined as the frequency range from 0.1-10 THz [25–27]. THz frequencies lie below the infrared range and above the microwave range (see Figure 1.1), but THz technologies have remained relatively undeveloped compared its neighbors. This is because THz frequencies lie in an awkward position where free carrier losses become too severe for traditional electronic techniques used by the RF and microwave communities, and photon energies are too small to utilize traditional optical techniques (typically based on semiconductor interband interaction). Therefore, THz work has developed into a rather multidisciplinary field that has encouraged engineering and development of a variety of novel optical and electronic techniques. One such technology, the THz quantum-cascade laser (QCL), is the subject of this thesis.

Terahertz applications generally stem from the strong interaction between THz waves and

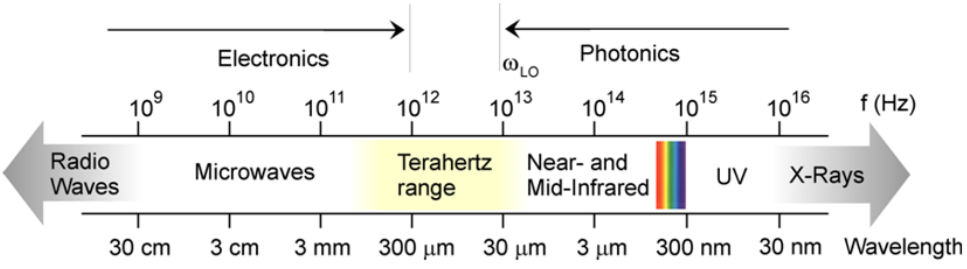

Figure 1.1: Electromagnetic spectrum with the terahertz range indicated between the microwave and infrared spectral domains. Figure taken from Reference [1]

many atomic, molecular, and crystal vibrational and rotational resonances, making THz a viable candidate for spectroscopic applications. Further, like many RF and microwave frequencies, THz waves are often transparent to materials such as plastics, fabrics, papers, etc., while simultaneously, the frequency and resolution are higher in the THz. This makes the THz range a good candidate for applications such as non-destructive evaluation and security screening. Presently, there are little to no large-scale applications in the THz range as the technology is simply not that developed, but there are many smaller companies developing products for specialty application (Virginia Diodes, LongWave Photonics, TeraSense, Tydex, Teraview, and more).

Perhaps the most notable and impactful THz technology (in the scientific community) has been THz time-domain spectroscopy (TDS), first demonstrated in the late 80's [28, 29]. THz TDS is a pump-probe technique for measuring the actual time-varying electric field of a THz signal (typically an ultra-short pulse). The technique has allowed for phase-resolved spectroscopy of ultrafast dynamics in various materials and even single molecules from anywhere between $\sim$0.1 to $>$40 THz in the most advanced systems [30–32]. THz pulses are typically generated from a femto-second optical laser either using optical rectification or conversion in a photoconductive antenna, and the pulses are similarly probed in time by the delayed optical pulse using the reverse nonlinear mechanisms (Pockel's effect or a photoconductive antenna). THz TDS is typically a table-top setup as it requires high-power ultrafast lasers, but with the increasing ubiquity of ultrafast fiber lasers, more compact versions of the system are becoming available from large companies such as Newport, Thorlabs, Menlo Optics, and Toptica Photonics.

Aside from TDS, there are still many applications such as imaging and high-resolution spectroscopy that require development of more traditional components. Currently, the leading sources for continuous THz power appear to be diode multiplier chains [33], molecular gas lasers, THz QCLs [34], and difference frequency generation either in a photomixer pumped by two diode lasers or in a two-frequency infrared (IR) QCL [34]. Both photomixers and diode multipliers are electronic techniques that see significant roll-off in power with increas-

ing frequency and are extremely weak above 3-4 THz (though improvements are still being made every day). Difference frequency generation in IR QCLs is a very compact and broadly tunable technique that can cover a range of ∼1-5 THz, limited by the *Reststrahlen* band of the IR QCL material, but is limited to microwatt power levels as it is based on parametric nonlinear conversion in the QC-material, which can be notoriously inefficient. THz QCLs are perhaps the best candidate for compact, high-power in the 1-5 THz range (again limited by the *Reststrahlen* band of the QC material), regularly generating tens of milliwatts of continuous wave power and in some cases >100 mW [35]. The down side of THz QCLs is that they must operate at cryogenic temperatures, and it is difficult to efficiently extract the THz power into a usable beam. It should be noted that free-electron lasers exist as a class of their own and are capable of generating high-power THz radiation at any frequency, but they are very large and expensive systems that can be maintained by few laboratories [36].

1.2 Quantum-cascade lasers

Quantum-cascade lasers are a type of unipolar semiconductor laser based on intersubband transitions between carefully designed electron states in the conduction band of a semiconductor heterostructure. Unlike traditional interband semiconductor lasers, where the laser emission wavelength is fixed by the band gap between the conduction and valence band of the material, the emission wavelength of an intersubband QCL can be chosen arbitrarily by simply adjusting the width of the quantum wells. Further, the energies of intersubband transitions can be made much smaller than any typically available material bandgaps, extending semiconductors to longer wavelengths than ever before. The currently covered wavelength range for QCLs is from 1.2 THz (250 μm) - 2.6 μm, with a gap from 5.4 THz (55 μm) - 28.3 μm due to the *Reststrahlen* band between the LO- and TO-phonon resonances of the semiconductor material, which restricts propagation of light [37–40]. By applying a DC magnetic field to further quantize the electron states into Landau levels, the lasing frequency can be reduced to 0.68 THz (440 μm) [41]. The shortest wavelength that can be emitted by a QCL is limited by the band offset of the materials used in the heterostructure, while the longest

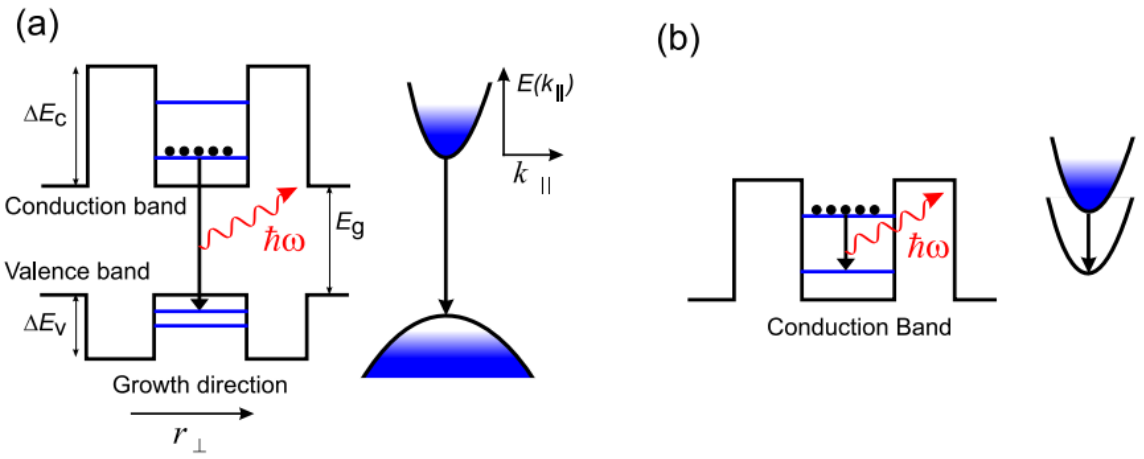

Figure 1.2: (a) Band diagram of an interband laser based on recombination of electrons and holes across the semiconductor material bandgap. Lasing frequency is given by the size of the bandgap per $E{=}h\nu$. (b) Band diagram of an intersubband laser based on electrons making radiative transitions between two confined states in the conduction band. The energy separation and thus lasing frequency can be engineered using the controllable widths of the quantum wells and barriers. Figure taken from Reference [2].

wavelength is limited by thermal excitation of carriers preventing population inversion (i.e. the energy of the laser transition is on the order of $k_B T$). A mostly up-to-date collection of lasing frequencies and operating temperature are shown in Figure 1.3 [3].

1.2.1 Active region design

The first QCLs were demonstrated in the mid-IR using the InGaAs/AlInAs/InP material system, grown in a molecular-beam epitaxy (MBE) chamber. Early designs essentially used a chirped superlattice consisting of a series of ∼10 sequentially narrowing quantum wells, and this module is cascaded tens of times for a total active region thickness of 1-2 μm. At zero-bias, the band diagram (tracking the lowest state in each well) has a sawtooth shape, with the step size designated by the intended lasing energy. As bias is applied, the ramp of the sawtooth levels out as the states align into a miniband that allow transport between modules via resonant tunneling (Figure 1.4). The structure can be described as a 3-level laser where the objective is to maintain a population inversion between states 2 and 3 (quick

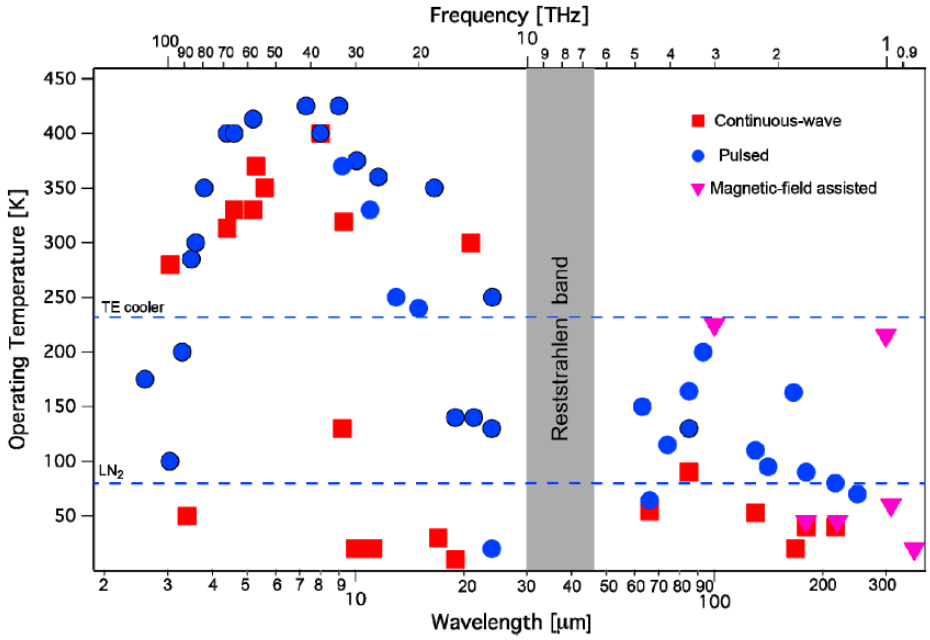

Figure 1.3: Summary of reported QCL lasing frequencies and operating temperatures. Lower frequencies require lower temperature operation as the photon energy becomes comparable to $k_B T$, making it difficult to maintain a population inversion. Figure taken from Reference [3].

depopulation of the lower level and long lifetimes for the upper level). The key elements of the design that allow for such a population inversion are:

- A large transition energy associated with the mid-IR photons (on the order of hundreds of meV) that increases the lifetime of the upper laser level thanks to a reduced non-radiative scattering rate. LO-phonons are the primary non-radiative scattering mechanism out of state 3, but because the LO-phonon energy is much smaller than the mid-IR transition, such a transition involves a large change in momentum and occurs with a low probability (small spatial overlap between the states). Non-radiative scattering times of several picoseconds are easily achieved.

- Fast depopulation of the lower laser level 2 into level 1. This is often accomplished by designing the energy separation between these states to be resonant with the LO-phonon. LO-phonon scattering is extremely fast when resonant, typically sub picosec-

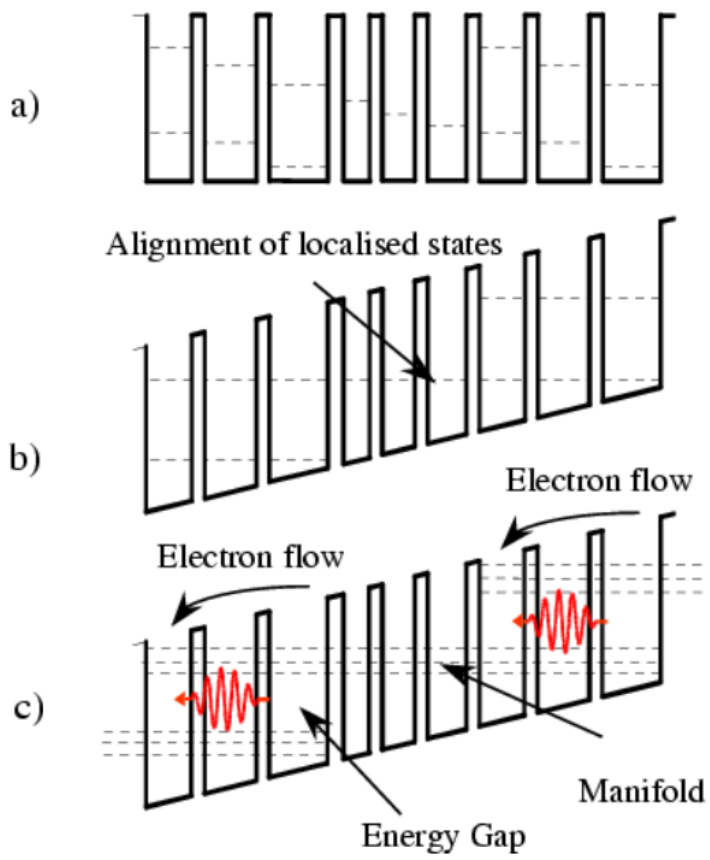

Figure 1.4: Basic quantum-cascade design concept. (a) Unbiased chirped superlattice. The bottom states of the wells form a step function with the period of the design. (b) Biased structure showing alignment of the bottom states of the wells, and (c) splitting of the aligned states into a miniband of coupled resonances and the resulting electron transport indicated. Figure taken from Reference [4].

ond.

- Efficient injection from level 1 into upper laser level 3 of the neighboring module via the miniband.

The first demonstrated mid-IR QCL (Faist, *et al.* 1994, Ref. [42]) operated in pulsed mode at cryogenic temperatures, lased at 4.2 μm, and emitted a peak power of $\sim$10 mW, but significant interest in the field led to rapid improvements. By 2002, continuous wave operation was demonstrated at room temperature [43], and today, up to 30 W of continuous

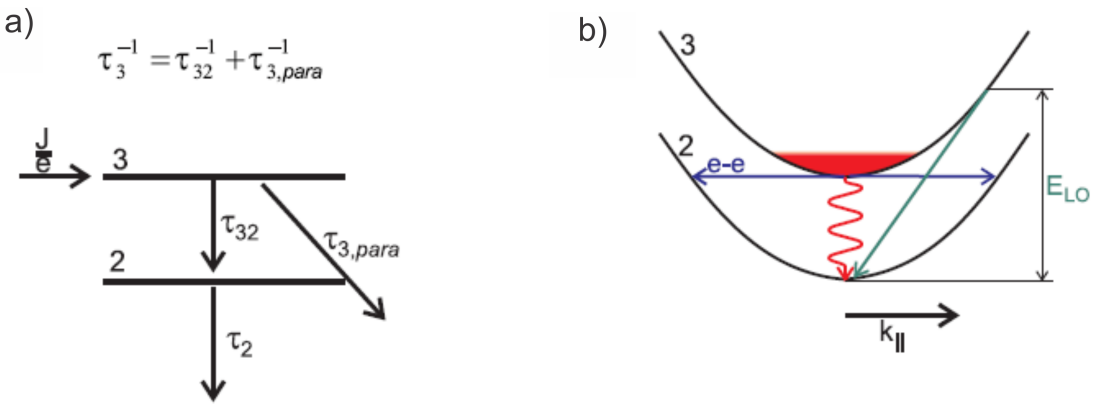

Figure 1.5: (a) Depiction of three-level laser model for a QCL. (b) Illustration of intersubband scattering mechanisms. At higher temperatures, the average in-plane momentum of the carriers in a subband rises, enabling non-radiative LO-phonon scattering that prevents population inversion. Figure taken from Reference [1].

wave output power has been demonstrated at room temperature from a single frequency source at 4.8 μm [44].

Though lasing in the THz (i.e. below the *Reststrahlen* band) was predicted by the seminal paper in 1994, the first THz QCL was not demonstrated until 2001 due to challenges in maintaining a population inversion between subbands with such small energy separations (order of magnitude smaller than mid-IR energies). These challenges typically amount to issues with selectively injecting into the upper laser state and not the lower, and similarly, selectively depopulating the lower laser state and not the upper. Other considerations include the need for a narrow miniband to avoid reabsorption of emitted photons and to prevent LO-scattering out of the upper laser state, the need to operate at cryogenic temperatures to suppress thermally activated LO-phonon scattering between the upper and lower lasing states (see Figure 1.5), and the need to develop low-loss, high confinement THz waveguides as dielectric waveguiding is not feasible at such long wavelengths (see below).

In 2002, the first demonstrated THz QCL by Kohler, *et al.* (4.4 THz, 2 mW peak power, 50 K maximum temperature, Figure 1.6(a)) was effectively an extension of the mid-IR design concept, but the lower radiative state is directly depopulated by the miniband, skipping

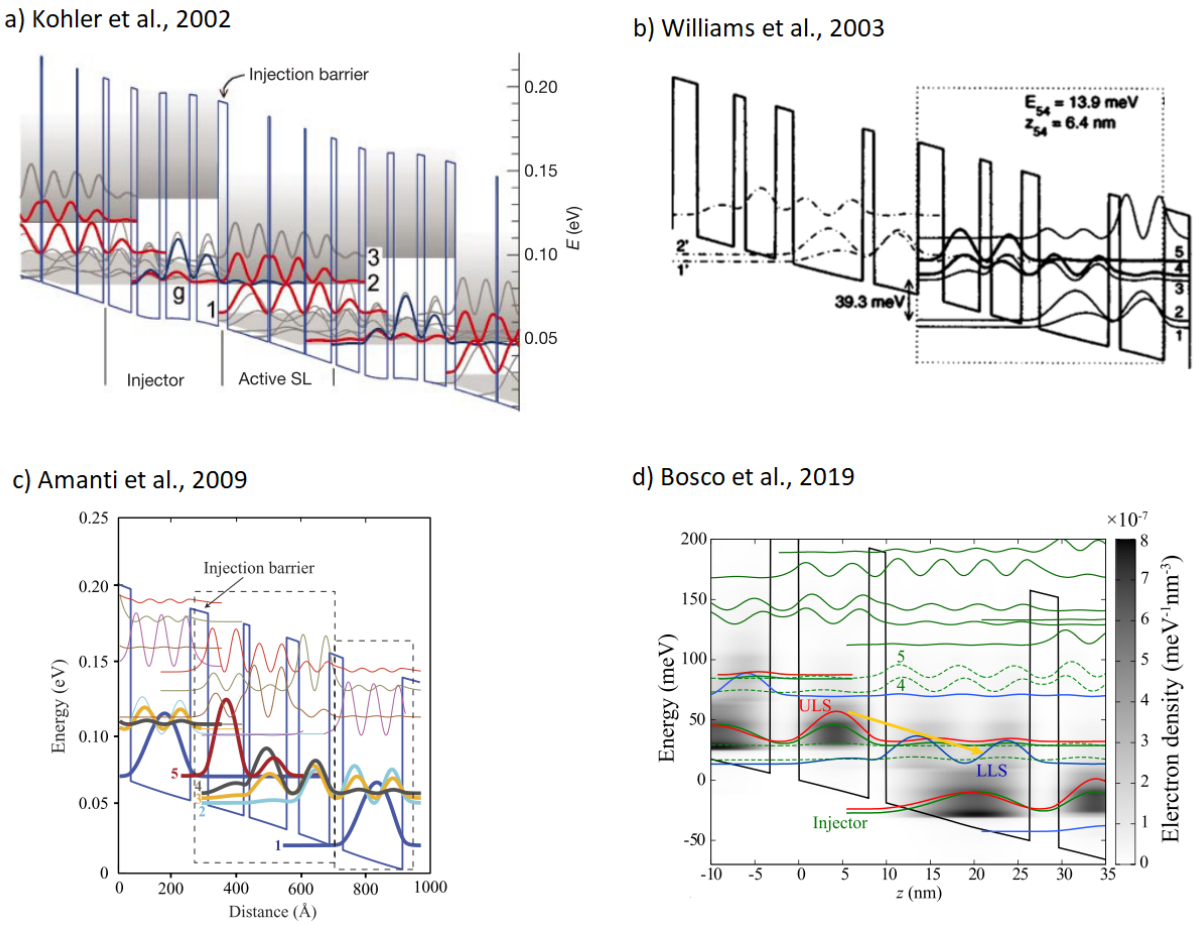

Figure 1.6: Development of THz QCL active regions (a) First demonstrated THz QCL based on the 'bound-to-continuum' design [5]. (b) First THz QCL using phonon depopulation of the lower radiative state, the 'resonant-phonon' design [6]. (c) 'Hybrid resonant-phonon bound-to-continuum', a modified version of which will be used through most of this thesis [7]. (d) A two-well resonant-phonon design that currently holds the record for operating temperature [8].

the intermediate step of depopulating the lower radiative state into the miniband via an LO-phonon [5]. In 2003, Williams, *et al.* demonstrated the first design based on phonon-depopulation of the lower radiative state (3.4 THz, 2.5 mW, 65 K maximum temperature, Figure 1.6(b)) [6]. Use of phonon-depopulation has proved over the years to result in higher temperature performance than miniband designs as phonon scattering is extremely fast, though miniband based designs operate at a lower bias, reducing their power consumption.

Interestingly, the record high operating temperature (in pulsed mode) is currently held by a 2-well phonon-depopulation design involving three states, the simplest possible phonon-depopulation scheme [8]. The success of the approach is attributed to this minimization of states. Bosco, *et al.* effectively argue that by minimizing the number of states per-module, it is easier to force a larger fraction of the population to the upper laser state while the lower laser level is still efficiently depopulated by the phonon resonance. By this logic, it seems possible that the lower laser level may also contain a larger fraction of the carriers, but presumably proper design can lean in the favor of adding more to the upper-state than the lower. Indeed, for many years now, increased temperature performance seems to be associated with simpler phonon-depopulation designs with fewer wells and states per-module [45, 46]. The downside of the 2-well design is that strong leakage channels result in very large current draw, making it a very bad design for continuous wave operation. Control of these leakage channels has been the subject of much investigation [47–49], but strangely the best temperature performance has come from a design that seems to embrace this leakage, as long as it does not affect the simulated population inversion.

The active region design that will be used for most of the devices in this thesis is based on a design by Amanti, *et al.* in 2009, which has been, from the author's experience, one of the most successful designs in terms of reliability and power [7]. The design is similar to the first resonant phonon design in Ref [6], but the lower laser level is not directly in resonance with the upper level of the phonon transition, and instead an extra well has been added between. This extra well in combination with a diagonal lasing transition appears to reduce non-radiative scattering out of the upper laser level while maintaining fast depopulation of the lower laser levels via resonant-phonon scattering. The possibility of radiative transitions between the upper radiative state and 3 possible lower radiative states (each separated by several meV) seems to result in very broad gain bandwidth as well.

1.2.2 THz QCL waveguides design

An equally important development in realizing QCLs in the THz regime was the design of low-loss, high confinement waveguides. Mid-IR QCLs can use dielectric waveguides as the thicknesses of the active region and cladding layers can be made proportional to the lasing wavelength (a couple micron given the refractive index of the material). This approach cannot be extended to THz frequencies as the wavelengths are an order of magnitude larger, but current semiconductor technology does not allow growth of QC-active regions or cladding layers that are an order of magnitude thicker, and such a doped semiconductor waveguide would be highly lossy anyways. Two solutions have become commonplace in the field: single surface-plasmon (SP) waveguides [5] and metal-metal (MM) waveguides [50].

SP waveguide design sandwiches the QC-active material (typically 5-10 μm thick) between a metallic waveguiding layer on top and a buried, highly-doped SP waveguiding layer underneath. The surface plasmon layer offers improved confinement of the THz field to the active material compared to a purely dielectric interface, but there are still substantial evanescent THz fields that leak into the substrate, so the substrate is made of high-resistivity semiconductor to minimize optical losses, and the current is instead extracted laterally through the SP layer. This modal leakage is both the advantage and disadvantage of the approach in that it offers improved outcoupling efficiency and beam quality compared to the MM waveguide, but it also results in higher threshold gain and worse temperature performance.

The MM waveguide design is similar to the SP design, except that both of the waveguiding layers are metallic. The advantage of the MM waveguide is that the higher confinement factor and low-losses associated with the double metal waveguiding layers results in lower threshold gains and higher temperature performance compared to SP waveguides. The disadvantage is that the extremely subwavelength confinement of the mode results in very high reflectivity facets and a very diffracted beam pattern [51, 52]. In response, a long list of alternative coupling techniques (primarily grating based) have been investigated including, but not limited to:

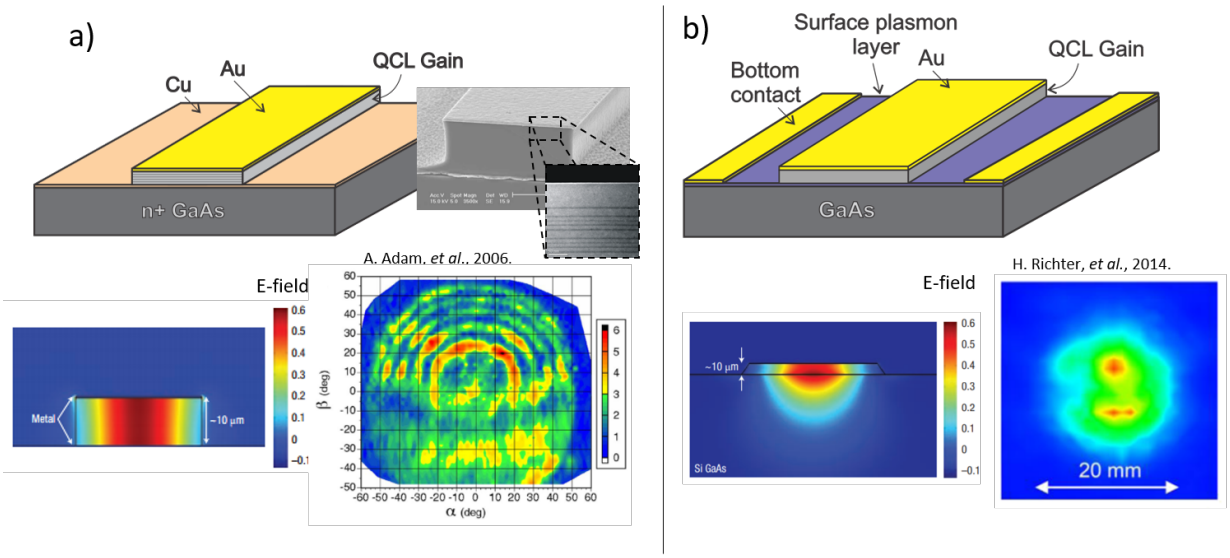

Figure 1.7: (a) Illustration and SEM of metal-metal waveguide for THz QCLs. The simulated field profile in the waveguide is plotted along with a measured output beam pattern which is observed to be very diffracted. (b) Surface-plasmon waveguide illustration, simulated waveguide fields, and measured output beam pattern. The beam is considerably improved thanks to the larger mode profile.

- *Surface coupling using a 2^{nd}-order distributed feedback (DFB) grating* [53–55]: by introducing a 2^{nd}-order diffraction grating with period Λ equal to the guided THz wavelength, surface emission occurs as dictated by the diffraction condition that incident wavevectors couple to wavevectors offset by an integer multiple of the grating wavenumber: $\vec{k}_f = \vec{k}_i \pm m\vec{k}_{grating}$. If $\vec{k}_i$ is equal to $\vec{k}_{grating}$ and m=1, then $\vec{k}_f = 0$, which gives a wave propagating in the out-of-plane direction. This approach has the advantage of a large radiating aperture that should produce a narrower beam (albeit an elliptical beam as the ridge is much longer than it is wide), but has seen little success as the grating coupled waveguide has two solutions with opposite symmetry; one that radiates and one that does not (dark mode). Typically, the dark mode will lase by virtue of a lower threshold gain, but in a finite structure the laser operates slightly off the grating wavenumber and a small amount of power is coupled out of the surface into an multilobed beam. Such was the case for the first 2^{nd}-order THz QCLs, but a couple of

modified techniques have found ways around this problem:

  - *Surface coupling using a graded 2^{nd}-order DFB* [56]: In Xu *et al.*, a design is presented using a graded 2^{nd}-order grating whose period was varied parabolically along the length of the ridge. This results in a parabolic photonic bandstructure that leads to a large frequency difference between the bright and dark modes of the cavity, allowing the designers to push the dark mode outside of the QC-gain bandwidth, forcing it to lase on a bright mode. Up to 50 mW of power was achieved with a slope efficiency of 230 mW/A.

  - *Surface coupling using a hybrid 2^{nd}- and 4^{th}-order grating* [11]: Perhaps the most clever and simplistic scheme, a 4^{th}-order grating is superimposed on a 2^{nd}-order grating. The 4^{th}-order grating is phase shifted from the 2^{nd}-order grating which introduces constructively radiating apertures for the previously dark 2^{nd}-order mode (which should otherwise be minimal effected by the addition of the 4^{th}-order grating). The phase-shift acts as a knob that can tune the degree of radiative coupling. High peak power of 170 mW and record slope efficiency of 993 mW/A was demonstrated.

- *Surface coupled photonic crystals* [57–59]: effectively a 2-D extension of the 2^{nd}-order grating coupled scheme. Improved beam patterns with up to 10's of mW of single-mode pulsed power have been demonstrated.

- *Edge emitting 3^{rd}-order DFB* [9, 55, 60–62]: The key principle in this approach is to design the refractive index of the metal-metal waveguide ridge (using control of ridge width) to be exactly n = 3, and to introduce a 3^{rd}-order grating. In this manner, if we again consider the diffraction equation above, we find that if the THz waveguide has an effective refractive index of 3, and the $\vec{k}_i$=1.5×$\vec{k}_{grating}$, then the first diffracted mode has an effective refractive index n = 1, the second n = -1, and the third n = -3. Therefore, the grating provides both feedback and coupling to free space (n = 1). 3^{rd}-order gratings have demonstrated excellent beam patterns, but the phase matched

condition is difficult to hit (waveguide with an index of exactly 3).

- *End-fire antenna-coupled grating structure* [10]: In this approach, a metallic grating is patterned into the top contact of a THz QCL and is used to couple the waveguided mode to an SP mode propagating in free space on the top side of the contact. The resulting standing wave radiates efficiently in the end-fire direction through the SP mode acting as a source of coherent radiators. The devices generated excellent beam patterns, but peak power was limited to a couple milliwatts.

- *Surface coupling with an array of patch antenna* [12,63]: Demonstrated milliwatt level power into a relatively directive surface emitting beam using a 3×3 array of circular patch antenna integrated at the end of a metal-metal ridge waveguide, separated by a small coupling gap.

Other noteworthy examples not discussed include [64–67].

1.3 THz QCLs for remote sensing

An application that has drawn particular attention for THz QCLs is remote sensing of interstellar dust clouds using frequency agile heterodyne spectroscopy [68–71]. Heterodyne detection is a passive technique for detecting small signals at a very specific frequency in a noisy environment. The key elements are the detector, the mixer (sometimes one in the same), and the local oscillator (LO). The incoming, noisy signal is received by the detector and mixed with a reference signal (the LO) at the desired frequency in a nonlinear element (the mixer), and the resulting beat note is observed on a spectrum analyzer, indicating the exact magnitude and frequency of the incoming signal. Astronomers have expressed interest in several molecular lines including a fine carbon line [CII] at 1.9 THz [72], an oxygen line [OI] at 4.7 THz, and a hydrogen deuterium [HD] line at 2.7 THz. These measurements must be performed from a space-based platform, or at least high altitude as atmospheric absorption in the THz is much too large to make observations from Earth's surface. For years, diode

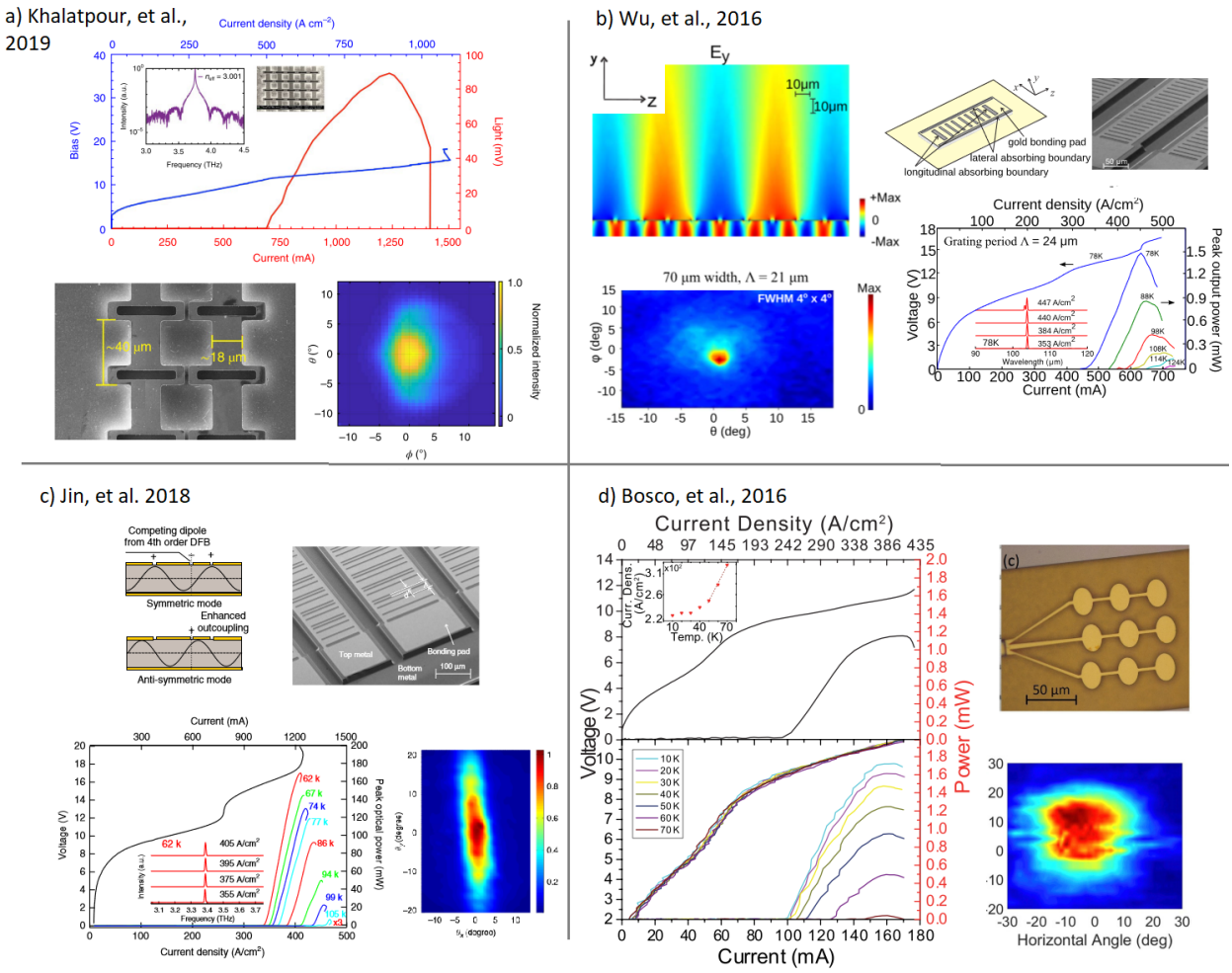

Figure 1.8: Selection of power outcoupling schemes. (a) 3^{rd}-order distributed-feedback laser arrays [9]. (b) End-fire surface-plasmon coupling scheme [10]. (c) Superimposed 4^{th}-order and 2^{nd}-order surface coupling scheme [11], (d) Surface-coupled patch array [12].

frequency multipliers have been the go-to source for high-frequency local oscillators as they are compact and reliable, but as mentioned above, the power from diode multipliers drops exponentially as the frequency is increased [33, 73, 74]. Above 2-3 THz, it is difficult to obtain more than microwatt power levels, which may be enough to pump a single detector, but for more reasonable observation times, the community is pushing for large array detectors [70]. THz QCLs are perhaps the leading candidate to replace diode multipliers at higher frequencies as THz QCLs are compact, high power, and perform very well in the 2-5 THz

range, but difficulties with poor beam qualities and inefficient coupling have made realization of such systems challenging.

To date, two QCL based heterodyne instruments have been utilized in the field, both at 4.7 THz (63 μm). One instruments was a single-pixel 4.7 THz heterodyne receiver designed for the Stratospheric Terahertz Observatory 2 (STO-2), a balloon based mission in Antarctica managed by NASA and the University of Arizona [75, 76]. The detector used a 3^{rd}-order DFB THz QCL developed at MIT as the LO, however communications with the controller for the QCL failed and no useful data could be collected. A follow-up balloon mission, the Galactic/Extragalactic ULDB Spectroscopic Terahertz Observatory (GUSTO), is set to launch in December of 2021 and will implement a 2×4 detector array, again pumped by a 3^{rd}-order DFB developed at MIT [77]. The second instrument is the German Receiver for Astronomy at Terahertz frequencies (GREAT), and subsequent upGREAT, which have flown since 2014 on the Stratospheric Observatory for Infrared Astronomy (SOFIA), an airplane based observatory developed and managed jointly by NASA and the German Space Agency (DRL) [13, 78, 79]. GREAT was a single pixel detector utilizing a 4.7 THz surface-plasmon QCL with a lateral 1^{st}-order DFB grating. The laser generated 6 mW of power directly from the facet, while 1.2-2.2 mW of power were actually available after passing through the cryostat window and beam shaping optics. A mechanical Stirling cooler (7 W cooling power) was used to maintain a heat sink temperature of 50 K. Only temperature control was used for frequency stabilization, and the linewidth was estimated at ∼1.6 MHz (using the edge of a methanol line as a frequency discriminator). The active region design was a 'modified bound-to-continuum design' where the bottom state of the miniband scatters into the upper laser level of the neighboring module via LO-phonon scattering. The design was intended to take advantage of phonon scattering to rapidly deplete the miniband while having lower bias requirements compared to a resonant-phonon design. The total thermal load of the device was ∼2.5 W (500 mA and 5 V).

GREAT operated during six flights on SOFIA between May 2014 and January 2015, after which it was replaced by upGREAT, a 7-pixel version of the system. Two QCLs (both

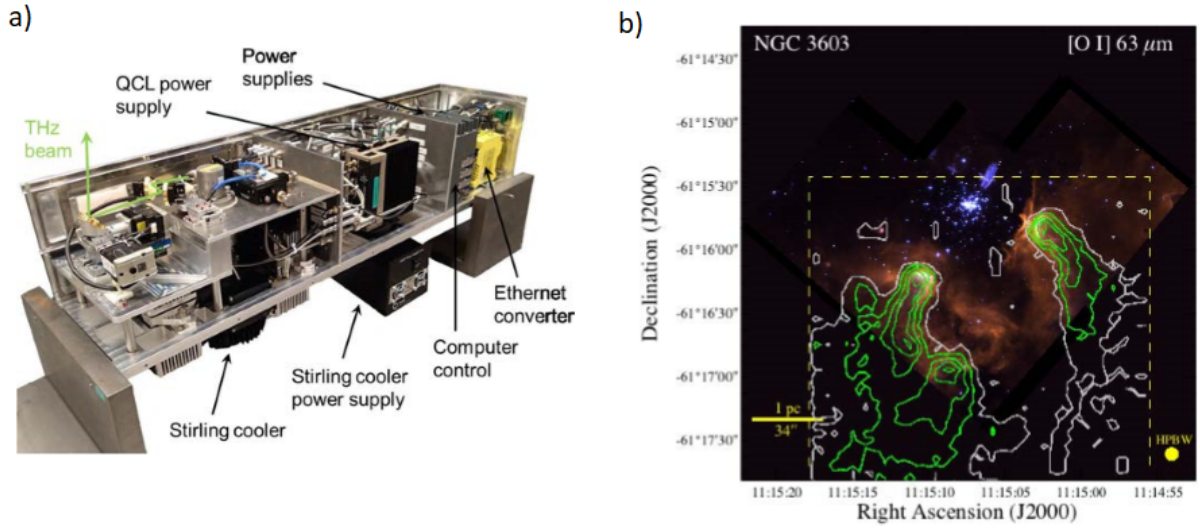

Figure 1.9: (a) Photograph of the upGREAT 4.7 THz local oscillator (including power supply, optics, electronics, etc.). Dimension are 100×23×23 cm. (b) Sample data collected with the upGREAT system. Contour plot shows velocity integrated intensity map of [O I] emission from star cluster NGC3603, one of the Milky Way's most active stellar nurseries. Figures taken from Reference [13].

4.7 THz) have been utilized with the upGREAT system [80]; the same DRL laser used with GREAT, as well as a laser based on the design developed by Bosco *et al.* at ETH Zurich [12] using a 3×3 patch array at one end of the device. The Bosco device is based on the hybrid bound-to-continuum resonant-phonon active region [7] and provided 2.4 mW with a frequency stability of <1 MHz. For both lasers, distribution of the LO-power into the seven identical beams for the seven pixels is accomplished with a Fourier grating [81]. The grating is reported to have 90% efficiency and <0.5% power fluctuation between the seven beams. Waveguide coupled NbN hot-electron superconducting bolometers have been used as the detectors/mixers in all studies [82,83]. Using the data from upGREAT, astrophysicist have primarily studied the outflow of [OI] from protostallar jets (see Figure 1.9) [84–88]. Understanding the details of star formation and lifecycle is crucial as it is one of the primary mechanisms by which matter is created and distributed throughout the universe. This was the subject of many measurements performed by the Herschel Space Observatory (managed

by the European Space Agency, operated from May, 2009 - June, 2013). The Herschel Observatory was capable of performing measurements from 55-672 μm, where emission is strongest from warm (30-100 K), dust shrouded star forming regions [89, 90]. Measurements targeted at investigating water and oxygen content outflow from protostars (forming stars that are still accumulating mass from an accretion disk, prior to the onset of fusion at the star's core) indicated a larger outflow of atomic oxygen [O I] than was expected, prompting a call for more data with higher spatial and spectral resolution to perform velocity resolved measurements [71, 91]. The "Origins Space Telescope" (OST) is one of the four "Flagship Surveyor Missions" being studied by NASA for consideration by the 2020 Decadal Survey of Astronomy and Astrophysics [92, 93]. The OST is envisioned to have a telescope diameter between 8 m and 12 m, which would be a factor of 3 larger than the Herschel's primary mirror. For a nominal diameter of 10 m, the diffraction-limited beam width is 4" at $\lambda =$ 158 μm (1.9 THz). However, the regions of interest are few to tens of arcminutes in size, requiring observations of thousands to tens of thousands of positions in order to follow the rapidly-varying kinematics and chemistry. To carry this out in reasonable amounts of time thus requires heterodyne focal plane arrays. A Heterodyne Receiver for OST (HERO) has been proposed for this platform with several frequency bands ranging from 0.5 THz to 2.7 THz and an optional band at around 4.7 THz [94]. Pumping such large arrays with diode mixers up to 4.7 THz may be difficult, but researchers in that field have proposed a 64-pixel detector for OST at 4.7 THz using diode multipliers, arguing that only 3 μW of power is needed per pixel, given that the signal and LO are superposed in orthogonal polarizations so there are no beam splitter losses. Regardless, QCLs may be able to provide the necessary power more efficiently, and offer enough power to pump even larger arrays, but work is still needed on the performance and reliability of QCLs to make them viable candidates for a space based telescope. Most of this thesis is focused on such improvements with regards to output power, beam quality, and tunability of THz QCLs.

CHAPTER 2

The THz QC-VECSEL

2.1 Introduction

The THz quantum-cascade vertical-external-cavity surface emitting laser (QC-VECSEL) is a new approach for designing THz QC-lasers developed in Prof. Benjamin Williams' lab at UCLA and first published in 2015 [16]. The fundamental concept is to use THz QC-active material to design a large-area, reflecting THz amplifier that can be inserted as a gain chip in an external cavity laser. The advantage of this approach is that the radiating aperture of the THz amplifier and external cavity optics can be made large (millimeter scale) compared to the THz wavelengths (on the order of 100 μm). Therefore, a high-quality, Gaussian shaped beam can coupled out of the cavity, and further, the laser power can be scaled by simply scaling the dimensions of the THz amplifier.

The VECSEL concept is borrowed orginally from the solid state laser community (often refered to as 'disk lasers'), where the technique was developed, similarly, for the purposes of high-power and good beam quality compared to ridge waveguide devices [95]. The VECSEL typically consists of a optically pumped solid state gain material on top of a reflective surface. The gain chip is then placed in an external cavity resonator to form a laser. The concept has been extended to semiconductor lasers, where the gain chip consists of a multiple quantum well gain material grown on top of a dielectric Bragg mirror that provides low-loss and high-reflectivity to normally incident waves (Figure 2.1(a)). Most interband VECSELs are optically pumped as electrical contacts would normally prevent surface coupling. Electrically pumped devices have been demonstrated but must be small in size, defeating much of the purpose [96]. In addition to high-power and beam quality, the external cavity bases for

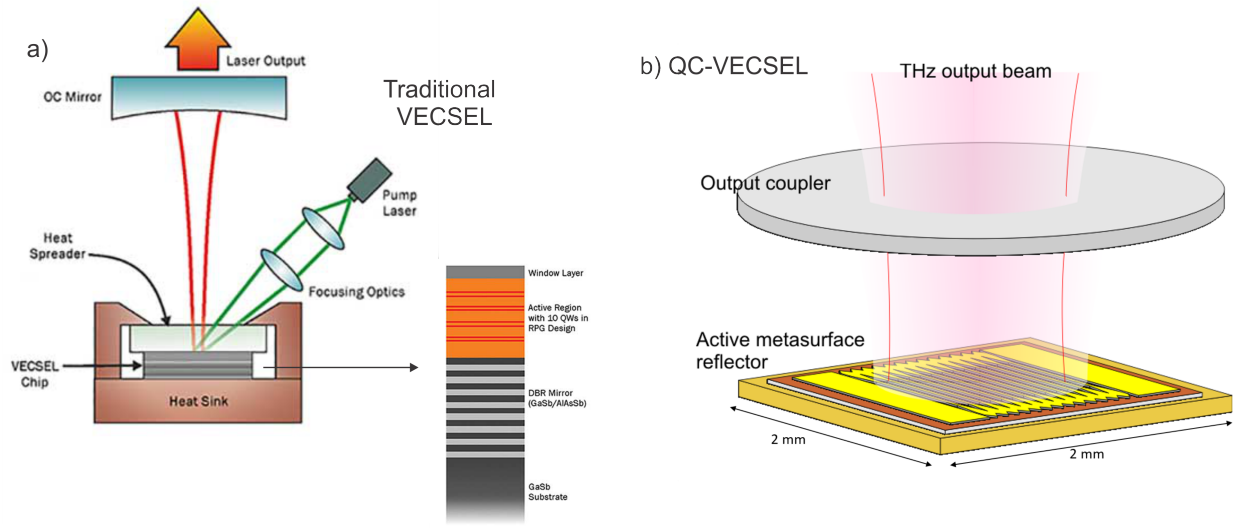

Figure 2.1: (a) Illustration of an optically pumped interband VECSEL utilizing a dielectric Bragg mirror for the bottom reflector. The gain chip sandwiched between two heat sinking layers to allow for higher pump and output powers. (b) Illustration of the THz QC-VECSEL. The copper ground plane acts as a reflector, removing the need for a Bragg mirror, and no pump laser is required as the metasurface is electrically pumped.

VECSELs have given access to a variety of techniques for mode-locking, broadband tuning, and nonlinear generation with semiconductor lasers [97–101].

The VECSEL concept cannot be directly extended to QC-lasers because the intersubband gain cannot be coupled to the in-plane polarization of the of waves in a vertical cavity. Therefore, a scheme must be implemented that rotates the in-plane polarization of normally incident THz waves, coupling them to the gain material and subsequently re-radiating the amplified waves back in the surface direction. In this chapter, we review the basic design and techniques used to realize such a surface-coupled QC-amplifier, henceforth to be referred to as the metasurface, and the subsequent results from early THz QC-VECSEL lasers.

2.2 QC-VECSEL metasurface design

The original metasurface design is illustrated in Figure 2.2. The metasurface consists of an array of narrow metal-metal ridge waveguides loaded with THz QC-gain material. The ridges are spaced with subwavelength periodicity to avoid diffraction effects ($\Lambda < \lambda_0$, hence the term 'metasurface') and are coupled to surface incident radiation on a unit-cell basis via the TM_{01} transverse cutoff resonance at $\nu_0 \approx c/(2nw)$, where w is the width of the ridges and n is the refractive index of the quantum cascade material filling the ridge. The odd symmetry of the fields on the two sidewalls of the ridge result in magnetic dipoles that constructively interfere, given by:

$$\vec{M}_s = 2\hat{n} \times \vec{E}. \tag{2.1}$$

Normally, phase variation along the length of the ridge would cancel such radiation or result in leaky wave radiation at an angle, but at the cutoff frequency, the group velocity is zero and there is no phase variation along the length of the ridges giving constructive interference in the surface direction. This is the same formalism used to describe the operation of patch antenna, which are ubiquitous in the microwave community and have been utilized by the THz and mid-IR QC-laser communities as well. Free-standing aeroth-order resonators for THz QCLs were first investigated by Tavallaee, *et al.* but were found to be too lossy to lase without feedback, partly inspiring the QC-VECSEL concept [102–104].

Periodic finite-element (FEM) simulations of an effectively infinite metasurface can be performed with COMSOL Multiphysics. In Figure 2.2(c), reflectance spectra of a metasurface with a period Λ=70 μm and ridge width w=11.5 μm are plotted for varying applied intersubband gain. When no gain is applied, an absorbing dip is observed at the designed frequency, and when sufficient gain is applied, it changes to an amplifying peak around the same frequency. The gain at which the metasurface switches from absorbing to amplifying (when reflectance R=1) is referred to as the transparency gain. The maximum amplification factor that can be achieved sets the limit on the amount of loss (output coupler and

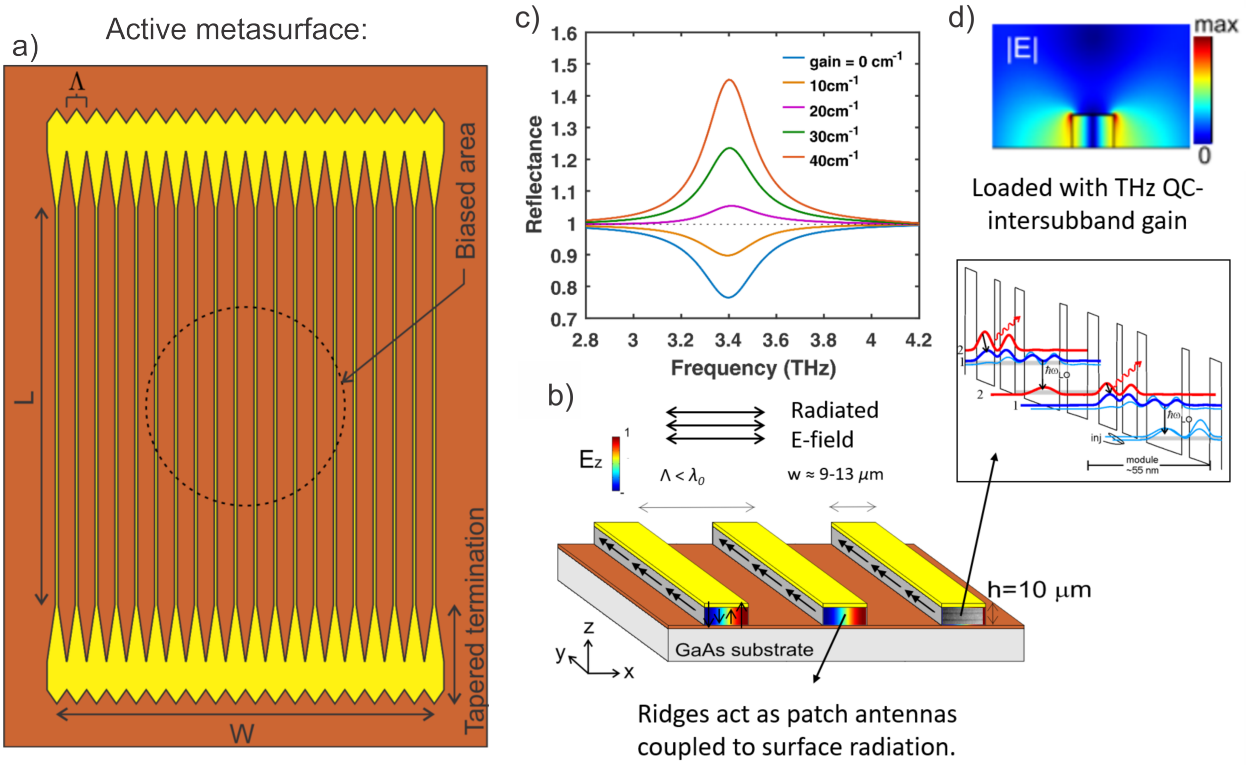

Figure 2.2: (a) Bird's eye illustration of typical metasurface with the biased area and tapered terminations indicated. (b) Illustration of a small portion of the metasurface with the TM_{01} field profile and corresponding radiation mechanism indicated. (c) FEM simulated reflectance spectra as a function of applied intersubband gain for a metasurface designed to operate at 3.4 THz (Λ=70 μm, w=11.5 μm), and (d) the corresponding fields from the simulation.

diffraction) that can be tolerated in the external cavity. As expected, there is a 2π phase shift associated with the metasurface as well. This is an important point as it gives access to a host of developed techniques for designing flat optics based on metasurfaces. A focusing metasurface, for example, is discussed below in Section 2.4. This phase also becomes relevant when considering frequency tuning techniques for the QC-VECSEL (see Chapter 4).

Another important observation about the metasurface is that it has a very broad spectral response. This is a result of the large radiative losses compared to stored energy in the

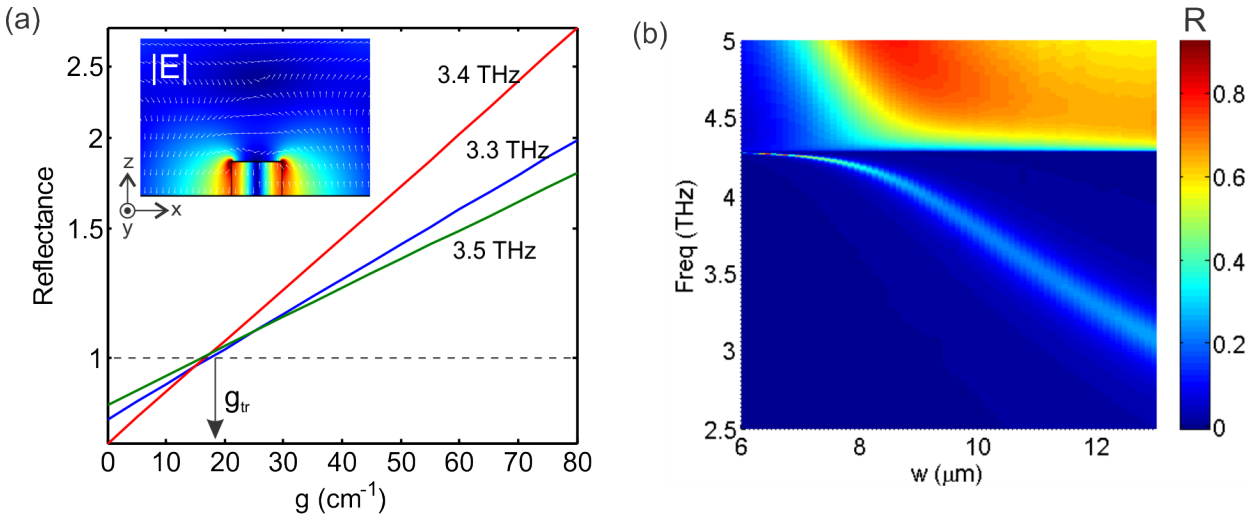

Figure 2.3: (a) Peak reflectance as a function of gain for metasurfaces with varying quality factor (resulting from varying the ridge width w while the period Λ is kept constant). Peak reflectance increases with quality factor because the THz waves spend more time in the metasurface accumulating gain. (b) Color plot showing the full reflectance spectrum as a function of quality factor (again by varying w while Λ is kept constant). A strong anticrossing is observed when the resonant frequency of the Bragg mode (associated with Λ, flat line at $\approx$4.25 THz) is equal to the resonant frequency of the ridge elements (associated with w.

metasurface, i.e. the metasurface has a low quality factor:

$$Q = \frac{\nu_0}{\Delta\nu} = \frac{\nu_0}{2\pi(\alpha_{abs} + \alpha_{rad})}, \tag{2.2}$$

where ν_0 is the center frequency of the metasurface resonance, $\Delta\nu$ is the full-width half-max (FWHM) bandwidth of the resonance, and α_{abs} and α_{rad} are the loss coefficients (in terms of power) resulting from material absorption and radiation respectively. For the THz metasurfaces discussed in this thesis, typical Q values are $\approx$ 5 - 10. The low quality factor of the metasurface is an important conceptual point as it is what allows the metasurface to operate as an amplifier, rather than a self-lasing structure. High-Q metasurfaces capable of self-lasing into a narrow surface-directed beam have been demonstrated by Kao *et al.* [21,105]. Such a self-lasing metasurface is very interesting as it also offers high beam quality and scalable power while doing so in a monolithic package. By moving to a low-Q metasurface

in an external cavity, the setup is modestly more complex, but the functionality of a single metasurface can be greatly increased, namely in broad tunability of the lasing frequency and outcoupling efficiency. A large number of self-lasing high-Q metasurfaces would be needed to cover the same parameter space, which becomes a significant problem as the wafer material is extremely expensive and metasurfaces are very large area devices. In order to prevent self-lasing of the individual ridges of the metasurface presented in this thesis, tapered termination have been added to the ends of each ridge to prevent strong facet reflections for propagating waveguide modes. These tapered ends lead to a large area for wire-bonding.

The radiative loss of the metasurface, and thus the quality factor, can be tuned by adjusting the period of the metasurface (see Figure 2.3(b)). This can be understood by considering coupled mode theory. The eigensolutions of an infinite metasurface are a superposition state of the radiating TM_{01} ridge resonance and a bound Bragg mode associated with the grating period. This coupling to the Bragg mode gives the metasurface solution a certain degree of in-plane momentum and reduces the radiative losses in the surface direction, increasing the quality factor of the metasurface. This bound in-plane coupling is of particular importance when considering a finite metasurface as it effectively results in a form of diffraction loss of energy off the edges of the metasurface traveling in the in-plane direction. As the resonances become closer, the degree of in-plane coupling and resulting diffraction loss increases. To prevent excessive losses, simulations of finite metasurfaces indicate that the metasurface period should be kept less than $\approx 80\%$ of the free space wavelength. Eventually, when period of the grating becomes greater than the wavelength of the TM_{01} resonance, the energy begins to couple to diffracted waves reflected at an angle: $\Lambda\sin(\theta)=m\lambda$, where Λ and λ are the grating wavelength and lasing wavelength respectively, and m is the diffraction order. Operating away well away from the diffraction condition so that the properties of the metasurface are primarily dependent on the unit cell design, not the period of the structure is, of course, the fundamental basis of the metamaterial field.

A second, similar way to think about the problem is based on array theory and representing the sidewalls of the ridges as dipoles. As the ridges become more sparse, the radiative

efficiency in the surface direction is reduced, and the quality factor and passive absorption increase. For the in-plane direction, there is effectively a phase mismatch between the grating wavenumber and the free space wavenumber of the lasing frequency. In an infinite metasurface, this prevents the constructive build-up of any energy propagating in the in-plane direction. In a finite metasurface, however, the symmetry is broken at the edges and some uncompensated radiation can leak out. As the phase mismatch becomes smaller (the grating period approaches the free space wavelength), the coherence length of the interference process gets longer, and more energy escapes out of the edges.

2.3 Full-cavity model

For a complete understanding of the QC-VECSEL's properties, the properties of the metasurface must be incorporated in a model for the full external cavity structure. This can be done both using an analytical model and with FEM simulations.

2.3.1 Analytic model

An analytical model for the QC-VECSEL is described in Ref. [18] The key concepts are summarized here, with some minor modifications. The basis of the model assumes that the reflectance of the metasurface can be represented as:

$$R_{MS} = R_1 G = e^{\xi(\nu)(g-g_{tr})}, \tag{2.3}$$

where $R_1{=}e^{-\xi(\nu)g_{tr}}$ is the passive (unbiased) reflectance of the metasurface, and $G{=}e^{\xi(\nu)g}$ is the intensity gain. The intersubband gain coefficient is given by g, and g_{tr} is the transparency gain value. The spectral properties of the metasurface are incorporated by the frequency dependent fitting factor $\xi(\nu)$. Using equation 2.3, we can write an expression for the threshold gain of the QC-VECSEL based on the condition that the roundrip intensity

change is unity:

$$1 = R_{MS}(\nu)R_2T^2 = R_1(\nu)R_2T^2e^{\xi(\nu)g_{th}}, \tag{2.4}$$

$$g_{th}(\nu) = \frac{-\ln(R_1(\nu)R_2T^2)}{\xi(\nu)} = g_{tr} - \frac{\ln(R_2T^2)}{\xi(\nu)}, \tag{2.5}$$

where T^2 is the roundtrip transmission through the cavity (primarily effected by diffraction losses if the cavity is built in a vacuum cryostat).

Equation 2.5 tells us that the threshold gain of the VECSEL will decrease if the metasurface absorption is reduced, metasurface quality factor (reflected by $\xi(\nu)$) is reduced, transmission loss is reduced, or output coupler reflection is increased; all logical conclusions. For a given metasurface modeled by equation 2.4, $R_1(\nu)$ and $\xi(\nu)$ are not independent variables, so it is also useful to consider equation 2.5 in terms of transparency gain, as shown on the right-hand side of equation 2.5. For the ridge-based metasurface, it's observed in Figure 2.3(a) that the transparency gain is relatively constant while the other three knobs in the second term can be tuned independently.

Next, we want to estimate the laser output power and slope efficiency as a function of the metasurface pump current. We start by writing an expression for the total fields in the VECSEL during stable operation:

$$\mathbf{E} = \underbrace{\hat{x}E_+\psi_{mode}(x,y)\left(e^{ik_0z} + r_1\sqrt{G_{th}}e^{-ik_0z}\right)}_{\text{External cavity fields}} + \underbrace{\sum_{i=1}^{N}\hat{z}E_0\psi_{mode}(x,y)\psi_{ridge}(x)}_{\text{Fields in metasurface ridges}}, \tag{2.6}$$

where $\hat{x}$ is the in-plane direction, and $\hat{z}$ is the surface-normal direction. The expression consists of a forward and backward wave propagating in the external cavity with peak field values of E_+ and $r_1\sqrt{G_{th}}E_+$, and a standing profile in the ridges with a peak field intensity of E_0 and a sinusoidal variation across the width. The shape of the external cavity mode is given by $\psi_{mode}(x,y)$ (preferably a Gaussian type profile), and the shape of the transverse mode in each ridge is given by $\psi_{ridge}(x)$, which is a sinusoidal standing wave shape in the

case of all demonstrated metasurfaces. Both functions are normalized such that ψ^2 has a maximum value of 1. G_{th}=$(R_1 R_2 T^2)^{-1}$ per equation 2.4.

What we want to calculate is intensity P_{out} (W) as a function of the pump current. We start by writing:

$$P_{out} = (1 - R_2)TP_{-} = \int_{mode} I_{out}\psi^2_{mode}(x, y)dxdy, \tag{2.7}$$

where P_{out} is the power of the output beam, P_{-} is the power incident on the output coupler after being amplified by the metasurface, and I_{out} is the peak intesity of the output beam.

To relate P_{out} to the pump current in the metasurface, we start by determining the relationship between the power ciculating in the external cavity and the energy in the metasurface.

$$P_{-} - P_{+} = \frac{dU}{dt} = \frac{\omega_0 U_0}{Q_{abs}}, \tag{2.8}$$

where P_{+} is the power of the incoming wave (after reflecting off the output coupler), ω_0 is the resonant frequency of the metasurface, Q_{abs} is the non-radiative quality factor of the metasurface given by:

$$Q_{abs} = \frac{\omega_0 n}{(g - g_{tr})c}, \tag{2.9}$$

where g is the QC-material gain coefficient, assumed to be uniform every where (circulating intensity is small compared to the saturation intensity), and n is the refractive index of the QC-material. U_0 is the energy stored in the metasurface given by:

$$U_0 = \frac{1}{2}\epsilon_r\epsilon_0|E_0|^2 hA \underbrace{\underbrace{\frac{w}{\Lambda}}_{\mathrm{F}_{elc}} \underbrace{\frac{\int_{mode}\psi^2_{mode}(x, y)dxdy}{A}}_{\mathrm{F}_{mode}} \underbrace{\frac{\int_{ridge}\psi^2_{ridge}(x)dx}{w_{ridge}}}_{\mathrm{F}_{ridge}}}_{\mathrm{F}_{opt}}, \tag{2.10}$$

where F_{elc} is the fill factor of the gain material across the metasurface, and F_{opt} is the fill factor of the electric field in the ridges (see Figure 2.4). Typical metasurface designs with a sinusoidal standing wave would have F_{opt}=0.5. Equation 2.8 can be written as an expression in terms of peak forward and backward field intensities:

$$A(I_- - I_+) = \frac{\omega_0 U_0}{Q_{abs} F_{mode}}, \tag{2.11}$$

By substituting equation 2.9 and 2.10 into 2.8, and using relationships I_-=$R_1 G I_+$=$c\epsilon_0 E_-^2/2$, we can solve for the ratio of the peak intensity in the ridges and the intensity of the outgoing plane wave (note that this expression and equation 2.9 have been corrected from [18], which had a sign error):

$$M = \frac{|E_0|^2}{|E_-|^2} = \frac{2(R_1 G - 1)}{R_1 G(g - g_{tr}) n h F_{elc} F_{ridge}}. \tag{2.12}$$

We can write the follow expression for the peak output intensity of the VECSEL beam:

$$I_{out} = (1 - R_2) T I_- = \frac{(1 - R_2) T}{nM} I_0, \tag{2.13}$$

where I_0=$nc\epsilon_0 E_0^2/2$ is the peak field intensity in the metasurface.

Now, the intensity in the ridges must be related to the gain coefficient and current draw in the QC-material. We start by writing a general expression for the QC-gain coefficient as a function of intensity:

$$g = \frac{g_0(J)}{1 + I/I_s} = \frac{(J - J_{leak})\sigma\tau_{eff}}{eL_p} \frac{1}{1 + I/I_s}, \tag{2.14}$$

where $g_0(J)$ is the small signal gain coefficient, I is the field intensity, I_s is the saturation intensity, J is the total current density draw, J_{leak} is a leakage current term (technically a function of gain g, but it should be relatively constant through the small bias range over which lasing occurs), σ is the stimulated emission cross section (and is technically frequency

dependent), e is the fundamental charge, and L_p is the length of a QC-module. The effective lifetime of the population inversion is given by τ_{eff}=$\eta\tau_{up}$-(1-η)τ_2, where the upper state lifetime (assuming a 3-level laser model) is given by τ_{up}=τ_3(1-τ_2/τ_{32}), and η accounts for non-unity injection efficiency. The saturation intensity is given by I_s=$h\nu/\sigma(\tau_{up}+\tau_2)$. Setting g=g_{th} and solving equation 2.14 for I gives the following:

$$I = \frac{h\nu}{eL_p}\frac{\tau_{eff}}{\tau_2+\tau_{eff}}\frac{J-J_{th}}{g_{th}}, \tag{2.15}$$

$$J_{th} = \frac{g_{th}eL_p}{\sigma\tau_{eff}} + J_{leak}. \tag{2.16}$$

To account for the mode profile across the ridge width and write an expression for I_0, we assume an effective uniform circulating intensity of $F_{ridge}I_0$, giving the expression:

$$I_0 = \frac{1}{F_{ridge}}\frac{h\nu}{eL_p}\frac{\tau_{eff}}{\tau_2+\tau_{eff}}\frac{J-J_{th}}{g_{th}}. \tag{2.17}$$

So finally, we can substitute equations 2.12 and 2.17 into 2.13, and use relationships R_1G_{th}=$(R_2T^2)^{-1}$, g_{tr}=-$\xi^{-1}\ln(R_1)$, and g_{th} from equation 2.5 to obtain an equation for output intensity as a function of pump current density:

$$I_{out} = N_p\frac{h\nu}{e}\underbrace{\frac{\tau_{eff}}{\tau_2+\tau_{eff}}}_{\eta_i}\underbrace{\frac{(T-R_2)\ln(R_2T^2)}{(1-R_2T^2)\ln(R_1R_2T^2)}}_{\eta_{opt}}F_{elc}(J-J_{th}). \tag{2.18}$$

Labels in equation 2.18 indicate how the expression can be broken into classical elements of a laser model including internal quantum efficiency η_i indicating the fraction of the pump current that is converted into photons, and optical efficiency η_{opt} reflecting the fraction of generated photons that are coupled into the output beam. By multiplying both sides by the

integral of $\psi^2(x,y)$, the expression can be converted back to power and absolute current:

$$P_{out} = N_p \frac{h\nu}{e} \eta_i \eta_{opt} (I - I_{th}). \tag{2.19}$$

According to equation 2.19, the slope efficiency of the laser shows no dependence on the optical fill factor F_{opt}. This is because the model has assumed that only optically active portions of the metasurface contribute to current draw above threshold (i.e. according to equation 2.17, if there is no optical field in the ridge, the current density is locked at the threshold value). This is equivalent to a laser in which the active region voltage is locked above threshold, such that the differential resistance goes to zero. In this case, it is true that the fill of the mode across the metasurface has no affect on the slope efficiency; a given amount of total current over threshold will always generate the same number of photons. In reality, this is not a correct representation of QC-gain material, which exhibits a finite differential resistance above threshold due to non-zero lower state lifetimes and parasitic resistances within the active region. As a result, the voltage bias (which is constant across the area of the device), increases above threshold, which results in a local increase in the population inversion, and the material gain (i.e. spatial hole burning) in regions of the metasurface and ridge with reduced optical intensity. Incorporation of this effect will result in some reduction to the slope efficiency, but the effect has not been investigated in detail at the moment.

The above discussion assumes that all of the metasurface is biased, but in reality, only a small central portion of the metasurface is usually biased to reduce pump power and promote lasing on the fundamental mode of the external cavity. In this situation, the only effect is to see an increase in threshold gain by a confinement factor Γ_t (see Figure 2.4):

$$J_{th,modal} = \frac{g_{th}}{\Gamma_t} \frac{eL_p}{\sigma \tau_{eff}} + J_{leak}, \tag{2.20}$$

$$\Gamma_t = \frac{\int_{biasarea} \psi^2(x,y)dA}{\int_{allarea} \psi^2(x,y)dA}. \tag{2.21}$$

This confinement factor should not be expected to affect the slope efficiency of the VECSEL, and this can be proved by replacing equation 2.3 with the expression:

$$R_{MS} = R_1 G = e^{\frac{\xi(\nu)(g-g_{tr})}{\Gamma_t}}. \tag{2.22}$$

Replacing equation 2.9 with the expression:

$$Q_{abs} = \frac{\omega_0 n}{(g-g_{tr})c}\Gamma_t, \tag{2.23}$$

and replacing equation 2.17 with the expression:

$$I_0 = \frac{1}{F_{ridge}}\frac{h\nu}{eL_p}\frac{\tau_{eff}}{\tau_2+\tau_{eff}}\Gamma_t\frac{J-J_{th}}{g_{th}}. \tag{2.24}$$

The Γ factors in equations 2.23 and 2.24 cancel when inserted into equation 2.13.

2.3.2 Numerical modeling

The Fox and Li approach is significantly less computationally intentisve than FEM modeling, and is the technique presented in most of the published THz QC-VECSEL work to date. The technique was first proposed with regards to maser design in 1961 (Ref. [14]), and is nothing more than application of a Huygen's integral to a wave bouncing back and forth in a cavity until a stable solution is reached. Huygen's theory assumes that the propagation of an electromagentic wave can be modeled as the sum of an infinite number of spherical point sources described by $E(R)=\frac{e^{-jk_0R}}{R}$, where k_0 is the free space wavenumber and R is the observation point relative to the source. Converting to 1-D (cylindrical wave sources rather than spherical) and integrating over the excitation wavefront $\psi(x)$, the field at each point

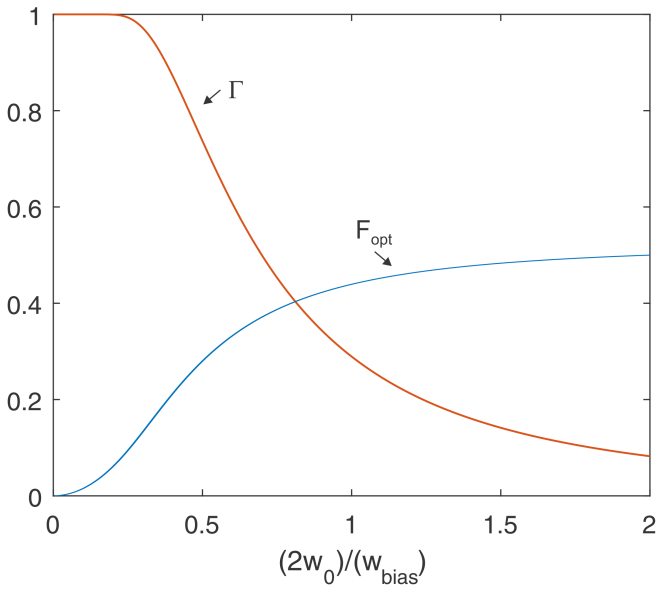

Figure 2.4: (a) Confinement factor Γ and optical fill factor F_{opt} as a function of the ratio of the beam waist of the presumed Gaussian mode profile to the width of the bias diameter. Γ decreases as the beam waist grows larger than the bias diameter while F_{opt} approaches a limit of F_{ridge}, which is a constant value of 0.5 for a sinusoidal standing wave pattern.

on the observation plane is given by:

$$E(R) = \sqrt{\frac{j}{\lambda_0}} \int_{source} \psi(x) \frac{e^{-jk_0 R}}{\sqrt{R}} \frac{1+\cos\theta}{2} dx, \tag{2.25}$$

where λ_0 is the free space wavelength. To find the eigensolutions of an optical cavity, we assumes an initial field distribution (a plane wave, for example), use equation 2.29 to calculate the fields on the output coupler after propagating across the cavity length, use equation 2.29 again to propagate the field reflected by the output coupler back to the metasurface (with the desired output coupler reflectance imposed), and repeat until a stable solution is reached:

$$\frac{E_n(x)}{E_{n+1}(x)} = \gamma. \tag{2.26}$$

Subscripts n and $n+1$ indicate the number of passes through the cavity. The per-pass

loss or gain coefficient for the cavity (in terms of field) is given by is γ. For a passive cavity with no material losses and PEC mirrors, γ gives the per-pass diffraction loss.

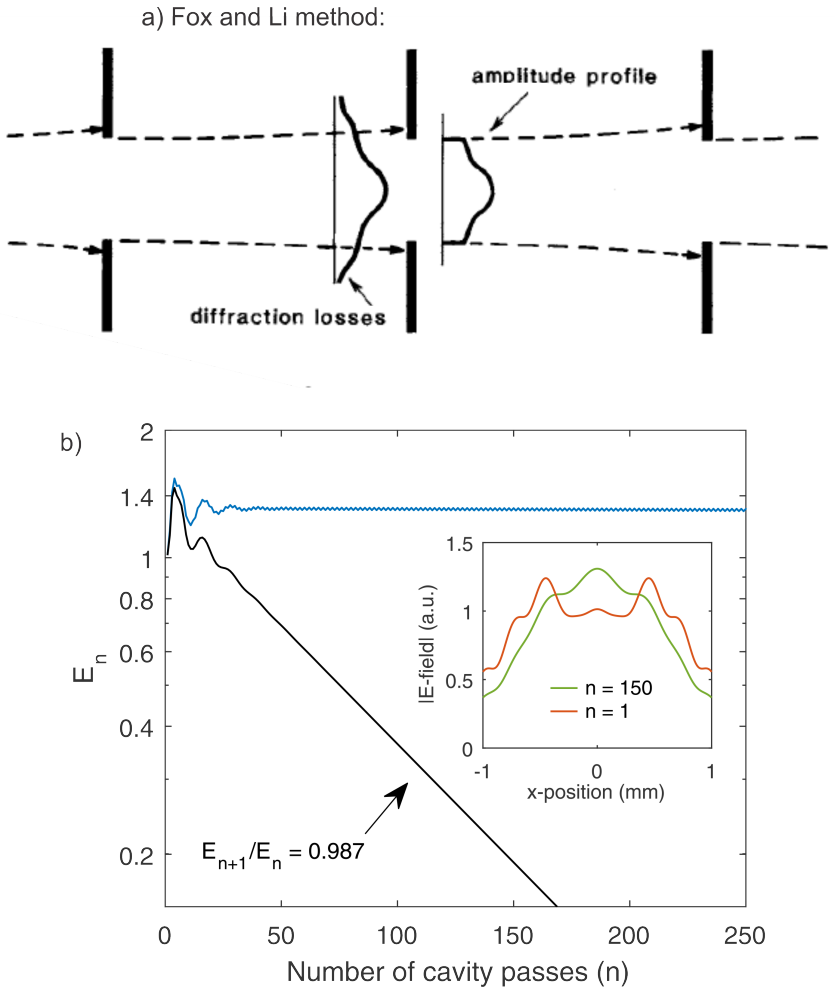

Figure 2.5: (a) Illustration of Fox and Li method taken from Ref. [14]. To simulate a QC-VECSEL with an active metasurface, every other aperture should be assigned an amplification factor and phase, and the alternate apertures should be assigned a loss factor to reflect the output coupler. (b) Simulations of a 2 mm metasurface with 5 mm cavity length at 3.4 THz. The black line indicates results for a passive cavity with per-pass diffraction power loss =100x(1-0.987^2)=2.6%. Blue line indicates the threshold condition with metasurface amplification factor =1.05. The mode shape is plotted in the inset.

This concept is illustrated in Figure 2.5(a), and a sample 1-D calculation for a plano-plano 3 mm long cavity with 2 mm wide PEC reflectors at 3.4 THz is shown in Figure 2.5(b) (comparable to a typical THz QC-VECSEL setup). In this passive case, the model converges

on a solution with 2.6% per-pass diffraction power loss, and the output field profile is shown in the inset. 2-D Fox and Li modeling can be done, but adds significant computation time while diffraction loss for a 2-D cavity can be approximated as simply twice that of a 1-D cavity. Amplitude and phase characteristics can be added to the mirrors to represent the metasurface. For example, in the inset of Figure 2.5(b), a uniform amplification factor of 1.05 has been added to compensate for the diffraction loss, resulting in a solution that converges to a constant value. This required amplification factor can then be related back to the required QC threshold gain using the FEM results for an infinite metasurface. However, if a finite bias area is to be considered, or a non-uniform design is used, the detailed local reflection characteristics of the metasurface are unknown. Further, effects of coupling to in-plane momentum (as discussed in Section 2.2) are not considered either. Therefore, only FEM simulations that incorporate the exact metasurface structure can accurately model the full VECSEL cavity. The disadvantage of FEM simulations is that it becomes computationally intensive to model longer cavities (while cavity length has no effect on Fox and Li computation time). To investigate more closely, we consider a number of basic scenarios.

In Figure 2.6(a), diffraction losses calculated using a 1-D Fox and Li model are plotted as a function of cavity length for a 2 mm metasurface operating at 3.4 THz. Results are plotted for both a plano-plano cavity and a plano-focusing cavity (focusing radius of 20 mm). PEC surfaces are used so that only diffraction loss is considered. As expected, the plano-focusing cavity shows a strong improvement over the plano-plano cavity at shorter cavities (<10 mm), but at longer cavity lengths, diffraction loss increases sharply. This is due to the finite size of the metasurface - around 10 mm cavity length, the divergence of the beam over the cavity length becomes significant enough that the majority of the power is simply lost off the edges of the metasurface (note, the fundamental stability requirement for a plano-focusing cavity is that the radius of curvature of the mirror, R, is less than the cavity length, so this is not the cause of the increase in diffraction loss). This effect is further demonstrated in Figure 2.6(b) by the simulated diffraction loss when the metasurface is increased to 3×3 mm^2. For comparison, the 2-D FEM simulated threshold gain (no selective biasing) is plotted for both

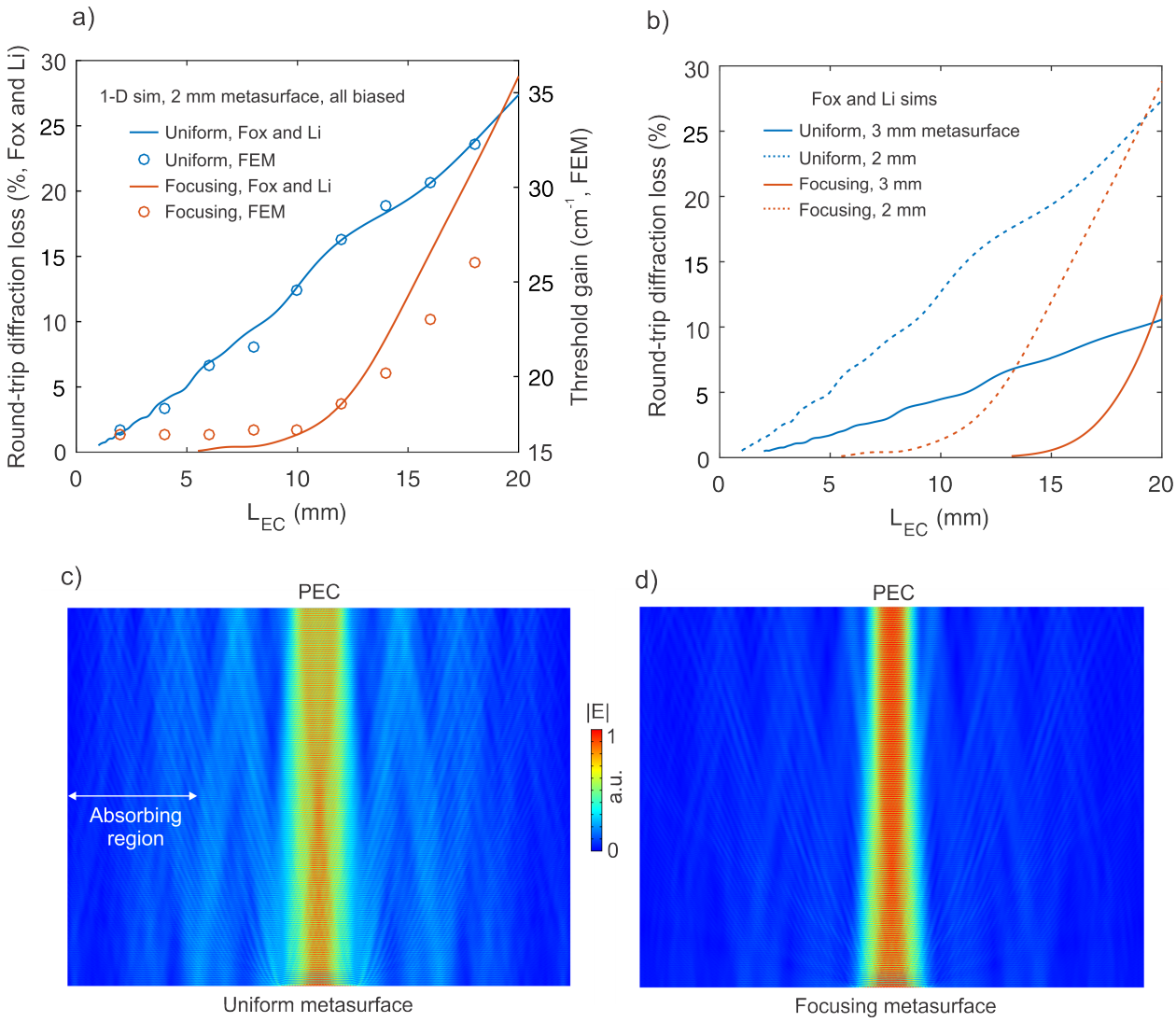

Figure 2.6: (a) Comparison between results using the Fox and Li model (lines) versus full FEM modeling (circles) as a function of the length of the external cavity. Results for both uniform (blue) and focusing (red) metasurfaces are shown. The focusing metasurface is represented as a perfect quadratic reflection phase, while the metasurface parameters for the FEM simulation were taken from Ref. [15]. (b) Comparison (using Fox and Li modeling only) between a 2 mm metasurface and a 3 mm metasurface. Both uniform and focusing results are shown. (c-d) Field plots of FEM simulated cavities clearly shoing the reduction in diffraction loss when using a focusing metasurface.

a uniform (Λ=70 μm, and w=11.6 μm) and focusing metasurface, using a PEC boundary in place of an output coupler. The focusing metasurface is implemented using a variable ridge width to spatially control the reflection phase of the metasurface, and is based on the design

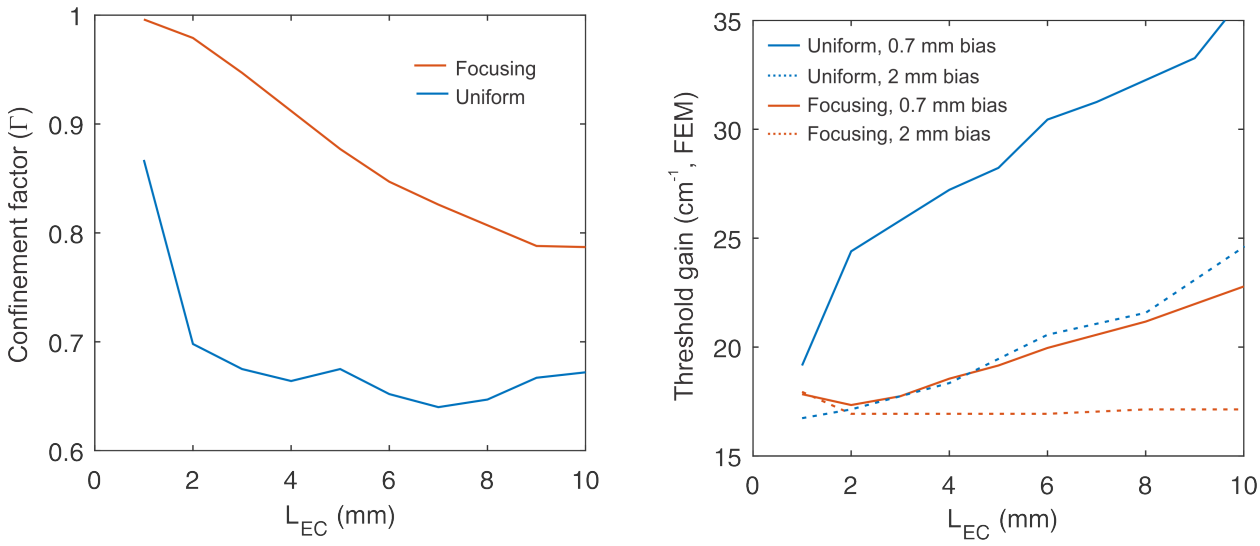

Figure 2.7: (a) Comparison of confinement of the mode on a 2 mm metasurface to the central 0.7 mm (calculated using FEM simulations) for a focusing and uniform metasurface. The confinement is much better for the focusing surface because the lossy, unbiased portions of the metasurface are detuned from the resonance and do not couple much field intensity into the ridges. (b) Comparison between focusing and uniform metasurfaces when the whole metasurface is biased and when only a central portion is biased. The affect of the confinement factor is observed to be much more detrimental to the threshold gain of the uniform metasurface compared to the focusing.

in Ref. [15].

The trend in the threshold gain for the uniform metasurface is in very good agreement with the Fox and Li simulated diffraction loss. The diffraction loss cannot be directly extracted from the simulation, but can be inferred from the reflectance required from the metasurface in the FEM simulation. For example, at a cavity length of 18 mm, the FEM simulated 2-D threshold is 32 cm^{-1}, and the Fox and Li simulated roundtrip diffraction power loss is 23.8 %. From FEM simulation of an infinite metasurface, we find that 32 cm^{-1} of applied QC-gain gives a metasurface power amplification factor of 1.27, giving a roundtrip condition of 1.27×(1-0.238)=0.97. The expression is relatively close to 1, indicating that the Fox and Li model and FEM simulation are predicting similar diffraction loss values.

For the focusing metasurface, the Fox and Li model and FEM simulations show a rel-

atively similar trend, but diverge a little at longer cavity lengths. This deviation may be partially a result of the fact that the spatially varying gain of the focusing metasurface is not accounted for in the Fox and Li model, and partially because the metasurface is discrete in nature, but represented by a continuous fit in the Fox and Li model. Actually, this spatially varying amplification, and thus spatially varying absorption in the passive case, should be of significant advantage when moving to metasurfaces with small bias diameters (important for continuous wave operation). This is because the unbiased ridges in the outer edges of the focusing metasurface are significantly detuned from the target frequency, reducing the losses that the outer edges of the beam experience compared to the case of a uniform metasurface. In other words, the confinement factor Γ (from equation 4.3) of the external cavity mode to the central portion of the metasurface is significantly higher for a focusing metasurface than a uniform one. This confinement factor can be extracted from FEM simulations, and is plotted in Figure 2.7(a) for a 2-D, 2 mm wide focusing and uniform metasurface. In Figure 2.7(b), FEM simulated threshold gain values are plotted for a 2-D uniform and focusing metasurface, both 2 mm wide with the central 0.7 mm biased (a common configuration that has been demonstrated, see Section 2.4). It is observed that the focusing metasurface shows considerably more improvement over the uniform metasurface when a small central bias area is used compared to the entire metasurface biased.

More realistic 3-D FEM modeling of the metasurface becomes far too computationally intensive, and 2-D Fox and Li models also become considerably more intensive. However, the 3-D results can be estimated from the 2-D results (in the case of FEM, 1-D in the case of Fox and Li). Moving to 3-D simulation should have the effect of doubling diffraction loss and reducing confinement. A quick bit of algebra yields the expression:

$$g_{th,2D} = \frac{1}{\Gamma_{1D}}(g_{th,1D} + \frac{2}{\xi} ln(\frac{T_{1D}}{T_{2D}})). \tag{2.27}$$

In order to estimate $g_{th,2D}$ from FEM simulation alone, one would need to simulate the threshold gain with both lossy and lossless materials to isolate diffraction loss, requiring a lot of simulation work. Alternatively, one could save simulation work by estimating the

diffraction loss using the Fox and Li model while $g_{th,2D}$ and Γ_{2D} can be extracted from a single FEM simulation. In the case where the entire metasurface is biased (Γ=1), the 3-D threshold can be interpolated from the 2-D result using the expression: $g_{th,2-D} = g_{tr} + 2\times(g_{th,1-D}\text{-}g_{tr})$.

2.4 Early results

Results from the first demonstrated THz QC-VECSEL are shown in Figure 2.8 (Ref. [16]). The metasurfaces were made by the author of this thesis, while the data was collected by L. Xu. The metasurface was 1.5×1.5 mm^2 and designed to operate at 2.94 THz with a ridge width of 13 μm and a period Λ of 90 μm. The entire square area was biased, but not the tapered terminations. The VECSEL was constructed with the metasurface inside a cryostat, while the output coupler was outside of the crystat (Figure 2.8(a)). As the cryostat window was part of the external cavity, a high-resistivity silicon (HR-Si) window was used to minimize round-trip cavity losses. It is more desirable in terms of threshold gain to construct the whole external cavity inside the cryostat, but for the initial demonstration, it was assumed that having the output coupler outside would be beneficial as it allows the user to play with the cavity alignment while testing. A wire-grid polarizer was used as the output coupler, which allows the output coupler reflectance to be tuned while testing by rotating the angle of the polarizer relative to the orientation of the metasurface ridges (which only couple to radiation orthogonal to the length of the ridges), however the exact reflectance is unknown. The output power was originally reported as 5.5 mW at 4 K with a slope efficiency of 16.7 mW/A. These are quite low values, and the authors have since declared an error in calibration of the detectors, and corrected power levels to ≈30 mW at 4 K with a slope efficiency of ≈100 mW/A; still not impressive values, but more reasonable. The maximum current density is significantly reduced compared to a typical metal-metal ridge resonator (Appendix 8.1), reflecting the non-uniformity of the TM_{01} field profile across the width of the ridge. Most importantly, a good quality beam pattern was observed with a FWHM divergence angle of ≈5°.

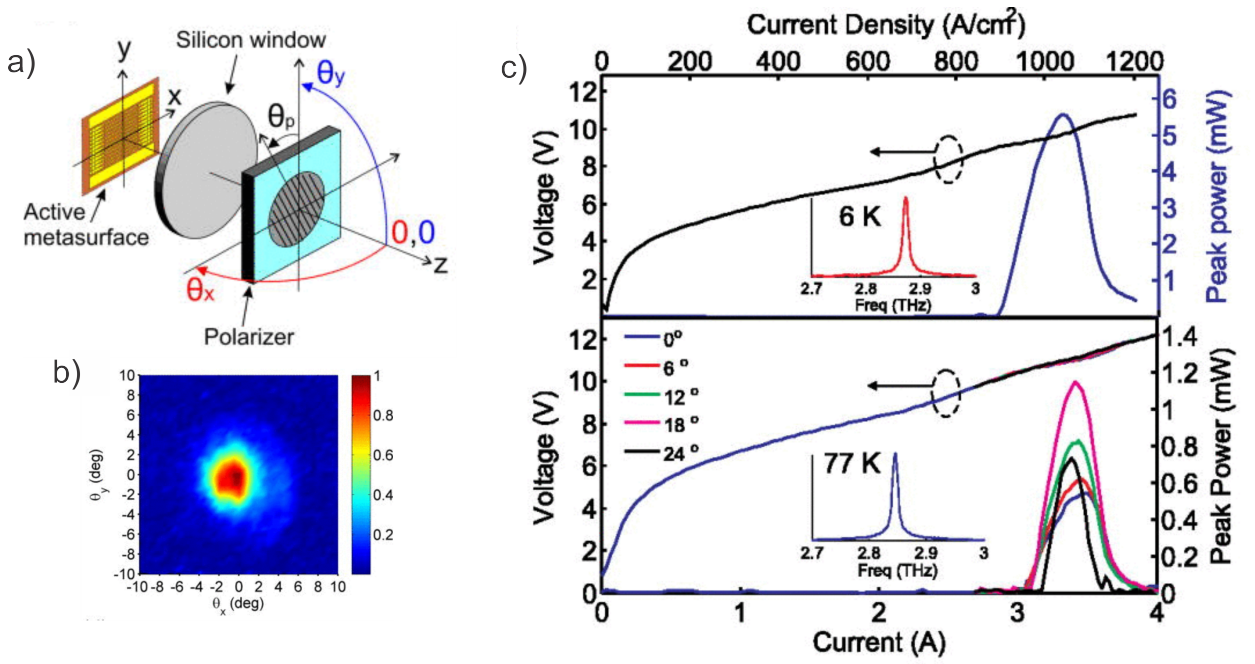

Figure 2.8: (a) Illustration of QC-VECSEL setup with the metasurface inside of the cryostat and the output coupler outside, with an HR-Si window in between. As indicated, the output coupler is a wire-grid polarizer whose reflectance can be tuned by rotation of the wire-grid with respect to the orientation of the metasurface ridges. (b) Beam pattern from the first demonstrated QC-VECSEL, and (c) the measured pulsed *L-I-V* curves at 6 K and 77 K. The 77 K figure includes *L-I-V* data at several output coupler angles, though the actual reflecance values have not been measured. The power has been corrected from Ref [16], as described in Ref [17]. Figures are taken from Ref [16].

It was presumed that the laser was operating on a transmission peak of the Si window, and the cavity length was reported to be $\approx$ 6 mm resulting in a roundtrip diffraction loss of 7%. However, the author of this thesis calculates 7% to be the single-pass loss, giving a roundtrip power loss of 14%. Further, these number are based on a 1-D Fox and Li model, so the proper roundtrip power loss for the actual 2-D metasurface would be 28%. And further yet, the effect of the refractive index of the silicon window on the optical cavity length was neglected. When this is incorporated, the optical cavity length is increased to 12 mm (3 mm silicon with $n\sim3$), and the expected roundtrip diffraction power loss is increased to $\sim$65%, requiring a uniform metasurface reflectance of $\sim$2.2. This is a rather significant difference

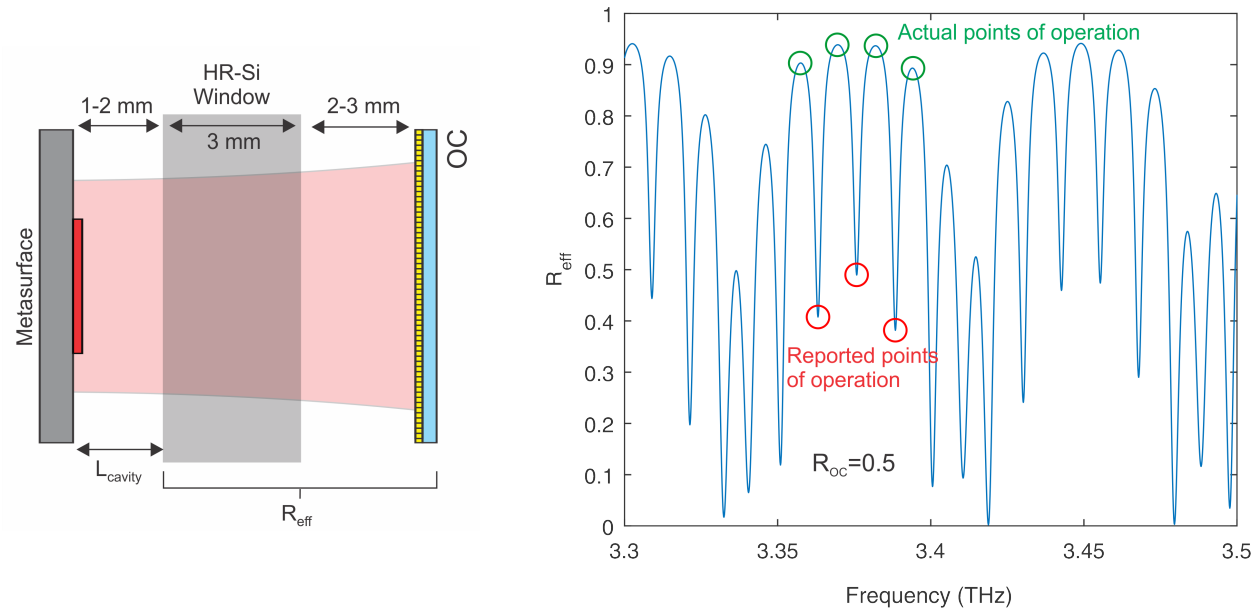

Figure 2.9: (a) Illustration of early QC-VECSEL configurations with the output coupler external to the cyostat and an HR-Si window in between. (b) Calculated effective reflectance of the HR-Si window in combination with the output coupler (assumed to have a flat reflectance of 0.5). Though early reporting of results assumed operation on the transmission peaks of the window (red circles), it seems more likely that operation would occur on the reflection maximums (green circles) as the threshold should be lower.

from the assumed conditions, though FEM simulations indicate that the peak reflectance of the metasurface can approach 2.2 with ∼50 cm^{-1} of intersubband gain. This is a high threshold, and it will only be larger by the introduction of output coupler loss. However, the author of this thesis believes it more plausible that the length of the external cavity was effectively the distance form the metasurface to the front of the Si-window (∼1-2 mm), and the Si-window and output coupler together act as an effective reflector with frequency dependent field reflection coefficient given by [106]:

$$r_{eff} = \frac{r_1 + r_{2,eff} e^{-j2k_{Si}L_{Si}}}{1 + r_1 r_{2,eff} e^{-j2k_{Si}L_{Si}}}, \tag{2.28}$$

where r_1 is the reflection coefficient between vacuum and silicon, L_{Si} is the thickness of the silicon window, k_{Si} the wavenumber in silicon, and $r_{2,eff}$ is the reflection coefficient of

the Fabry-Perot cavity defined by the exterior face of the Si-window and the output coupler using the same equation:

$$r_{eff,2} = \frac{-r_1 + r_{oc}e^{-j2k_0L_{atm}}}{1 - r_1 r_{oc}e^{-j2k_0L_{atm}}}, \tag{2.29}$$

where k_0 is the freespace wavenumber, and L_{atm} is the distance between the cryostat window and the output coupler (typically reported as 1-2 mm). This concept is illustrated in Figure 2.9. Under these conditions, effective diffraction loss is reduced to ∼5%, and a high output coupler reflectance is maintained, resulting in a much lower threshold VECSEL than one operating on the transmission peak of the window. This calculation for effective reflectance is standard and can be cascaded to incorporate as many reflections as desired. Full treatment of the VECSEL with an external output coupler should include a fourth mirror for reflection from the backside of the output coupler. Inclusion of this fourth mirror adds a modulation to the whole r_{eff} term with frequency. Typically, thin output couplers have been used, which would result in a very slow modulation of r_{eff} compared to the silicon window and L_{atm}. This discussion does not take away from the operation principle of the QC-VECSEL in terms of power and beam quality, just modifies the analysis of the results. For example, Ref. [18] estimates the value of the internal quantum efficiency of the QC material and the passive reflectance of the metasureface (η_i and R_1 respectively from Section 2.3) on the basis that R_2 was equal to the reflectance of the output coupler. The result will surely be different assuming the conditions in Fig. 2.9, however it may be futile to try and make more accurate estimates as the cavity length is not known very precisely, and neither is the alignment of the metasurface with the window, which will also affect the feedback and diffraction loss in the cavity. Though much of the early data was collected with an external output coupler and may be a bit confused, intracryostat configurations were developed soon after and have been used exclusively ever since, allowing for better understanding of the VECSEL's performance and potential.

The output power and slope efficiency of the VECSEL were quickly increased primarily by switching to a more high power active region design based on Ref [107], and also by

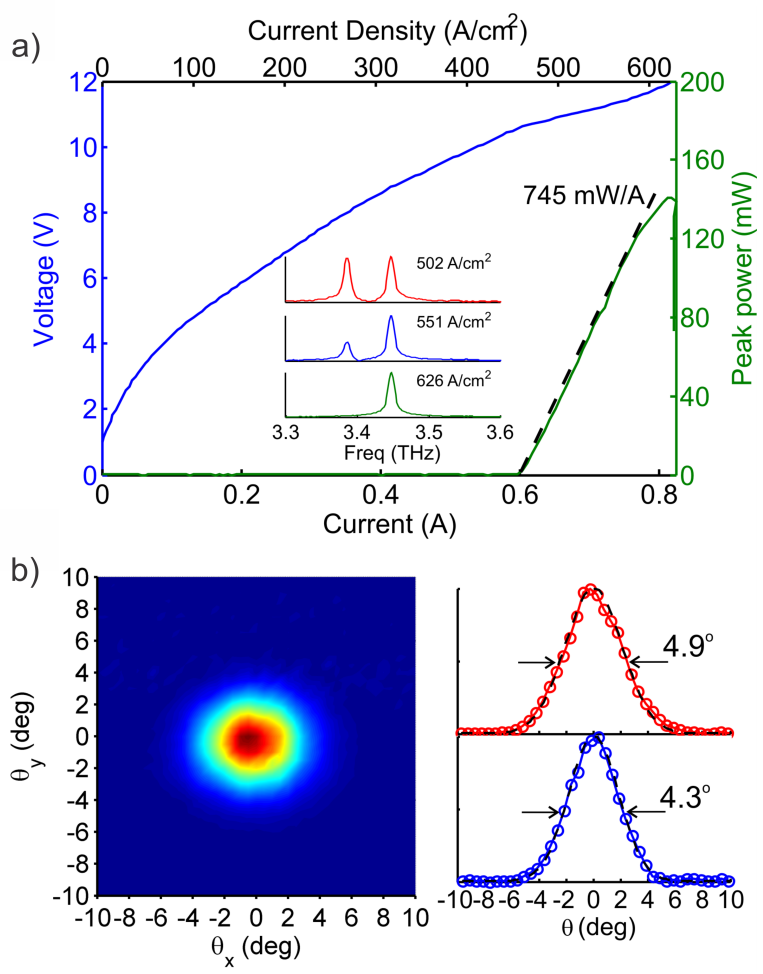

Figure 2.10: (a) Pulsed *L-I-V* data collected at 77 K for a 2×2 mm^2 metasurface (Λ=70μ, w=11.5μm) with a 1 mm bias diameter. The cavity length is ∼2.5 mm, intracryostat, and the output coupler has a reflectance of ∼19%. The slope efficiency of 745 mW/A is a record at 77 K at the time of writing this. (b) Measured far-field beam pattern. Figure taken from Ref. [18].

moving to intracryostat VECSEL construction, which allows precise cavity alignment, short cavity lengths, and and a more controllable output coupler reflectance. The thicknesses of the $Al_{0.15}Ga_{0.85}As$/GaAs active region layers in a single module were, starting from the injection barrier: **51**/103/**17**/107/**37**/88/**37**/<u>172</u> Å, where the barrier layers are in bold and the central 88 Åof the underlined will is Si-doped at 5×10^{16} cm^{-3}. The wafer was grown at Sandia National Labs by John Reno and was labeled wafer VB0739. With this wafer, up to

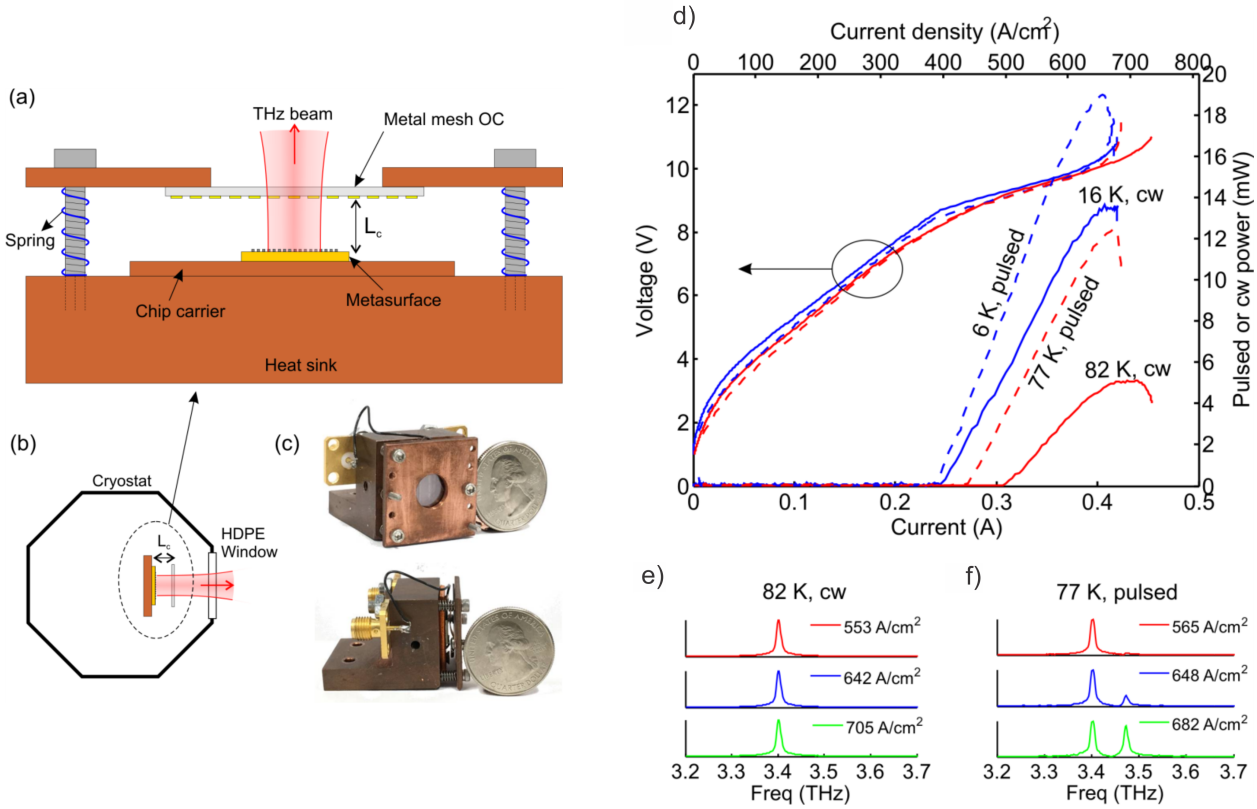

Figure 2.11: (a-c) Illustrations and photographs of a typical intracryostat QC-VECSEL setup (output coupler inside the cryostat). (b) First published results with an intracryostat QC-VECSEL and a 2×2 mm^2 focusing metasurface with a 0.7 mm bias diameter. Most notably, up to ∼5 mW of continuous wave power was demonstrated at a measured heat-sink temperature of 82 K. Figures taken from Ref. [19].

140 mW of peak pulse power was demonstrated at 77 K with a slope efficiency of 745 mW/A (a record high for 77 K at the time of writing this) using uniform TM_{01} metasurface 2×2 mm^2 with a bias diameter of 1 mm (see Chapter 3 for high power TM_{03} results). The output coupler was ∼19% transmittive, and the cavity was built inside the cryostat with a cavity length of ∼2.5 mm. Further, continuous wave power up to 5 mW has been demonstrated at 77 K using a 2×2 mm^2 focusing metasurface with a bias diameter of 0.7 mm. The continuous wave device was built intracryostat with an output coupler reflectance >95%, and at the time of publishing was the highest continuous wave output power ever demonstrated from a THz QCL operating above 77 K (Figure [19]).

Other noteworthy demonstrations with the THz QC-VECSEL include:

- Investigation of a focusing metasurface based on the principle that the laser operates at a single frequency, so the phase of the metasurface reflection can be controlled by varying the ridge width (Figure 2.12. In Ref. [20], this technique was used to implement a parabolic phase shift across the metasurface, mimicking reflection from a spherical mirror, presumably resulting in a more stable cavity with less diffraction loss compared to the previous plano-plano demonstrations (Figure 2.6). Results indicated that focusing metasurfaces were more robust to cavity misalignment, however, this was investigated using an output coupler placed outside of the cryostat, so effect of misalignment on threshold gain is considerably more complicated than was presumed. Regardless, the focusing effect seemed to work, and although cavity alignment does not appear to be an issue with intracryostat cavities, focusing metasurfaces still have significant potential to reduce threshold gain values at longer cavity lengths (as discussed above in Section 2.3.2). Proper investigation of this aspect should be undertaken in the future.

- Investigation of a polarization switchable metasurface. Metasurfaces designed to be electrically switchable between two orthogonal polarizations were investigated in Ref. [21]. The intention was to effectively have two interdigitated arrays of patch resonators, with one array of patches rotated 90° from the other. In reality, each array must be electrically connected for biasing, so the resulting structure utilizes narrow connecting elements that were carefully designed to reduce cross-polarization scattering. Experimental results indicated that both sets of patches lased with ∼75-80° difference in polarization between the two. Failure to obtain exact 90° switching is likely due to fabrication error, or error in estimated material properties in the simulation. However, a variety of self-lasing modes have been observed from the metasurface, and results seem to be sensitive to the output coupler position. Further, an external output coupler was used for this experiment as well, so the exact nature of the cavity is uncertain. Investigations into the properties of the metasurface are still underway.

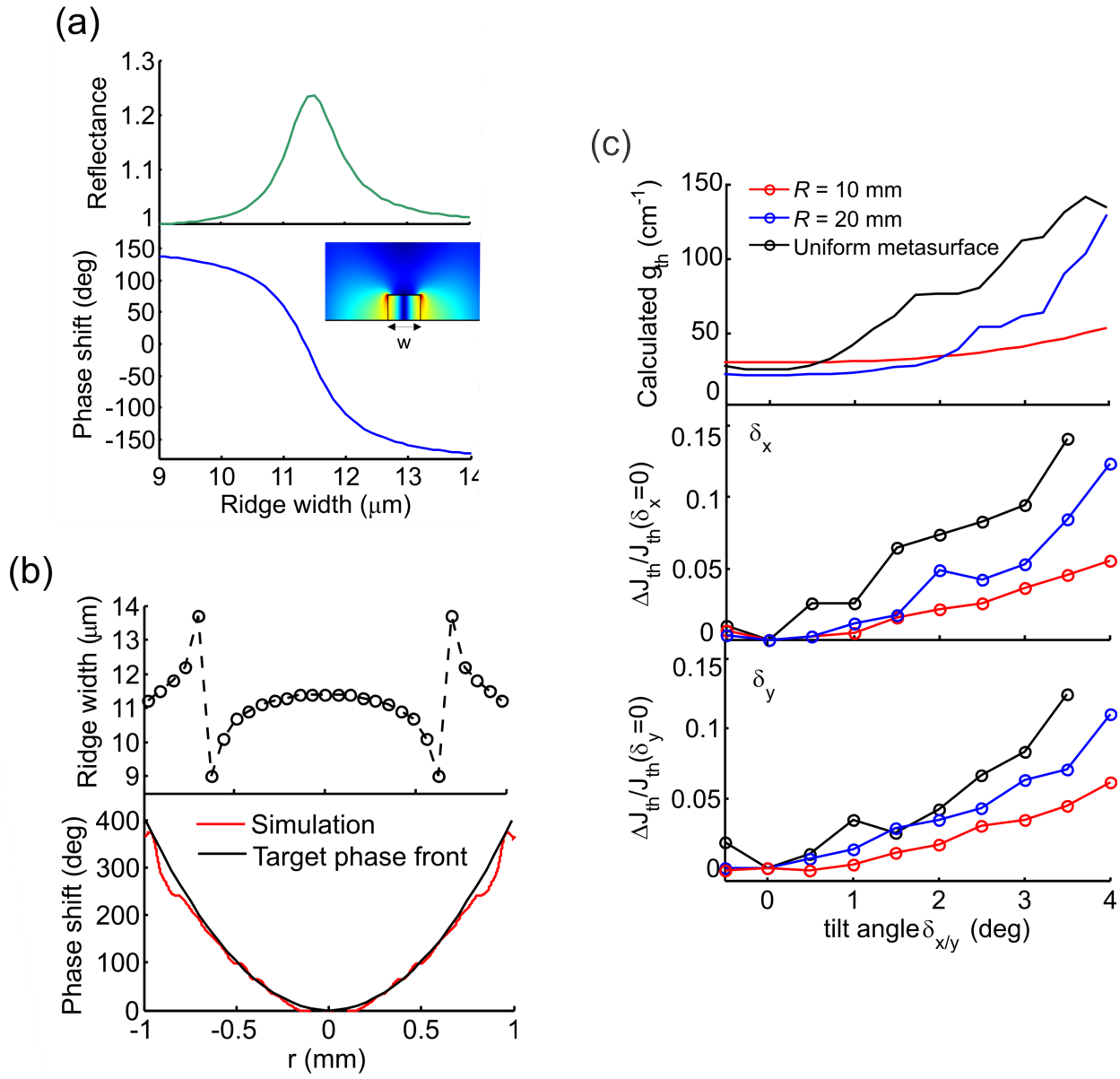

Figure 2.12: (a) Simulated magnitude and phase of a metasurface reflectance as the excitation frequency is kept constant, but the ridge width is varied. (b) Using the ridge width to control the reflection phase, the reflection phase can be varied spatially across the metasurface to approximate a quadratic phase response (spherical mirror). (c) The simulated diffraction losses for the (presumed) cavity tested, and the experimentally measured threshold as a funtion of misaligning the mirror external to the cryostat. It is observed that the diffraction loss was simulated to be very large, without even considering the optical thickness of the silicon window. Figures taken from Ref. [20].

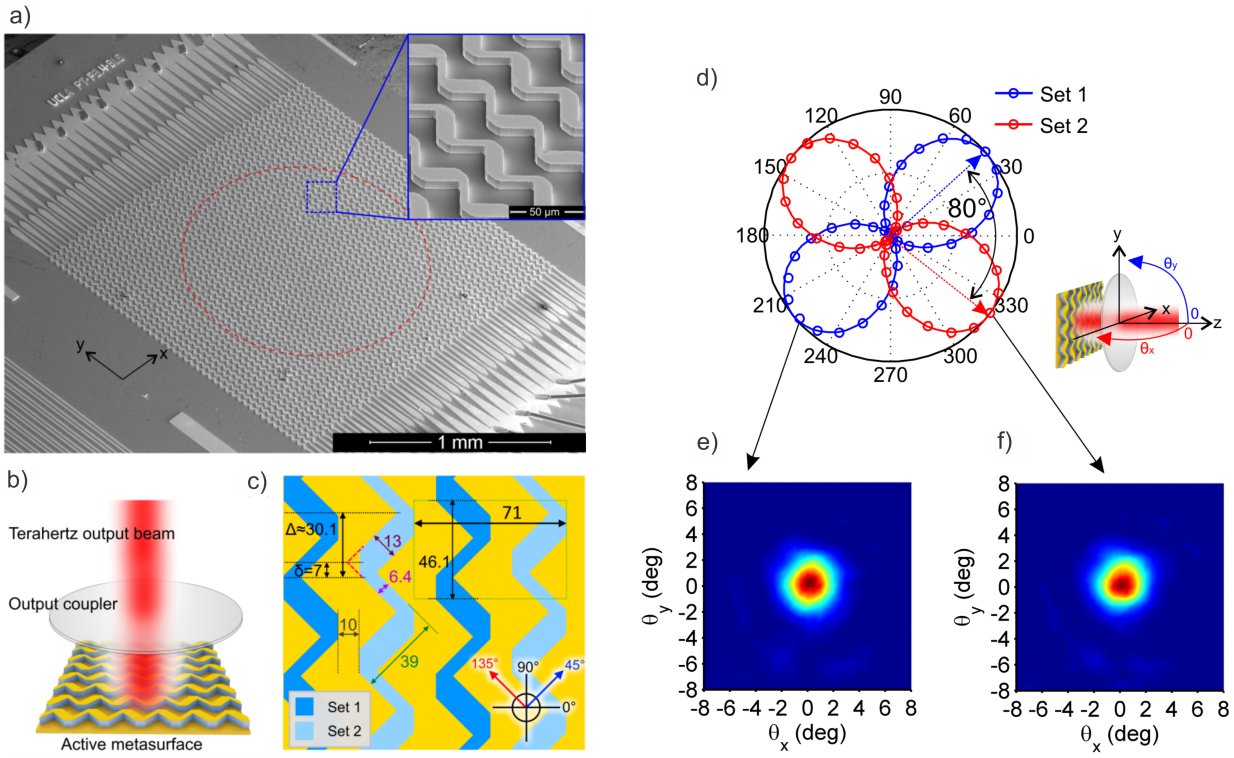

Figure 2.13: (a) SEM of fabricated polarization switchable device metasurface. (b) Illustration of the VECSEL setup, and (c) birds eye illustration of metasurface design. The different shades of blue indicate sets of ridges designed to lase at orthogonal polarizations. (d-f) Measured polarization characteristics and beam pattern of the VECSEL output beam. The two sets of ridges did not quite lase orthogonally, but at about 80° to each other. Figures taken from Ref. [21]

CHAPTER 3

High-power TM_{03} THz QC-VECSEL

3.1 Introduction

One of the most important characteristic of THz QCLs is their ability to produce much higher THz power than any other source of similar size, even considering the poor outcoupling efficiency of typical ridge waveguide based devices. At the time of writing this, the largest peak power that has been demonstrated is >2.8 W from each facet of a heavily multimoded surface-plasmon waveguide device (∼0.7% total wall-plug efficiency, ∼0.35% per facet). This high power was achieved by using a ridge with 20 μm of active material, made by wafer bonding two 10 μm thick active regions. The thicker ridge helps to both add more power (more photons per electron passing through) and improve outcoupling efficiency at the facet. Other approaches to achieving high-power and single-mode behavior were discussed in Chapter 1. With the advent of the THz QC-VECSEL, we now have a way to fully control the outcoupling efficiency in a power scalable device, providing a way to extract the maximum potential from any active region. In this chapter, we investigate scaling the QC-VECSEL to higher output power by means of an increased metasurface fill factor. Greater than 1 W of peak power is demonstrated.

3.2 Higher order metasurface designs

To increase the THz output power of the QC-VECSEL, there are two obvious routes: a) make the metasurface larger, or b) make the metasurface more dense (larger fill factor). Making the metasurace larger has a considerable drawback of consuming the valuable QC-

wafer material in a less efficient manner, as well as placing higher demands on fabrication quality to produce such large areas without any flaws. The most obvious way to increase the fill factor of the metasurface is to reduce the period. An alternative approach is to increase the width of the metasurface ridges to operate on a higher order resonance - all odd ordered TM cutoff modes of the ridges (TM_{01}, TM_{03}, TM_{05}, etc.) should couple to surface radiation in the same manner because they all have the same odd symmetry in the fields at the two sidewalls (see Fig. 3.1(a) and (e)). So, which approach is better? The answer lies in the difference of metasurface quality factor.

Based on the discussion in Chapter 2, reducing the period of the metasurface leads to stronger radiative coupling in the surface direction, which leads to lower quality factor, reduced amplification, and requires higher reflecting output couplers. Keeping the period constant while moving to a higher order resonances, on the other hand, should increase the quality factor of the metasurface as the total stored energy has increased, but the density of radiating apertures has not. What we find in simulation though is that the TM_{03} metasurface has a very similar quality factor to the TM_{01} surface with the same period (Fig. 3.1(d) and (e)). Presumably, this is because the more uniform distribution of the radiating dipoles in the TM_{03} geometry results in more efficient radiative coupling in the surface direction compared to the more peaked distribution associated with the TM_{01} ridges and could be proved with some basic array theory. The TM_{05} metasurface shows an increase in quality factor, which again, without doing an array analysis, all we can say is the radiative loss relative to the energy stored has apparently been reduced.

With regards to output power, if we assume no diffraction loss ($T = 1$ in equation 2.4), equation 2.13 reduces to (at threshold):

$$I_{out} = hF(g_{tr} - g_{th})TI_0. \tag{3.1}$$

Given that g_{tr} is largely independent of the quality factor (as material losses are similar for all modes), equation 3.1 indicates that the same output power would be achieved with

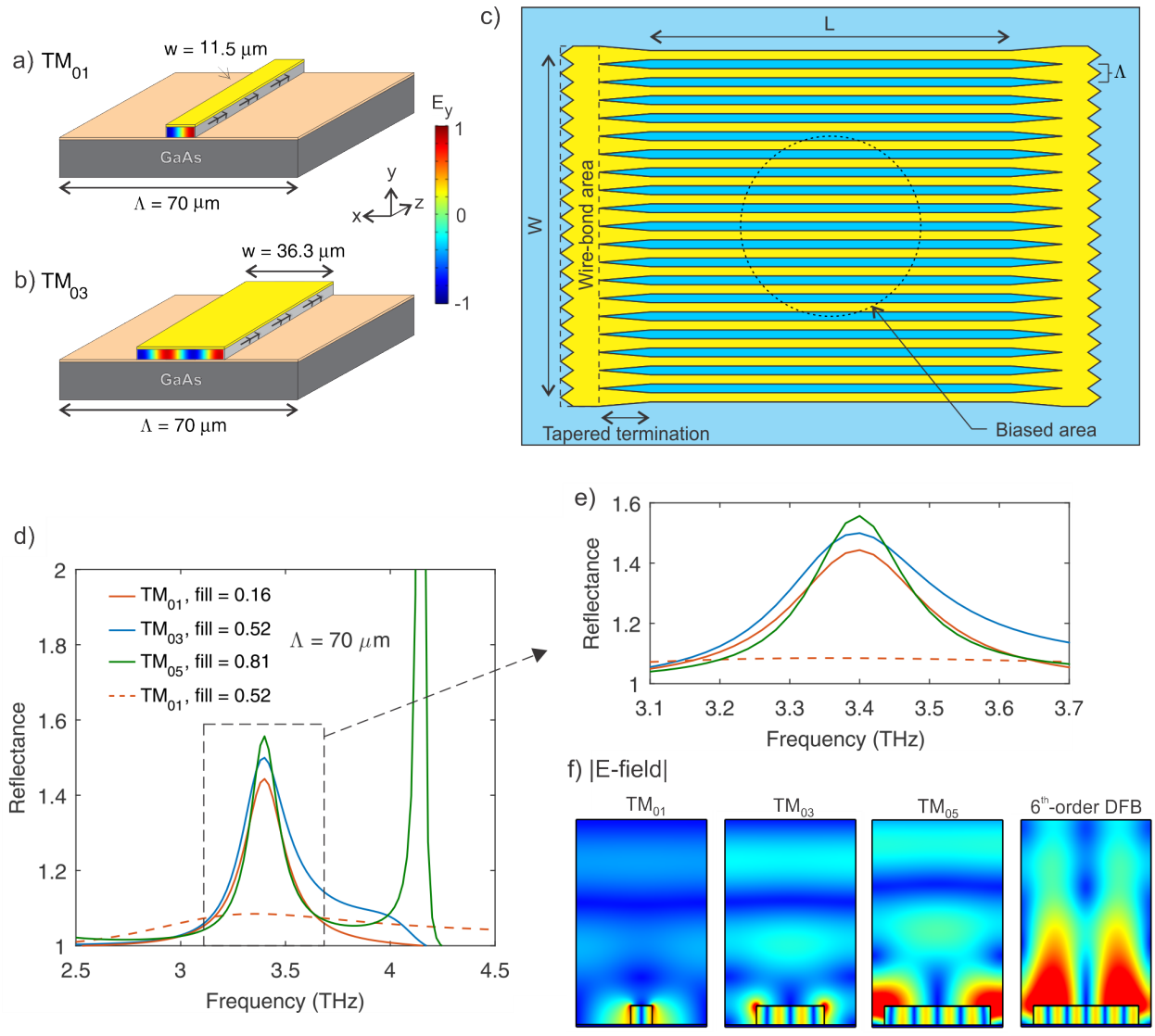

Figure 3.1: Cross-sectional illustration with transverse field profile of a metasurface unit cell operating on the (a) TM_{01} resonance and (b) TM_{03} resonance. The magnetic dipoles are indicated on the sidewalls and observed to be the same between the two designs. (c) Areal illustration of a TM_{03} metasurface (fill factor is to scale) with absorbing, tapered facets and wire bonding area indicated. (d-e) Comparison of simulated reflectances of infinite metasurfaces with a constant period but varying fill factor to operate on the TM_{01}, TM_{03}, and TM_{05}. 40 cm^{-1} of gain is applied (f) Simulated field plots for the different ridge resonances.

a low-Q vs a high-Q metasurface with the same fill factor as long as the output coupler reflection R_2 is modified in either case to yield the same threshold gain value g_{th}. Physically, this is a reflection the effect of the metasurface quality factor on the confinement of the

resonating THz energy to the metasurface. For a low-Q metasurface, the output coupler reflectance is high, but most of the energy is in the external cavity, so the field intensity incident on the output coupler is larger, and the output power is the same as the high-Q metasurface with a low R_2 but similarly reduced field intensity in the external cavity. This concept can be verified by considering the enhancement equation 2.12. Given this argument, however, it should be expected that diffraction loss is more detrimental to a low-Q than a high-Q metasurface as diffraction loss effects the fraction of energy stored in the external cavity. Indeed, when diffraction loss is added, equation 2.13 reduces to:

$$I_{out} = hF(\frac{1-R_2}{1-R_2T^2})(g_{tr}-g_{th})TI_0. \tag{3.2}$$

In which case, the larger R_2 required for the low-Q metasurface to maintain the same threshold as the high-Q metasurface results in a lower slope efficiency and output power. Therefore, using a metasurface based on a higher order resonance is a better solution than using one based on a smaller period. We note from Figure 2.6 that there is relatively little diffraction loss for short cavity lengths, however, using a high-Q metasurface still has the advantage of using lower reflectance output couplers, which practically, should make it easier to find the optimal coupling point as the metasurface is less sensitive to small fluctuations in feedback. In this chapter, we review experimental results of a high-power TM_{03} metasurface based on wafer VB0739.

3.3 Experimental results

The fabricated TM_{03} metasurface was 3×3 mm^2 with a central circular bias area 1.5 mm in diameter. As usual, the ends of the ridges were tapered into wire-bonding areas, as indicated in Figure 3.1. The device was tested with both a low reflectance (capacitive) and a high reflectance (inductive) output coupler. The measured transmittance and simulated efficiencies of these output couplers are plotted in Figure 3.2. For all measurements, the output coupler was mounted inside the cryostat on a single axis piezoelectric stepping stage

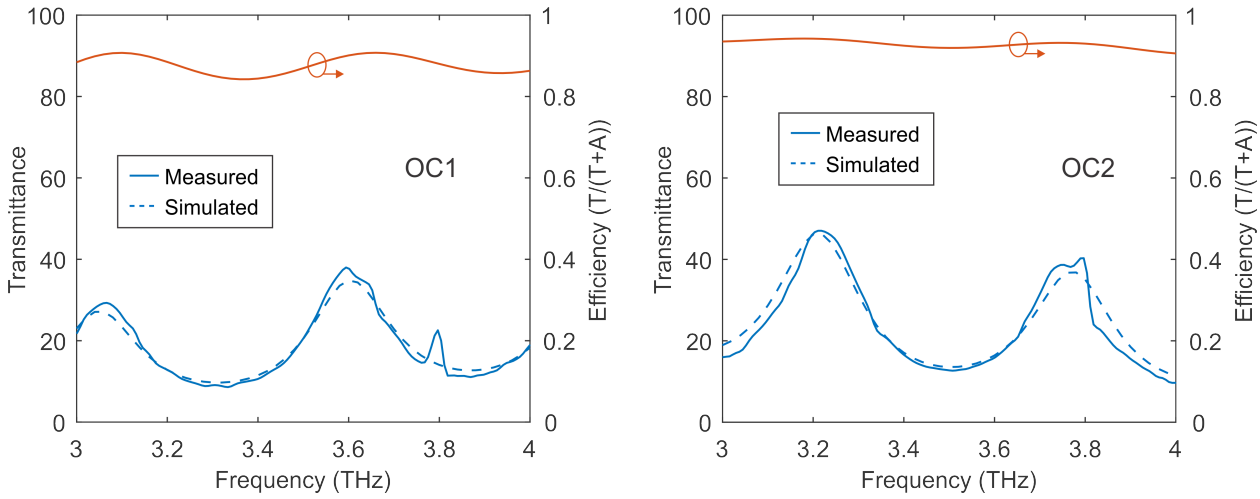

Figure 3.2: (a) Measured and simulated transmittance for the high reflectance inductive mesh (OC1). The mesh was designed to have a 15 μm period and metallic lines 2.5 μm wide. The simulated parameters that best match the measured result, however, is a period of 15 μm with line widths of 2.7 μm. (b) Measured and simulated transmittance for the low reflectance capacitive mesh (OC2). The mesh was designed to have a 17 μm period and metallic squares 14.5 μm per side. The simulated parameters that best match the measured result, is a period of 17 μm with squares 15.7 μm per side.

(see Figure 4.6) that can be used to adjust the cavity length (and correspondingly the frequency). The cavity is aligned with a He:Ne laser. Having tunablility of the lasing frequency is not only useful for its fundamental functionality (see discussion in Chapter 4), but it is also interesting as the output coupler reflectance has a strong Fabry-Perot dependence associated with the thickness of the crystal quartz substrate, so as the frequency is tuned, we can also observe the effect of R_2 on the VECSEL properties.

Results using an inductive mesh output coupler with ~9% transmission (OC1) are plotted in Figure 3.3. Measurements were taken in pulsed mode (550 ns pulses at a 2 kHz repetition rate); the large electrical power dissipation (~65 W) prevents continuous-wave operation. Power vs. current (P-I) curves were measured with a pyroelectric detector (Gentec), and absolute power levels were measured using a calibrated thermopile. Peak power levels of 0.79 W and 1.1 W were measured at 77 K and 6 K respectively, and the output intensity with current is observed to be very linear with slope efficiencies (dP/dI) of 380 mW/A

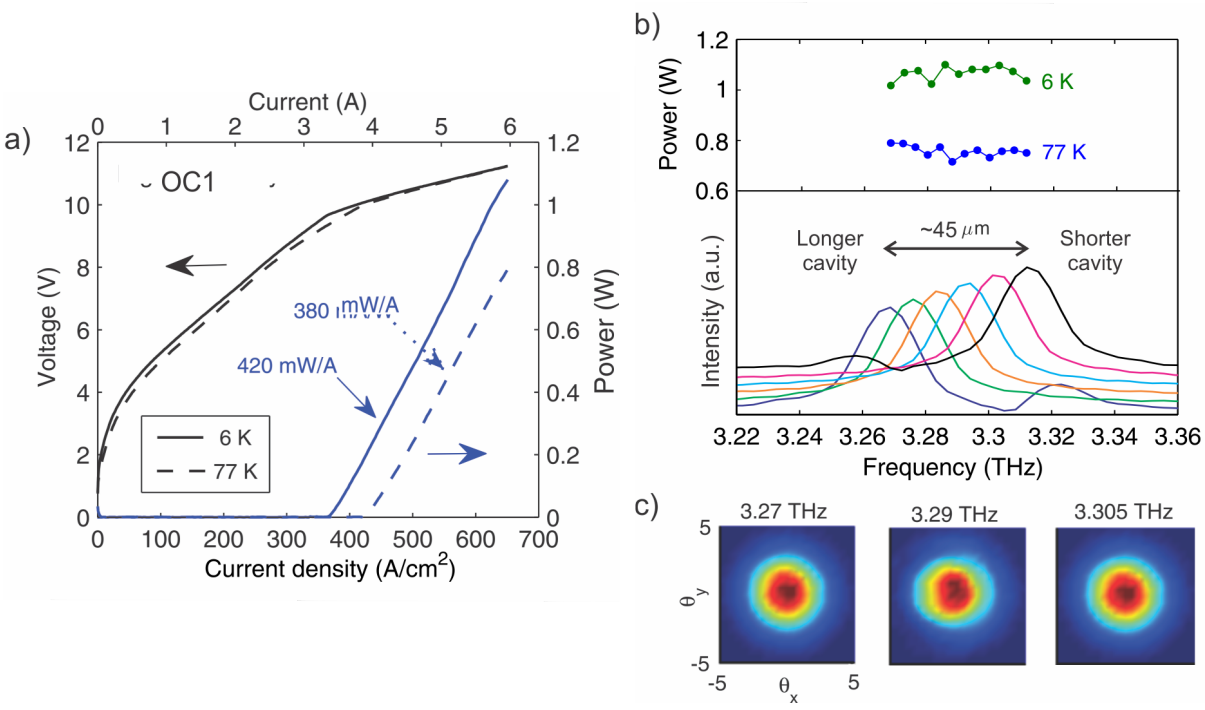

Figure 3.3: (a) Pulsed-mode poser and voltage vs. current characteristics from a TM_{03} VECSEL (3×3 mm^2 with a 1.5 mm bias diameter) using a highly reflective output coupler with a measured transmittance of ∼9%. (b) Normalized FTIR spectra collected as the VECSEL cavity length is tuned via a piezoelectric stepping stage, and corresponding output power as a function of frequency at 77 K and 6 K. (c) VECSEL far-field beam patterns.

and 420 mW/A at 77 K and 6 K respectively. The cryostat was equipped with a parylene anti-reflection coated high-resistivity silicon window whose measured transmission is ∼90% (Appendix 8.3) at 3.3 THz; the 10% window absorption has been accounted for in the reported power data. Spectra were measured using a Fourier-transform infrared (FTIR) spectrometer with 0.5 cm^{-1} resolution. By stepping the piezoelectric stage, continuous tuning of the laser frequency was observed from ∼3.27-3.32 THz. This 50 GHz tuning range is limited by the FSR of the external cavity; as the lasing mode is tuned away from the lowest threshold point, the adjacent longitudinal mode is tuned closer to the lowest threshold point and eventually a mode hop occurs. Using this FSR, we can estimate the length of the external cavity to be ∼3 mm, limited by the resolution of the FSR. The piezoelectric stage is operated with an open-loop controller that does not have a position readout, but we can estimate its

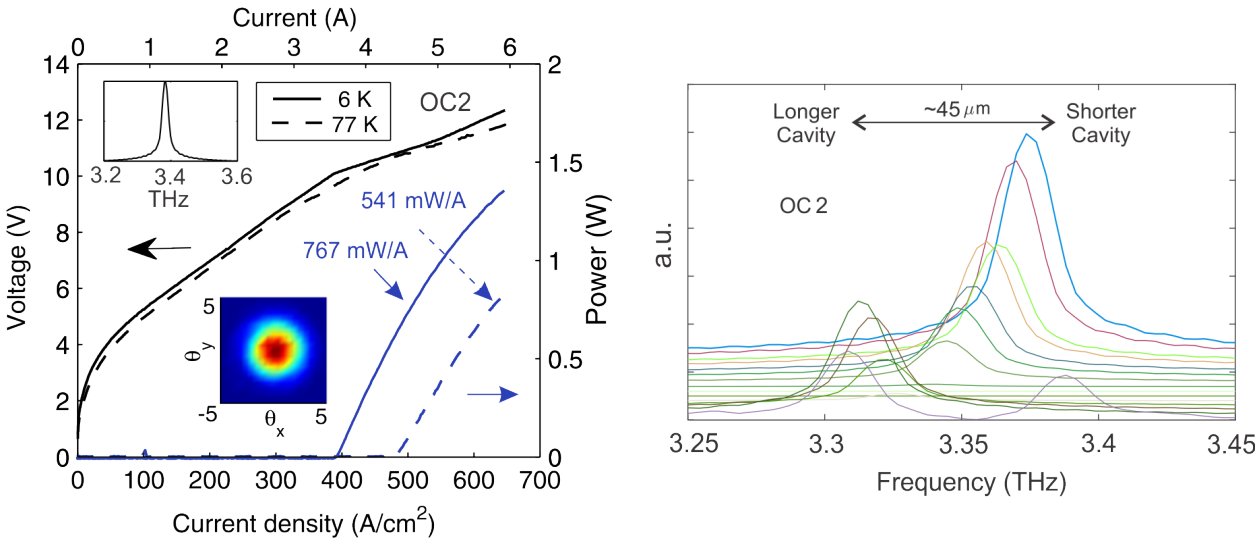

Figure 3.4: (a) *P-I-V* data from a TM_{03} VECSEL using a low reflective output coupler (OC2) with a measured transmission of ∼18%. The beam pattern and spectrum are indicated in the insets. (b) FTIR spectra collected collected with OC2 as the cavity length is tuned using the piezoelectric stage. The power was not tracked as the device tuned through a strong atmospheric absorption at ∼3.33 THz. The spectra have intentionally not been normalized so the absorption is apparent.

change since we know the cavity length must change by half of a wavelength to hop back to the starting frequency. The reflectivity of the output coupler is relatively flat through the tuning range, as is the measured output power and threshold current, which suggests that the QC-gain material and the metasurface reflectance are also relatively constant through this range. Two-axis beam measurements were performed using a 2-mm diameter pyroelectric detector scanned in a spherical pattern at a constant distance of 15 cm from the VECSEL (0.8° resolution). Circular, high-quality beams are consistently observed as the VECSEL is tuned with a full-width half-maximum divergence angle of ∼4°; 1-D beam cuts with Gaussian curve fits in Figure 3.5 show excellent fitting down to 25-30 dB in intensity.

Results of the same TM_{03} metasurface using the low reflectance capacitive mesh (OC2, ∼18% transmittance, see Figure 3.2(b)) are plotted in Figure 3.4. Threshold currents, slope efficiencies, and maximum powers all increase at both 77 K and 6 K compared to the high reflectance ouput coupler (OC1), which indicates that the laser is closer to the optimum

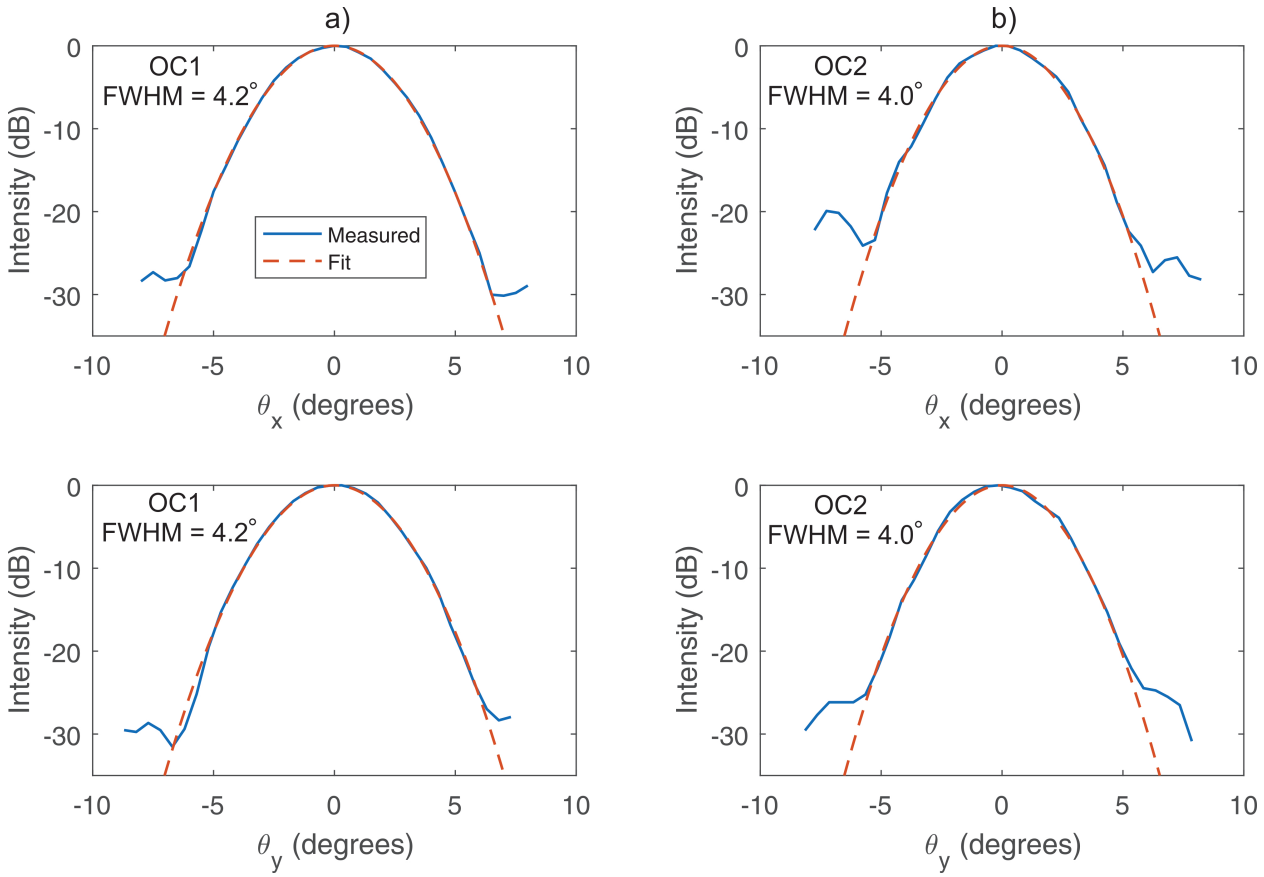

Figure 3.5: Fitting 1-D beam pattern cuts to Gaussian curves for (a) OC1 and b) OC 2.

outcoupling condition. A maximum peak power of ∼1.35 W and peak slope efficiency of 767 mW/A is observed in a single mode with a narrow, Gaussian shaped beam and peak wall-plug efficiency of ∼2% at 6 K (see Figure 3.6(a)). The lasing frequency when using OC2 was ∼3.38 THz, slightly higher than OC1, which lased closer to 3.3 THz. This can be explained by observing that OC2 is more reflective at higher frequencies, which results in lower threshold currents at higher frequencies. The VECSEL was again tuned through the cavity FSR of ∼80 GHz, from 3.31-3.39 THz (Figure 3.4(b), cavity length ∼1.9 mm), however, there is a strong atmospheric absorption line at ∼3.335 THz that makes it difficult to accurately characterize the power and slope efficiency as a function of tuning.

In Ref. [18], results from a TM_{01} metasurface using the same QC-wafer (wafer VB0739) and the same period as the TM_{03} metasurface (Λ=70 μm) are presented. Per the discussion

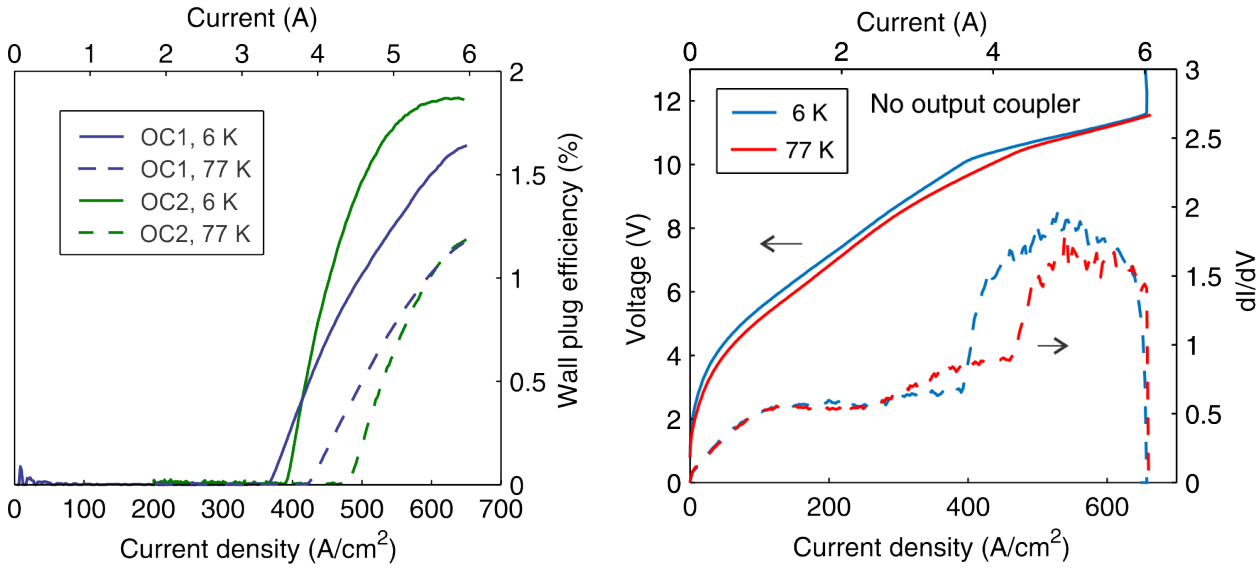

Figure 3.6: (a) Wall plug efficiency as a function of electrical pump power for the TM_{03} metasurface. Results for both OC1 and OC2 at 77 K and 6 K are presented. (b) Measured I-V and $\mathrm{d}I/\mathrm{d}V$ curves from the TM_{03} metasurface when no output coupler is used. Onset of such self lasing may be the cause of the roll-off in wall plug efficiency at higher bias.

in the introduction of this chapter, because these two metasurfaces have almost the same quality factor, we would expect the same slope efficiency between the two metasurfaces when they're paired with the same output coupler; the increased fill factor of the TM_{03} metasurface should simply result in larger output power by virtue of larger total pump current. However, in Ref. [18], when the TM_{01} metasurface is paired with a ∼17% output coupler, a slope efficiency of 745 mW/A is reported at 77 K through the entire dynamic range of the laser. The TM_{03} metasurface, on the other hand, only reached a peak slope efficiency of 541 mW/A at 77 K when paired with a similar output coupler measuring ∼18% transmittance. The most likely explanation we have for this result is that simultaneous self-lasing of TM_{00} modes propagating along the length of the ridges is competing for gain and reducing the power coupled into the VECSEL mode. In Figure 3.6(b), measured I-V curves from the metasurface without an output coupler both at 77 K and 6 K indicate that self lasing is occurring. The signal from the self-lasing mode could not be measured by the pyroelectric detector as very little of the self-lasing radiation should be coupled to

the surface direction, but the distinct discontinuity in the slope of the I-V curve associated with the onset of stimulated emission is a sure sign of lasing. In fact, at 77 K, the threshold current density J_{th} of the VECSEL with OC2 and the threshold for the self-lasing mode $J_{th,self}$ are measured to be nearly identical at 484 A/cm^2, so modal competition is likely. At 6 K, however, the TM_{03} VECSEL with OC2 has J_{th}=390 A/cm^2, while $J_{th,self}$=415 A/cm^2, potentially allowing for more effective discrimination between the modes. Threshold currents for the VECSEL when using OC1, on the other hand, are notably below the self-lasing values (J_{th}=421 A/cm^2 and 363 A/cm^2 at 77 K and 6 K respectively). This may explain why OC2 shows a much much more significant boost in slope efficiency when going from 77 K and 6 K operation compared to OC1, and why more linear slope efficiencies are observed with OC1 than OC2. In fact, there is a rather distinct second discontinuity in the I-V curve taken with OC2 at 6 K that lines up well with a sudden rolloff in the wall-plug efficiency at $\sim$5 A pump current.

It is a little surprising that self-lasing was observed in the TM_{03} metasurface as the relative length of the absorbing regions at the ends of the ridges are similar to those used in most TM_{01} designs. While the propagation losses for the TM_{00} mode are slightly larger in a narrow TM_{01} ridge compared to a TM_{03} ridge that is 3$\times$ as wide, the difference is not significant enough to expect issues (g_{th}= 19.8 cm^{-1} for an 11.5 μm wide TM_{01} ridge compared to 18.2 cm^{-1} for a 36.3 μm TM_{03} ridge). Perhaps the power reflected by the facet at the end of the wire-bond area feeds back more strongly into the wider TM_{03} ridges, or perhaps similar sized TM_{01} metasurface are coincidentally very close to self-lasing, and the 1-2 cm^{-1} difference in loss made the difference. Self-lasing has been observed from TM_{01} metasurfaces with larger bias areas (1.5 mm bias diameter in a 2$\times$2 mm metasurface). As long as sufficient loss is maintained at the ends, the author does not see any particular reason why this approach could not be scaled to even larger metasurfaces and TM_{05} designs. Suppression of the self-lasing alone without increasing the bias diameter has the potential to increase the power and wall-plug efficiency substantially.

CHAPTER 4

Broadband tuning of THz QC-VECSELs

4.1 Introduction

Widely tunable single-mode laser sources are interest for applications such as broadband spectroscopy, frequency-agile heterodyne receivers, and optical coherence tomography [108, 109]. While there are countless specific techniques for tuning laser emission [110–112], most can be categorized by modeling the laser as a simple Fabry-Perot (FP) cavity oscillating at a frequency $\nu_m = mc/2nL$. The order of the longitudinal mode is given by m, L is the physical length of the cavity, and n is the index of refraction of the constituent medium (or modal effective index in the case of a waveguide). Tuning the frequency over a range $\delta\nu$ occurs through some combination of tuning n, m, or L; continuous tuning requires control of n or L. Changing the index n - for example using temperature - usually provides fractional tuning $\delta\nu/\nu$ of not more than 1% since the achievable $\delta n/n$ is similarly small for most laser materials. Use of monolithic sampled-grating or coupled-cavity approaches can increase tuning ranges to a few percent by stitching together tuning regimes [113–115]. Changing the cavity length L also provides limited tunability since laser cavities are typically orders of magnitude longer than their lasing wavelengths, resulting in a small tuning range $\delta\nu \approx$ FSR before mode-hopping occurs. In most cases, broadband tuning is accomplished by introducing tunable intracavity spectral filters such as gratings, etalons, prisms, etc. These techniques typically amount to hopping between longitudinal modes m, while continuous tuning between modes can often be obtained with fine control of L. If enough parameters are synchronously tuned, tracking of a mode with constant m over broad bandwidths can be often be recovered [116, 117], but such approaches require careful design and are often

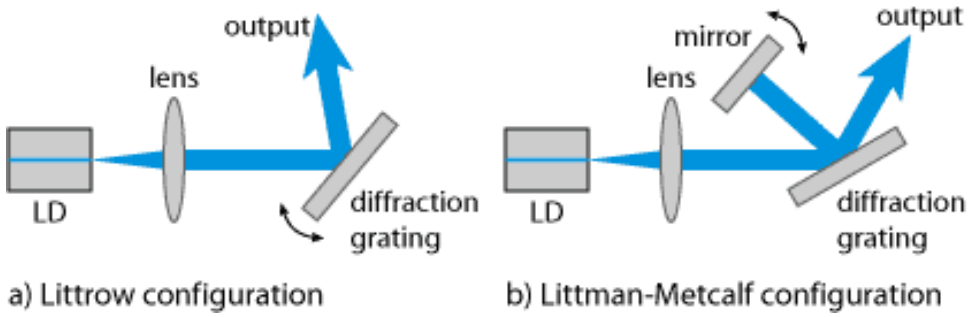

Figure 4.1: Typical frequency tunable diode laser external cavity configurations using diffraction gratings. (a) The Littrow configuration is generally more efficient. The beam steers while tuning. (b) Littman-Metcalf configuration, less efficient, but beam position is fixed. Both techniques require anti-refelction coatings on the facet of the laser ridge. Figure taken from RP-Photonics [22].

limited in speed and repeatability.

For example, with semiconductor laser diodes, small scale tuning is typically achieved with n using either temperature (more broad, but slow), or electrical pump current (narrow, but fast). Tuning of the cavity length L requires the laser to be coupled to an external cavity and is very narrowband as diode laser ridges are typically hundreds to thousands of wavelengths long. With exception of the MEMS tunable diode VCSEL, broadband tuning of diode lasers is almost exclusively achieved by integrating the laser into an external cavity utilizing a diffraction grating for feedback, notably the Littrow and Littman-Metcalf configurations (Figure 4.1). The diffraction grating acts as a spectral filter that can be tuned by simple rotation of the grating about its axis. Using only rotation, however, leads to mode-hopping across the longitudinal modes of an approximately fixed cavity length. By incorporating adjustment of L, the longitudinal modes of the cavity can be tune simultaneously with the angle of the grating, allowing a single mode to be tracked over broad bandwidths. In the Littrow configuration, the grating is moved both rotationally and longitudinally. In the Littman-Metcalf configuration, the grating is fixed while the incidence angle and cavity length are both tuned by rotation of the second mirror (reflecting the 1^{st} diffracted order). The advantage of the Littman-Metcalf configuration is that the direction of the output beam

– the specular reflection of the laser facet output off of the grating – is fixed as the position of the laser and the grating are fixed. The disadvantage is that the power is often lower because the efficiency of the grating into the 1^{st} diffracted order is typically quite high to maintain good frequency selectivity and minimize walk-off losses associated with specular reflection of the light from the second mirror off of the grating. Despite the lower power, Littman-Metcalf configurations seem to be the preferred choice in industry and commercially available systems routinely achieve ∼5% fraction tuning, and in some cases >10% [118]. In some cases, particularly optical coherence tomography (OCT) imaging, mode hopping is acceptable (assuming the FSR is small), but the speed of the tuning is of more concern for fast imaging times. A variety of "swept wavelength" sources are commercially available based on EC diode lasers integrated with a rapidly tunable spectral filter. For example, diode laser amplifiers can be integrated into fiber laser cavities and the lasing wavelength is swept across the gain spectrum of the semiconductor material using an acousto-optic tunable filter. In recent years, MEMS tunable VCSELs, which use high-reflectivity MEMS Bragg mirrors to allow cavity lengths of only a few wavelengths, have demonstrated broadband continuous tuning of a single mode and can also offer the fastest tuning speeds thanks to the high frequency MEMS and are perhaps becoming the most sought after solution [119].

Quantum-cascade (QC) lasers are particularly appealing for broadband tuning as the short upper-state lifetimes of the intersubband transitions give QC-material naturally broad bandwidth. Further, active region designs with different center frequencies can be stacked to provide even broader gain from a single device. Such stacking is only possible because intersubband transitions are transparent on either side of the transition energy (unlike interband lasers, which are absorbing on the high frequency side). For example, in the mid-IR, stacking of up to five different active regions has been used to yield continuous coverage (by mode hopping) from 7.6-11.4 μm (34% fractional around 9.5 μm) [120]. In Ref. [121], 15% fractional continuous tuning of a single longitudinal mode around 8.25 μm has been demonstrated with mid-IR QCL using a modified Littrow configuration with added piezoelectric control of the cavity length to enable tracking of a single mode. In the terahertz, using a

stack of three different QC active region designs, continuous octave spanning gain has been demonstrated from 1.64-3.35 THz (68% fractional coverage around a center frequency of 2.5 THz) [122]. THz QCLs exhibit broader bandwidths than mid-IR devices thanks to the shorter upper-state lifetime, but are more challenging to implement in EC configurations because the sub-wavelength sized metal waveguide resonators exhibit extremely poor coupling to free space [51]. The most successful examples are EC lasers based on QC surface-plasmon waveguides with facet-mounted silicon lenses. In Ref [123], up to ∼4% total fractional tuning around 4.4 THz was demonstrated using a standard Littrow configuration, but significant mode hopping occurred and only a handful of modes were observed across the tuning range.

As a result, researchers have turned to more exotic, creative schemes for broadly tuning THz QCLs. The most successful strategy has been to use a MEMS "plunger" to perturb the evanescent fringing fields of a narrow metal-metal waveguide with a 1^{st}-order distributed feedback grating [124, 125]. The plunger can be actuated with a piezoelectric stage mounted in the cryostat, and up to 8.6% fractional continuous tuning (no mode-hopping) around 3.85 THz has been demonstrated with this technique, though the power is very small and the beam pattern extremely poor as the approach is based on a small metal-metal waveguide. It was reported that the tuning range of the MEMS plunger approach was limited by the gain bandwidth of the QC-material, not the plunger technique itself. Another noteworthy demonstration for broadly tuning THz QCLs used EC coupling to a metal-metal waveguide via surface emission from a second order distributed feedback grating patterned into the ridge [126, 127]. The grating mode and external cavity mode couple together and anticross, allowing the resonant frequency of the total mode to be tuned by adjusting the length (and therefor resonant frequency) of the external cavity. This approach has demonstrated up to 5% continuous fractional tuning of a single mode around 3.2 THz, limited by mode-hopping across the FSR of the external cavity. Presumably, if the EC was made shorter, the spacing between modes would increase, but the tuning range may not increase much as it will likely be limited by the narrow bandwidth of the 2^{nd}-order grating. This surface-coupled EC approach is effectively the same approach that will be presented in this chapter for tuning

of the QC-VECSEL, the difference is that the QC-VECSEL is based on very broadband, low-Q resonant elements that allow for more broad tuning. Aside from these techniques, a number of less successful attempts have been made to tune terahertz QCLs that have mostly amounted to very narrow band tuning, and loosely controlled mode hopping.

Broadly tuning a laser's wavelength using only control of the cavity length L is possible if the laser resonator can be made extremely short, which forces it to operate on a low-order longitudinal mode ($\delta\nu/\nu$=1/(m+1/2) in a simple FP cavity). This is a difficult criterion for most infrared and optical lasers as such a short cavity requires very highly reflective mirrors to compensate for the short propagation length within the gain medium. Swept-wavelength VCSELs are perhaps the only successful realization of broadband continuous tuning using L. Up to 12% fractional tuning (close to the material gain bandwidth) has been demonstrated from optically pumped VCSELS based on an undisclosed InP-based multiple-quantum well active region operating from 1225-1375 nm [119], and up to 6% fractional tuning has been demonstrated with an electrically pumped VCSEL based on InGaAs quantum wells operating from 1010-1070 nm [128]. In both cases, the tuning range was limited by the FSR of the cavity; a smaller FSR is obtained with the electrically pumped device because the need for thick current spreading layers limits how short the cavity can be made. While the large tuning bandwidth is impressive, the primary advantage of the MEMS VCSEL approach over other techniques is the fast wavelength sweep rates associated with the high resonant frequency of the suspended Bragg mirror, allowing for high-speed OCT imaging. Resonant frequencies as high as 500 kHz have been reported, allowing for bi-directional scan rates of up to 1 MHz [128].

With the THz QC-VECSEL enabling vertical cavities based on QC-gain material, we can now explore the possibility of broadband tuning by making the cavity ultra-short. In fact, the THz QC-VECSEL offers several some advantages over the diode VCSEL in that:

- **The metasurface is thin (10 μm) compared to the operating wavelength (on the order of 100 μm), allowing the cavity length to be reduced to the lowest m=1 Fabry Perot mode.** Diode VCSEL cavities cannot be reduced below a couple

wavelengths.

- **The gain is based on a per-reflection basis rather than a per-unit-length basis, so reducing the cavity length has no adverse effect on the laser threshold.**
  - While this is true for a given metasurface, it should be noted that (as discussed in Chapter 2) there is a trade-off between metasurface bandwidth and amplification factor as the quality factor of the resonance reflects the amount of time the coupled radiation spends accumulating gain in the metasurface. In theory, if the quality factor were reduced enough, the gain-per-reflectance could approach the equivalent gain associated with propagation through 10 μm of QC-gain material (the thickness of the metasurface). Therefore, if one wishes to tune through the full bandwidth of the QC-gain material, it is likely that highly reflective mirrors are still needed. However, while the gain-per-pass in a diode VCSEL laser is $\sim$1% requiring 99% reflectance mirrors, even broadband THz metasurfaces with 20% fractional wavelength coverage can provide gain-per-reflectance on the order of 10%.

Further, the QC-VECSEL is a good candidate for a variety of broadband tuning schemes as it is fundamentally an external cavity approach, sidestepping the need for coupling through the facets of the ridges. Introducing a spectral filter such as a diffraction grating into the external cavity would be the obvious choice, however, the drawbacks to such an approach is the need for highly efficient gratings over broad bandwidths and very careful management of diffraction associated with longer external cavities.

This chapter details the results of using change in the external cavity length L_{EC} to tune the THz QC-VECSEL. Lasing is observed even at subwavelengths cavities, and upwards of 20% fractional tuning is observed.

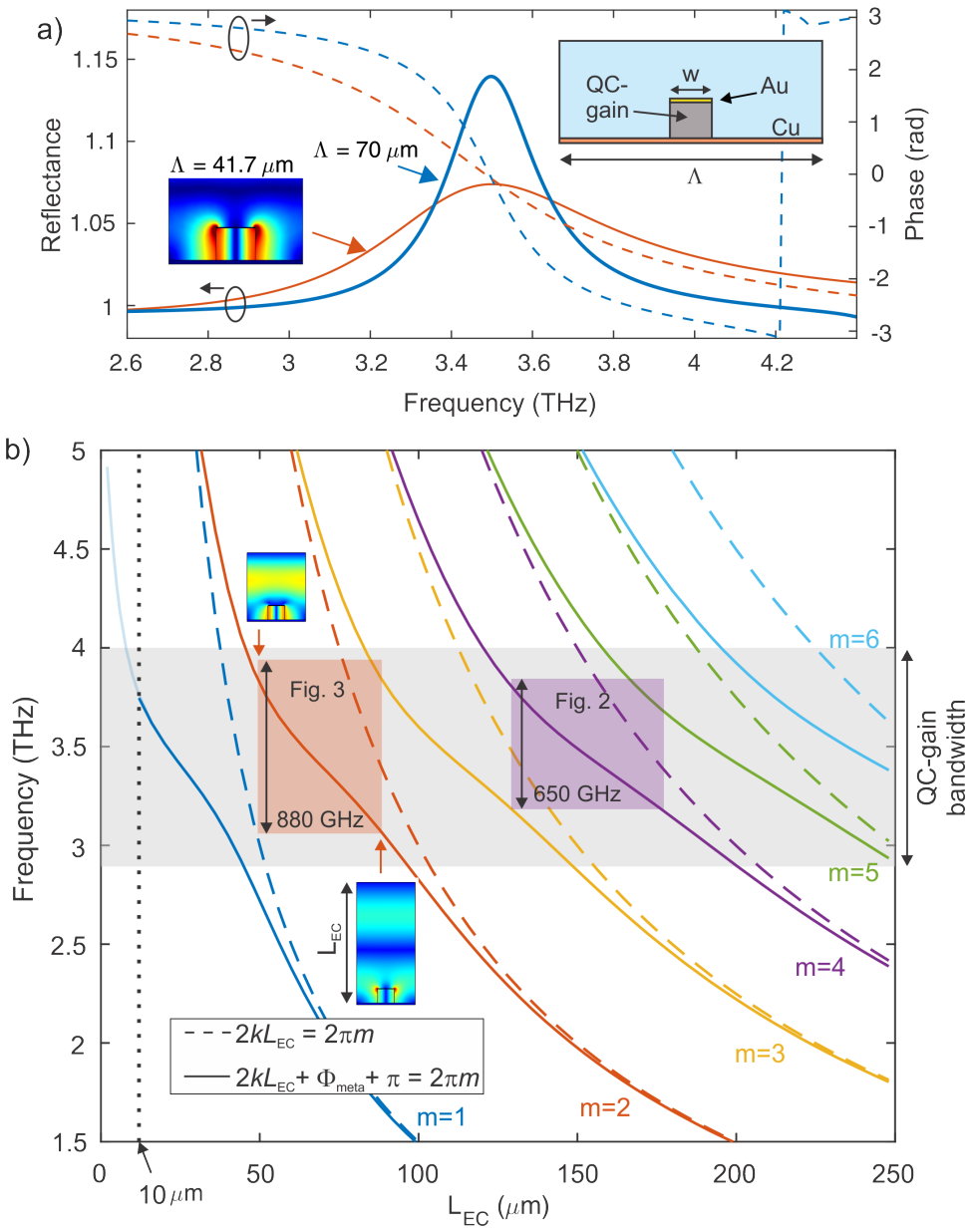

Figure 4.2: (a) Simulations of the metasurface reflectance and reflection phase spectra when 25 cm^{-1} of intersubband gain is added to the ridges. Two metasurface periods are simulated for comparison, $\Lambda = 70$ μm and 41.7 μm. The trade-off between bandwidth and amplification is apparent. (b) Cavity eigenfrequencies vs. cavity length for both a bare Fabry-Perot cavity neglecting reflection phase (dashed lines), and complete cavity modes including metasurface phase (solid lines). Colored boxes indicate the particular cavity modes over which tuning is presented in this work. Insets show the E-field magnitude at the two extremes of the m=2 mode.

4.2 Short-cavity tuning: theory and limitations

While the concept of tuning laser frequency using the length of the cavity is rather simple, there are some important considerations to be made when working with a resonant metasurface. Consider the full expression for the resonant modes of the QC-VECSEL cavity:

$$2kL_{EC} - \phi_{meta} - \phi_{oc} = 2\pi m \tag{4.1}$$

Where $k{=}2\pi\nu/c$ is the free space wavenumber, L_{EC} is the length of the external cavity, ϕ_{meta} and ϕ_{oc} are the frequency dependent reflection phases of the metasurface and output coupler respectively. This is simply the familiar condition requiring the roundtrip phase accumulation in the cavity to be an integer multiple of 2π. In the canonical example, where the phase terms are equal to π and have no frequency dependence, the equation reduces to $kL_{EC}{=}\pi m$, and the single-mode frequency tuning that can be achieved is an octave (66% fractional) since $\nu_{m=2}{=}\nu_{m=1}$ (assuming symmetric operation around a homogeneously broadened gain curve).

In the case of the QC-VECSEL, however, ϕ_{meta} demonstrates nearly 2π phase shift across the resonance (Figure 4.2(a)). This phase accumulation represents a group delay ($\tau_g{=}d\phi_{meta}/d\omega$), which has the effect of compressing the FSR near resonance, and reduces the maximum single-mode tuning range for a given order m. This effect is illustrated Figure – for a broadband metasurface designed to have a center frequency of 3.5 THz (41.7 μm period and 11.9 μm ridge widths). The cavity mode frequencies (determined by periodic FEM eigensimulations) are plotted including the effects of metasurface phase (see inset). Based on the figure, assuming octave spanning gain around the center frequency of 3.5 THz, the fractional single-mode tuning to be expected around the center frequency of 3.5 THz for the first few modes is:

- $m{=}1$ can theoretically tune over a 32% fractional range (1.13 THz from 2.93-4.06 THz, $L_{EC}{=}$44-7 μm), but in practice, the thickness of the metasurface prevents one from making the cavity length less than 10 μm, limiting the highest frequency of the $m{=}1$

mode to 3.76 THz, reducing the tuning range. The tuning range is significantly below an octave in any case.

- m=2: 22% fractional tuning range (0.78 THz from 3.11-3.89 THz, L_{EC}= 87 - 48 μm).
- m=3: 18% fractional tuning range (0.62 THz from 3.19-3.81 THz, L_{EC}= 90 - 129 μm).
- m=4: 15% fractional tuning range (0.52 THz from 3.24-3.76 THz, L_{EC}= 132 - 171 μm).

Interestingly, even at extremely short cavity lengths, the simulated eigensolutions for an infinite structure show almost no deviation from those predicted by equation 4.1, which is based on the simulated far field response, assuming that the length of the cavity is defined as the distance from the ground plane of the metasurface to the output coupler. One might expect a perturbation from equation 4.1 as the output coupler gets close enough to the metasurface to perturb the fringing fields, but this does not appear to be the case, or at least is a very weak effect.

Utilizing a smaller period more broadband metasurface reduces the group delay and increases the potential tuning range, however, as discussed, this comes at a cost of competition with reduced metasurface amplification and higher threshold gain values. The optimal point depends on the maximum gain coefficient, which cannot be easily measured.

4.3 Early results

Earlier tuning experiments were performed on whatever metasurfaces were available. These earlier experiments were conducted by simply adding three piezoelectric stack actuators (purchased from Noliac) to the three spring loaded screws of the intracryostat cavity setup, as illustrated in Figure 4.3(a), allowing a small degree of control over the cavity length while testing the device. Each stack was rated for ≈50 μm actuation range at 77 K (which should be enough to tune through an FSR of the cavity) for a bias range of 0-200 V. The three stacks were biased in parallel with a single DC power supply (Agilent 2410). Such piezoelectric

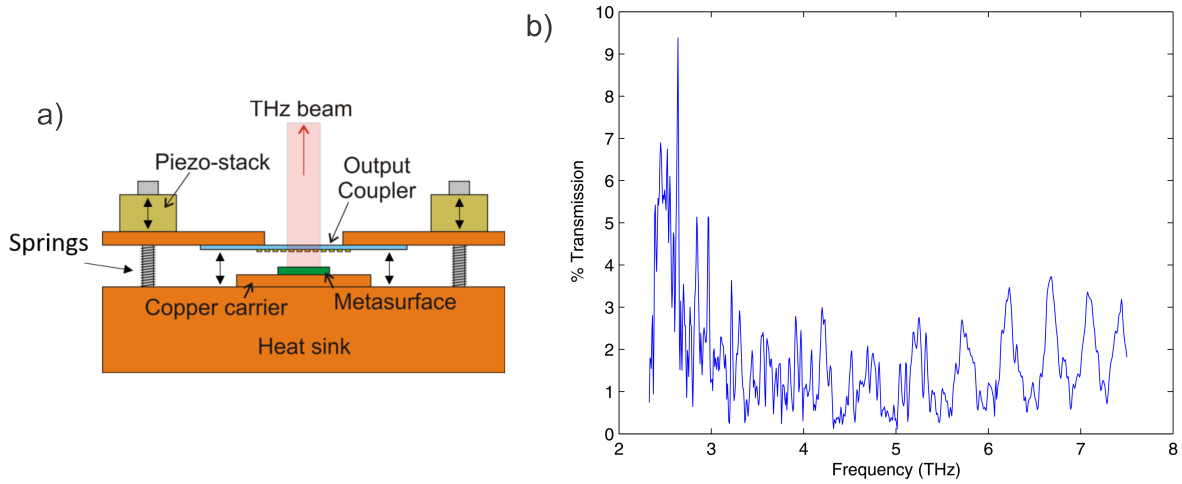

Figure 4.3: (a) Illustration of intracryostat VECSEL setup with piezoelectric stacks added to allow the cavity length to be tuned. (b) Measured transmittance of inductive mesh output coupler with a period of 10 μm and a line width of 4 μm. Substrate is $\sim$130 μm of crystal quartz. Measurement was done with room temperature DTGS detector.

stacks are much less ideal than a piezoelectric stepping stage as they are subject to significant hystoresis and drift, and cannot be reliably controlled in parallel, however, uncoincidentally, piezoelectric stacks are a much cheaper solution and so were used at the start. In this section, we review such early results obtained using piezoelectric stacks. All of the data was collected using a inductive mesh output coupler (to keep threshold current low) with a period of 10 μm and a line width of 4 μm. The FTIR transmission measured with a room temperature DTGS detector is plotted in Figure 4.3. The DTGS detector is not sensitive enough to capture the detailed transmission, but it is clear that it is low (<3%). A duplicate output coupler has been measured with a cryogenic detector in Ref. [17], but there could be slight variation in lithography or substrate thickness from fab to fab.

4.3.1 Tuning uniform metasurface with a 60 μm period

Results of tuning a uniform 2×2 mm^2 metasurface with a 60 μm period, 750 μm bias diameter, and w=12 μm ridge width designed to operate at 3.4 THz are presented in Figure 4.4.

Simulations in Figure 4.4(a) indicate that the full-width half-maximum (FWHM) of the 60 μm period surface is $\sim$ 375 GHz, compared to a FWHM of $\sim$ 800 GHz for the 41.7 μm periodic surface (Figure 4.2). Experimentally, $\sim$400 GHz of tuning was observed centered around 3.3 THz, comparable to the simulated FWHM. Based on the observed FSR, and properly accounting for the metasurface phase, the estimated cavity length varied from 234-277 μm, and the fabricated ridge width was 11.4 μm. The tuning was limited by the FSR of the external cavity, so it is possible that even more tuning is available at shorter cavity lengths. Beam patterns measured at 3.28 THz and 3.41 THz indicate distorted and inconsistent beam shapes, suggestive of cavity misalignment presumably resulting from non-uniform movement between the three piezo-stacks. For this reason, further measurements were not performed. The advantages of upgrading to the piezo-stepping stage are that the cavity alignment is fixed while the stage moves very precisely along a fixed axis, and the stepping stage can move on a millimeter scale, allowing the user to scan through a much larger range of cavity lengths without having to open the dewar. The entire actuation range of the piezo-stacks was used to collect the data in Figure 4.4. In order to try for more tuning at shorter cavity lengths, the dewar would have to be opened and the cavity manually adjusted. Detailed power and threshold data were not collected as it takes significant time and the beams were unsatisfactory. The bottom spectra in Figure 4.4 also shows two modes lasing right next to each other around 3.15 THz, suggesting poor cavity alignment.

4.3.2 Tuning a focusing metasurface with a 70 μm period

Results of tuning a focusing metasurface with a 70 μm period designed to operate at 3.4 THz (ridge width w=12 μm) are presented in Figure 4.5. The metasurface was designed to mimic a spherical mirror with a 20 mm radius by spatially varying the ridge width, as described in Chapter 2. However, the phase response of the metasurface will only be quadratic for a single frequency, so such focusing metasurfaces were never intended for broad frequency tuning and were only used as they were the only available devices at the time. That said, it is likely that the metasurface will lase over a broad frequency range as the individual ridges

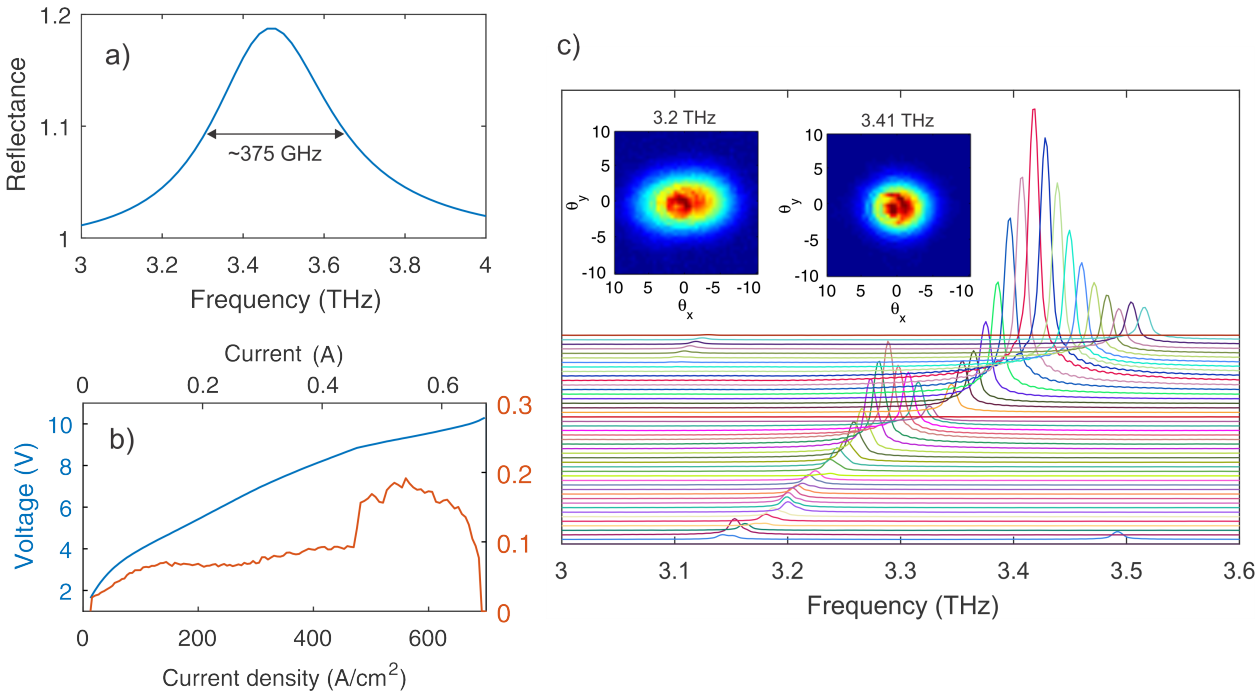

Figure 4.4: a) Simulated reflectance spectrum of a 60 μm metasurface with 40 cm^{-1} of gain applied. (b) Measure I-V and corresponding dI/dV, which clearly indicates the lasing threshold. (c) Spectra collected as the bias on the piezoelectric stacks is increased, and two sample beams collected at different frequencies. The dips in the intensity line-up well with atmospheric absorption lines.

of the metasurface are still very broad, but the beam pattern and threshold characteristics may be less predictable; in order to plot a reflectance curve as a function of frequency, the full metasurface would have to be simulated, not just a single period of a uniform surface.

Indeed, the experiment showed that the focusing metasurface lased over ∼250 GHz, limited by the FSR of the cavity. However, also as expected, a variety of higher-order beam shapes and multimoding were observed (Figure 4.5(b)). It is likely that cavity misalignment associated with the piezo-stacks further complicated the situation. In some cases, the spectra indicates at least three modes are lasing at once. Single-mode lasing could likely be maintained with use of a smaller bias diameter, but the beam shape would still change with frequency in response to a changing phase shape of the metasurface. As with the uniform surface in the previous Section 4.3.1, detailed power and threshold data were not collected,

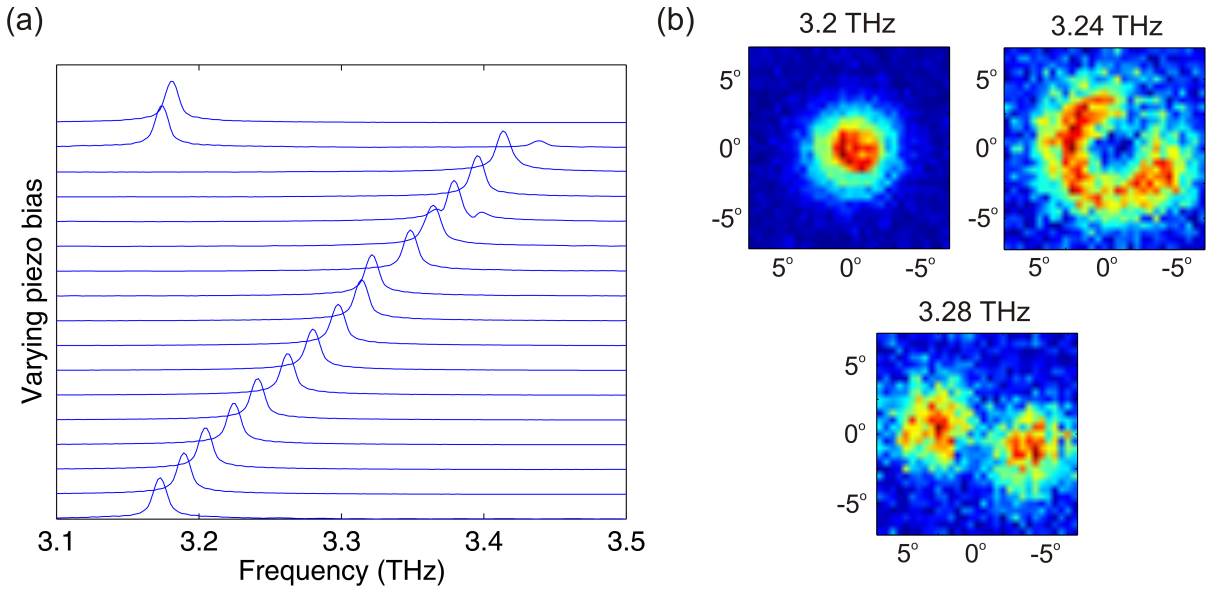

Figure 4.5: (a) Tuning spectra collected from a focusing metasurface (20 mm bias diameter) using the piezoelectric stacks. some of the spectra show two nearby modes lasing simultaneously. (b) Beam patterns collected at different frequencies. Higher order beams are observed.

and the cavity length could not be further changed without opening the dewar, but no such efforts were made due to the poor beam quality.

4.4 Experimental results - broadband single-ridge metasurface

The metasurface tested was 1.5×1.5 mm^2 with a bias diameter of 460 μm, Λ=41.7 μm, and w=11.9 μm (as simulated in Figure 4.2). The active region used was the same as that in Chapters 2 and 3 (wafer VB0739). The specific period of 41.7 μm was not the product of any optimized design, it was originally fabricated for comparison with broadband metasurfaces of the same period (see Section 4.5). The FWHM of the 41.7 μm period metasurface resonance is simulated to be about twice as broad as that of a 70 μm period surface (∼500 GHz, compared to ∼250 GHz), though the peak amplification is also reduced by about half for the 41.7 μm period surface.

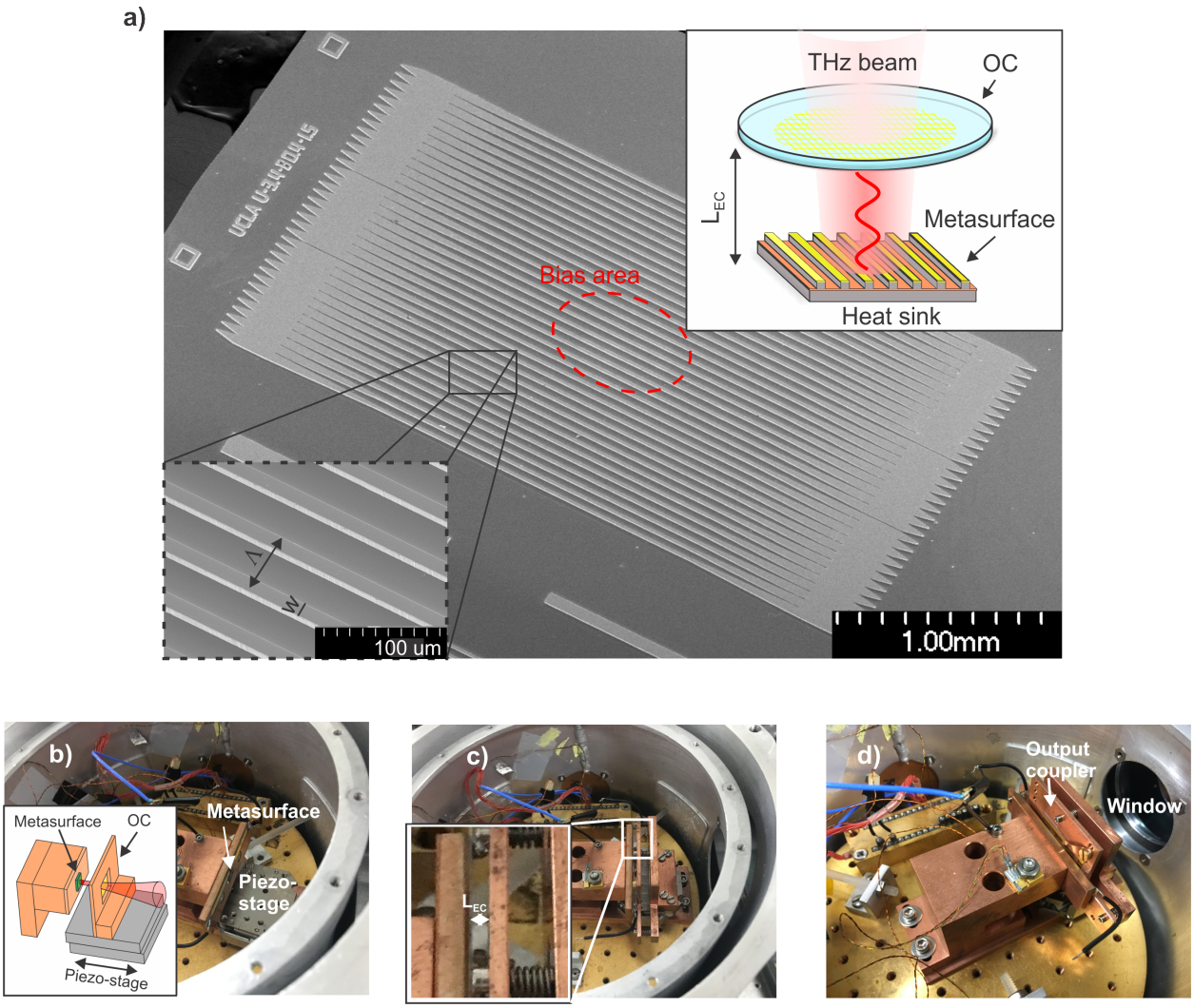

Figure 4.6: (a) SEM of fabricated device. Metasurface is 1.5×1.5 mm^2 with a period of 41.7 μm and a ridge width of 11.9 μm. Current is only injected into a circular central bias area 500 μm in diameter, indicated with a dashed line. The ridges are tapered out to lossy terminations that also serve as wire-bonding areas. (b-d) photographs of the setup from the front, side, and back of piezoelectric setup respectively. The output coupler has been removed in (b) so that the metasurface and piezoelectric stage are visible. The inset in (b) illustrates the setup for clarity, and the inset in (c) offers a close-up on the location of the actual QC-VECSEL cavity.

The tunable QC-VECSEL cavity setup is shown in Figure 4.6. The metasurface is mounted to a fixed copper block, while the output coupler is mounted on a piezoelectric stepping stage. The output coupler is attached to a homemade kinematic mount and is

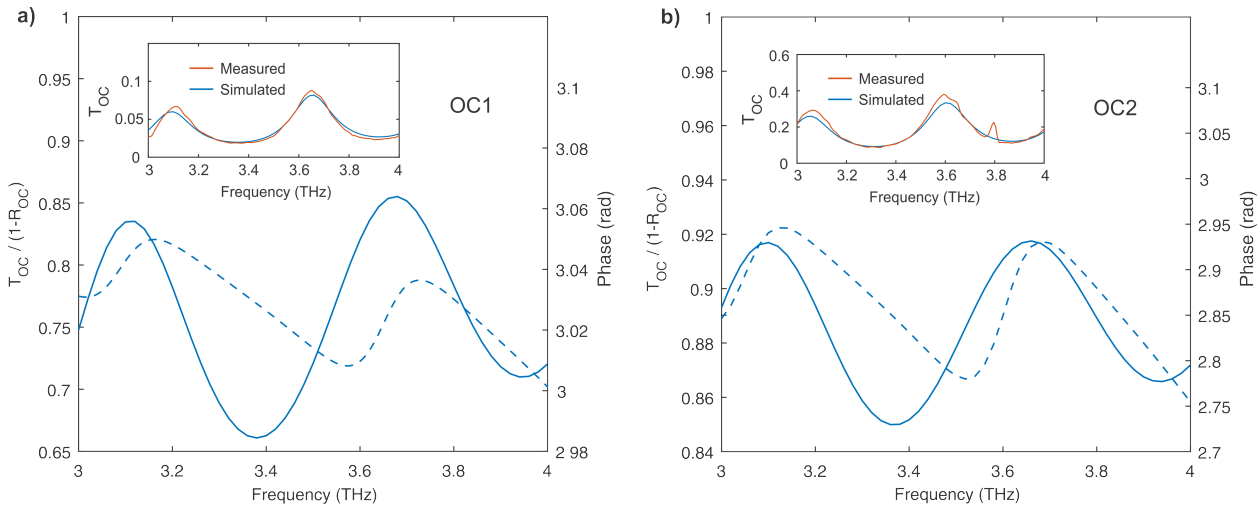

Figure 4.7: (a) High reflectance, and (b) low reflectance output couplers used for tuning experiments. Main plot shows output coupler efficiency and phase, while the simulated and measured reflectances are plotted in the insets. The output coupler in (a) is an inductive mesh designed to have a period of 10 μm and metallic lines 3 μm wide, but is best fit by simulations using a line width of 2.65 μm. The output coupler in (b) is the same as that from Chapter –, Figure —.

aligned to the metasurface using the diffraction patterns of a retroreflected HeNe laser beam. The alignment cannot be adjusted once the cryostat is closed. The cryostat window was 3.3-mm-thick high-resistivity silicon with an anti-reflective (AR) parylene coating deposited on each side and measured to have a ∼90% transmittance between 3-4 THz (see Appendix 8.3). The AR window serves to both maximize power output and minimize feedback into the VECSEL cavity. In Figure 4.6(a), a photograph show the metasurface mounted without an output coupler; the piezoelectic stage (Attocube ANPx311) for holding the output coupler is indicated, and the inset illustrates the setup for clarity. The Attocube stepper is operated in an open loop mode without position readout, so the relative OC position cannot be directly determined. In Figure 4.6(c), a profile of the setup with the output coupler in place is photographed. The output coupler is mounted on a set of three spring-loaded screws that are used to adjust the alignment. Last, Figure 4.6(d) shows the setup photographed from the back with the output coupler in place.

The VECSEL was tested with two different output couplers (see Figure 4.7 for output

coupler properties) in both pulsed and continuous wave modes. Pulsed measurements were performed at 1% duty cycle with a 10 kHz repetition rate. Relative output power was measured using a pyroelectric detector (GentecEO), and absolute power levels were directly measured with a calorimeter (Scientech) that was calibrated against a Thomas Keating absolute terahertz power meter. Reported powers refer to the emitted laser power, having accounted for the measured transmittance of the cryostat window. Far-field beam patterns were measured using a 2-axis scanning pyroelectric detector with a 2 mm diameter aperture rotating at a constant distance ≈15 cm from the device. Spectra were measured using a Fourier-transform infrared-spectrometer (FTIR, Nicolet 8700) and a DTGS pyroelectric detector.

4.4.1 High reflectance output coupler

Results of tuning on the m=4 longitudinal mode using a highly reflective inductive mesh output coupler (OC3, ∼2-8% transmission) are shown in Figure 4.8. Up to 650 GHz of continuous, single-mode tuning is observed centered around 3.47 THz (19% fractional tuning), and a consistent, circular beam pattern is observed throughout the tuning range with a FWHM divergence angle of ∼15°. The threshold and peak current densities (J_{th} and J_{pk} respectively) are plotted in Figure 4.9(b), and the peak power and slope efficiency of the VECSEL in pulsed and continuous wave mode is plotted in Figures 4.9(c-d). The variations in power, slope efficiency, and threshold are primarily a result of the changing OC reflectivity. There is a deviation from the expected behavior between ≈3.55 THz and 3.7 THz where, though the OC transmission is increasing, J_{th} shows little change while J_{pk} is actually increasing. This suggests a sudden increase in gain per injected current at a bias of 440 A/cm^2 (or 9.2 V) possibly due to alignment of a second lasing state, or misalignment of a leakage channel though no such distinct feature is predicted by density matrix modeling of the active region design. In continuous wave mode, the effects of the output coupler are more dominant as a result of the generally reduced material gain, and lasing is nearly extinguished at the peak transmittance of the output coupler. At the edges of the tuning range, the VECSEL

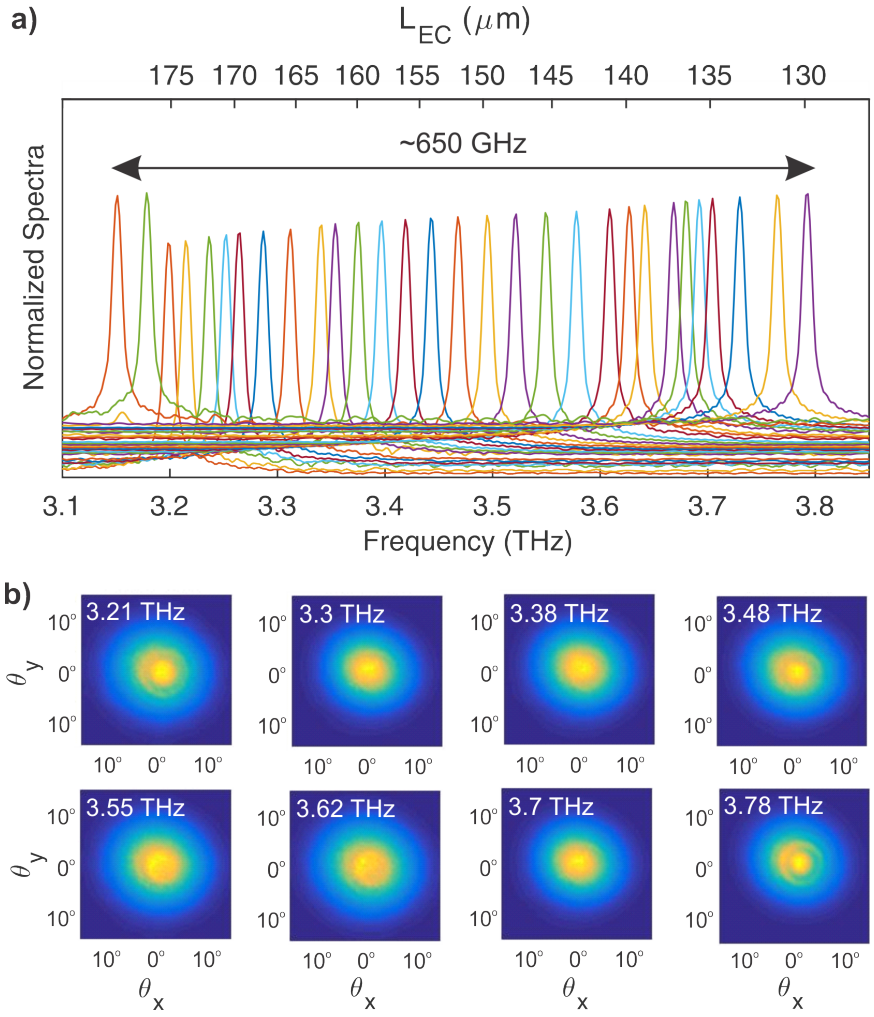

Figure 4.8: Measurement results on longitudinal mode m=4 with 19% fractional tuning at 77 K(a) Single-mode FTIR spectra and (b), beam patterns measured as the piezoelectric stage is stepped with OC3, tuning the VECSEL's external cavity length and lasing frequency. It is noted that the tuning is not linear with cavity length as the reflection phase of the metasurface is frequency dependent.

lasing frequency becomes bias dependent, hopping from the low frequency resonance of the cavity to the high frequency resonance when the bias voltage is increased (Figure 4.9(f)); the two modes are generally not observed to lase simultaneously outside of a narrow transition range. Such behavior is consistent with the Stark shift of intersubband transitions with applied field and/or the simulated contribution of the multiple intersubband transitions that contribute to the gain spectra for this active material. Neither the length of the external

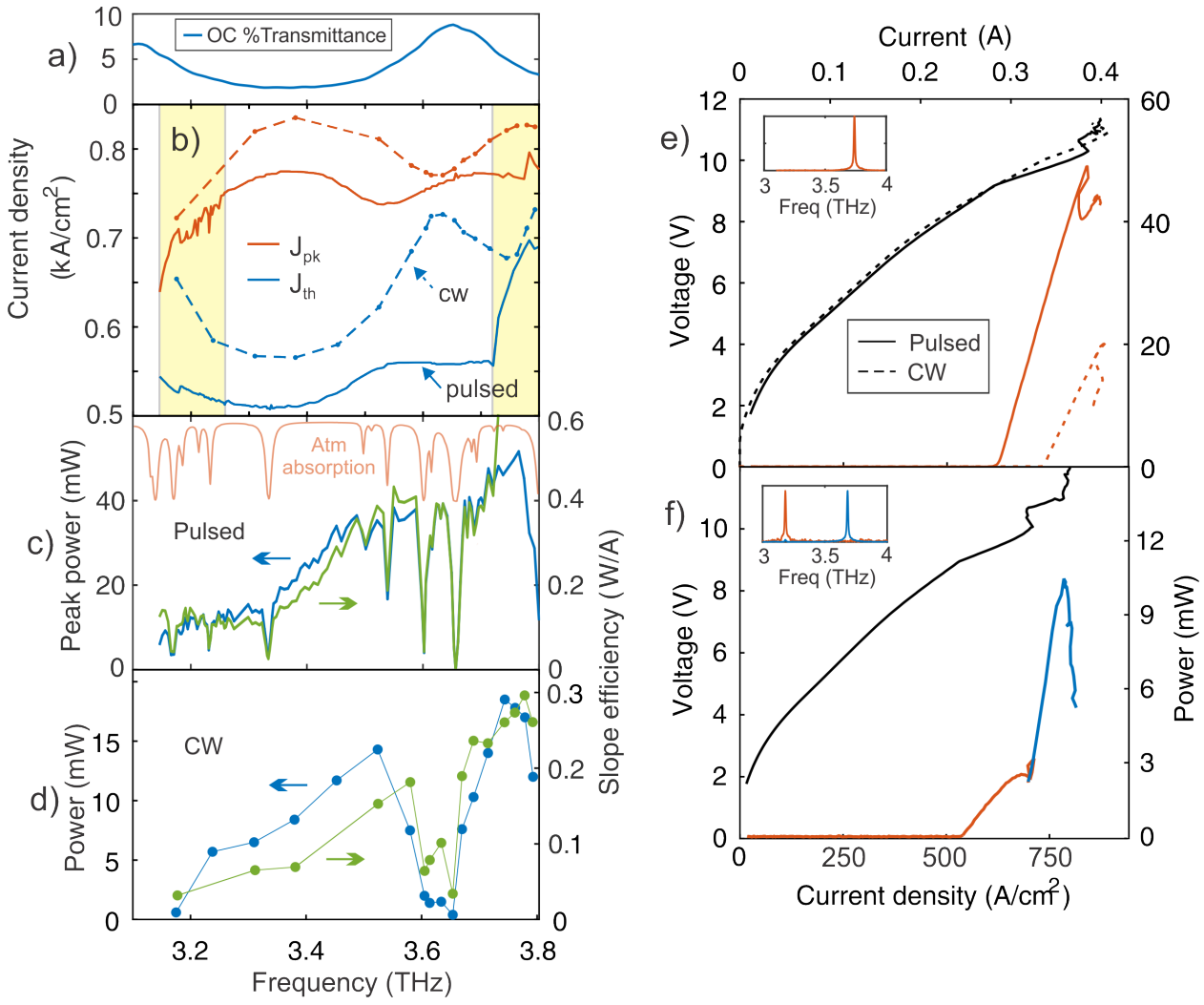

Figure 4.9: (a) Output coupler transmission measured using FTIR. (b) Threshold and peak current density in pulsed-mode as the QC-VECSEL frequency is tuned. (c) Peak-pulsed and (d) continuous wave power and slope efficiency as a function of lasing frequency. Faded curve in (c) indicates atmospheric transmission features within the demonstrated tuning range simulated from the HITRAN database. (e) Pulsed and continuous wave P-I-V curves taken at 3.75 THz, and (f) pulsed L-I-V curve indicating two distinct lasing regions at 3.18 THz and 3.68 THz (separated by the cavity FSR).

cavity, nor the relative position of the output coupler can be measured directly with the equipment available, but this information can be inferred from the observed FSR at the edges of the tuning range. The observed FSR at the longest and shortest cavity lengths was 500 GHz (3.18 – 3.68 THz) and 610 GHz (3.79 – 3.18 THz) respectively, and using equation

(1), the inferred change in cavity length is 177 - 130 μm. The resonant frequencies and FSR predicted by equation 4.1 match very well (<1% difference) with the experimentally observed values, indicating that the fabricated device behaves very close to the simulated design. A collection of pulsed and continuous wave *L-I-V*'s at a variety of frequencies are plotted in Appendix 8.1.

To push for maximum tuning, the length of the cavity was further reduced to operate on the m=2 mode. 25.1% fractional tuning was achieved from 3.11 – 3.99 THz as the cavity length was varied from 86 – 48 μm (Figure 4.10). However for such short cavities, higher order beams are regularly observed, and multimoding begins to occur in some instances, which can be explained as follows - when using a metasurface with a small bias diameter, a small THz spot size ($\psi(x,y)$ as defined in Chapter 2) helps to reduce threshold gain (larger confinement factor Γ), but also increases diffraction loss, which competes to increase threshold gain. This trade-off is, in fact, typically to our advantage as it allows for discrimination of higher-order beams by only biasing the central portion of the metasurface. At extremely short cavity lengths, however, diffraction loss is very small, even for spot sizes much smaller than the bias diameter. In this case, the confinement factor (and thus threshold gain) for the fundamental and higher-order beams becomes very comparable, making it more likely for higher order modes to lase. This demonstrated via FEM simulations in Figure –, where the threshold gain for the first three eigenmodes of the cavity (TEM_{00}, TEM_{01}, and TEM_{02}) as a function of cavity length. Below 100 μm, the threshold gain of the three modes rapidly gets very close. The rather divergent output beam measured compared to previous VECSELs also supports the assumption of a small cavity mode. Stronger suppression of higher-order modes should be possible by moving to even smaller bias diameters, and this is confirmed by simulation in Figure 4.12, but the threshold gain of the fundamental mode is also increases notably as the bias diameter shrinks, which will reduce the potential tuning range.

For comparison, the QC-VECSEL threshold gain calculated using the Fox and Li model is plotted as a function of cavity length in Figure 4.11. Simulation of the 2-D VECSEL cavity are performed using MATLAB. Using a simple step function to represent the boundary

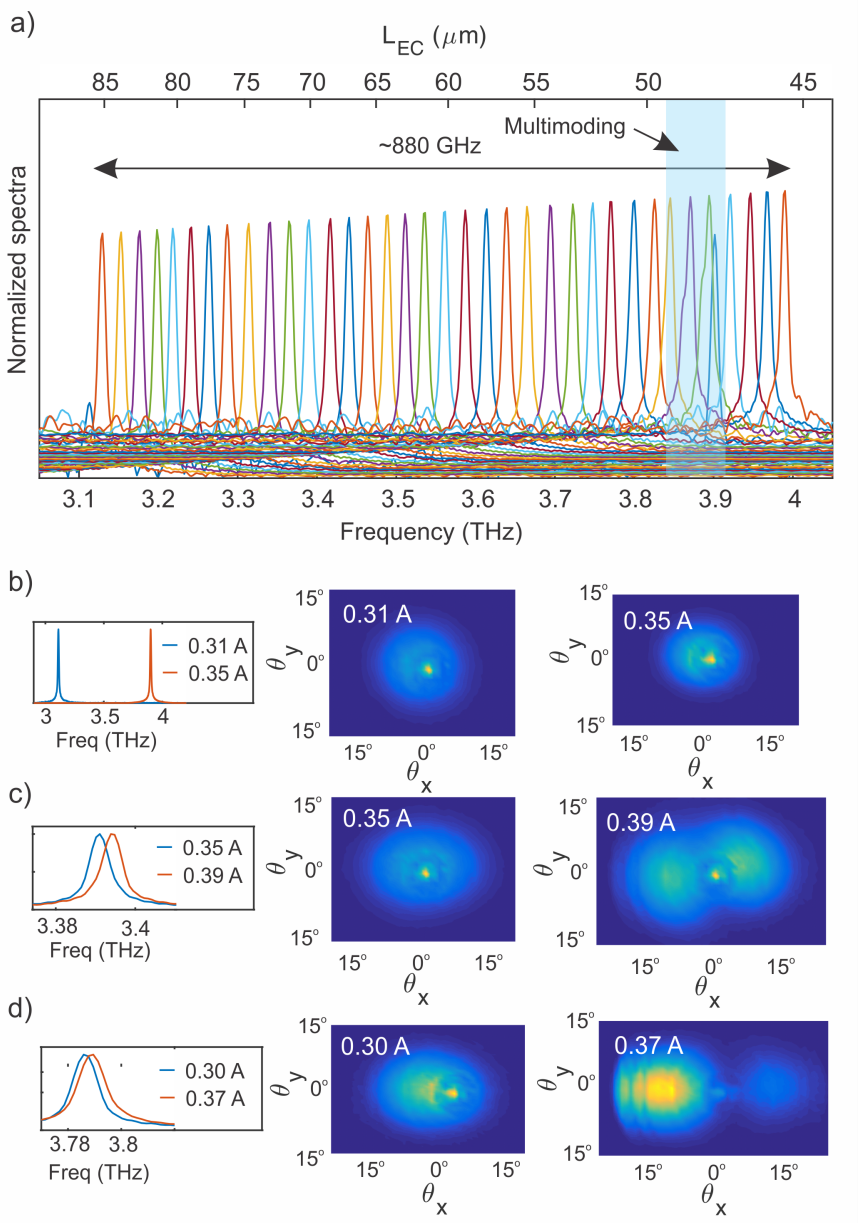

Figure 4.10: Measurement results on longitudinal mode m=2 with 25% fractional tuning at 77 K. (a) FTIR spectra collected as the external cavity length is tuned. The region in which multimode lasing is observed is indicated by the blue shaded area. (b-d) Selected spectra and beams taken between the longest cavity (b) and the shortest cavity (d). The beam quality is observed to degrade at shorter cavity lengths and at high bias.

between the biased and unbiased portion of the metasurface, we find that the Fox and Li results better match with FEM simulations when the width of the step function is reduced

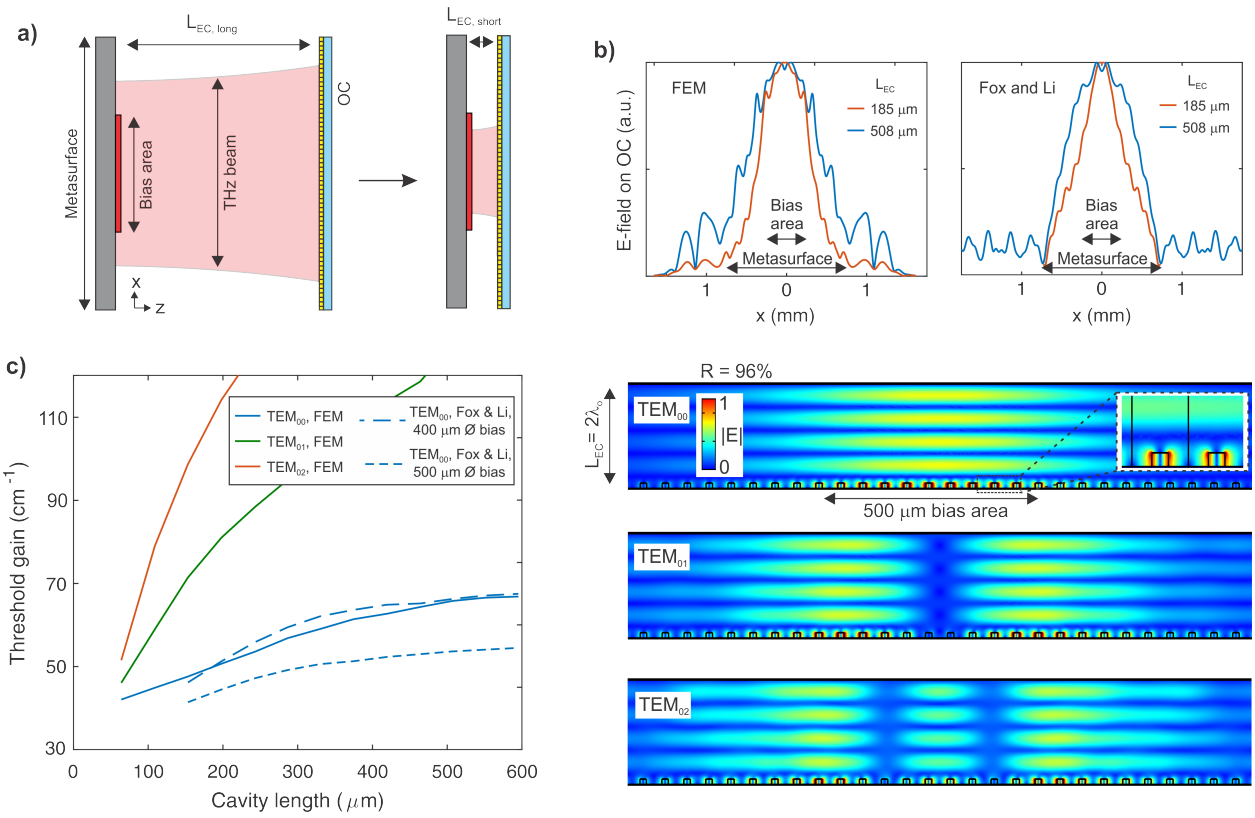

Figure 4.11: Numerical modeling of THz QC-VECSEL cavity. (a) Effect of the THz beam shrinking as the external cavity length is reduced, leading to stronger confinement of the beam to the biased portion of the metasurface. (b) Normalized electric field magnitude of the output beam at the surface of the output coupler extracted from FEM eigenmode simulations, and numerical Fox and Li simulations for comparison. Narrowing of the emitted beam is observed as the cavity length is reduced (leading to a broader beam in the far-field). (c) QC-VECSEL Threshold gain as a function of external cavity length for the first three modes of the 2-D cavity. Plots of the electric field in the full 2-D VECSEL cavity for the first three modes. Inset shows close-up of fields at the metasurface.

to 400 μm rather than 500 μm, indicating that a more sophisticated spatial gain distribution should be used. Additionally, diffraction losses from the edge of the metasurface observed in the FEM simulations are not well captured by the Fox and Li model, as indicated by comparison of the field distributions in Figure 4.11(b). While Fox and Li modeling can provide some rough estimates, full FEM simulations should be used if possible.

Last, for completeness, the effects of cavity misalignment up to 1° on a 156 μm long

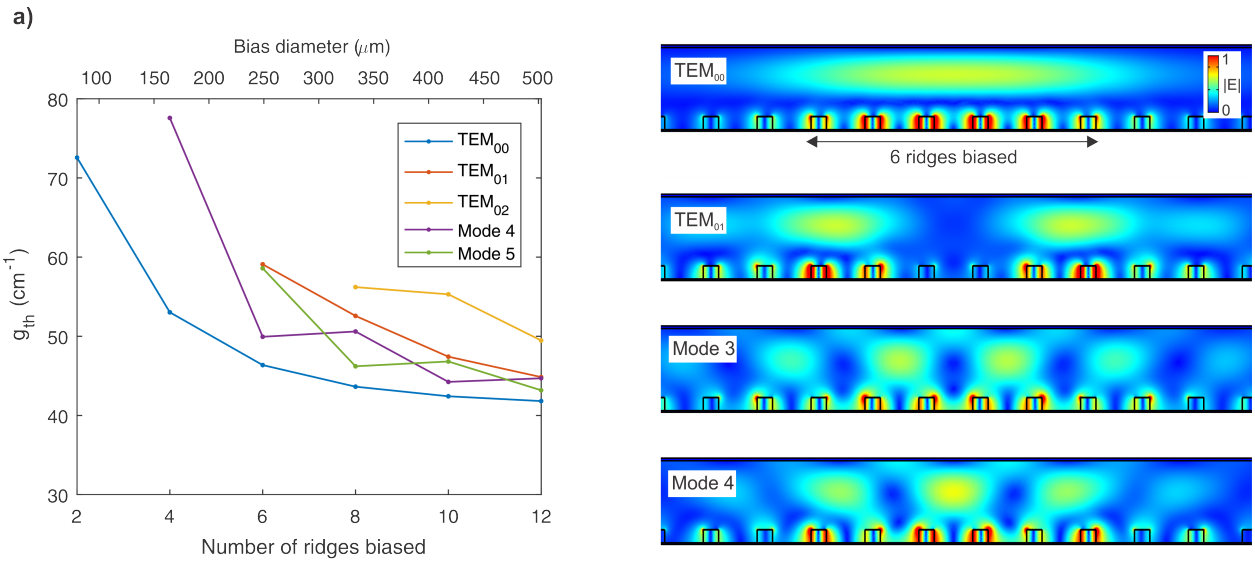

Figure 4.12: Threshold gain and corresponding field plots of various cavity modes as a function of the number of metasurface ridges with gain (which is equivalent to the bias area diameter). The simulated cavity length is L_{EC}=63.5 μm.

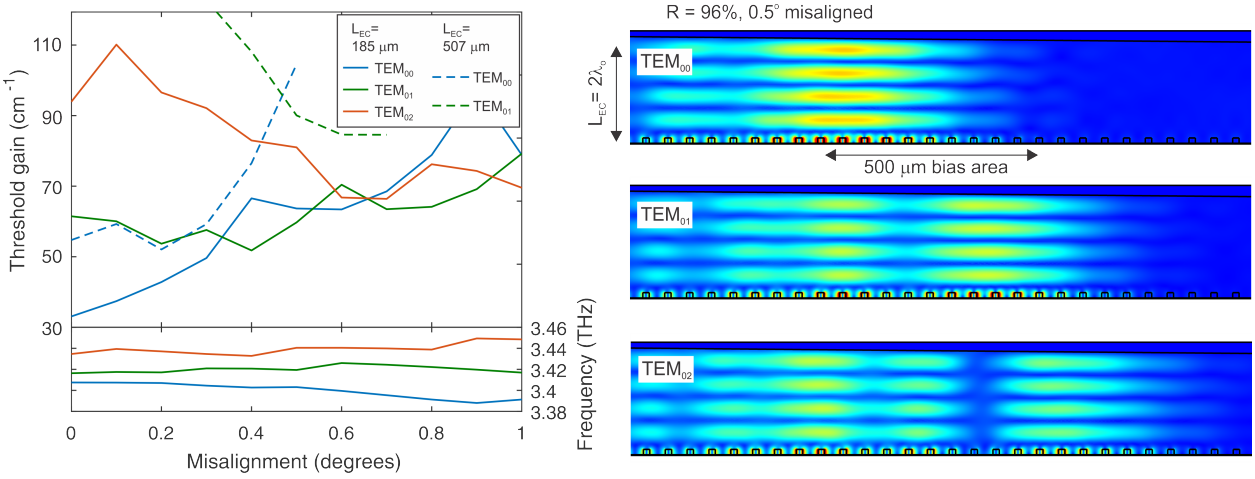

Figure 4.13: Effect of cavity misalignment on threshold gain. Threshold gain and corresponding field plots of VECSEL cavity as a function of output coupler misalignment. Selectivity between TEM modes is reduced with even small degrees of misalignment.

cavity are simulated with data presented in Figure 4.13. Even at such short cavity lengths and for such small degrees of misalignment, the treshold of the fundamental TEM_{00} mode

is observed to increase rapidly; by 0.3° misalignment, the TEM_{00} and TEM_{01} have similar thresholds. Even more significantly, the modal distribution for the TEM_{00} mode moves off-center from the bias area, which will result in a spatial hole burning effect at higher biases, further encouraging lasing of the TEM_{01} mode even if its gain threshold is nominally higher. The observed multimoding at short cavity lengths is likely a combination of a small degree of misalignment and reduced diffraction loss. For longer cavity lengths (L_{EC} ≈500 μm), the situation is more favorable for single mode operation as the threshold of higher order modes increases much quicker than the TEM_{00} mode, but the effects of cavity misalignment on threshold for all modes is more severe.

Below L_{EC}=48 μm, the threshold current increases quickly until lasing ceases. This could be caused by contact between the OC stage and the metasurface mount resulting in sudden cavity misalignment; at such short cavity lengths, a cavity misalignment of only 0.1 ° would cause contact between the outer edges of the mount (which are 3 cm wide). This explanation would also be consistent with the significantly degraded beam pattern of Figure 4.10(d).

4.4.2 Low reflectance output coupler

Tuning results using a lower reflectance ouptut coupler (OC1, same as from Figure 3.2(a), inductive mesh, 15 μm pitch, 2.5 μm wire width, ∼8-40% transmission) are shown in Figure 4.14(c). With OC1, only 200 GHz of tuning is achieved as a result of the OC transmission increasing the threshold gain beyond the gain capabilities of the metasurface. Specifically, the metasurface's limits in pulsed mode were 10.5% OC transmission at 3.23 THz, and 13.5% transmission at 3.44 THz, suggesting that there is more metasurface gain at 3.44 THz. This results makes sense as the center frequency of the metasurface is designed to be 3.5 THz, though variation in gain coefficient of the QC-material could also be a factor. Because of the higher OC transmission, the measured slope efficiencies were generally higher with OC1 than with OC3, but peak-power levels were generally lower with OC2 due to the trade-off between increased outcoupling loss and reduced dynamic range. The device was not tested in continuous wave mode with this output coupler as the author did not want to

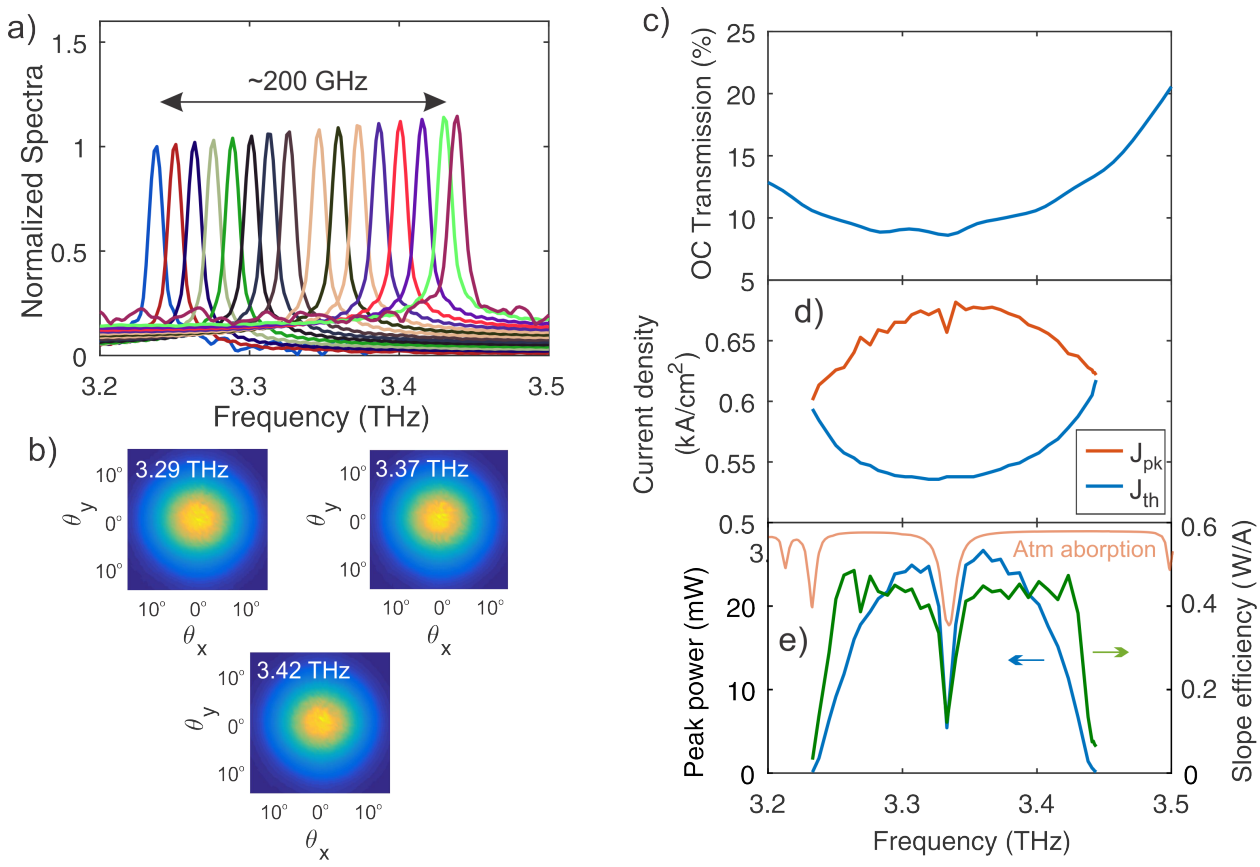

Figure 4.14: Data collected over 6.6% fractional tuning around 3.34 THz at 77 K using OC2. (a) FTIR laser spectra and (b) beams collected as the external cavity length is tuned. (c) OC2 transmission measured using FTIR. (d-e) Threshold current density, peak current density, peak-pulse power, and slope efficiency as a function of lasing frequency. Faded curve in (e) indicates atmospheric transmission features within the demonstrated tuning range.

risk damaging the device at the time, but based on the continuous wave results with OC3, it seems unlikely that the any appreciable continuous wave lasing would be observed with the higher transmission of OC1. In Figures 4.14(d) and (e), threshold and power are plotted as a function of cavity length. Data was taken at a constant frequency (3.33 THz), while the cavity length was adjusted by increments of an FSR. The span of the FSR was never observed, so the exact cavity length is unknown, but it must be < 700 μm to be larger than 200 GHz.

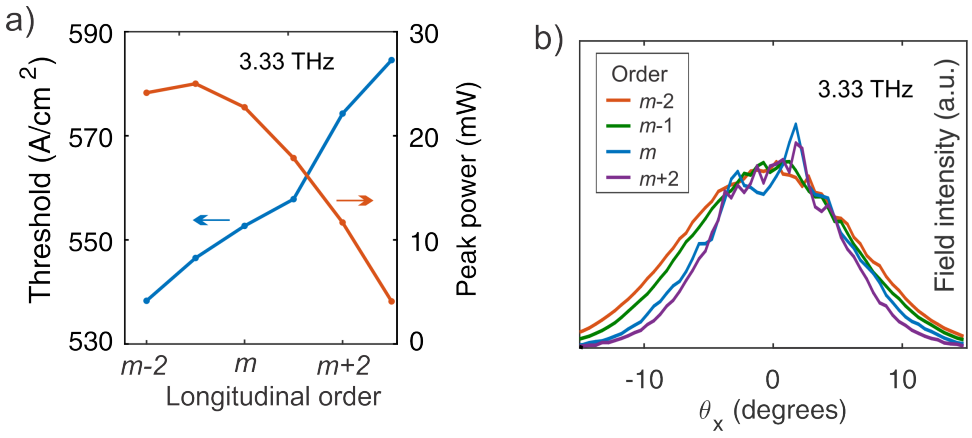

Figure 4.15: Effects of cavity length on VECSEL. (a) Threshold current and peak power as a function of cavity length. At longer cavity lengths, diffraction loss becomes too large and lasing is not observed. (b) 1-D beam cuts as a function of cavity length. Narrowing of the beam to reduce diffraction loss at longer cavity lengths is observed

4.4.3 Extracting QC-material parameters

Because the threshold conditions of the QC-VECSEL can tuned relatively easily, it is a good platform for investigating the properties of the QC-gain material. Consider, for example, a general expression for the threshold gain of a QCL used in Chapter 2:

$$J_{th} = \frac{g_{th} e L_p}{\sigma \tau_{eff}} + J_{leak} \tag{4.2}$$

where J_{th} and J_{leak} are the threshold and leakage current densities respectively. L_p is the length of the module of the QC active region design, g_{th} is the intersubband threshold gain coefficient, σ is the stimulated emission cross section, and τ_{eff} is the effective lifetime of the population inversion(which includes effects of intersubband lifetimes, tunneling injection efficiency, thermal backfilling, etc.). The only diretly measurable quantity in equation 4.2 is J_{th}, but by using the g_{th} values obtained from the full cavity model simulation described above, we can estimate the gain per injected current ($\sigma\tau_{eff}/eL_p$ [cm/A]) and leakage current. In Figure 4.16, the measured threshold current densities and FEM simulated threshold gain values are plotted for a metal-metal waveguide, the TM_{03} metasurface of Chapter 3, and the

broadband metasurface data presented in this chapter. All of the VECSELs were made with wafer VB0739 and operating at the same frequency (3.33 THz) as the material properties are spectrally dependent. Because the cavity length could not be determined for the data in section 4.4.2, only the relative length, a series of plots are shown assuming different cavity lengths and the resulting fit. Based on the figures, the estimated gain per injected current is around 2.5-3 A/cm, and the estimated leakage current is ∼370 A/cm^2. This is considerably smaller than the value estimated in Ref. [18] presumably because the output coupler reflectance was significantly underestimated in that reference.

Another example is to use equation 2.18, written here in terms of slope efficiency, to estimate the internal quantum efficiency:

$$\frac{dP}{dI} = N_p \frac{h\nu}{e} \eta_i \eta_{opt} \tag{4.3}$$

The slope efficiency $\frac{dP}{dI}$ is measured experimentally; N_p, h, ν, and e are known quantities, so we can calculate η_i. In Figure 4.17, η_i is plotted as a function of frequency using the measurements in Section 4.4.1. Around 3.4-3.5 Thz, the calculated value of η_i approaches the maximum theoretical value of 1. This would be a surprisingly high efficiency, and we have not acounted for the affects of the optical fill factor, which will further increase the η_i (as discussed in Chapter 2), suggesting the value is somehow being overestimated. The error may be in the estimate of η_{opt}, where R_1 may be too small, or R_2 may be too large.

4.5 Broadband double-ridge designs

Though the typical, single-ridge metasurface design is already inherently broad, as discussed at length to this point, there is still plenty of room for designs that may be even more broad. For example, one of the most obvious ideas, given that the resonant frequency of the metasurface is determined by the ridge width, is to simply have multiple ridges per-period of the metasurface with different widths. One such design, using two ridges per-period, is presented in Figure 4.18. The metasurface has a period of 41.7 μm, and the two ridges

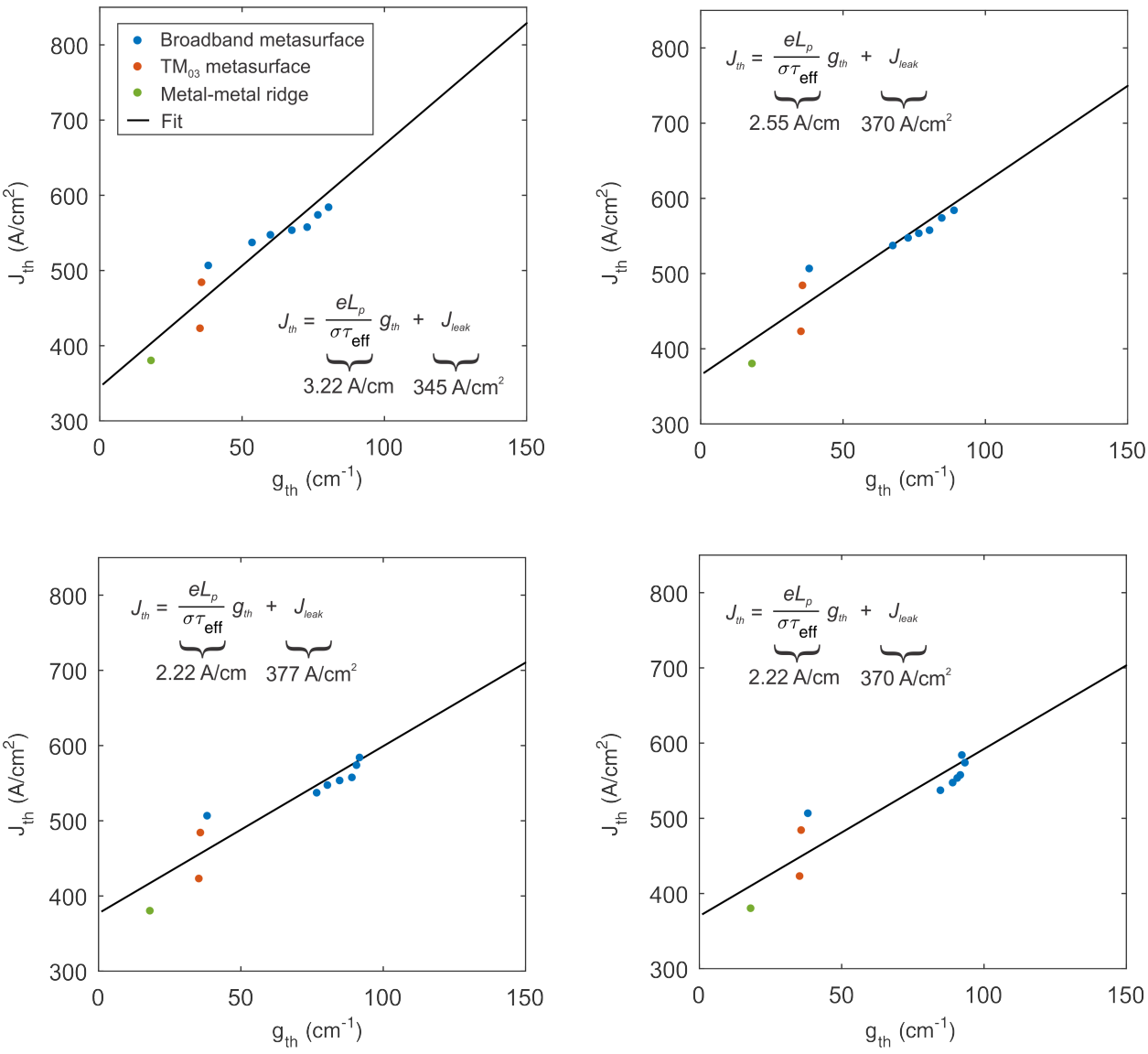

Figure 4.16: Fitting the measured VECSEL threshold current densities and simulated threshold gain values to the model for gain in equation 2.16. The cavity length of the data collected in Figure 4.15 is not know for sure because the FSR was not observed, but it must be less than ∼700 μm for this to be the case, so a set of fits are shown assuming the data in Figure 4.15 is centered around (a) 340 μm, (b) 430μm, (c) 520 μm, and (d) 610 μm.

are 9.45 μm and 13.65 μm spaced apart by 9.3 μm. The design is intended to provide a relatively flat gain spectrum centered around 3.4 THz (note - this is the reason the uniform metasurface in Section 4.4 has a period of 41.7 μm, it was intended as a comparison to this double-ridge design). While one could make a single ridge metasurface just as broad by

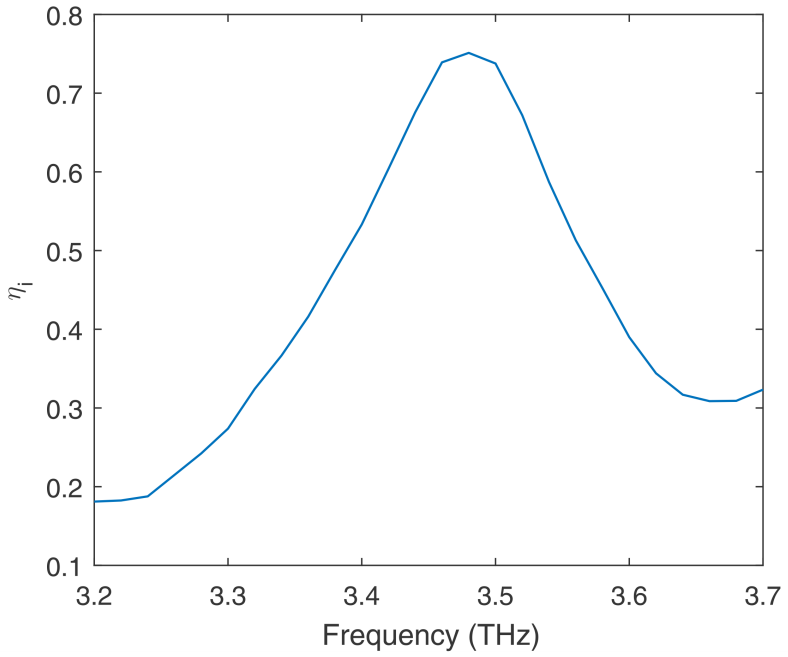

Figure 4.17: (a) Calculated internal quantum efficiency η_i using equation 4.3.

reducing the period of the metasurface, the advantages of the multi-ridge metasurface are that it broadens the gain without sacrificing on amplification factor, and it offers a more flat amplification factor over the bandwidth. It should be noted that the gain spectrum is not simply a superposition of the responses one would expect from uniform metasurfaces with the two different ridge widths, but the close proximity of the ridges allows for significant coupling leading to a more complex response. The design presented here is admittedly based on optimization in simulation, no analytical model has been applied.

While the author's initial intent with designing such a broadband, spectrally flat metasurface was for the purpose of achieving maximum single-mode tuning with minimal fluctuations in output power and threshold, the impact of the metasurface phase on the frequency tunability was not appreciated at the time. In hindsight, upon proper consideration of the metasurface phase, we find that such a double-ridge design has a more dense set of external cavity modes and has a smaller expected single-mode tuning range than the uniform metasurface with the same period (Figure 4.2). This is illustrated in Figure 4.18(c), where

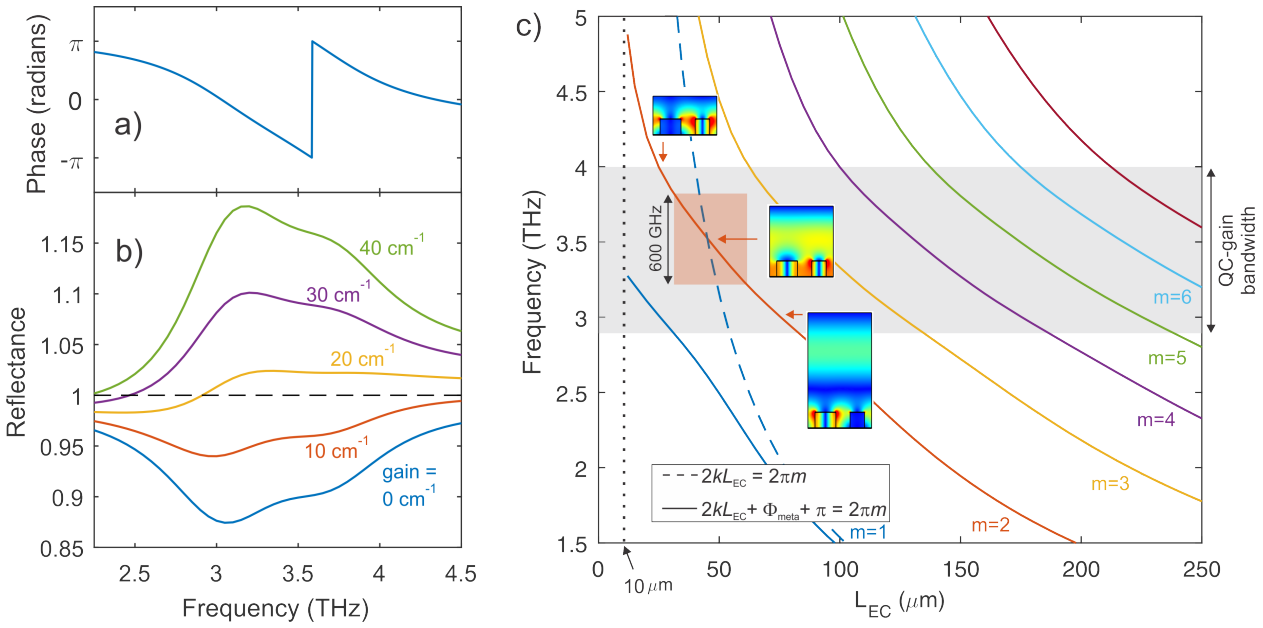

Figure 4.18: (a) Simulated phase and (b) reflectance of a double-ridge broadband metasurface (Λ= 41.7 μm, ridge widths are 9.45 μm and 13.65 μm, and uniform spacing of 9.3 μm). The total phase accumulation across the metasurface is 4π (though the high frequency tail is cutoff). (c) Eigenfrequencies vs. cavity length for both a bare Fabry-Perot cavity neglecting reflection phase (dashed line), and complete VECSEL cavity including metasurface phase (solid lines, FEM simulated). The colored boxes indicates the maximum single-mode tuning that could be expected given the observed gain bandwidth of the underlying QC-material. Insets show the E-field magnitude at the extremes and center of the m=2 mode. The field is concentrated in the narrower ridge at high frequencies, and the wider ridge at low frequencies.

the FEM simulated eigensolutions of an infinite VECSEL are plotted as a function of cavity length. It is found that the maximum expected single-mode tuning that can be achieved is ~600 GHz from a cavity length ~30-60 μm. To clarify, the double-ridge metasurface is more likely to lase over a broader range of frequencies than a single ridge metasurface of the same period as the amplification factor is indeed larger over a broader range; the problem is that the double-ridge metasurface VECSEL is more likely to be multimoded. This is what is observed experimentally.

The experiments were performed with the piezoelectric stack actuators as it was before the stepping stage was purchased. Two attempts were made at achieving broad tuning, both with the high reflectance output coupler in Figure 4.3. In the first attempt, Figure

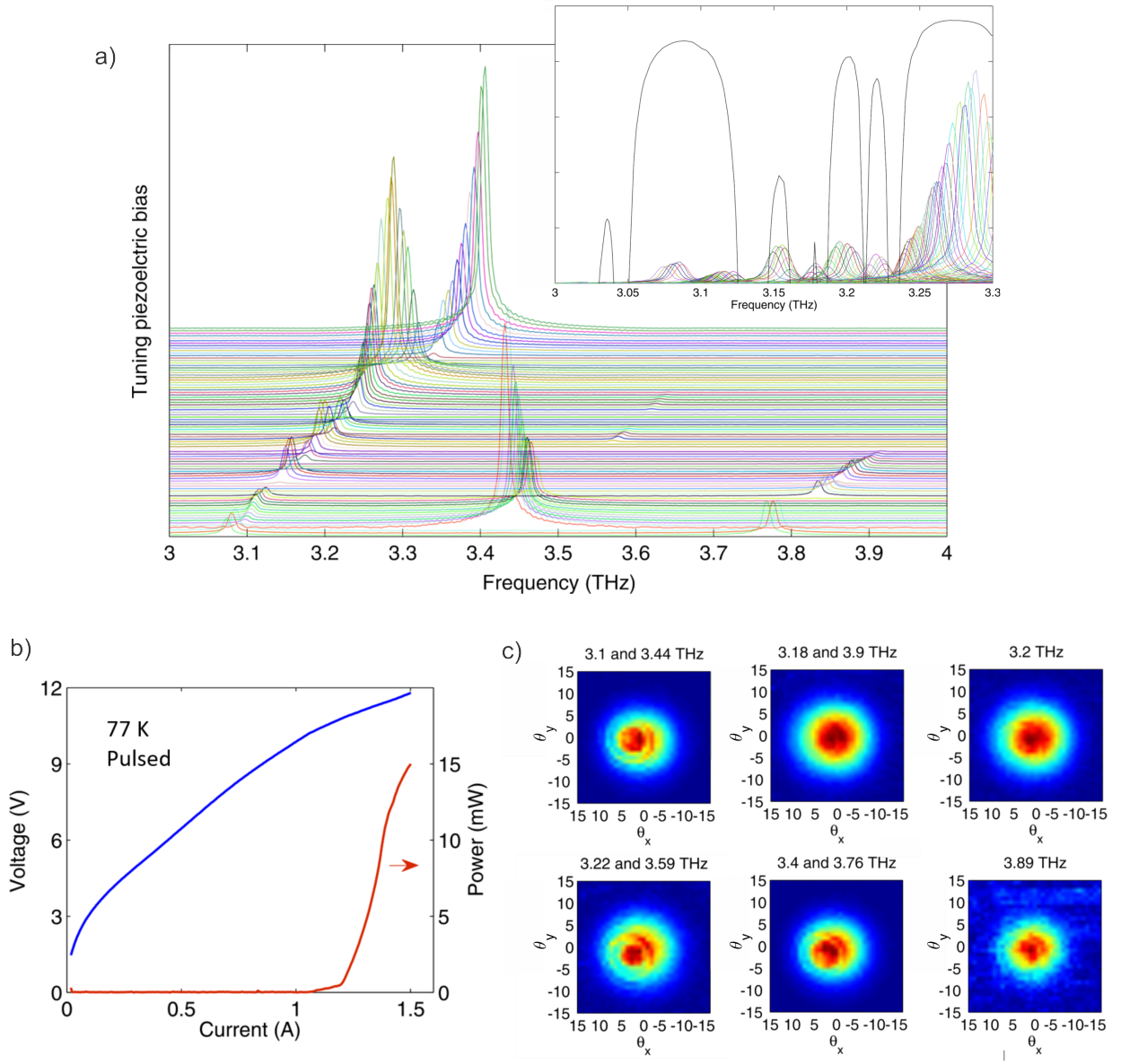

Figure 4.19: (a) Spectrum collected while tuning the cavity length of a double-ridge metasurface (2×2 mm^2 with a 1 mm bias diameter) using piezoelectric stacks. Cavity length is estimated to be centered around ∼300 μm. Inset shows alignment of spectral dips with atmospheric absorption features [23]. Total cavity length change is one FSR, ∼45 μm. (b) Sample L-I-V collected at 3.4 THz. (c) Collection of beams measured throughout the tuning range.

4.19(a), the spectrum measured by FTIR are plotted as the cavity length is tuned. Three distinct modes that are clearly tracked, but not all three modes lase at all times through

the tuning range. The mode closest to the center of the metasurface resonance appears to consume most of the pump power. Based on the spacing between the modes, the cavity length is estimated to vary from ∼270-315 μm. The beam patterns plotted Figure 4.19(c) are improved compared to other attempts at tuning with piezo-stacks, but the intensity profile is asymmetric in many cases, suggestive of cavity misalignment and/or multiple modes lasing below the resolution of the FTIR. The inset of Figure 4.19(a) shows alignment of the observed drops in output power with absorption lines in the atmosphere.

Despite the imperfect beam patterns, the observed bandwidth of the metasurface prompted further testing. Data collected after manually shortening the cavity even further is presented in Figure 4.20. Remarkably, continuous lasing was observed between 2.85-3.9 THz, but as expected, the device was multimoded the majority of the time between two modes separated by the cavity FSR. The cavity length is estimated to vary from ∼70-115 μm. The metasurface's functionality is verified both by the fact that, when comparing to the uniform surface above (Section 4.4), the observed FSR are smaller and the amplification is more broadband. However, the observed beam patterns are very poor, which is likely due to cavity misalignment and the large bias diameter on the metasurface compared to the cavity length. Further, as mentioned above, even a small fraction of a degree of misalignment can cause physical contact between the output coupler and metasurface mounts at the outer edges. Further testing was not performed as the metasurface was decidedly too broadband to allow for single-mode lasing, and it was decided that a peizoelectric stepping stage was need to improve alignment and maintain better beam quality at short cavity lengths. Reducing the bias diameter may help discriminate against the modes closer to the tail edges of the metasurface response, but this would reduce the total potential tuning range, making it unlikely that such an approach would ultimately offer more tuning that was achieved with the uniform surface in Section 4.4.

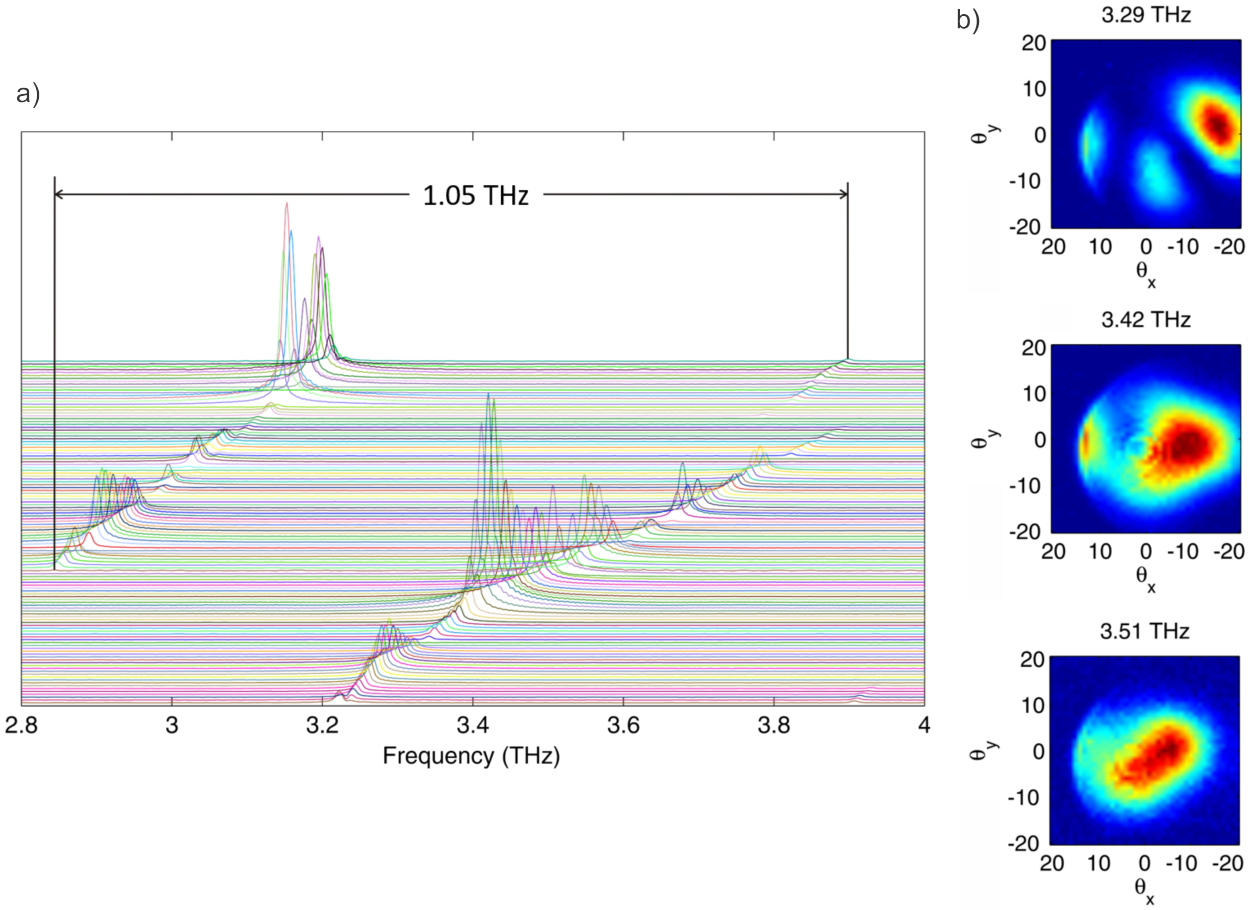

Figure 4.20: Spectrum collected while tuning on the m=2 and m=3 modes of a double-ridge metasurface VECSEL (2×2 mm^2 with a 1 mm bias diameter) using piezoelectric stacks. Cavity length is estimated to be centered around ∼90 μm. Inset shows alignment of specral dips with atmospheric absorption features [23]. Total cavity length change is one FSR, ∼45 μm. (b) Collection of beams measured throughout the tuning range; they are clearly non-ideal.

4.6 Towards THz QC-VECSEL frequency combs

A subject that has recently garnered much attention from the QCL and spectroscopy communities is frequency combs. Frequency combs are lasers that generate a set of evenly spaced modes in the spectral domain given by: f_n=f_{CEO}+nf_{rep}, where n is an integer, f_{rep} is the free-spectral range of the laser resonator, and f_{CEO} is the carrier offset frequency (CEO) describing the offset of the modes from zero in the spectral domain. The terminology comes

from the fact that the field of frequency combs grew out of the mode locked laser community - the Fourier transform of a stable pulse train emitted by a mode locked laser is a 'comb' of evenly spaced modes [129]. While mode locked lasers were primarily of interest for their high intensity at first, interest in their spectral properties grew in the nineties when the spectral coverage of ultrafast pulses grew to octave scales and researchers realized the potential for self-referencing two teeth of a comb to a stable microwave reference. The technique is often referred to as an f-$2f$ measurement; the lower frequency is given by $f_n{=}nf_{rep}{+}f_{CEO}$, the upper frequency by $f_{2n}{=}2nf_{rep}{+}f_{CEO}$, so if the two frequencies are mixed, the difference can be used to measure the carrier offset: $2f_n$-$f_{2n}{=}f_{CEO}$. With the ability to measure both the repetition rate and the carrier offset to the accuracy of modern day microwave references, the exact frequencies of the comb teeth can be measured with an unprecedented level of precision in a relatively simple manner, making way for a new time keeping and frequency metrololgy standards orders of magnitude more precise than the present standards. The potential scientific and engineering applications of this have led to Nobel prizes awarded in 2005 and 2012 to contributors to the field [130, 131]. Another interesting application is dual-comb spectroscopy, where two frequency combs with slightly different properties (different repetition rate or carrier offset) are mixed to produce a comb of beat notes in the microwave regime [132–134]. If a sample is inserted into the beam path of one of the combs, the broadband spectral characteristics can be determined in a single shot with very high accuracy in the microwave regime.

Quantum-cascade lasers are an interesting candidate for frequency comb development as they span a rich spectroscopic domain, and they are the only semiconductor lasers capable of octave spanning gain bandwidth [122], making them the only candidate for a chip scale self-referenced comb. Unfortunately, QCLs have been notoriously difficult to mode-lock as the intersubband dynamics result in an extremely fast gain recovery time, which prevents stable oscillation of a single pulse (other pulse trains try to form in between) and acts as a fast saturable gain that broadens pulses as they propagate rather than sharpening them. Active mode-locking has been demonstrated with THz QCLs [135, 136] and cryogenically

cooled mid-IR QCLs (to increase lifetimes) [137] by modulating the bias current to generate sidebands, but strong modulation is required and pulse widths are unimpressive (limited number of modes in the frequency domain). In 2012, however, it was demonstrated that mid-IR QCLs can form combs by the mechanism of four-wave mixing [138], and this was further demonstrated with THz QCLs in 2014 [139]. In four-wave mixing, the Kerr nonlinearity of the QCL can naturally mix two frequencies to produce a third that is spaced by the same amount as the first two: f_3=2f_2-f_1, and any of those three frequencies can mix to produce more, and so on in a chain until a large comb of modes is established. This method of generation has been well established with so-called Kerr combs based on microdisk resonators pumped by an external laser source and does not result in a pulse train [140]. Four-wave mixed combs produce a continuous arbitrary output representative of a comb of modes with a fixed, but random phase relationship (unlike a pulse train where all modes have the same phase).

The detailed dynamics of QCLs with fast gain recovery times has been, and continuous to be the topic of much discussion [141–143]. The exact means by which a QCL decides to operate in a comb regime is not well understood, but the general consensus seems to be that a frequency modulated output should most efficiently use a fast recovering gain material both spatially and spectrally by having a flat, uniform field intensity and a broad spectrum [144–146]. Such a mode would therefore have the lowest threshold. Presumably, the reason comb behavior is not normally observed is because the dispersion of the gain material and/or the waveguide of the QCL prevents efficient four-wave mixing. Therefore, the name of the game has primarily been dispersion compensation [147–149].

Given this current understanding, there are two important points to consider for realizing a QC-VECESL frequency comb. First, in a typical ridge based metasurface VECSEL, the same portion of gain in the QC-ridges of the metasurface are stimulated by all modes of the external cavity at all frequencies. This is because only TM_{01} resonance can couple to the surface direction. Effectively, spatial hole burning has no effect on the VECSEL's laser dynamics, while it has been one of the main discussion points in the formation of combs in

QCL ridges, and has been one of the main discussion points historically in the dynamics of multimode behavior. However, it is not clear to the author how this lack of hole burning in the VECSEL will effect the solution to the current models; it may just result in a more structured distribution of mode intensities, rather than an apparently random one, or it may encourage single mode behavior.

The second point is with regards to dispersion. In ridge waveguide devices, the QC-gain material is believed to be the primary source of dispersion and results in accumulated phase mismatch along the length of the ridge. Group velocity dispersion (GVD) is reported in fs^2mm^{-1}, and total dispersion is calculated based on the length of the ridge. In a metasurface VECSEL, on the other hand, very little of the energy circulating in the VECSEL cavity is confined to the QC-ridges, and instead most of it is in the external cavity. If tracking the roundtrip of a photon in the VECSEL, this is saying that the photon spends most of its time traveling through the vacuum of the external cavity, where there is no dispersion, and only spends a very brief time resonating in the metasurface, effectively traveling through a very short distance of QC-material, resulting in a negligable GVD (assuming it is a broadband metasurface). Instead, dispersion in the VECSEL should be largely associated with the TM_{01} waveguide resonance, with minimal contribution from the material resonances. The total group delay (GDD) associated with the metasurface is given by the $d^2\phi_{meta}/d^2\omega$, which directly gives the total delay upon a single reflection in fs^2. The total roudtrip GDD of the VECSEL is the sum of the GDD associated with the metasurface, and that associated with the output coupler.

In Figure 4.21(a), the simulated GDD of three different metasurfaces is plotted: a 70 μm single ridge metasurface, a 41.7 μm single ridge metasurface, and the 41.7 μm double-ridge design. As expected, the more broadband designs feature a more slowly varying phase term that leads to a much smaller GDD than the higher-Q 70 μm metasurface. In Figure 4.21(b), the simulated GDD is plotted for the two output couplers in Figure 4.7. Not surprisingly, the high reflectance output coupler has less phase fluctuation as there is less feedback from the multiple reflections of the crystal quartz substrate, and therefore the high reflectance

ouptut coupler has a flatter response and a smaller GDD. The numbers in Figure 4.21 are actually quite promising. Reported dispersion values for working THz QCL frequency combs (measured by THz TDS) are typically between 0 - 2×10^5 fs^2mm^{-1}, and ridges are typically a few millimeter long, giving total roundtrip dispersion values on the order of 0-10 ps^2 [150,151]. Based on Figure 4.21, if a broadband metasurface and a high reflectance output coupler are used, the total roundtrip dispersion could be as low as a few ps^2. Note that the output coupler does not actually have to have high reflectance, only low dispersion; high reflectance is just a way to get low dispersion from an output coupler with a thick substrate. For example, future output couplers based on thin silicon-on-insulator (SOI) membranes would help reduce dispersion as well. It is interesting to note though, that the dispersion of the output coupler takes on the opposite shape as the single-ridge metasurfaces, so it may be possible to design the two carefully so that the output coupler dispersion cancels that of the metasurface. The phase response and dispersion of some of the first metasurfaces made (operating at 2.6 THz, $\Lambda = 90$ μm) were measured by Hou-Tong Chen at the Los Alamos National Laboratory (Center for Integrated Nanotechnologies). The results (unpublished) are plotted in Figure 4.22(a), and are in relatively good agreement the simulated GDD in Figure 4.22(b).

Experimentally, the short cavity data presented in this chapter generally showed a tendency towards single-mode lasing on the mode closest to the peak in the gain spectrum of the metasurface. A certain degree of multimoding was observed from the double-ridge data in Figure 4.19, but this may be more a result of cavity misalignment, and generally the mode near the center of the gain is still favored. When multimoding is observed, it is mostly between the lowest frequency mode and the highest frequency mode, which are ~600 GHz apart and may not compete for gain anyways. The data in Figure 4.20 also shows multimoding, but again, the modes are very far apart, and misalignment is clearly an issue based on the beam patterns, which indicate the two modes may not even spatially overlap and so wouldn't compete for gain.

With regards to longer cavities built intracryostat, the results in [19] showed two modes

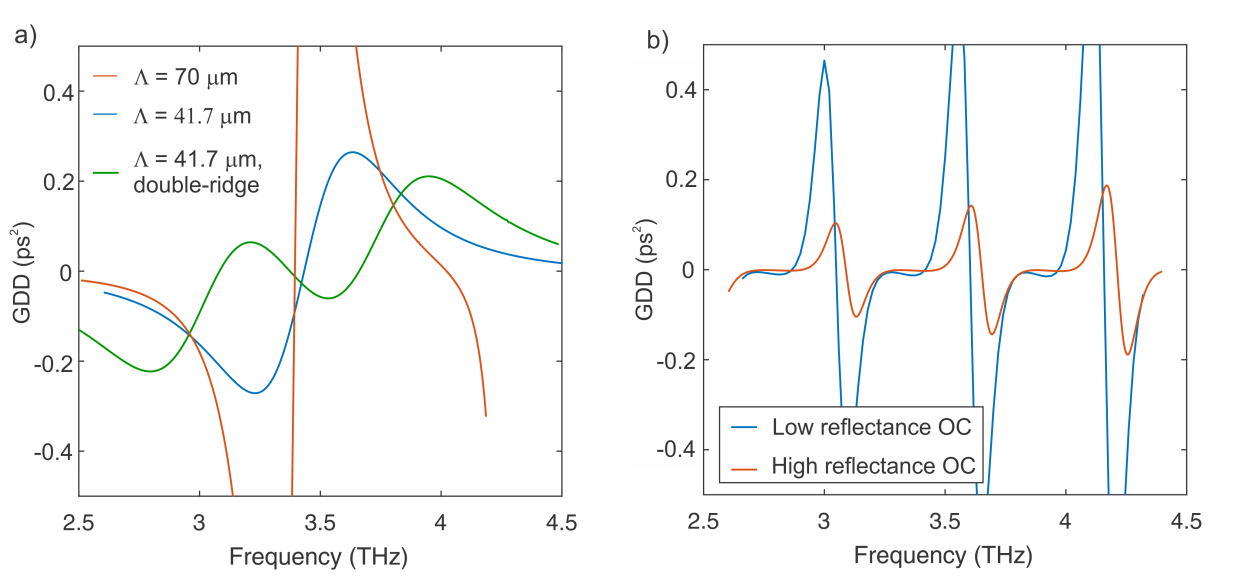

Figure 4.21: (a) Simulated group-delay dispersion (GDD) of three different metasurfaces. The more broadband, low-Q metasurfaces show significantly reduced GDD. (b) Simulated GDD for the two output couplers from Figure 4.7. The higher reflectance output coupler shows lower GDD.

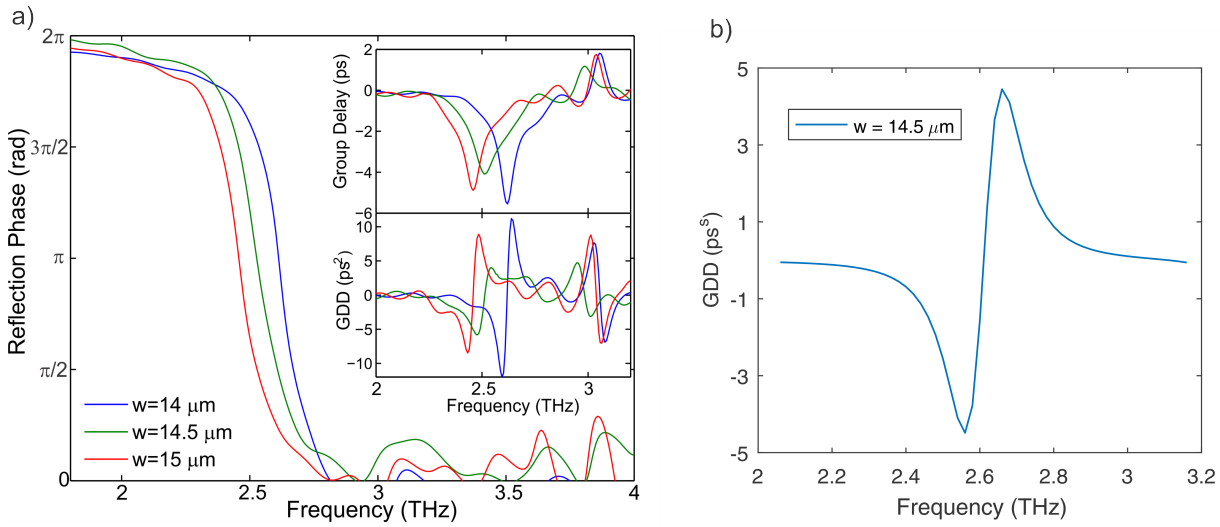

Figure 4.22: (a) Metasurface phase and resulting GDD measured by time-domain spectroscopy at Los Alamos National Laboratory by Hou-Tong Chen. (b) Corresponding simulated GDD is in relatively good agreement.

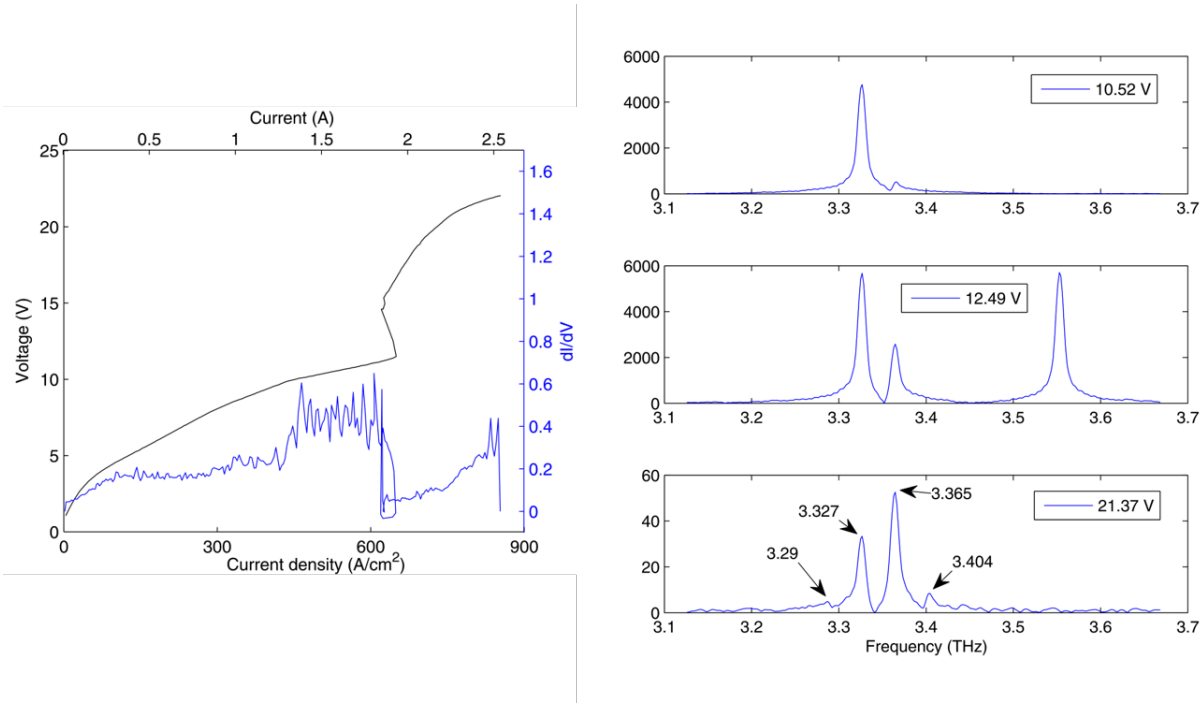

Figure 4.23: Measured I-V and spectra for the 2×2 mm^2, 1 mm bias diameter double-ridge metasurface with a ∼5 mm long external cavity and a higher reflectance output coupler (Figure 4.3). The corresponding $\mathrm{d}I/\mathrm{d}V$ is also plotted. Spectra show multimoded behavior throughout, and at high bias (post-NDR), four modes are observed to lase simultaneously.

lasing simultaneously in pulsed mode for a cavity length of 1-2 mm, and a single mode lasing in continuous wave. These are plausible results as the FSR is still relatively large, so the output coupler could filter out modes closer to wings of the metasurface gain (lower metasurface amplification and higher output coupler transmission results in much higher threshold gain). Further, the metasurface was focusing, which is not intended for broadband operation. Single-mode continuous wave lasing may be a result of reduced gain as a result of the heating. In Chapter 3 of this thesis, a ∼3 mm cavity was used with a large (1.5 mm bias diameter) uniform TM_{03} metasurface. The results were all single-mode, but given the FSR of ∼50 GHz, it is again plausible that the output coupler reflectance filtered out further modes (Figure 3.2).

To date, the most modes the author has observed at once is 4, using a 2×2 mm^2 double-

ridge metasurface with a 1 mm bias diameter, and the high reflectance output coupler in Figure 4.3. The modes appear to be evenly spaced by the FSR of the cavity, but are only spread across ∼100 GHz, when we know that the measurface gives gain over more than 1 THz of bandwidth. However, this evenly spaced multimoded behavior is occurring well into the unstable NDR portion of the bias, so it is unknown what the gain spectrum of the material may look like. Based on the results the author's suggested approach to looking for comb behavior would be to make as large and broad of a metasurface as possible, mount it in the tunable cavity setup with the piezoelectric stepping stage, and very carefully sweep the cavity length and metasurface bias while monitoring the bias line for a beat note. A large metasurface will be needed to allow for longer cavity lengths while minimizing diffraction loss (Figure 2.6), especially with a broadband metasurface that has weak amplification. The most important question to answer is whether the lack of spatial hole burning will fundamentally counteract multimoding and comb operation. If so, perhaps there are less homogeneous metasurface designs that can exploit other portions of the gain material. Otherwise, from a dispersion point of view, the VECSEL seems well suited for comb operation, though it may be difficult to make the cavity long enough to achieve the density of modes that are usually observed from ridge-based combs.

CHAPTER 5

Low power-consumption, high-efficiency QC-VECSEL designs

5.1 Introduction

While the THz QC-VECSEL's strength is in its large radiating area which allows for narrow beam emission and high peak-pulsed output power, this is actually a bit of a weakness when it comes to continuous wave operation, which is essential for applications such as heterodyne spectroscopy. This is because the large thermal load associated with driving devices at a DC-bias causes significant heating, ruining the THz intersubband gain as a result of increased non-radiative scattering. To operate in continuous wave (CW) mode, THz QCLs are typically kept at very low temperatures (<77 K) and/or the device is made very small so that the current draw is low [152, 153].

In Chapter 4, up to ∼20 mW of CW power was demonstrated at 3.4 THz at 77 K, which is by far a record for CW power from a THz QCL at 77 K. However, this is largely attributed to the high-performance of the active region, which lased up to 170 K in a metal-metal waveguide and had sufficient gain at 77 K to allow strong performance. While the VECSEL was essential to maximizing the potential of this particular active region, one might not expect such impressive results from other QC-active regions, especially those designed closer to the limits of the THz QCL operating range (such as 4.7 THz) where the maximum operating temperature is lower. Further, while the CW output power from the device in Chapter 4 (Figure 4.9) was impressive, the electrical power consumption was ∼4 W, which is generally outside of the power and/or thermal budget for a remote application such as a

balloon or space based telescope. For such missions, power budgets are typically much lower, less than 1 W. If the bias diameter of the device in Chapter 4 was reduced until the total power consumption was <1 W, the device would likely not lase as the bias diameter would be much smaller than the external cavity mode leading to very high threshold gain values (Figure 4.12), even at very short cavity lengths. The device in Chapter 4 had a small period with a fill factor of 28.5% for the purpose of obtaining broadband performance, but earlier metasurfaces, such as those in Chapters 1 and 2 (also operating at 3.4 THz with the same active region) use a more sparse 70 μm period with a fill factor of 16.4% (for TM_{01} designs), reducing the expected power consumption by almost half. Further, sparse metasurfaces have a higher amplification factor, so the bias area could perhaps be made a little smaller, likely bringing the thermal load down to <2 W (with correspondingly reduced THz output power). This is certainly an improvement, but still twice as much thermal load as we would like, and it is not desirable to further reduce the bias diameter of the metasurface as that leads to higher threshold gain values and lower output power. In this chapter we consider two options for further reducing the fill factor of the metasurface, which reduces electrical power draw without having to decrease the size of the metasurface.

5.2 Patch-based metasurface

5.2.1 Patch metasurface design

One was to reduce the fill factor compared to the ridge-based metasurfaces discussed up to this point is to use a metasurface based on an array of patch antennas, illustrated in the inset of Figure 5.1. The physical principles of the patch metasurface and ridge metasurface are the same: radiative coupling via the TM_{01} cutoff resonance and subwavelength spacing of elements. Each patch simply acts as a very short ridge. Because the TM_{01} cutoff has no phase variation along the length of the ridge (energy does not propagate in this direction), the resonance and material losses should generally be uneffected by the length of the element, only the width. This kind of patch resonator is directly analogous to the patch antenna

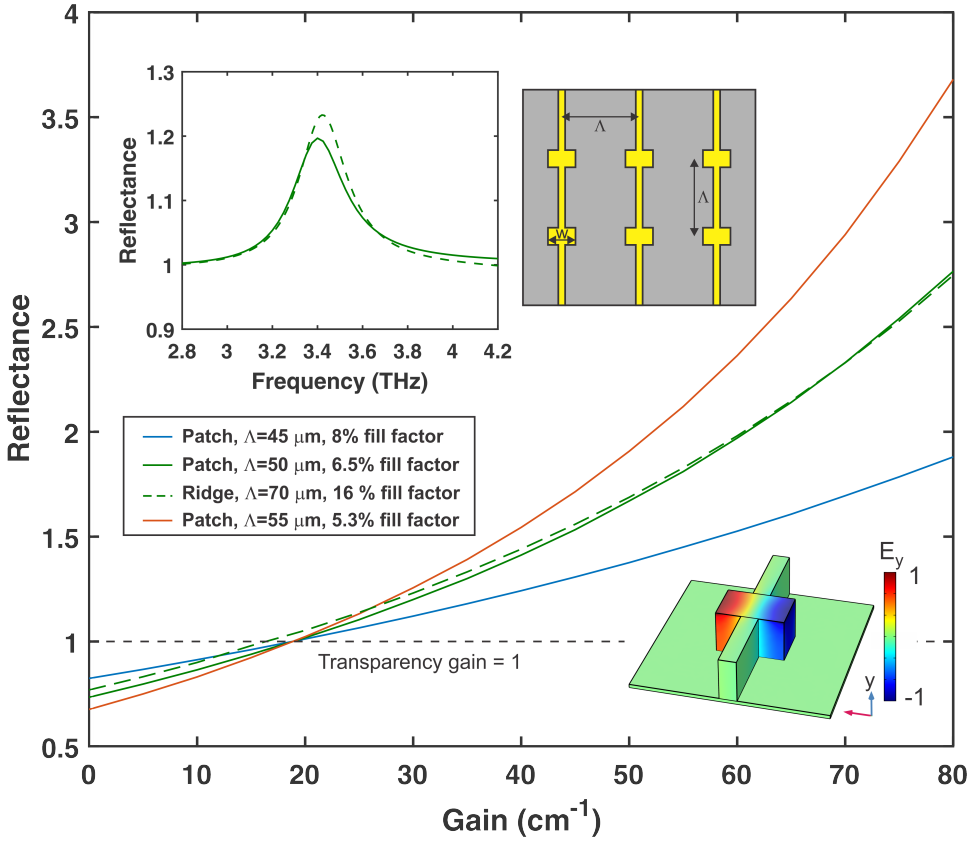

Figure 5.1: Simulation of patch-based metasurfaces with different periodicity. Reflectance plots with gain show that a patch surface with a square unit cell 50 μm on each side has a similar quality factor as a ridge-based metasurface with a period of 70 μm. This is not surprising as the diagonal of the 50 μm unit cell is 70.7 μm. Insets show a bird's eye illustration of the patch metasurface, simulated electric fields, and simulated reflectance data as a function of frequency.

developed and used by the microwave community, and the resulting metasurface is a direct parallel with the large body of work done on reflectarrays in the microwave [154].

Active arrays of patches have been the subject of many studies in the THz and mid-IR QCL communities for use as amplifiers, detectors, and self-lasing structures [155–159]. Active arrays of patches were first used with the THz QC-VECSEL in Xu, *et al.* Ref. [21], where two sets of orthogonally oriented patch arrays were used to demonstrate a VECSEL with electrically switchable polarization (also measured to self-lase, see Chapter 2). That metasurface, however, was rather dense as CW operation was not the concern, but rather

functionality. In this section, the discussion will be focused on using patch arrays for the purpose of minimizing the metasurface fill factor.

While conceptually, the idea would be to have an array of isolated patch elements, in practice, to make an active array, the patches need to be connected to a bias, as indicated in the inset of Figure 5.1. These connecting elements have relatively little impact on the VECSEL operation as they are much too narrow to couple to surface incident radiation, and the energy the couples into the patches does not propagate along the length of the ridge (see Figure 5.2). They do introduce a 2^{nd}-order DFB waveguided solution along the length of the ridges that is coupled to surface-directed light polarized along the length of the ridges. The frequency of this mode naturally depends on the exact period of the structure, and it also depends strongly on the width of the connecting ridges because that is where the mode is primarily confined. Using these parameters, this Bragg mode can easily be tuned outside of the gain bandwith of the QC-material, but regardless, the mode should not experience much gain as the connecting ridges are not biased (insulated by a layer of oxide between the QC-growth and the metal) because they represent wasted pump power with regards to the targeted VECSEL mode. Despite this insulation, it is likely that current spreading from the patches into the connecting elements via the in-plane conductivity of the QC-material still results in a certain degree of wasted pump power. The in-plane conductivity of the QC-material is not known, so it is difficult to determine the degree of this effect, but making the connecting ridges as thin as possible should minimize the effect. How thin the connecting elements can be made is limited by either fabrication capabilities, or the possibility of burning the metal due to resistive heating associated with pushing large currents through such as small channel.

Another consequence of having a 2-dimensional periodic structure is a modified diffraction condition: the lowest wavenumber along the edge of the Brillouin zone of the metasurface should be greater than the incident THz wavenumber. In the case of a square array of patches, the lowest wavenumber of the Brillouin zone is associated with the diagonal of the square unit cell, giving us the condition: $\Lambda\sqrt{2}¡\lambda_0$, where Λ is the length of the edge of the

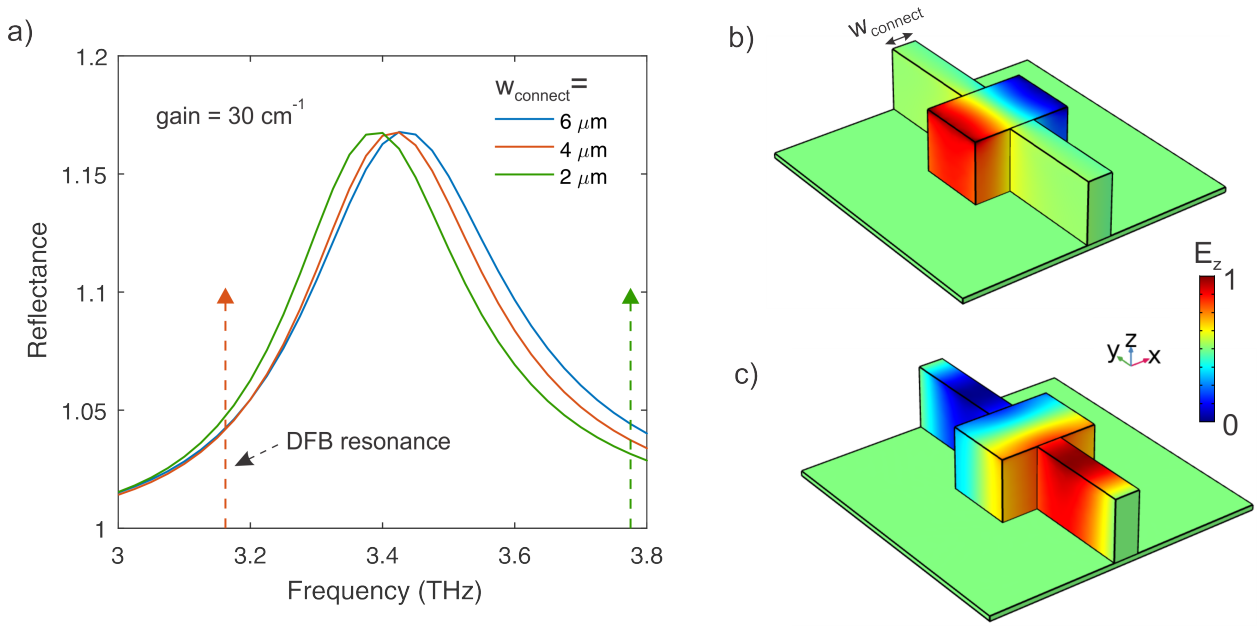

Figure 5.2: (a) Simulated reflectance from a patch metasurface designed to operate at 3.4 THz. The width of the connecting ridges is varied, but shows little effect on the targeted TM_{01} mode (b). (c) A 2^{nd}-order distributed feedback mode is also observed, but the mode is largely confined to the connecting ridges, which are not biased. The frequencies of these solutions are indicated in (a).

unit cell, and λ_0 is the incident wavelength. In comparison, the diffraction condition for the typical 1-dimensional ridge-based surface was simply $\Lambda ¡ \lambda_0$, where Λ was the period of the 1-D ridge grating. In Figure 5.1, the simulated reflectance from a square array of patches designed to operate at 3.4 THz with varying unit cell size is plotted along with the simulated reflectance for a typical 70 μm period ridge design also intended to operate at 3.4 THz. We find that the reflectance magnitude and quality factor is most similar between the 70 μm period ridged design and the patch design with a unit cell 50 μm on each side, giving a diagonal of 70.1 μm, indicating a similar degree of coupling to the grating modes.

Based on the discussion, to minimize the fill-factor and resulting electrical load from the metasurface, one should keep the width of the patch constant while reducing the length of the patch to as small a dimension as possible. However, this concept is quite so simple; when the length of the patch gets very short, the increased amount of fringing field effectively resulting

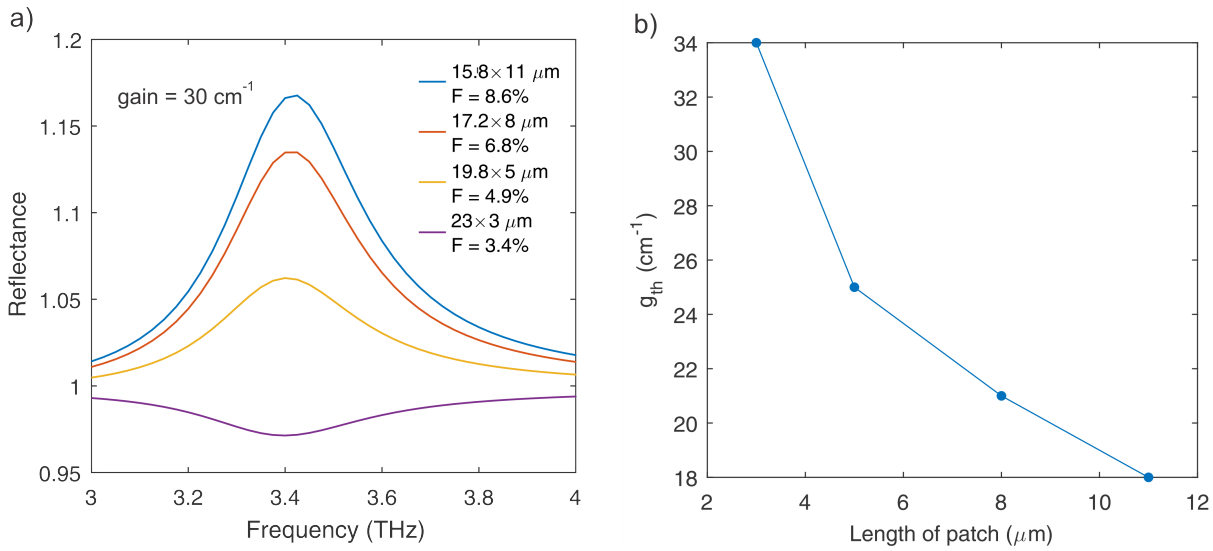

Figure 5.3: (a) Simulated reflectance spectra for narrowing patch elements. 30 cm^{-1} of gain is applied in all cases. As indicated in (b), narrowing of the patch elements increases the threshold gain considerably

in a lower refractive index for the wave bouncing back and forth in the patch, forcing the width of the patch to increase in order to maintain the same resonant frequency. This is also manifested by a small, but noticeable increase in threshold gain values. Therefore, the fill factor cannot be made arbitrarily small. In Figure 5.3, a set of simulations is presented for a patch surface with a fixed unit cell size, but varying patch length. The Figures indicates that, at best, the fill factor of the metasurface can be reduced to ∼7% by switching to a patch metasurface (5.5% if a 50 μm period is used) before the threshold gain starts to increase substantially.

5.2.2 Experimental Results

One patch device has been successfully tested using wafer VB0739 (same as previous chapters). The design used a square unit cell 45 μm on each side, and patch elements that were 16.8 μm wide and 11 μm long (note the width is considerably increased from ridge designs targeted at 3.4 μm). The connecting ridge elements were 4 μm wide and the top

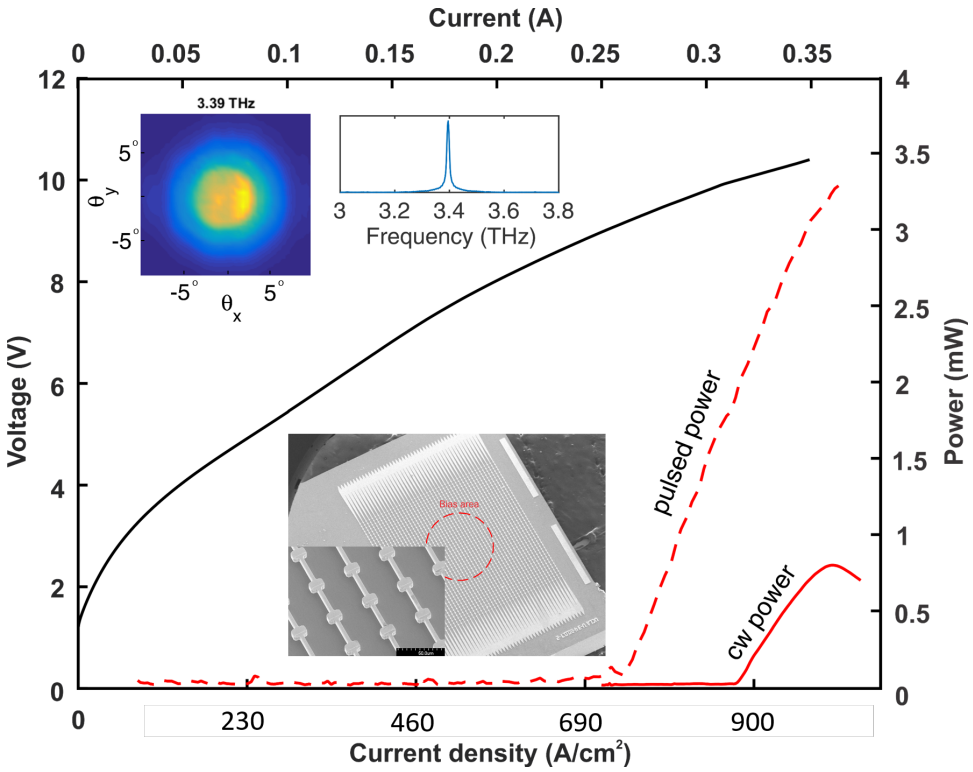

Figure 5.4: Experimental result using patch-based metasurface. A 2×2 mm^2 metasurface was tested with a 0.75 mm bias diameter. The device was able to operate in continuous wave mode at 77 K, and a relatively good beam pattern is observed. Inset shows SEM of fabricated device. Current densities are large compared to previous devices from this wafer, indicating significant leakage current into the connecting ridge elements.

contacted of the connecting elements was isolated from the QC-material by a layer of oxide. The fill factor of the metasurface is 9.1% (assuming the connecting ridges don't draw any current, $F{=}wl/\Lambda^2$), compared to 16.4% for the 70 μm ridge surface, so we should expect a 45% reduction in current draw. The metasuface was 2×2 mm with a bias area 0.7 mm in diameter. Assuming a peak current density of 700 A/cm^2, the longest chain of biased patches (the middle set) should draw ∼19 mA of current. State-of-the art 3^{rd} order DFB lasers regularly draw 10's to 100's of mA of continuous electrical current through narrow elements ∼2 μm wide, so burning of the ridges should not be a problem with 19 mA and 4 μm wide connecting elements.

The measured *L-I-V*, spectrum, and beam pattern are plotted in Figure 5.4. The current

density for the patch is calculated assuming there is no current draw in the connecting ridges, so as a result of current spreading, the apparent current densities are considerably higher than those previously observed from this wafer, indicating a clear effect of current spreading into the connecting ridges and only resulting in a 20% reduction in total current draw compared to that expected from a ridge-based metasurface with the same bias diameter. The in-plane conductivity of the QC-material can be simulated to match this result, but such a simulation has not been performed yet. CW lasing with less than 1 mW of output power was demonstrated at 77 K. It is noted, that the performance of the ridge metasurface in terms of power and threshold current was much poorer than previous devices made from this wafer. Because the current draw is similar to previous device, it is assumed that the reduced performance was a results of additional optical losses, most likely in the top metal contact as a different Ni etchant was used in the process that appears to have damaged the underlying gold. It is also noted that the alignment of the oxide used to isolated the connecting ridges was a couple of microns off, as can be seen the inset SEM of Figure 5.4. Due to the fabrication issues, further testing was not conducted, but the initial result tells us that this can be an effective way to reduce the fill factor and thus the thermal loading of the metasurface. However, this technique does not improve the efficiency of the metasurface as the TM_{01} mode structure is unchanged, so the same fraction of pump power is being stimulated as in the case of a ridge metasurface.

5.3 Hollow-ridge metasurface

An alternate route to reducing the fill factor of the metasurface, and simultaneously increasing the efficiency is to remove the gain material from the center of the ridge, where the optical intensity is minimal. This center portion of the ridge is drawing significant electrical power while contributing relatively few THz photons as there is not much stimulating field. Removing this portion should reduce the total current draw while having minimal effect on the output power. This idea is simulated in Figures 5.5 and 5.6, where the uniformity of the

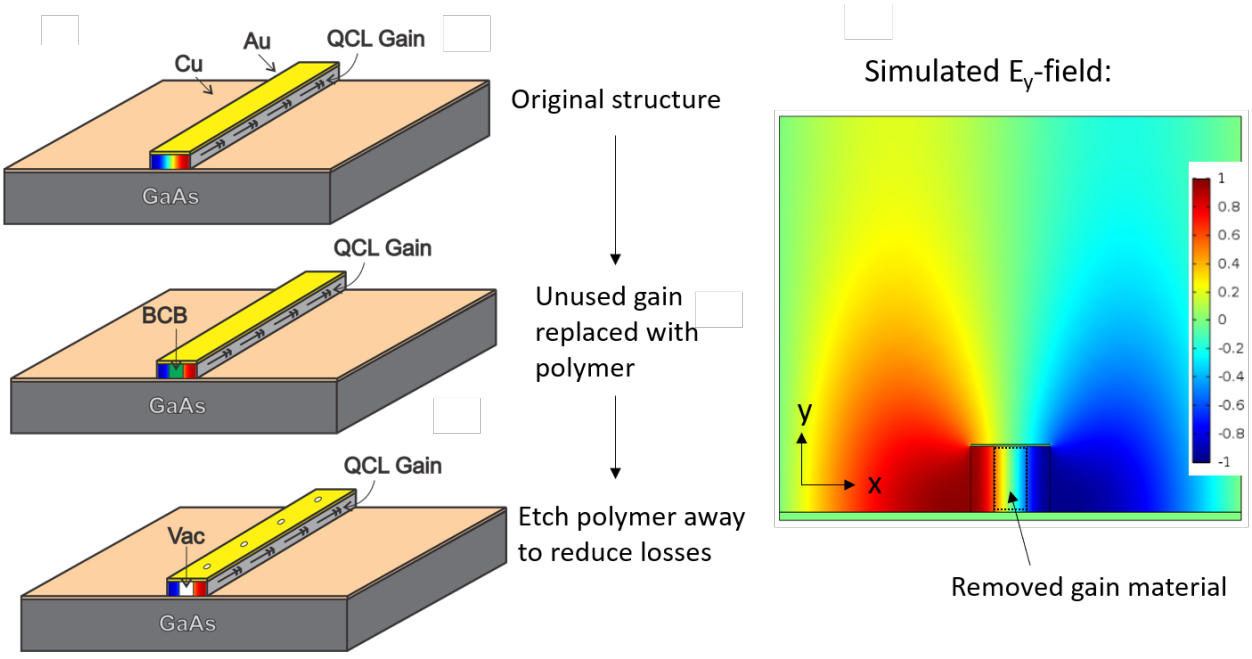

Figure 5.5: (a) Proposed designs for metasurfaces with the QC-material removed from the middle of the ridges (where there is little optical stimulation, but significant electric current draw). One option is to fill the empty space in with BCB, the other is to use a polymer that can be subsequently removed by an isotropic oxygen plasma etch.

stimulating field over the gain is plotted as given by:

$$\eta_u = \frac{(\int_{active} |E_z|^2 dA)^2}{A_{active} \int_{active} |E_z|^4 dA} \tag{5.1}$$

For a typical ridge design, the uniformity is intuitively 2/3 reflecting the average energy of a standing sine wave. Simulations in Figure 5.6 indicate that as more of the material is removed from the center of the ridge, the uniformity factor approaches one, in which case the current should be reduced by ∼33% and the efficiency improved by ∼50%. The theory is relatively simple, but the challenges come in fabricating such a structure.

Two options for fabricating ridges with the center material removed are plotted in Figure 5.6. The first option is to follow the typical metal-metal waveguide fabrication procedure (Appendix 8.1), but leaving an opening in the center of the top contact that allows the

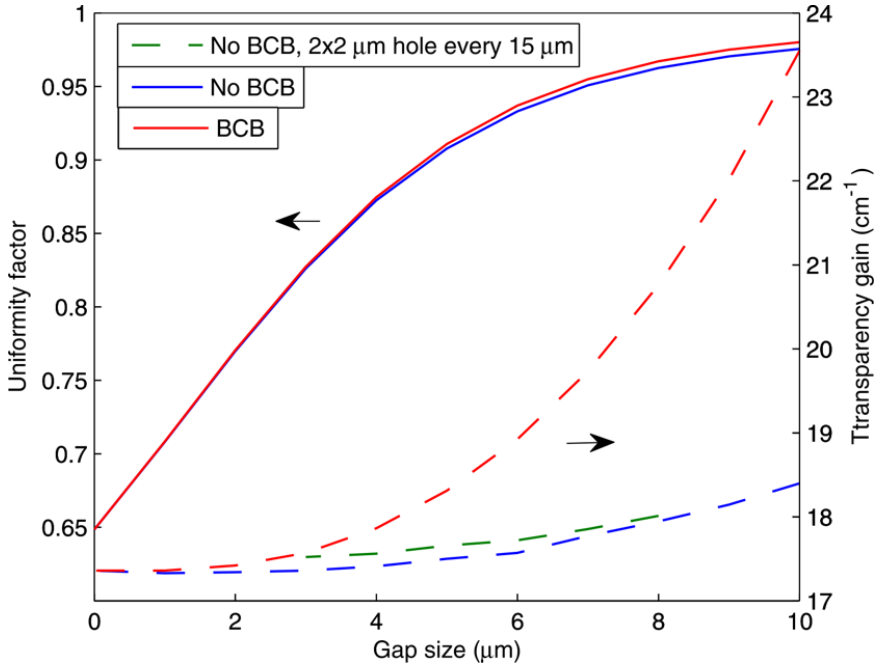

Figure 5.6: Plot of uniformity factor and threshold gain as a function of the gap size in the ridge. The simulation indicates that much more efficient use of the QC-material can be obtained with little-to know effect on the threshold gain (even with BCB in the cavity).

middle material to be removed during the mesa etch. Next, BCB is spun onto the sample to fill in the middle of the ridges and planarize the whole surface. While BCB is specifically designed for planarization, it is not recommended for such long tall structures as THz QCL ridges, and from the author's experience, this is true, especially when working with small pieces rather than full wafers. An alternative approach would be to chemical-mechanically polish the BCB and then etch-back with reactive ion etching (RIE) to expose the ridges once the surface is smooth. Once the tops of the ridges are exposed, metal can be deposited on the top of the ridges, including the BCB-filled centers. This second top contact should include a Nickel mask that can withstand a subsequent dry-etch to remove the remaining BCB on the surface. BCB is a good choice of material as it has low losses in the THz. According to the simulations, the uniformity of the stimulating field can be increased to >95% while the BCB only increases the threshold gain by 5-10 %. To fully optimize the approach and remove the polymer from the middle of the ridge, one can add periodic, subwavelength spaced openings

in the top contact and then remove the polymer inside with an isotropic oxygen plasma etch. Simulations indicate that such openings in the top contact have negligible effect on the metasurface properties. BCB is not etched by oxygen plasma, so a different polymer, such as polyimide, which etches very fast in oxygen plasma, should be used. Polyimide is very lossy in the THz though, so one should make certain none of it is left behind.

Perhaps the ultimate limit in low power consumption, high efficiency metasurface design would be to combine the presented approaches to make a patch-based metasurface where the middle portion of QC-gain material has been removed from each patch.

CHAPTER 6

Mid-infrared QC-VECSEL designs

6.1 Introduction

While the previous chapters have been focused on development of QC-VECSELs in the terahertz frequency range, in this chapter, we explore the possibility of demonstrating a QC-VECSEL in the mid-infrared (IR) range (∼3-28 μm). Mid-IR QCLs are a more developed technology than THz QCLs, and have a much larger commercial market, making it an attractive idea to extend the VECSEL concept to the mid-IR. In particular, there is considerable interest in developing high-power mid-IR QCLs with good beam quality and broad spectral coverage for the purpose of infrared-countermeasures and remote sensing.

Typically, mid-IR QCLs are patterned into narrow dielectric waveguides (on the order of a wavelength wide) for efficient heat removal, enabling room-temperature operation. While the power can be scaled to a certain extent by simply making the ridge longer and high-reflection coating one facet while anti-reflection coating the other, such techniques are ultimately limited by saturation of the gain material and efficiency of the facet coatings. To further increase the power, broad area devices, or arrays of devices must be used. Broad area devices have strong potential for high peak-pulse powers, but the reduced efficiency of heat removal makes them non-ideal for continuous wave operation. Arrays, on the other hand, have more potential for continuous wave operation but require a beam combining technique. In the case of infrared-countermeasures, the most important factor is high average power, so either pulsed or continuous wave operation can be considered.

Several approaches to increasing the output power of mid-IR QCLs have been investigated by other researchers. The current records at the time of writing (at room temperature) are

203 W peak pulse power at 4.8 μm using an angled facet cavity [160], and 8.2 W of continuous wave power at 8 μm using an array of 8 phase-locked narrow ridges [161]. Both approaches suffer from limited beam quality. The beam from a single wide-facet device is typically elliptical as the emitting facet is much wider than it is tall, and the beam from a phase-locked array is multi-lobed due to the interference of the emitting ridge. Incoherent beam combining using a diffraction grating has also been investigated [162–164], and devices with thin active regions are under investigation for improving the temperature performance of large area devices [165, 166]. Using mid-IR QC-material as the basis for a mid-IR VECSEL, as demonstrated in previous chapters in the THz, is one possible way to further scale the peak-pulse power of large area mid-IR QCLs while maintaining single-mode operation and excellent beam quality.

Unfortunately, the design concept used for the THz QC-VECSEL cannot be directly applied to the mid-IR because the metasurface design is based on metal-metal waveguides, which are far too lossy in the mid-IR. Instead, mid-IR QCLs use dielectric waveguides (as discussed in Chapter 1). A narrow dielectric waveguide also supports a surface-coupled TM_{01} transverse resonance, but only a small fraction of the mode is coupled is coupled to the gain resulting in very low amplification factors (see Appendix 8.4). Here, we will discuss an alternative approach to designing a QC-VECSEL by using a periodic grating to couple the QC-gain to surface directed radiation. Given the grating coupling equation: $\vec{k}_f = \vec{k}_i \pm m\vec{k}_{grating}$, if $\vec{k}_i$ is equal to $\vec{k}_{grating}$, then the first diffracted order, m=1, gives $\vec{k}_f = 0$ (waves propagating in the surface direction), while the second diffracted order, m=2 gives $\vec{k}_f = -\vec{k}_i$. Assuming material losses are small, such a structure could operate as either a surface-emitting laser or as a surface-coupled amplifier, depending on whether the radiative losses are smaller or larger than the available gain, respectively. The former situation has been demonstrated in most semiconductor frequency ranges, taking advantage of the 2^{nd}-order diffraction to simultaneously provide distributed feedback and single-mode emission, but has not seen widespread success as there are typically 'dark', non-radiating modes with lower threshold that preferentially lase over the desired radiating mode. With THz QCLs,

a number of techniques have been demonstrated to encourage lasing on the radiating mode (see Chapter 1), but even in such cases, the laser ridge must be made long and narrow to prevent high-order modes, limiting the power scaling potential and resulting in a highly elliptical output beam.

In this chapter, we propose designing in the alternative regime, where the radiative losses have been increased so that the surface only acts as an amplifier, not a self-lasing structure. We can then build this amplifying surface into an external cavity to act as the gain chip in a mid-IR QC-VECSEL. In this VECSEL configuration, the external cavity controls the shape of circulating power and output beam, allowing the grating surface to be scaled to larger areas while maintaining a single-lobed, high-quality output beam. It is still possible for non-radiating modes of the grating surface to 'self-lase' and compete with VECSEL lasing, but as will be shown, a strongly coupled metallic grating can be used to simultaneously increase surface losses for the radiating mode, and increase material losses for the non-radiating mode, favoring lasing on a VECSEL mode. One downside of this approach is that the grating is a very narrowband resonance, unlike the THz metasurface, so it will not be ideal for broadband frequency tuning.

6.2 Design

6.2.1 Infinite structure

A sample design for a grating-coupled amplifying is shown in Figure 6.1. The base of the structure is a standard mid-IR dielectric waveguide, where the InGaAs/InAlAs active region (n≈3.27) is sandwiched between two dielectric cladding layers consisting of a thin InGaAs layer (n≈3.349) and a thicker InP cladding (n≈3.08). To provide the surface and co-directional coupling, a metallic grating is patterned into the upper InP cladding layer. In most semiconductor lasers, DFB gratings are implemented as a weak dielectric perturbation that breaks the waveguide solution into two band-edge modes with opposite symmetry; one couples to surface radiation, while the other does not. The eigenmodes of the unperturbed

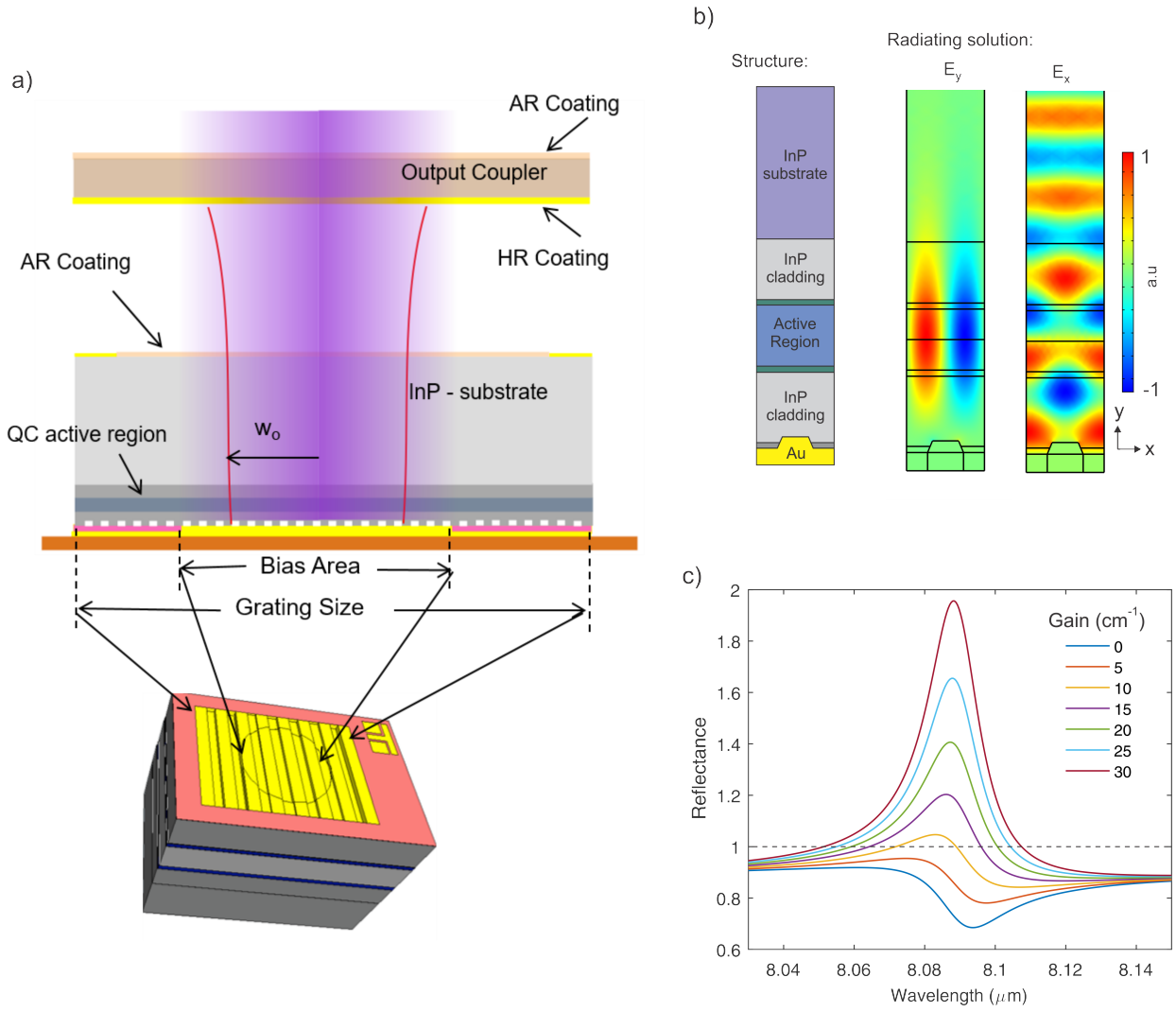

Figure 6.1: (a) Overview of mid-IR VECSEL design. A large-area metallic grating is patterned into the upper cladding layer of the QC-growth to provide coupling of the QC-gain to the surface direction (down through the substrate in this case). A nitride layer is used to allow for selective biasing of a circular portion in the middle of the grating area, the device is mounted epi-down to a heat sink, and feedback is provided by either the back of the substrate or an external output coupler. (b) Simulated electric fields for the radiating solution in the infinite case, and (c) simulated reflectance of the infinite structure as a function of applied QC-gain.

waveguide can used as a set of basis states to approximate the solutions of the perturbed waveguide modes, and the coupling coefficient between the unperturbed waveguide modes is proportional to the photonic bandgap of the grating. These waveguides are usually topped

with a continuous metallic top contact that supports surface-plasmon modes, but these plamson modes are sufficiently detuned from the waveguide modes that they do not interact with the waveguide modes and are not included in the expansion of the perturbed modes. When a grating is patterned into this top contact, however, the resonance of the surface-plasmon modes can be brought in tune with the waveguide modes, and this plasmon resonance should be included in the modal expansion of the perturbed modes, and the coupled system has three eigensolutions. The anticorossing of theses modes can be very large. Such an interaction between waveguide modes and a plasmonic grating was first investigated in Reference [167] at optical wavelengths, where they refer to the resulting solutions as 'waveguide-plasmon polaritons'.

Such waveguide-plasmon polaritons have also been studied with mid-IR QCLs for use as both 1^{st}- ($2\Lambda=\lambda_g$, where Λ is the grating period, and λ_g is the guided wavelength), and 2^{nd}- ($\Lambda=\lambda_g$) order DFBs. In Reference [168], the strong coupling regime between the plasmonic and waveguide modes was discussed theoretically, but experimentally, the devices were designed to operate in the weak coupling regime, where the plasmonic mode is detuned from the waveguide mode and the problem is essentially the same as a traditional, 2-mode coupling problem [169, 170]. In Reference [171], the plasmonic mode of a 2^{nd}-order grating was designed to be in-tune with the waveguide mode as it adds considerable loss to the non-radiating solution, but very little material loss to the radiating mode, encouraging the laser to operate on the radiating mode (a problem that has traditionally plagued 2^{nd}-order DFB lasers). However, the interaction was designed to be weak by spatially separating the grating from the waveguide by several wavelengths (reduced mode overlap results in weaker coupling). Here, to design a mid-IR QC-based amplifying reflector, we propose a structure operating in the more strongly coupled regime of the waveguide-plasmon interaction by placing the grating much closer to the waveguide. In this way, the radiative losses induced by the grating are increased (with minimal increase in material losses), preventing the structure from lasing without feedback.

The proposed structure in Figure 6.1 is targeted at 8.1 μm. Per the surface-coupled

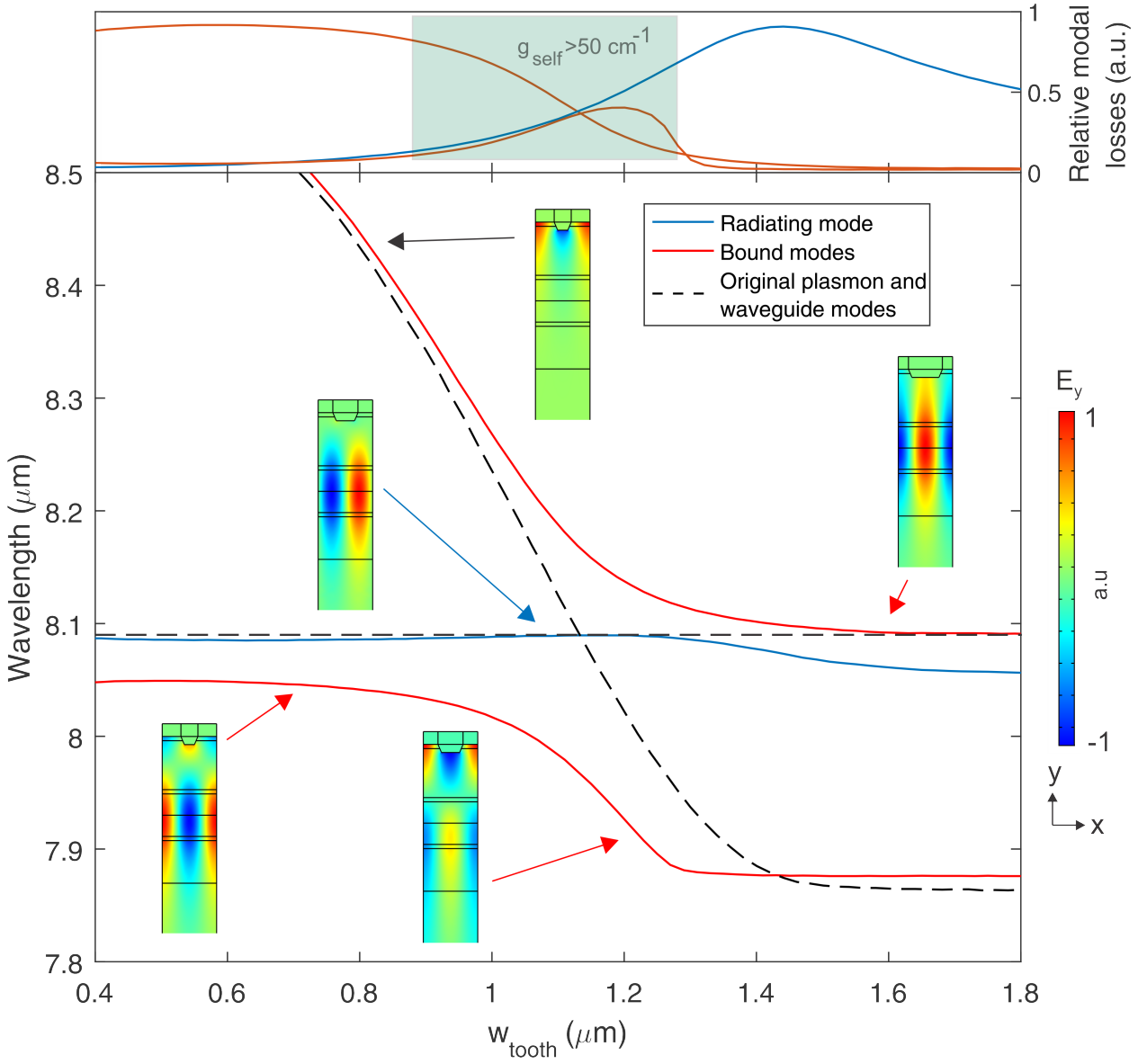

Figure 6.2: Eigensolutions of an infinite grating structure as a function of the width of the grating tooth. A strong coupling is observed when the plasmonic mode supported by the metallic grating is in tune with the waveguide mode. Electric field profiles are plotted at various points in the figure. The relative losses associated with each mode are plotted above. Within the shaded region, the self-lasing threshold for all modes is >50 cm^{-1}.

diffraction condition, the period of the grating is equal to the wavelength of the guided wave, which is ∼2.56 μm given the refractive index of the waveguide. The grating consists of a single 'tooth' per period, whose dimensions determine the frequency of the plasmonic mode.

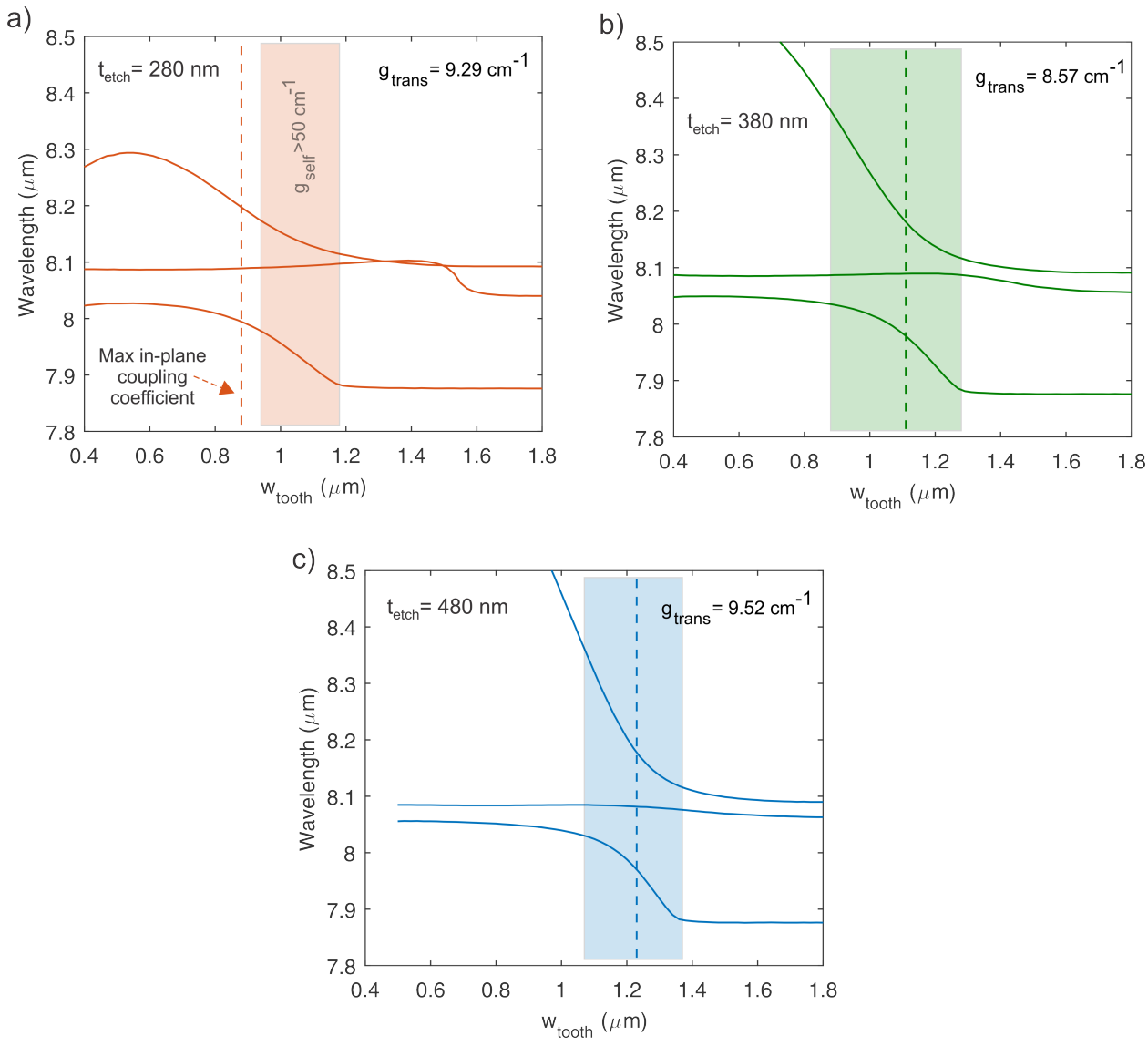

Figure 6.3: Eigensolutions of an infinite grating structure as a function of the width of the grating tooth for etch depths of (a) 280 nm, (b) 380 nm (same as Figure 6.2), and (c) 480 nm. Within the shaded region, the self-lasing threshold for all modes is >50 cm^{-1}. The point of strongest feedback is also indicated, as determined by finite device simulations (see Section 6.2.2).

In Figure 6.2, the FEM simulated eigensolutions of an infinite surface are plotted as a function of the width of the grating tooth (defined as the width at the top of the tooth, i.e the size of the opening in the etch mask), along with the electric fields of the solutions at various points. As the width of the tooth tunes the grating resonance through the waveguide resonance, a

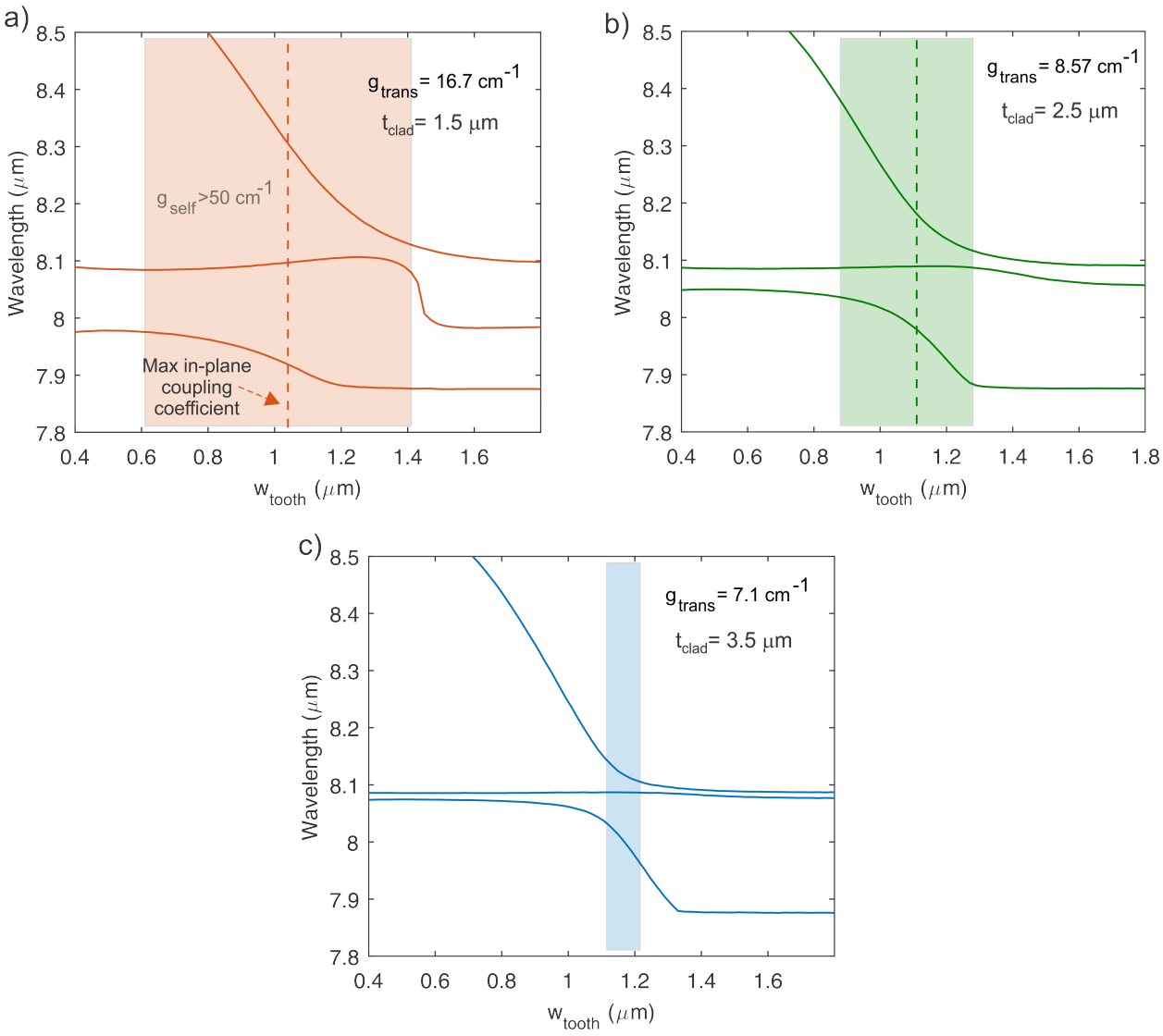

Figure 6.4: Eigensolutions of an infinite grating structure as a function of the width of the grating tooth for upper cladding thickness (separation between grating and waveguide) of (a) 1.3 μm, (b) 2.3 μm (same as Figure 6.2), and (c) 3.3 μm. Within the shaded region, the self-lasing threshold for all modes is >50 cm^{-1}. The point of strongest feedback is also indicated, as determined by finite device simulations (see Section 6.2.2).

large anticrossing is observed between the non-radiating waveguide mode and the plasmonic mode as they have the same symmetry, while the radiating waveguide mode (with opposite symmetry) is nearly unaffected, as previously predicted [168]. The relative losses for the three solutions are plotted as well. Within the shaded region, around the anticrossing point,

all modes have a self-lasing threshold >50 cm^{-1} due to either large material or radiative losses, while the transparency gain for reflected waves is small (∼10 cm^{-1}). This is the region in which we want to operate. The effects of the depth of the grating tooth on the anticrossing are plotted in Figure 6.3 and indicate that the size of the anticrossing is relatively unaffected by the depth of the etch, but the frequency of the plasmonic mode is tuned, so the anticrossing occurs at a different tooth width. Last, the effect of the distance of the grating from the waveguide on the anticrossing is simulated in Figure 6.4. The size of the anticrossing is strongly effected by this parameter, while the frequency is not.

6.2.2 Finite structure - coupling coefficient

The most significant difference between the mid-IR and THz approaches to the QC-VECSEL is that the grating used in the mid-IR design diffracts incident waves to the in-plane direction, and these waves propagate some distance before they couple back to the reverse- or surface-direction. The THz metasurface, on the other hand, is based on a subwavelength structure of locally resonant elements that do not propagate energy. This is an important difference. With the THz metasurface, the only thing limiting how small one can make the device is the need to have a large enough radiating aperture to support a narrow output beam (i.e., the metasurface should be at least a few wavelengths in each dimension). In contrast, with the DFB-based mid-IR scheme, the surface must be large enough to allow sufficient time for the in-plane propagating waves to couple back to the reverse- or surface-directions. Otherwise, a fraction of the in-plane coupled energy will be lost off the edges of the surface, increasing round-trip losses and threshold gain values for the VECSEL.

The rate at which energy is transferred from the forward to backwards direction should be given by one coupling coefficient κ_{2nd} (cm^{-1}), and the rate of energy transfer from the forward to surface direction should be given by another κ_{1st} (cm^{-1}). The total decay rate of the forward propagating wave is then simply the sum of the two: $\kappa_{total}=\kappa_{1st}+\kappa_{2nd}$ (cm^{-1}). In order to minimize diffraction losses, the lengths L of DFB lasers should be chosen such that $\kappa L >$ 2-3. In typical, weakly perturbed DFBs, the coupling coefficient is usually on the order

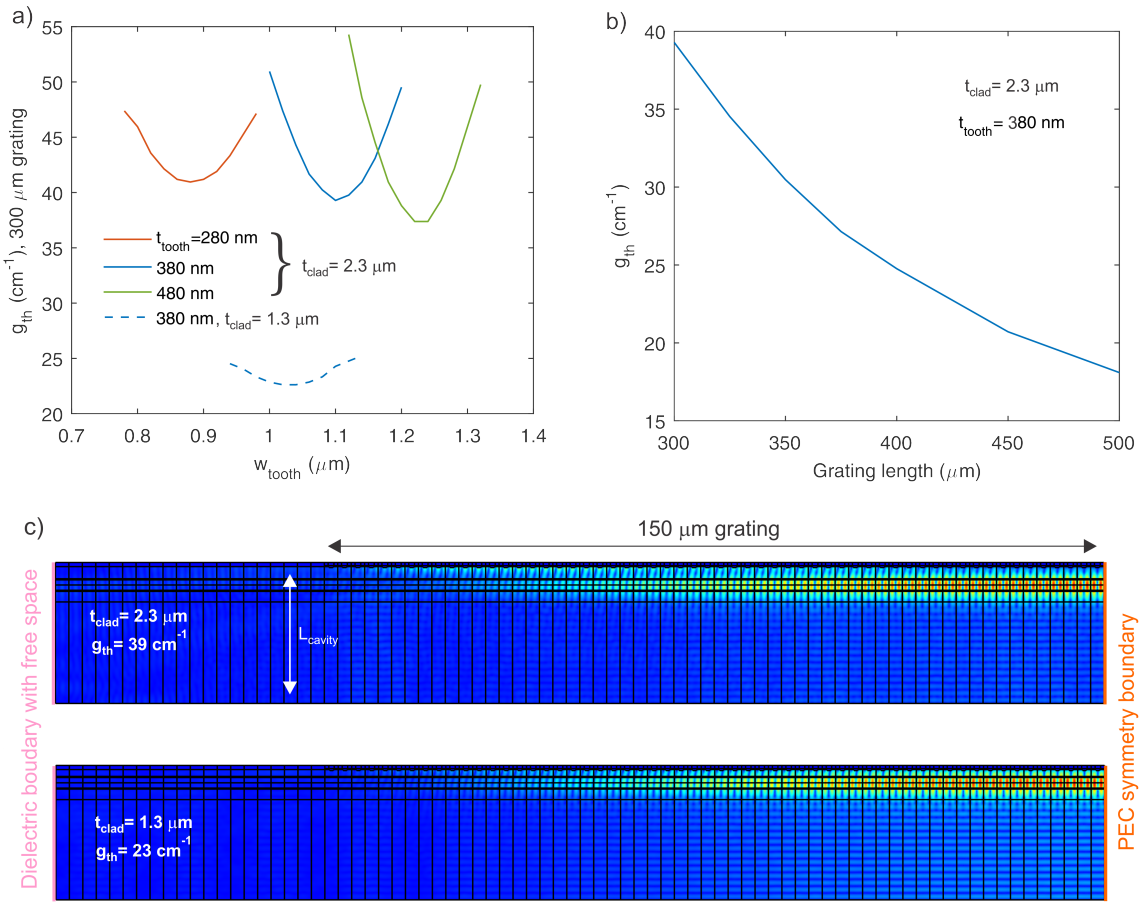

Figure 6.5: (a) Threshold gain values of a finite grating structure as a function of the width and depth of the grating tooth. Simulations with a 2.3 μm upper cladding thickness (separation between grating and waveguide) are plotted as solid lines, while the dashed line is plotted for a simulation with a 1.3 μm upper cladding thickness. (b) Threshold gain plotted as a function of the length of the grating (2.3 μm upper cladding, w_{tooth}=1.1 μm, t_{tooth}=380 nm). (c) Sample E-field solutions of the mid-IR VECSEL cavity simulation. PEC boundaries were used to take advantage of symmetry and only simulate half of the cavity, and impedance boundary conditions are added to the other end of the simulation to mimic a dielectric reflection with free space (as would be present in the actual cleaved device). Feedback from reflections at this boundary seem to have minimal impact, again suggesting a strong coupling coefficient. The substrate has no loss in the x-direction so as to isolate the effect of the diffraction grating on the threshold. The cavity length shows little to no effect on the threshold gain thanks to the large size of the surface compared to the wavelength.

of 10 cm^{-1} or less, requiring cavity lengths that are hundreds to thousands of wavelengths long to provide sufficient feedback. For narrow ridge-waveguide devices in the mid-IR and

optical, this is not an issue as cavities are usually on the order of millimeters compared to the guided wavelengths on the order of a micron. The purpose of the mid-IR QC-VECSEL, however, is to design a large area emitter that can provide a diffraction limited beam in 2-dimensions with a low M^2 value. Therefore, the surface is designed to be as wide as it is long (though the grating is only in 1-dimension), as illustrated in Figure 6.1. In theory, there is no problem with making the metasurface millimeter scale, but in practice, the current levels become very large. For example, a 3-mm diameter device with a current density of 5 kA/cm^2 (a somewhat modest value for mid-IR QCLs) would draw 350 A of peak current. Sending 350 A pusles that are <1 μs long is a challenging task in itself that would require a perfectly impedance matched setup, and even if it could be done, the heating may be too severe to see lasing regardless of how short the pulse is. Therefore, maintaining a very high coupling coefficient to reduce the area of the device is essential. Luckily, operating in the strongly coupled waveguide-plasmon polariton regime should result in a larger coupling coefficient along with satisfying our other requirements of high radiative loss for bright modes and low radiative loss for dark modes.

The rate at which energy is transfered from the forward to the backwards direction is given by the coupling coefficient κ (cm^{-1}), and at the Bragg condition, it is proportional to the width of the stopband [172].

It has not yet been determined how to define the coupling coeffiecient between forward and backwards waves for the waveguide-plasmon polariton regime as there are 3-modes, so the solution cannot be expanded into only a forward and backward wave. However, it is intuitive to assume that the strongest coupling occurs at the center of the anticrossing, as this is the location where the modes are most strongly interacting and the solutions are most dislocated from their original unperturbed results. In absence of a definitive analytical model, the subject can be studied by brute force using simulations. In Figure 6.5, the full mid-IR VECSEL cavity is simulated in 2-D space using an FEM eigensolver (as done for the THz VECSEL in Chapter 2). Figure 6.5 (a) shows the threshold gain for a device with a 300 μm wide grating (116 periods), 2.3 μm upper cladding, and a PEC boundary for

the output coupler (see figure caption for more details). The grating is terminiated by a dielectric boundary with free-space (representing a cleaved facet). Results are plotted as a function of grating tooth width for three different etch depths (matching the three sets of data plotted in Figure 6.3). As expected, the strongest coupling (where the threshold gain is a minimum) appears to occur at the center of the anticrossing (as indicated by the vertical dashed lines in Figure 6.3), and this minimum/anticrossing moves to wider tooth widths as the tooth depth is made deeper.

For comparison, the simulation was repeated for the 380 nm deep tooth, but with an upper cladding of 1.3 μm (closer to the waveguide). Also as expected, the larger anticrossing leads to much stronger in-plane feedback and much lower threshold gain. In fact, with a 1.3 μm upper cladding, the threshold nearly approaches that of the infinite case, suggesting the that the coupling length, given by $\kappa L = 1$, is very small. For consideration, if we assume the coupling coefficient can be approximated by the expression $|\kappa| = \pi n_{eff} \Delta f / c$, where Δf is the difference in frequency between the radiating mode and either of the two non-radiating modes (assuming we're operating at the center of the waveguide-polariton anticrossing), then the coupling coefficient is estimated as $\sim$250 cm^{-1} for the 1.3 μm cladding structure ($L =$ 40 μm), and $\sim$180 cm^{-1} for the 2.3 μm cladding ($L = 73$ μm). Again, this may not be the correct way to calculate κ, but it is noted that the numbers seem reasonable for the results of the simulated full VECSEL. Last, of course, to reduce the threshold for all modes, the grating size can be increased. In Figure 6.5 (b), it is observed that the threshold of the 2.3 μm cladding design can be reduced from 40 cm^{-1} to 18 cm^{-1} by increasing the grating from 300 μm to 500 μm, though this corresponds to a nearly 3-fold increase in current draw.

6.2.3 Finite structure - facet reflections

Another parameter that must be considered when designing a DFB laser (that goes hand-in-hand with discussion of coupling coefficient) is feedback from the the ends of the grating. A ridge waveguide based DFB would ultimately be terminated by a cleaved facet that can reflect the remaining power that has not been coupled to the reverse or surface direction. In the

optical regime, AR coating are used to minimized this effect, The position of the facet with respect to the grating is not precisely controlled, so the phase of these reflections in 'random', and these reflections can interfere significantly with the mode shape and resuting output beam. In typical, optical DFBs, the facets are AR coated to minimize these reflections, but AR coatings are difficult to implement in the mid-IR. If the length of the grating is much longer than the coupling length ($\kappa L = 1$), then the modal intensity is very small at the ends of the grating, and reflections have minimal effect. For example, the simulations in Figure 6.5 were performed assuming a cleaved facet boundary at the end of the grating (reflectance $R{\sim}0.35$). If this boundary is replaced by a perfect reflector (PEC boundary, $R{=}1$), the result for a 300 μm grating with a 1.3 μm upper cladding (dashed blue line) is almost unaffected (regardless of the specific phase of the reflection) as the coupling coefficient is strong enough that almost no power reaches the facet in the first place. However, the 300 μm grating with a 2.3 μm upper cladding (solid blue line) is highly effected by replacing the terminating boundary with a PEC, and in fact, no particularly structured solution can be found at all in simulation. If the grating size is increased to 500 μm, a PEC termination can be acceptable with a 2.3 μm upper cladding layer. Therefore, to promote a well structured solution, the grating should either be made sufficiently large compared to the coupling length of the grating (possibly demanding very large pump current), or a dielectric termination should be used. Of course, if the coupling coefficient is extremely weak, then even reflections from a dielectric boundary will prevent formation of a well structured mode. If the coupling coefficient is too large, it may be possible to see smaller, localized modes that are also undesirable.

A third option, which is useful if the coupling coefficient is weak but the device cannot be made larger for reasons of pump power, is to use a large grating, but only bias the central portion of the grating (as proposed by the illustration in Figure 6.1 (a)). The passive portion of the grating can provide controlled feedback without drawing current. This is a standard practice for DFB lasers, but to be implimented effectively, the electromagnetic solutions in the unbiased portion (which includes an extra dielectric layer) shold be matched to that in the biased portion of the grating. For weakly perturbed dielectric gratings, this can be

accomplished with a small adjustment to the period and grating parameters. This technique does not work well for the the proposed mid-IR amplifying surface, however, because the device operates in the strongly coupled waveguide-plamon polariton regime, which does not occur when an insulating layer is added between the metal and semiconductor layers because the frequency of the surface plasmon mode is completley detuned as it exists at the metal-insulator interface rather than the metal-semiconductor interface.

6.3 Experimental progress

Work is actively under way to experimentally demonstrate the proposed mid-IR QC-VECSEL, but the result has not yet been obtained. Work done to date includes:

- Obtaining QC-gain material at 8 μm. The active region design was been copied from Ref [24], and the wafer was grown by IQE.
- Testing the QC-material in a standard ridge-waveguide configuration. Measurements in pulsed mode at both 77 K and room temperature are plotted in Figure 6.6. The results are promising, with lasing observed at the target frequency, peak-pulse powers in the hundreds of mW, modest current densities, and low threshold current density (especially at 77 K).
- Obtaining ZnSe output couplers from II-VI Optical Systems (ZnSe being a low-loss material in the mid-IR) with one side HR coated to have 90% reflectance at 8μm, and the other side AR coated at 8 μm.
- Fabricating and initial testing of the proposed grating-based surface amplifiers.

The fabrication process for these initial devices is illustrated in Figure 8.1. The grating is defined over a large 2.5×2.5 mm^2 area using an oxide hard mask, electron beam lithography, and dry etching with BCl_3 (see SEMs in Figure 6.8). Silicon nitride is used to selectively bias a central portion of the grating to reduce current draw, but in hindsight, as explained

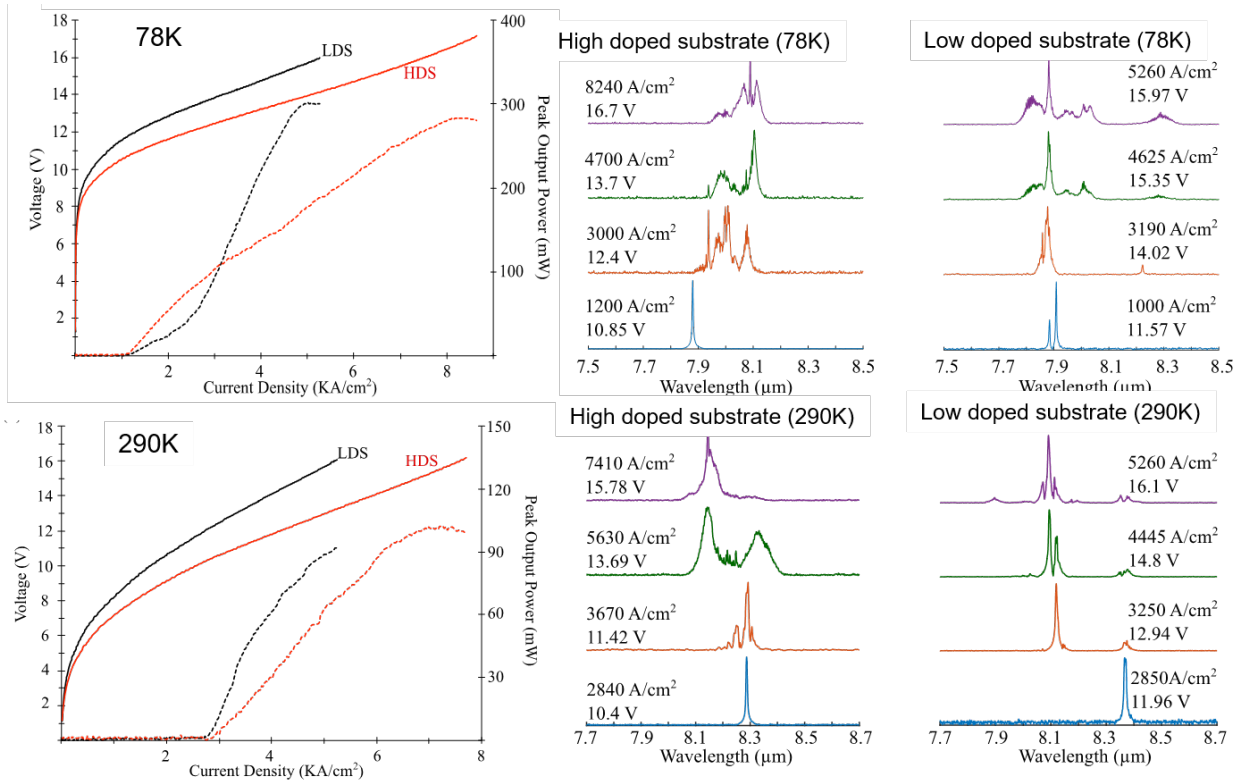

Figure 6.6: Power-current-voltage (P-I-V) data and emission spectra collected from ridge waveguides fabricated from the wafers made by IQE. Two types of wafers were tested, both using the 8 μm active region design in Reference [24], but one grown on a highly doped substrate (1-4$\times10^{17}$ cm^{-3}), and one on a lower doped substrate (2-5$\times10^{16}$ cm^{-3}). Both wafers were grown in the same chamber at the same time and so should otherwise be equal. Measurements were performed at both 78 K and room temperature. At 78 K, the threshold current densities are lower, and the center of the lasing spectrum is red-shifted from ~8.2 μm to ~8.0 μm. These results are courtesy of Sudeep Khanal, who fabricated and tested these devices.

above in Section 6.2.3, such an scheme is not affective as the insulating material prevents the formation of a waveguide-plasmon polariton. Instead, a facet should be wet etched around the circular grating area, and a metal contact should be deposited on top, leaving the sidewalls uncoated so that the grating is terminated by a dielectric interface, not a metallic one. At the time of designing these devices, the full-cavity VECSEL simulation had not been developed, so the devices were made very large out of fear that the coupling coefficient may not be strong enough for smaller devices. With the more recent simulation

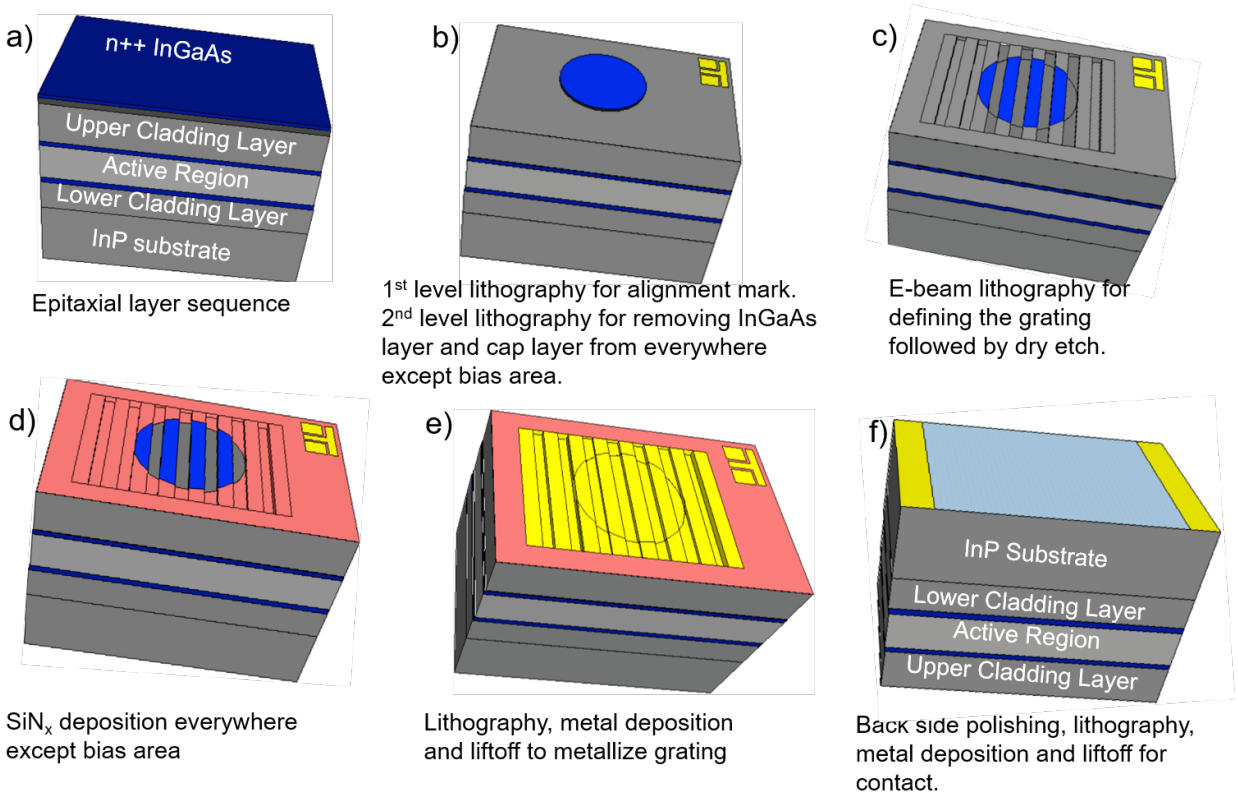

Figure 6.7: Fabrication process for mid-IR 2^{nd}-order grating based QC-VECSEL. The grating is not drawn to scale, but is actually much finer (hundreds of periods long). Figure courtesy of Sudeep Khanal.

results in Section 6.2.3, it seems such large areas are not needed, and in the future, the author recommends designing small area devices between 300-500 μm in diameter, with the entire device biased and terminated by either a dielectric or PEC boundary. This is beneficial for many reasons: it reduces the power draw from the structure, increases the density of fabricated devices (using the QC-material more effeciently), and removes the need to try and match the solution in the biased portion of the grating to the solution in the nitride coated portion. Despite the various design flaws, experimental testing of these initial devices has provided worthwhile information.

The fabricated devices (photographed in Figure 6.9) were mounted epi-side down to copper carriers using indium solder foil, and apertures were left in the back contact to allow

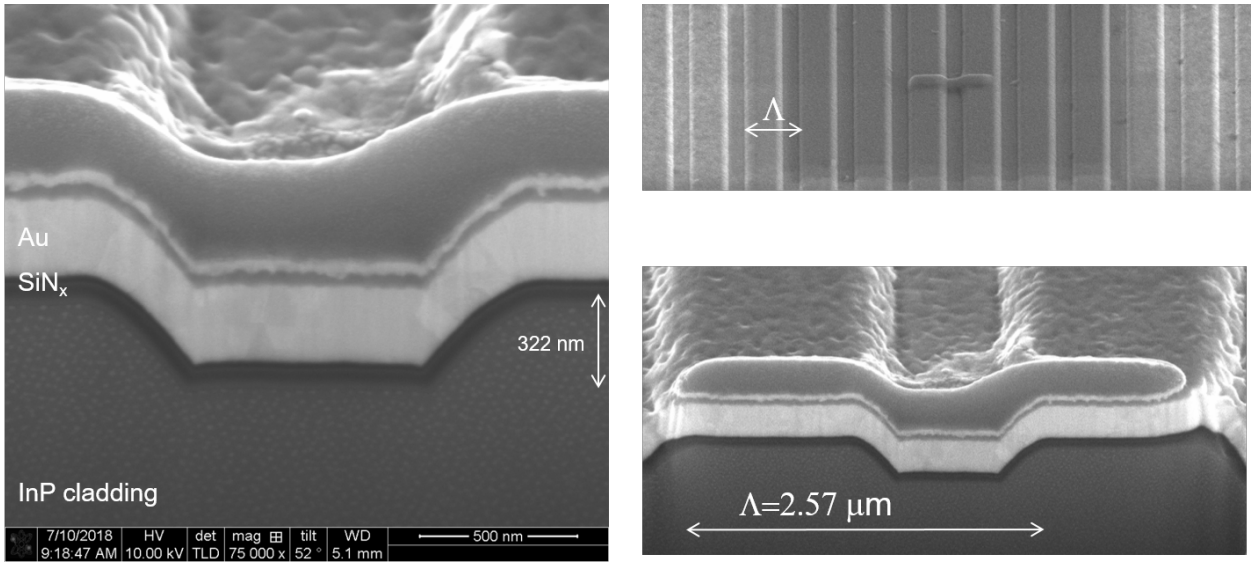

Figure 6.8: SEMs of the fabricated grating designed to operate at 8 μm. The period of the grating is 2.57 μm. The intended width of the grating tooth (at the top) was 1.14 μm, but the fabricated width was ∼1.27 μm. The intended etch depth was 380 nm, but actual was ∼320 nm. Cross-sectional cuts were taken by cutting into the grating with a focused-ion-beam etcher (ruining the sample locally).

emission of the substrate-coupled light. Measured IV-curves for grating surfaces with a 400 μm bias diameter and a 750 μm bias diameter are plotted in Figure 6.10. The current density cannot be defined directly defined as no ridge has been etched, so the injected current can spread to the unbiased area, making it difficult to define a pump area. In Figure 6.11, we assume there is no current spreading and the pump area is simply the bias area, and compare the resulting current density from the 750 μm grating surface to that measured from a ridge waveguide device (where there is no current spreading). After including the effect of a small series resistor and offset voltage (factors that become significant due to the large current draw from the device, see discussion in Chapter 3), the$I$-Vs match quite well, suggesting that the current spreading is minimal. However, again, no VECSEL lasing was ever observed.

Currently, the assumed reason that the mid-IR QC-VECSEL is not working is because there is too much substrate loss. The request made by the authors was for the QC-active

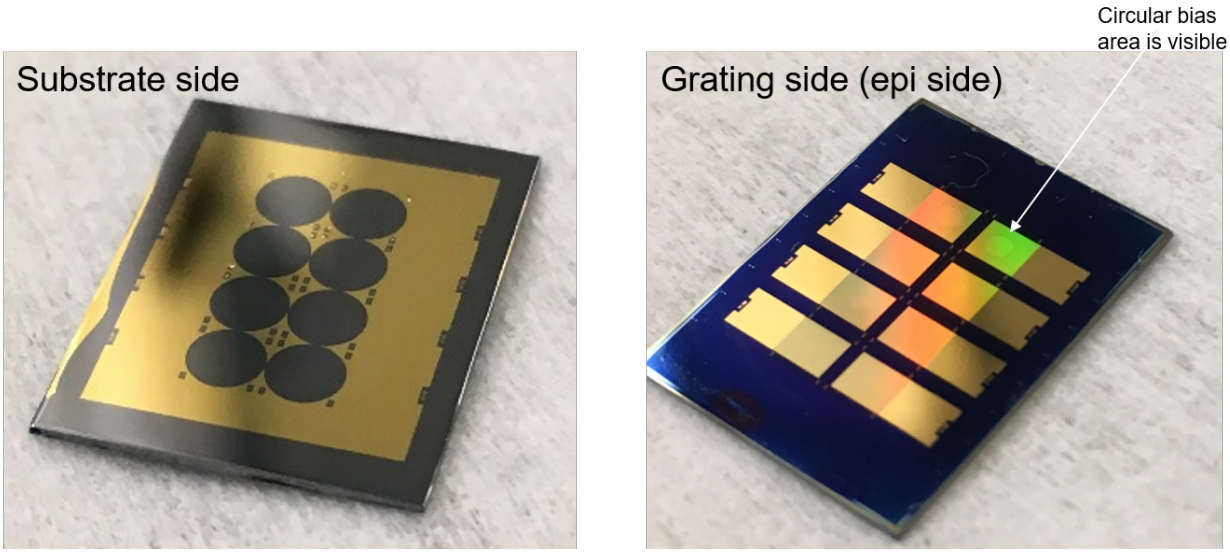

Figure 6.9: Photographs of fabricated devices. Sample contains 8 individual devices - 4 designed to operate at 8.2 μm, and 4 designed to operate at 7.9 μm. Every device has a 2×2 mm^2 grating, but each set consists of 4 different bias areas - 400 μm, 550 μm, 750 μm, and 1000 μm. The apertures on the backside are all circular with a 2.5 mm diameter.

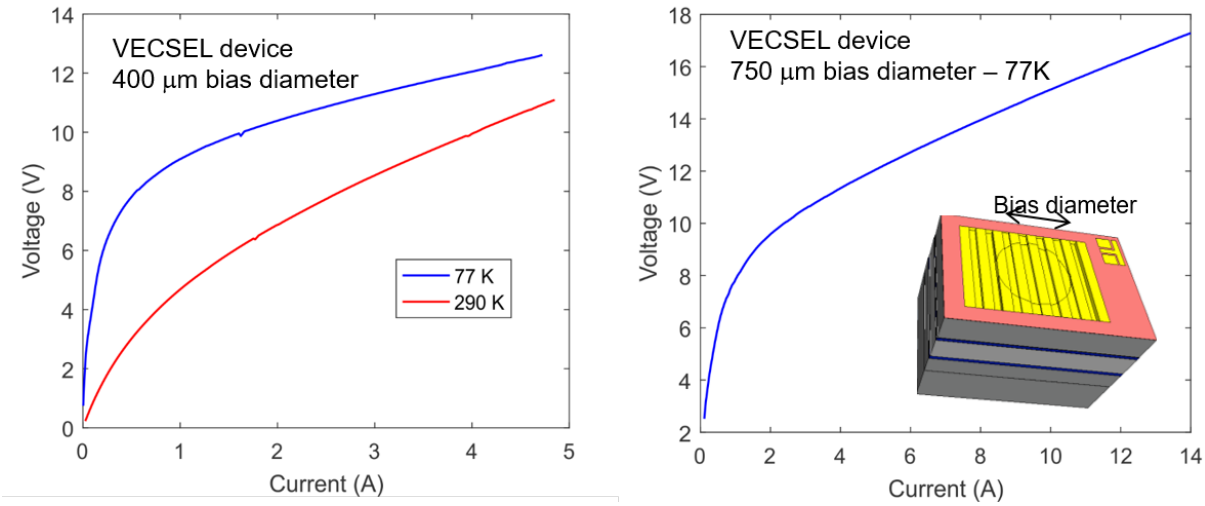

Figure 6.10: (a) Measured current-voltage (I-V) data from a 400 μm bias diameter grating surface at 77 K and room temperature. (b) I-V for a 750 μm diameter device at 77 K. Lasing was not observed from either device.

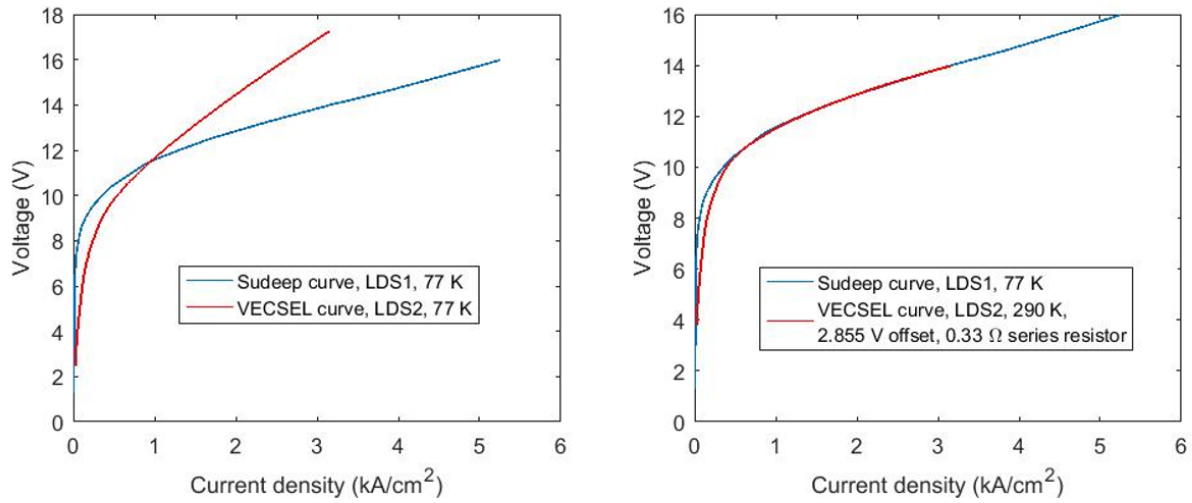

Figure 6.11: (a) Comparison between the I-V raw data collected from the 750 μm diameter grating surface and a ridge waveguide. (b) Comparison after correcting for the grating surface data for an assumed series resistance and offset voltage, an issue that is more apparent with the VECSEL surface due to its very large current draw compared to the ridge device. The corrected curve shows the expected result, that there is noteworthy current spreading at low bias, where the QC-material is less conductive, but the spreading is reduced and almost not noticeable at higher bias.

material to be grown on two different InP substrates, one doped at 2-5$\times10^{16}$ cm^{-3} (a rather low doping density), and one doped at 1-4$\times10^{17}$ cm^{-3} (more standard). Based on the Drude model and the mobility taken from [173], the predicted single-pass loss for an 8μm wave propagating through an InP substrated doped at 5$\times10^{16}$ cm^{-3} is $\sim$8.5% at room temperature (scattering time of 160 fs, α=2.5 cm^{-1}). However, measurement of the absorption using an FTIR spectrometer (Figure 6.12) shows single pass losses of $\sim$75% (α=40 cm^{-1}), much larger than expected and more than likely to prevent VECSEL lasing as the threshold gain would be very high to overcome these losses. The predicted Drude losses can be increased to 40 cm^{-1} if the doping is assumed to be 5$\times10^{17}$ cm^{-3}. The reason for this large discrepancy is unknown, but based on previous measurements the mid-IR properties of sulfur doped InP (not many are available), the properties can be very sensitive to the exact doping and wavelength and are not particularly well matched by the Drude model [174]. The measurement result in Figure 6.12 seems to agree with this conclusion as the trend shows an increase in free carrier

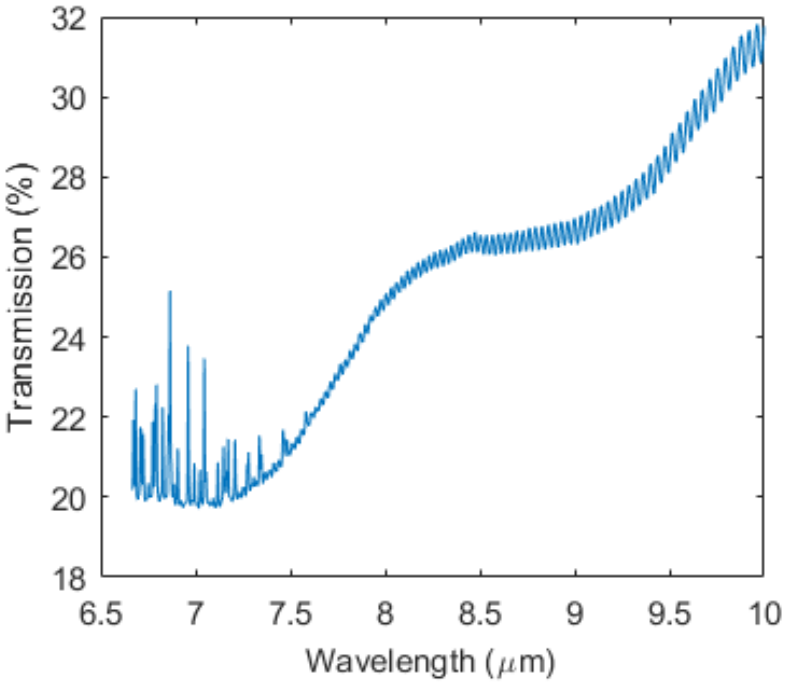

Figure 6.12: Transmission through a 350 μm thick InP substrate (sulfur doped at 2-5$\times 10^{16}$ cm^{-3}) with the IR QC-gain material grown on the surface. The absorption should be largely dominated by the first pass through the wafer given that the Fabry-Perot fringing is quite small. The backside of the substrate is not polished, so some of the losses could be associated from scattering off this rough surface.

losses with decreasing wavelength, which is opposite of the expected trend from the Drude model. It is plausible that either the doping density is a bit higher than reported, or the optical losses are simply higher than predicted by the Drude model (possibly due to the contribution of ionized impurities). It should also be noted that the backside of the sample was not polished, so some of the losses could be associated from scattering off this rough surface. Scattering from a rough surface would agree with the measured trend of reduced transmission at shorter wavelengths, so to be more conclusive, the measurement should be performed on a sample that is polished on both sides.

Assuming the losses in the substrate cannot be reduced, the only solution appears to be thinning the substrate as much as possible. There are two issues with doing this:

1. The sample must be bonded to a carrier wafer to provide structural support once the sample is thinned. This could be accomplished by simply soldering the sample to a carrier piece, but in such a process, the grating metal will react with the solder to produce a new alloy that would likely have reduced mid-IR properties, increasing the losses experienced by the VECSEL as the mid-IR modes interact strongly with the grating. Alternatively, the sample can be directly bonded to another metal-coated carrier using thermo-compressive bonding, same as is done with THz QCL metal-metal waveguides. However, the this bonding would occur after defining the grating and selective biasing (either with oxide, or etching a facet), resulting in a non-flat surface that may lead to a poor bond. Perhaps the best solution is to electroplate the top grating contact with several microns of copper, and then polish the copper to a smooth surface before thermo-compressive bonding. This is a standard technique in semiconductor processing.

2. As the substrate gets thinner, the current has to be extracted more laterally (since there is no back contact directly beneath the biased portion of the grating), leading to non-uniform bias across the active region. This effect can be studied using electrostatic FEM simulations. In Figure 6.13, a number of sample curves demonstrate the simulated voltage profile across the biased area as a function of the substrate thickness and the size of the aperture in the back contact. To perform the simulation, the conductivity of the active region was determined from the measured I-V of a ridge waveguide device, while the other conductivies were taken from [47], and the in-plane conductivity of the active region is taken from [48] (though this is really not a well known value). As long as the variation in the voltage across the active region are comparable to the dynamic range of the QC-gain ($\sim$5 V for the available growth), then the surface should still provide considerable amplification and enable VECSEL lasing, but the P-I-V dynamics may be more complicated than a ridge waveguide. For example, the ridge waveguides measured in Figure 6.6 shows lasing from $\sim$10-16 V. Therefore, based on the color plot in Figure 6.13, VECSEL lasing should be possible as long as the device

is not operating in the bottom left corner of the figure (substrate thickness below ∼50 μm with apertures of <1000 μm).

From the color plot, it would appear that the situation is actually improved by making the aperture larger when the substrate is very thin. However, while the uniformity of the bias is increased, as we can see from the plots in Figure 6.13, the voltage across the active region is very low (∼5 V) compared to the applied voltage (16 V) because almost all of the voltage drop occurs across the substrate, which is acting like a large series resistor. One could consider operating in this regime, but very high voltage pulses would be required. Going to the other extreme, the uniformity of the bias can also be improved with thin substrates by making the aperture very small, but goes against the purpose of making a large area emitter. Increasing the doping of the substrate increases the optical losses, but also improves lateral current removal.

The optimal design depends on whether optical losses or conductivity scale faster. It is possible that the losses in the substrate are not associated with inaccurate carrier density, but a high number of defects or impurities, in which case it would be more beneficial to increase the doping of the substrate and reduce the thickness as much as possible. Perhaps adding a thin (hundreds of nanometers), highly doped layer below the lower cladding could help enable lateral current extraction without adding too much loss. Another possibility is to deposit a subwavelength array of metal stripes on the backside of the substrate. If these stripes are orthogonal to grating teeth, then they can act as a polarizer that transmits the surface coupled radiation from the 2^{nd}-order grating, while introducing an electrically conductive route for the current to be extracted. One would have to consider the losses associated with this polarizing contact as well as the effects of misalignment between the polarizer and the emitting radiation.

6.3.1 Conclusions

The design concept for a mid-IR QC-VECSEL has been developed, and the practical considerations for fabricating a working device have been discussed. Devices have been fabricated, but VECSEL lasing has yet to be observed, presumably due to high material losses in the substrate of the QCL. For future attempts, the devices should be wafer bonded to a carrier piece, and the majority of the substrate should be removed by mechanical polishing.

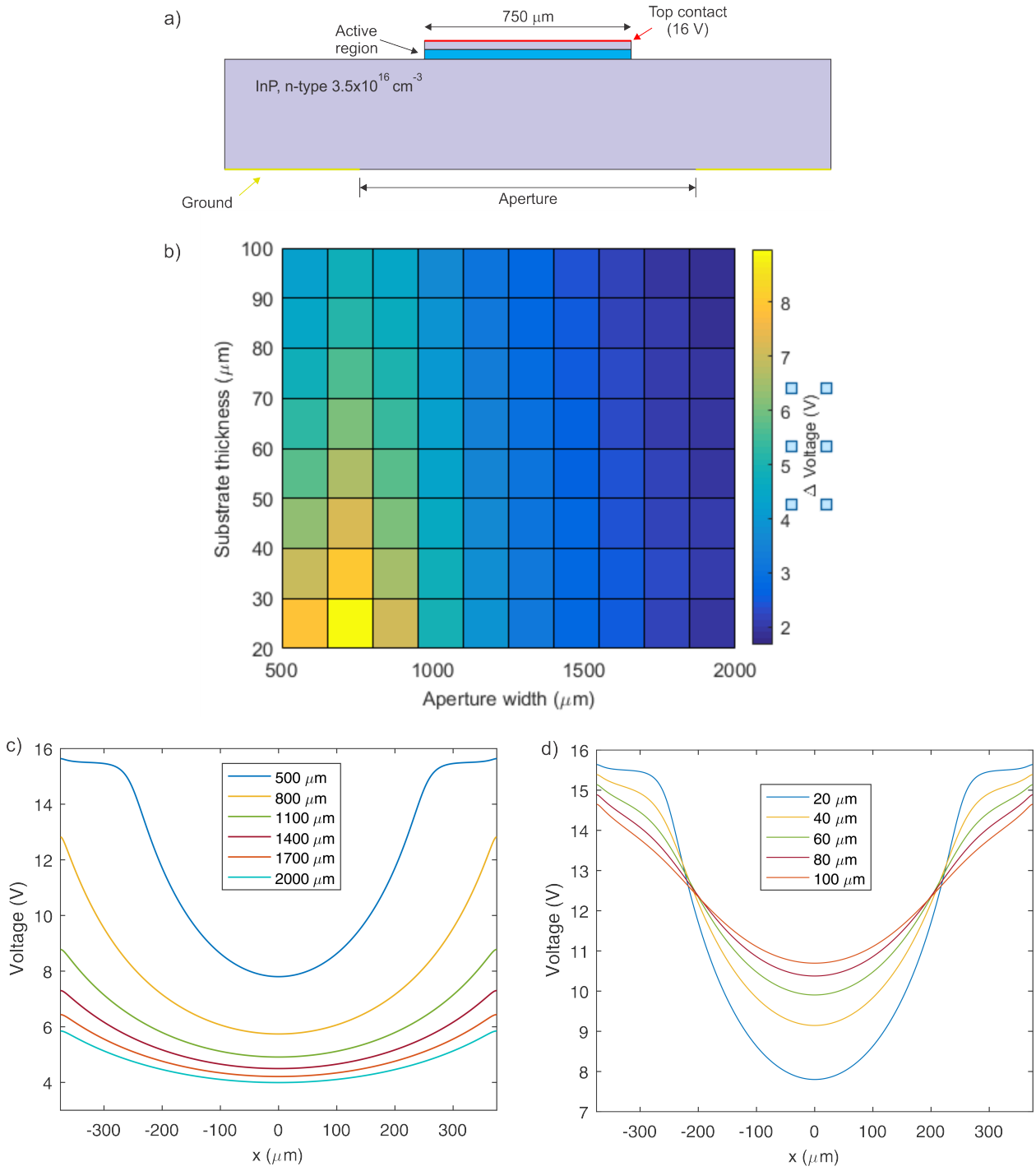

Figure 6.13: (a) Illustration of electrostatic simulation of the mid-IR QC-VECSEL structure. A portion of the QC-gain material is biased at the top (at 16 V), and the ground contacts are off to the sides, leaving an aperture for the light to emit. The bias diameter is kept at 750 μm, and the substrate doping is 3.5×10^{16} cm^{-3}. (b) Voltage difference between the edge and the center of the biased region as a function of two parameters - substrate thickness and aperture size. (c) Sample curves plotting the voltage distribution across the bias area under various conditions.

CHAPTER 7

Conclusions

7.1 Key experimental results

In this thesis, we have built upon our understand of the THz QC-VECSEL, whose first results are described in detail in Ref. [17]. Important experimental results that have been described in this thesis include:

- Demonstration of the power scaling capabilities of the QC-VECSEL by using wider ridges resonant on the TM_{03} cutoff mode. In this manner, the fill factor is increased by a factor of ≈3, and the output power of a VECSEL operating at 3.38 THz was scaled to 1.35 W in pulsed mode at 4 K with a wall plug efficiency of almost 2%, and 800 mW at 77 K with a wall plug efficiency of 1.15%. Self lasing was observed because wider ridges have lower losses for the fundamental TM_{00} mode compared to the original TM_{01} metasurface. Future work with higher-order designs should give careful consideration to increasing the losses to the fundamental mode. This could be accomplished by simply using a larger metasurface compared to the bias diameter, or by designing a more absorbing termination.

- Demonstration of >20% fractional, single-mode, continuous wave tuning centered around 3.5 THz by tuning the length of the external cavity with a piezoelectric stepping stage. This large single-mode tuning range was achieved by operating at extremely short cavity lengths so that the free spectral range is large, pushing other modes outside of the gain bandwidth of the metasurface. The VECSEL was operated on the m=2 longitudinal mode of the external cavity, which is only a wavelength long. Good, circular beam

patterns were observed throughout with a divergence angle of ∼15°, and continuous wave (CW) power levels of up to 20 mW were demonstrated at 77 K, which at the time of writing this is the most CW power from a THz QCL operating at 77 K to date. It should be noted that this high-temperature power result is mostly thanks to the high-performing QC-material, which ultimately limits the performance. The large tunability (which is also a record for THz QCLs at the time of writing this) and good beam patterns, however, are a testament to the capabilities of the VECSEL.

- Demonstration of a QC-VECSEL using a sparse array of patch elements intended to reduce the electrical power draw of the metasurface without reducing the area. Preliminary results showed limited success with a reduction in current draw of ∼20% compared to a typical ridge-based metasurface as significant leakage is observed into the connective ridges biasing the patches. In future work, studies, the connective elements can be made thinner to reduce leakage currents, and the patches can be made shorter and the unit cell larger to reduce the fill factor even further.

7.2 Design and development of mid-IR QC-VECSEL

The design concept for the THz metasurface cannot be directly extended to the mid-IR due to excessive material losses associated with metals. An alternative design for a mid-IR QC-VECSEL has been presented using a diffraction grating to couple the QC-gain to the surface direction ($\Lambda=\lambda_{guided}$, where Λ is the period of the grating, and λ_{guided} is the guided wavelength of the light. The key design objective is to maintain high material losses for any non-radiating modes, and high radiative losses for the surface-coupled mode. This way, none of the modes can lase on their own, but the surface-coupled mode can lase if feedback is provided by an external mirror - i.e. building a VECSEL. This approach is much more narrow band than the metasurface approach used in the THz, so broadband tuning is not possible. Further, because the grating approach is based on coupling between propagating waves, the size of the amplifying surface must be much larger (relative to the operating

wavelength) to prevent excessive diffraction losses. The strength of the suggested design should be obtaining very high peak-pulse powers into very high-quality beams. Progress in experimental demonstration has been reviewed, but lasing has not yet been observed. Suggestions have been made for continued efforts.

7.3 Towards QC-VECSEL local-oscillators for remote sensing

Development of the QC-VECSEL is still in its infancy, and there is still much work to be done. On the immediate horizon, the :

- Demonstrating THz QC-VECSELs at 2.7 THz and 4.7 THz, which are relevant spectral lines for remote sensing applications. To date, almost all experiments with the QC-VECSEL have been performed with a single high-performing active region (wafer VB0739), with the exception of the original demonstration with another wafer (resonant-phonon design FL178C-M7, wafer NG-E14315, grown at Northrop Grumman). Despite the QC-VECSEL's advantages, it generally comes at the cost of higher threshold gain values, so it remains to be seen if most QC-material will work in a VECSEL configuration, or only the most high-performing.

- Perform high-resolution spectral measurements to determine the linewidth of the QC-VECSEL and demonstrate frequency- and phase-locking. In theory, the VECSEL should be less susceptible to thermal and electrical fluctuations in the QC-material, which is the primary limiting factor on the linewidth of typical semiconductor lasers based on ridge waveguides. In the QC-VECSEL, such fluctuations in the material parameters would manifest themselves as fluctuations in the reflection phase of the metasurface, which lead to the fluctuations in the external cavity resonance and output frequency. However, because the metasurface is extremely broadband, and the THz energy spends very little time in the metasurface per-round-trip, small changes in the QC-material have a trivial effect on the reflection phase of the metasurface. This is the same argument made in Chapter 5 for why the QC-material dispersion has little

effect on the group-delay dispersion (GDD) of the metasurface - it is as if only a very small portion of the cavity length is filled gain material, so modulation of the refractive index of the gain material has a much smaller effect on the round-trip phase change than iff the whole length of the cavity was filled with it. For example, the change in refractive index with temperature for GaAs can be estimated around $\sim 2.22 \times 10^{-4}$/K [175]. Plugging this into our FEM simulations of the broadband metasurface in Section 4.4, the simulated change in metasurface reflection phase is $\sim 3.5 \times 10^{-4}$radians/K. If the external cavity of the VECSEL is 1 cm long and operating at 4.7 THz, then the frequency tuning would be ~1.7 MHz/K, compared to ridge waveguides that are typically on the order of 100 MHz/K [176–178]. Even if the cavity is only 1 mm long, that gives a tuning of 10.7 MHz/K, which is still an order of magnitude improved. Therefore, the QC-VECSEL has the potential to be much more stable than ridge based devices, perhaps allowing for high-resolution spectroscopy without the need for a reference source and feedback loop.

- Further testing of low fill-factor patch based metasurface in combination with a focusing phase design (which supports smaller bias diameters) for optimization of devices for low power-consumption, high-temperature continuous wave operation.

CHAPTER 8

Appendix

8.1 Appendix A - Fabrication process

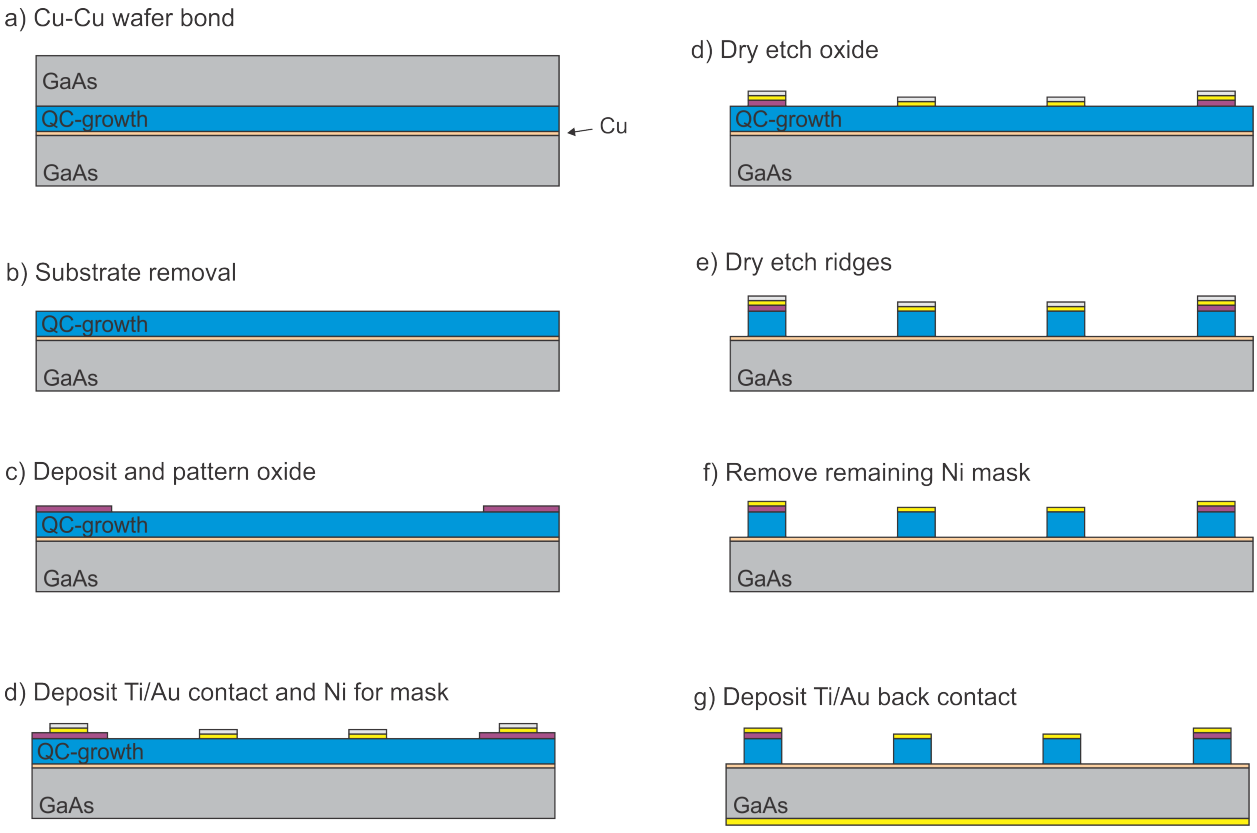

Figure 8.1: Metal-metal waveguide QCL fabrication procedure including oxide layer for selective biasing.

The fabrication process for THz QC-VECSELs is illustrated in Figure 8.1; it follows the standard procedure developed in Reference [50] with some minor modifications. The detailed

steps are:

1. Deposit Ta/Cu at thicknesses 10/300 nm on the QC-wafer piece and recieving GaAs piece (do a BOE dip first).

2. Wafer bond the two samples at 350 °C for 90 minutes.

3. Deposit oxide on the backside to protect it during subsequent wet etch.

4. Mechanically polish the substrate of the QC-wafer substrate down to ∼50 μm, and wet etch the remaining substrate away with H_2O_2:NH_4OH at a ratio of 5:1. Typically etches around 5 μm/min. Stops on AlAs etch stop layer.

5. Remove etch stop layer with brief HF dip (∼10 seconds).

6. Remove highly doped top contact to prevent current spreading into insulated areas, H_2O_2:NH_4OH:H_2O at a ratio of 3:5:490 for 1-2 minutes. Use Dektak to measure amount of material removed.

7. Deposit *sim*200 nm of PECVD oxide and pattern with positive lithography, hard bake at 150 °C for 2 minutes, and wet etch with BOE. Wet etch rates from PECVD oxide are inconsistent, have to calibrate each time.

8. Deposit top contact and self-aligned mask using negative resist (nLOF 2020) and liftoff: Ti/Au/Ni at thicknesses 15/250/200 nm.

9. Dry etch (RIE ICP) ridges using recipe 'atgaas' on the nanolab chlorine etcher. Recipe is primarily BCl_3 with a small fraction of Cl_2 added.

10. Remove remaining Ni mask using wet etchant from Transene (TFB, room temperature).

11. Deposit Ti/Au back contact at thickness 15/200 nm.

8.2 Appendix B - Extended *L-I-V* data from tuning experiments

Figure 8.2 shows a collection of pulsed and continuous wave *L-I-V* measured from the 41.7 μm period single-ridge metasurface tuning data presented in Figure 4.9.

8.3 Appendix C - Antireflection HR-Si window

Figure 8.3 shows the transmittance of the parylene anti-reflection coated high-resistivity Si window used on the cryostat for the data presented in this thesis. The data was collected with an FTIR at a resolution of 0.5 cm^{-1} and a cyogenically cooled Ga doped Ge-detector. The window is 3.3 mm thick, so any potentially remaining fringing cannot be resolved. This may be part of the reason why the data apprears somewhat noisy.

8.4 Appendix D - Mid-IR metasurface based on dielectric resonant antennas

In Chapter 6, the design of a mid-IR QC-VECSEL based on a 2^{nd}-order diffraction grating was discussed. An alterative design strategy is to more closely mimic the THz metasurface design, based on a subwavelength array of locally resonant elements. This approach can offer several advantages over the grating approach, such as broader bandwidth, and ability to locally control the phase and frequency response. As mentioned in Chapter 6, this does not appear to work well because the TM_{01} resonance of a narrow dielectric waveguides does not confine the mode strongly to the vertical field component (normal to the QC-growth), leading to very weak amplification. Such a high aspect ratio structure is also a problem because there are many higher-order resonances that can interact with the target solution. A sample design and simulation results are shown in Figure 8.4, where the structure, electric fields, and reflectance data are plotted. The amplification is observed to be very weak compared to the grating based design, and the shape of the spectral response is complicated by the existence of other solutions. Such a structure would also be practically challenging

in terms of fabrication because the dielectric waveguide (including cladding layers) is much thicker than the wavelength, the subwavelength resonant elements would require rather deep, high aspect ratio etching of InP and InGaAs/InAlAs materials.

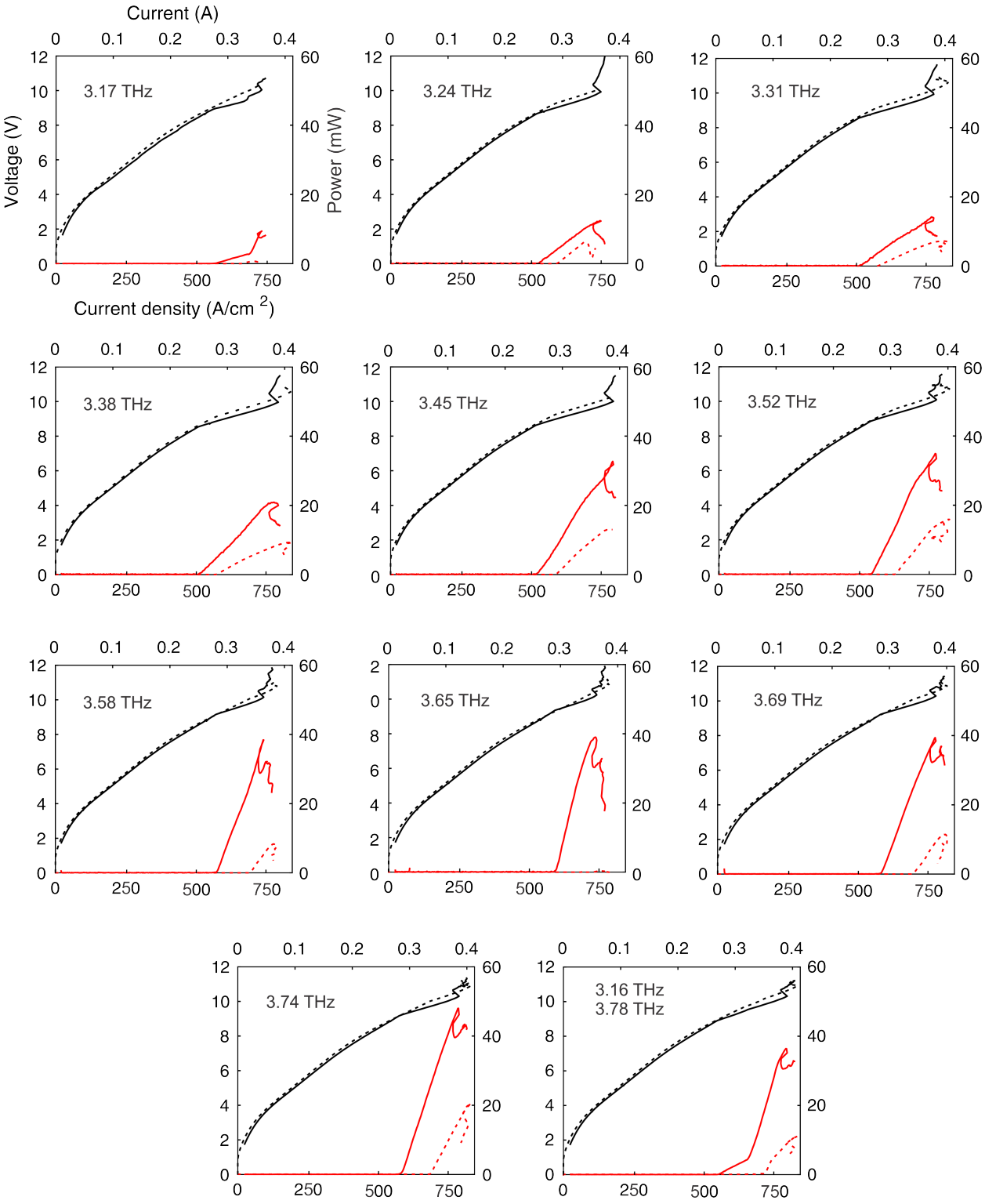

Figure 8.2: Collection of pulsed and continuous wave LIVs corresponding to the data in Figures 4.8 and 4.9. Pulsed data is in solid lines, continuous wave data in dashed lines.

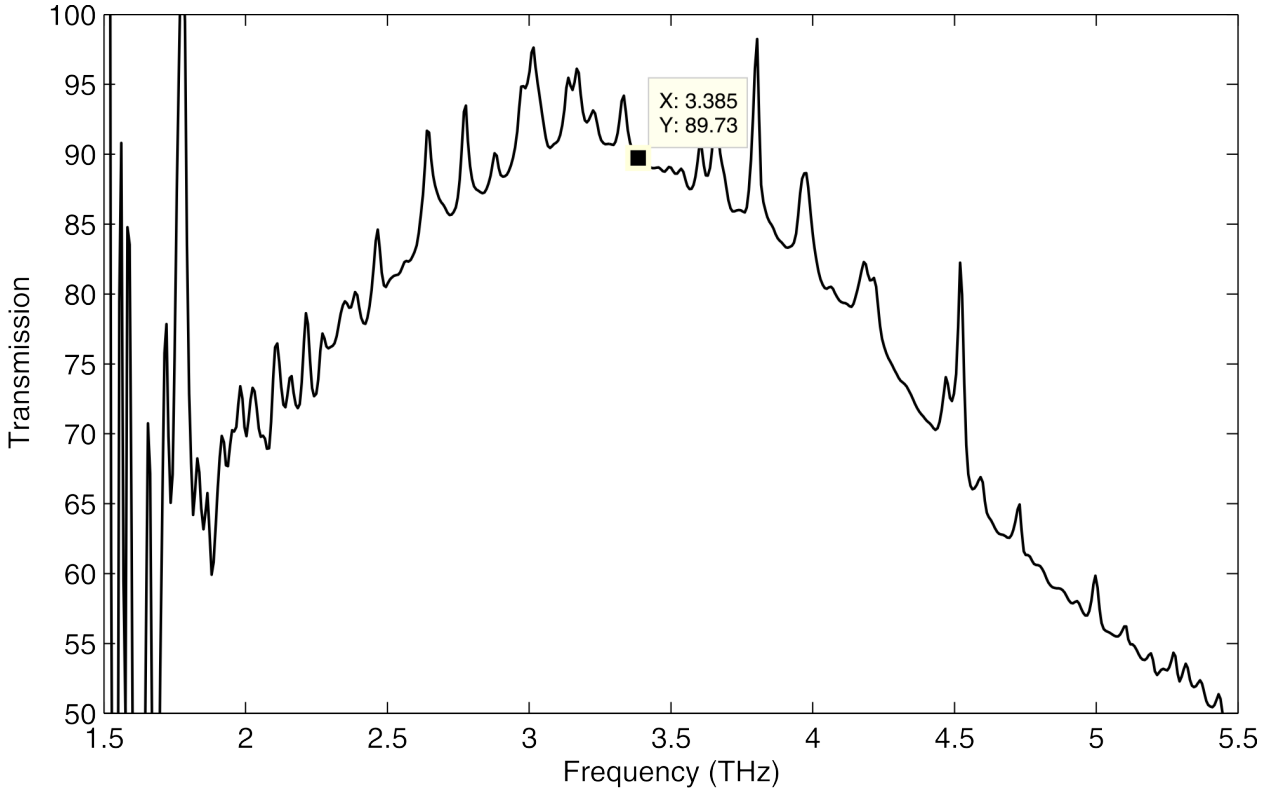

Figure 8.3: FTIR measured transmission of 3.3 mm HR-Si window with antireflection parylene coatings on both sides targeted at 3.4 THz.

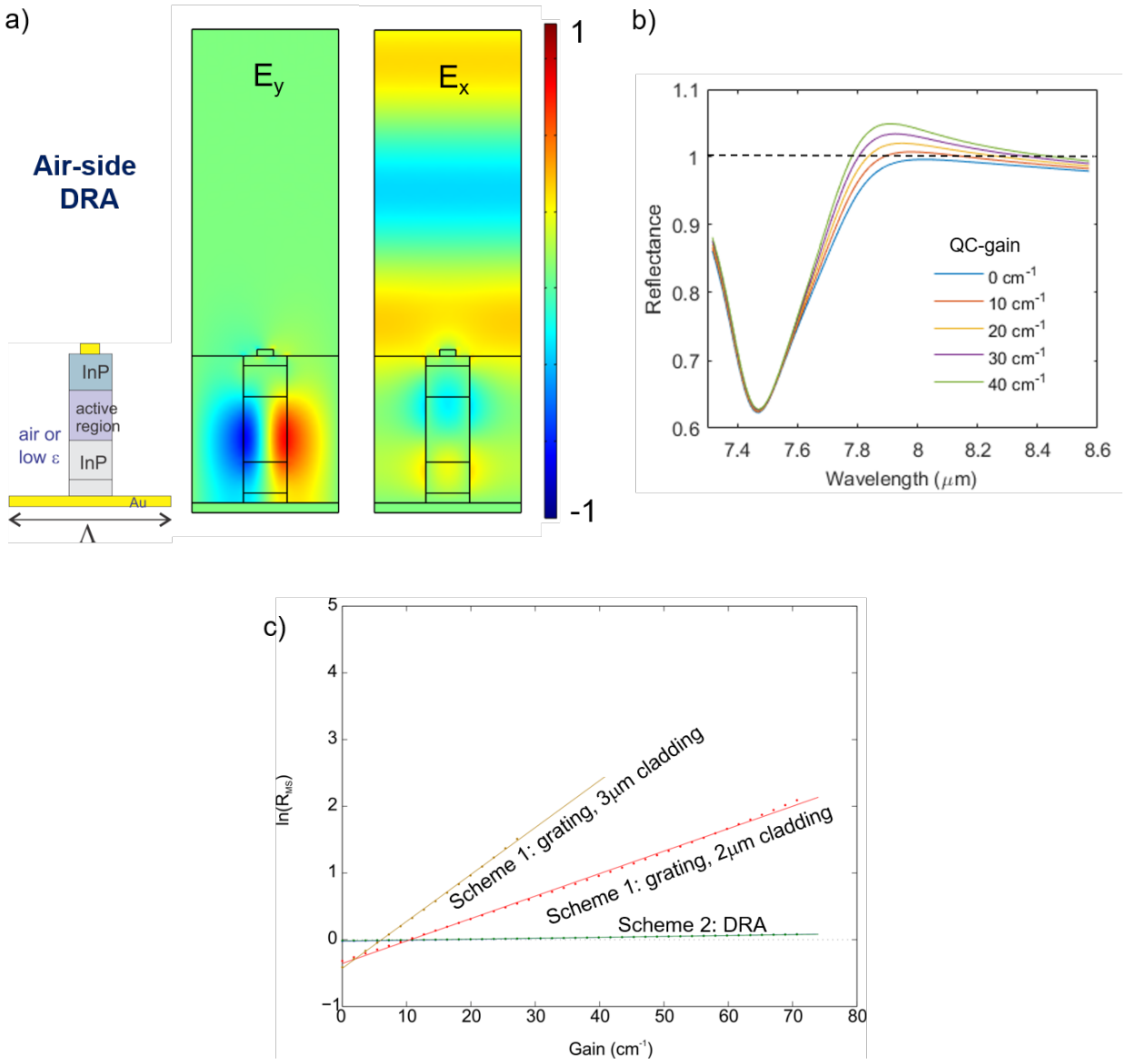

Figure 8.4: (a) Single period of DRA-based mid-IR metasurface design and resulting fields for the target radiating solution. The asymmetric field profile in the verticle direction is associated with gain and surface coupling, similar to the THz design. (b) Reflectance spectrum as a function of gain for the infinite structure. The reflectance is very weak as a result of the weak confinement of the mode to the gain. (c) Comparison of the reflectance from a DRA design and a 2^{nd}-order grating design.

Bibliography

[1] B. S. Williams. *Terahertz quantum cascade lasers*. Thesis, 2003.

[2] S. Kumar. *Development of Terahertz Quantum-Cascade Lasers*. Thesis, 2007.

[3] M. S. Vitiello, G. Scalari, B. Williams, and P. De Natale. Quantum cascade lasers: 20 years of challenges. *Optics Express*, 23(4):5167–5182, 2015.

[4] H. Page, C. Sirtori, S. Barbier, P. Kruck, M. Stellmacher, and J. Nagle. Design and operation of mid-infrared light-emitting devices (lambda approximate to 11 mu m) based on a chirped superlattice. *Semiconductor Science and Technology*, 15(1):44–50, 2000.

[5] R. Kohler, A. Tredicucci, F. Beltram, H. E. Beere, E. H. Linfield, A. G. Davies, D. A. Ritchie, R. C. Iotti, and F. Rossi. Terahertz semiconductor-heterostructure laser. *Nature*, 417(6885):156–159, 2002.

[6] B. S. Williams, H. Callebaut, S. Kumar, Q. Hu, and J. L. Reno. 3.4-thz quantum cascade laser based on longitudinal-optical-phonon scattering for depopulation. *Applied Physics Letters*, 82(7):1015–1017, 2003.

[7] M. I. Amanti, G. Scalari, R. Terazzi, M. Fischer, M. Beck, J. Faist, A. Rudra, P. Gallo, and E. Kapon. Bound-to-continuum terahertz quantum cascade laser with a single-quantum-well phonon extraction/injection stage. *New Journal of Physics*, 11, 2009.

[8] L. Bosco, M. Franckie, G. Scalari, M. Beck, A. Wacker, and J. Faist. Thermoelectrically cooled thz quantum cascade laser operating up to 210k. *Applied Physics Letters*, 115(1), 2019.

[9] A. Khalatpour, J. L. Reno, and Q. Hu. Phase-locked photonic wire lasers by pi coupling. *Nature Photonics*, 13(1):47–+, 2019.

[10] C. Z. Wu, S. Khanal, J. L. Reno, and S. Kumar. Terahertz plasmonic laser radiating in an ultra-narrow beam. *Optica*, 3(7):734–740, 2016.

[11] Y. Jin, L. Gao, J. Chen, C. Z. Wu, J. L. Reno, and S. Kumar. High power surface emitting terahertz laser with hybrid second- and fourth-order bragg gratings (vol 9, 1407, 2018). *Nature Communications*, 9, 2018.

[12] L. Bosco, C. Bonzon, K. Ohtani, M. Justen, M. Beck, and J. Faist. A patch-array antenna single-mode low electrical dissipation continuous wave terahertz quantum cascade laser. *Applied Physics Letters*, 109(20), 2016.

[13] C. Risacher, R. Gusten, J. Stutzki, H. W. Hubers, R. Aladro, A. Bell, C. Buchbender, D. Buchel, T. Csengeri, C. Duran, U. U. Graf, R. D. Higgins, C. E. Honingh, K. Jacobs, M. Justen, B. Klein, M. Mertens, Y. Okada, A. Parikka, P. Putz, N. Reyes, H. Richter,

O. Ricken, D. Riquelme, N. Rothbart, N. Schneider, R. Simon, M. Wienold, H. Wiesemeyer, M. Ziebart, P. Fusco, S. Rosner, and B. Wohler. The upgreat dual frequency heterodyne arrays for sofia. *Journal of Astronomical Instrumentation*, 7(4), 2018.

[14] A. G. Fox and T. Li. Resonant modes in a maser interferometer. *Bell System Technical Journal*, 40(2):453–+, 1961.

[15] L. Y. Xu, D. G. Chen, T. Itoh, J. L. Reno, and B. S. Williams. Focusing metasurface quantum-cascade laser with a near diffraction-limited beam. *Optics Express*, 24(21):24117–24128, 2016.

[16] L. Y. Xu, C. A. Curwen, P. W. C. Hon, Q. S. Chen, T. Itoh, and B. S. Williams. Metasurface external cavity laser. *Applied Physics Letters*, 107(22), 2015.

[17] L. Y. Xu. Terahertz metasurface quantum-cascade laser. *Thesis - UCLA*, 2017.

[18] L. Y. Xu, C. A. Curwen, D. G. Chen, J. L. Reno, T. Itoh, and B. S. Williams. Terahertz metasurface quantum-cascade vecsels: theory and performance. *Ieee Journal of Selected Topics in Quantum Electronics*, 23(6), 2017.

[19] L. Y. Xu, C. A. Curwen, J. L. Reno, and B. S. Williams. High performance terahertz metasurface quantum-cascade vecsel with an intra-cryostat cavity. *Applied Physics Letters*, 111(10), 2017.

[20] L. Y. Xu, D. G. Chen, T. Itoh, J. L. Reno, and B. S. Williams. Focusing metasurface quantum-cascade laser with a near diffraction-limited beam. *Optics Express*, 24(21):24117–24128, 2016.

[21] D. G. Chen, L. Y. Xu, C. A. Curwen, M. Memarian, J. L. Reno, T. Itoh, and B. S. Williams. Metasurface terahertz laser with electronically-controlled polarization. *2017 Conference on Lasers and Electro-Optics (Cleo)*, 2017.

[22] RP-Photonics. External-cavity diode lasers.

[23] I. E. Gordon, L. S. Rothman, C. Hill, R. V. Kochanov, Y. Tan, P. F. Bernath, M. Birk, V. Boudon, A. Campargue, K. V. Chance, B. J. Drouin, J. M. Flaud, R. R. Gamache, J. T. Hodges, D. Jacquemart, V. I. Perevalov, A. Perrin, K. P. Shine, M. A. H. Smith, J. Tennyson, G. C. Toon, H. Tran, V. G. Tyuterev, A. Barbe, A. G. Csaszar, V. M. Devi, T. Furtenbacher, J. J. Harrison, J. M. Hartmann, A. Jolly, T. J. Johnson, T. Karman, I. Kleiner, A. A. Kyuberis, J. Loos, O. M. Lyulin, S. T. Massie, S. N. Mikhailenko, N. Moazzen-Ahmadi, H. S. P. Muller, O. V. Naumenko, A. V. Nikitin, O. L. Polyansky, M. Rey, M. Rotger, S. W. Sharpe, K. Sung, E. Starikova, S. A. Tashkun, J. Vander Auwera, G. Wagner, J. Wilzewski, P. Wcislo, S. Yu, and E. J. Zak. The hitran2016 molecular spectroscopic database. *Journal of Quantitative Spectroscopy and Radiative Transfer*, 203:3–69, 2017.

[24] Z. J. Liu, D. Wasserman, S. S. Howard, A. J. Hoffman, C. F. Gmachl, X. J. Wang, T. Tanbun-Ek, L. W. Cheng, and F. S. Choa. Room-temperature continuous-wave quantum cascade lasers grown by mocvd without lateral regrowth. *Ieee Photonics Technology Letters*, 18(9-12):1347–1349, 2006.

[25] P. H. Siegel. Terahertz technology. *Ieee Transactions on Microwave Theory and Techniques*, 50(3):910–928, 2002.

[26] M. Tonouchi. Cutting-edge terahertz technology. *Nature Photonics*, 1(2):97–105, 2007.

[27] M. Hangyo. Development and future prospects of terahertz technology. *Japanese Journal of Applied Physics*, 54(12), 2015.

[28] P. R. Smith, D. H. Auston, and M. C. Nuss. Subpicosecond photoconducting dipole antennas. *Ieee Journal of Quantum Electronics*, 24(2):255–260, 1988.

[29] D. Grischkowsky, S. Keiding, M. Vanexter, and C. Fattinger. Far-infrared time-domain spectroscopy with terahertz beams of dielectrics and semiconductors. *Journal of the Optical Society of America B-Optical Physics*, 7(10):2006–2015, 1990.

[30] R. Huber, A. Brodschelm, F. Tauser, and A. Leitenstorfer. Generation and field-resolved detection of femtosecond electromagnetic pulses tunable up to 41 thz. *Applied Physics Letters*, 76(22):3191–3193, 2000.

[31] A. Sell, A. Leitenstorfer, and R. Huber. Phase-locked generation and field-resolved detection of widely tunable terahertz pulses with amplitudes exceeding 100 mv/cm. *Optics Letters*, 33(23):2767–2769, 2008.

[32] T. L. Cocker, D. Peller, P. Yu, J. Repp, and R. Huber. Tracking the ultrafast motion of a single molecule by femtosecond orbital imaging. *Nature*, 539(7628):263–+, 2016.

[33] J. V. Siles, K. B. Cooper, C. Lee, R. H. Lin, G. Chattopadhyay, and I. Mehdi. A new generation of room-temperature frequency-multiplied sources with up to 10x higher output power in the 160-ghz-1.6-thz range. *Ieee Transactions on Terahertz Science and Technology*, 8(6):596–604, 2018.

[34] B. S. Williams. Terahertz quantum-cascade lasers. *Nature Photonics*, 1(9):517–525, 2007.

[35] X. M. Wang, C. L. Shen, T. Jiang, Z. Q. Zhan, Q. H. Deng, W. H. Li, W. D. Wu, N. Yang, W. D. Chu, and S. Q. Duan. High-power terahertz quantum cascade lasers with similar to 0.23 w in continuous wave mode. *Aip Advances*, 6(7), 2016.

[36] J. M. J. Madey. Stimulated emission of bremsstrahlung in a periodic magnetic field. *Journal of Applied Physics*, 42(5):1906–, 1971.

[37] C. Walther, M. Fischer, G. Scalari, R. Terazzi, N. Hoyler, and J. Faist. Quantum cascade lasers operating from 1.2 to 1.6 thz. *Applied Physics Letters*, 91(13), 2007.

[38] M. Wienold, B. Roben, X. Lu, G. Rozas, L. Schrottke, K. Biermann, and H. T. Grahn. Frequency dependence of the maximum operating temperature for quantum-cascade lasers up to 5.4 thz. *Applied Physics Letters*, 107(20), 2015.

[39] K. Ohtani, M. Beck, M. J. Suess, J. Faist, A. M. Andrews, T. Zederbauer, H. Detz, W. Schrenk, and G. Strasser. Far-infrared quantum cascade lasers operating in the alas phonon reststrahlen band. *Acs Photonics*, 3(12):2280–2284, 2016.

[40] O. Cathabard, R. Teissier, J. Devenson, J. C. Moreno, and A. N. Baranov. Quantum cascade lasers emitting near 2.6 mu m. *Applied Physics Letters*, 96(14), 2010.

[41] A. Wade, G. Fedorov, D. Smirnov, S. Kumar, B. S. Williams, Q. Hu, and J. L. Reno. Magnetic-field-assisted terahertz quantum cascade laser operating up to 225 k. *Nature Photonics*, 3(1):41–45, 2009.

[42] J. Faist, F. Capasso, D. L. Sivco, C. Sirtori, A. L. Hutchinson, and A. Y. Cho. Quantum cascade laser. *Science*, 264(5158):553–556, 1994.

[43] M. Beck, D. Hofstetter, T. Aellen, J. Faist, U. Oesterle, M. Ilegems, E. Gini, and H. Melchior. Continuous wave operation of a mid-infrared semiconductor laser at room temperature. *Science*, 295(5553):301–305, 2002.

[44] W. J. Zhou, D. H. Wu, Q. Y. Lu, S. Slivken, and M. Razeghi. Single-mode, high-power, mid- infrared, quantum cascade laser phased arrays. *Scientific Reports*, 8, 2018.

[45] S. Kumar, Q. Hu, and J. L. Reno. 186 k operation of terahertz quantum-cascade lasers based on a diagonal design. *Applied Physics Letters*, 94(13), 2009.

[46] S. Fathololoumi, E. Dupont, C. W. I. Chan, Z. R. Wasilewski, S. R. Laframboise, D. Ban, A. Matyas, C. Jirauschek, Q. Hu, and H. C. Liu. Terahertz quantum cascade lasers operating up to similar to 200 k with optimized oscillator strength and improved injection tunneling. *Optics Express*, 20(4):3866–3876, 2012.

[47] A. Albo, Y. V. Flores, Q. Hu, and J. L. Reno. Split-well direct-phonon terahertz quantum cascade lasers. *Applied Physics Letters*, 114(19), 2019.

[48] A. Albo, Y. V. Flores, Q. Hu, and J. L. Reno. Two-well terahertz quantum cascade lasers with suppressed carrier leakage. *Applied Physics Letters*, 111(11), 2017.

[49] A. Albo, Q. Hu, and J. L. Reno. Room temperature negative differential resistance in terahertz quantum cascade laser structures. *Applied Physics Letters*, 109(8), 2016.

[50] B. S. Williams, S. Kumar, H. Callebaut, Q. Hu, and J. L. Reno. Terahertz quantum-cascade laser at $\lambda \approx 100$ μm using metal waveguide for mode confinement. *Applied Physics Letters*, 83(11):2124–2126, 2003.

[51] E. E. Orlova, J. N. Hovenier, T. O. Klaassen, I. Kasalynas, A. J. L. Adam, J. R. Gao, and T. M. Klapwijk. Antenna model for wire lasers. *Physical Review Letters*, 96(17), 2006.

[52] P. W. C. Hon, A. A. Tavallaee, Q. S. Chen, B. S. Williams, and T. Itoh. Radiation model for terahertz transmission-line metamaterial quantum-cascade lasers. *Ieee Transactions on Terahertz Science and Technology*, 2(3):323–332, 2012.

[53] J. A. Fan, M. A. Belkin, F. Capasso, S. Khanna, M. Lachab, A. G. Davies, and E. H. Linfield. Surface emitting terahertz quantum cascade laser with a double-metal waveguide. *Optics Express*, 14(24):11672–11680, 2006.

[54] S. Kumar, B. S. Williams, Q. Qin, A. W. M. Lee, Q. Hu, and J. L. Reno. Surface-emitting distributed feedback terahertz quantum-cascade lasers in metal-metal waveguides. *Optics Express*, 15(1):113–128, 2007.

[55] T. Y. Kao, Q. Hu, and J. L. Reno. Phase-locked arrays of surface-emitting terahertz quantum-cascade lasers. *Applied Physics Letters*, 96(10), 2010.

[56] G. Y. Xu, R. Colombelli, S. P. Khanna, A. Belarouci, X. Letartre, L. H. Li, E. H. Linfield, A. G. Davies, H. E. Beere, and D. A. Ritchie. Efficient power extraction in surface-emitting semiconductor lasers using graded photonic heterostructures. *Nature Communications*, 3, 2012.

[57] Y. Chassagneux, R. Colombelli, W. Maineult, S. Barbieri, H. E. Beere, D. A. Ritchie, S. P. Khanna, E. H. Linfield, and A. G. Davies. Electrically pumped photonic-crystal terahertz lasers controlled by boundary conditions. *Nature*, 457(7226):174–178, 2009.

[58] Y. Chassagneux, R. Colombelli, W. Maineult, S. Barbieri, S. P. Khanna, E. H. Linfield, and A. G. Davies. Graded photonic crystal terahertz quantum cascade lasers. *Applied Physics Letters*, 96(3), 2010.

[59] Y. Halioua, G. Xu, S. Moumdji, L. H. Li, A. G. Davies, E. H. Linfield, and R. Colombelli. Thz quantum cascade lasers operating on the radiative modes of a 2d photonic crystal. *Optics Letters*, 39(13):3962–3965, 2014.

[60] M. I. Amanti, M. Fischer, G. Scalari, M. Beck, and J. Faist. Low-divergence single-mode terahertz quantum cascade laser. *Nature Photonics*, 3(10):586–590, 2009.

[61] T. Y. Kao, Q. Hu, and J. L. Reno. Perfectly phase-matched third-order distributed feedback terahertz quantum-cascade lasers. *Optics Letters*, 37(11):2070–2072, 2012.

[62] A. Khalatpour, J. L. Reno, N. P. Kherani, and Q. Hu. Unidirectional photonic wire laser. *Nature Photonics*, 11(9):555–+, 2017.

[63] M. Justen, C. Bonzon, K. Ohtani, M. Beck, U. Graf, and J. Faist. 2d patch antenna array on a double metal quantum cascade laser with ¿90thz. *Optics Letters*, 41(19):4590–4592, 2016.

[64] S. Biasco, K. Garrasi, F. Castellano, L. H. Li, H. E. Beere, D. A. Ritchie, E. H. Linfield, A. G. Davies, and M. S. Vitiello. Continuous-wave highly-efficient low-divergence terahertz wire lasers. *Nature Communications*, 9, 2018.

[65] G. Z. Liang, Y. Q. Zeng, X. N. Hu, H. Yu, H. K. Liang, Y. Zhang, L. H. Li, A. G. Davies, E. H. Linfield, and Q. J. Wang. Monolithic semiconductor lasers with dynamically tunable linear-to-circular polarization. *Acs Photonics*, 4(3):517–524, 2017.

[66] N. F. Yu, Q. J. Wang, M. A. Kats, J. A. Fan, S. P. Khanna, L. H. Li, A. G. Davies, E. H. Linfield, and F. Capasso. Designer spoof surface plasmon structures collimate terahertz laser beams. *Nature Materials*, 9(9):730–735, 2010.

[67] R. Degl'Innocenti, Y. D. Shah, R. Wallis, A. Klimont, Y. Ren, D. S. Jessop, H. E. Beere, and D. A. Ritchie. A hybrid plasmonic waveguide terahertz quantum cascade laser. *Applied Physics Letters*, 106(8), 2015.

[68] M. Harwit, G. Helou, L. Armus, C. M. Bradford, P. F. Goldsmith, M. Hauser, D. Leisawitz, D. F. Lester, G. Rieke, and S. A. Rinehart. Far-infrared/submillimeter astronomy from space: Tracking an evolving universe and the emergence of life. a white paper and set of recommendations for the astronomy and astrophysics decadal survey of 2010. 2009.

[69] C. Kulesa. Terahertz spectroscopy for astronomy: From comets to cosmology. *Ieee Transactions on Terahertz Science and Technology*, 1(1):232–240, 2011.

[70] C. Walker, C. Kulesa, J. Kloosterman, D. Lesser, T. Cottam, C. Groppi, J. Zmuidzinas, M. Edgar, S. Radford, P. Goldsmith, W. Langer, H. Yorke, J. Kawamura, I. Mehdi, D. Hollenbach, J. Stutzski, H. Huebers, J. R. Gao, and C. Martin. Large format heterodyne arrays for observing far-infrared lines with sofia. *Millimeter, Submillimeter, and Far-Infrared Detectors and Instrumentation for Astronomy V*, 7741, 2010.

[71] M. Benedettini, A. Gusdorf, B. Nisini, B. Lefloch, S. Anderl, G. Busquet, C. Ceccarelli, C. Codella, S. Leurini, and L. Podio. The shocked gas of the bhr71 outflow observed by herschel: indirect evidence for an atomic jet. *Astronomy & Astrophysics*, 598, 2017.

[72] W. D. Langer, T. Velusamy, J. L. Pineda, P. F. Goldsmith, D. Li, and H. W. Yorke. C+ detection of warm dark gas in diffuse clouds. *Astronomy & Astrophysics*, 521, 2010.

[73] G. Chattopadhyay, E. Schlecht, J. S. Ward, J. J. Gill, H. H. S. Javadi, F. Maiwald, and I. Medhi. An all-solid-state broad-band frequency multiplier chain at 1500 ghz. *Ieee Transactions on Microwave Theory and Techniques*, 52(5):1538–1547, 2004.

[74] A. Maestrini, I. Mehdi, J. V. Siles, J. S. Ward, R. Lin, B. Thomas, C. Lee, J. Gill, G. Chattopadhyay, E. Schlecht, J. Pearson, and P. Siegel. Design and characterization of a room temperature all-solid-state electronic source tunable from 2.48 to 2.75 thz. *Ieee Transactions on Terahertz Science and Technology*, 2(2):177–185, 2012.

[75] D. J. Hayton, J. L. Kloosterman, J. R. Gao, N. Vercruyssen, C. K. Walker, Q. Hu, and T. Y. Kao. A 4.7 thz heb/qcl heterodyne receiver for sto-2. *2014 39th International Conference on Infrared, Millimeter, and Terahertz Waves (Irmmw-Thz)*, 2014.

[76] D. J. Hayton, J. L. Kloosterman, Y. Ren, T. Y. Kao, J. R. Gao, T. M. Klapwijk, Q. Hu, C. K. Walker, and J. L. Reno. A 4.7 thz heterodyne receiver for a balloon borne telescope. *Millimeter, Submillimeter, and Far-Infrared Detectors and Instrumentation for Astronomy Vii*, 9153, 2014.

[77] J. R. G. Silva, B. Mirzaei, W. Laauwen, N. More, A. Young, C. Kulesa, C. Walker, A. Khalatpour, Q. Hu, C. Groppi, and J. R. Gao. 4x2 heb receiver at 4.7 thz for gusto. *Millimeter, Submillimeter, and Far-Infrared Detectors and Instrumentation for Astronomy Ix*, 10708, 2018.

[78] H. Richter, M. Wienold, L. Schrottke, K. Biermann, H. T. Grahn, and H. W. Hubers. 4.7-thz local oscillator for the great heterodyne spectrometer on sofia. *Ieee Transactions on Terahertz Science and Technology*, 5(4):539–545, 2015.

[79] S. Heyminck, U. U. Graf, R. Gusten, J. Stutzki, H. W. Hubers, and P. Hartogh. Great: the sofia high-frequency heterodyne instrument. *Astronomy & Astrophysics*, 542, 2012.

[80] C. Risacher, R. Gusten, J. Stutzki, H. W. Hubers, D. Buchel, U. U. Graf, S. Heyminck, C. E. Honingh, K. Jacobs, B. Klein, T. Klein, C. Leinz, P. Putz, N. Reyes, O. Ricken, H. J. Wunsch, P. Fusco, and S. Rosner. First supra-thz heterodyne array receivers for astronomy with the sofia observatory. *Ieee Transactions on Terahertz Science and Technology*, 6(2):199–211, 2016.

[81] U. U. Graf and S. Heyminck. Fourier gratings as submillimeter beam splitters. *Ieee Transactions on Antennas and Propagation*, 49(4):542–546, 2001.

[82] F. M. Boussaha, J. H. Kawamura, J. A. Stern, A. Skalare, and V. White. A low noise 2.7 thz waveguide-based superconducting mixer. *Ieee Transactions on Terahertz Science and Technology*, 2(3):284–289, 2012.

[83] D. Buchel, P. Putz, K. Jacobs, M. Schultz, U. U. Graf, C. Risacher, H. Richter, O. Ricken, H. W. Hubers, R. Gusten, C. E. Honingh, and J. Stutzki. 4.7-thz superconducting hot electron bolometer waveguide mixer. *Ieee Transactions on Terahertz Science and Technology*, 5(2):207–214, 2015.

[84] A. Gusdorf, S. Anderl, B. Lefloch, S. Leurini, H. Wiesemeyer, R. Gusten, M. Benedettini, C. Codella, B. Godard, A. I. Gomez-Ruiz, K. Jacobs, L. E. Kristensen, P. Lesaffre, G. P. des Forets, and D. C. Lis. Nature of shocks revealed by sofia oi observations in the cepheus e protostellar outflow. *Astronomy & Astrophysics*, 602, 2017.

[85] L. E. Kristensen, A. Gusdorf, J. C. Mottram, A. Karska, R. Visser, H. Wiesemeyer, R. Gusten, and R. Simon. Oxygen budget in low-mass protostars: the ngc 1333-iras4a r1 shock observed in [o i] at 63 mu m with sofia-great. *Astronomy & Astrophysics*, 601, 2017.

[86] S. Leurini, F. Wyrowski, H. Wiesemeyer, A. Gusdorf, R. Gusten, K. M. Menten, M. Gerin, F. Levrier, H. W. Hubers, K. Jacobs, O. Ricken, and H. Richter. Spectroscopically resolved far-ir observations of the massive star-forming region g5.89-0.39. *Astronomy & Astrophysics*, 584, 2015.

[87] L. Rezac, P. Hartogh, R. Gusten, H. Wiesemeyer, H. W. Hubers, C. Jarchow, H. Richter, B. Klein, and N. Honingh. First detection of the 63 mu m atomic oxygen line in the thermosphere of mars with great/sofia. *Astronomy & Astrophysics*, 580, 2015.

[88] H. Wiesemeyer, R. Gusten, S. Heyminck, H. W. Hubers, K. M. Menten, D. A. Neufeld, H. Richter, R. Simon, J. Stutzki, B. Winkel, and F. Wyrowski. Far-infrared study of tracers of oxygen chemistry in diffuse clouds. *Astronomy & Astrophysics*, 585, 2016.

[89] G. L. Pilbratt, J. R. Riedinger, T. Passvogel, G. Crone, D. Doyle, U. Gageur, A. M. Heras, C. Jewell, L. Metcalfe, S. Ott, and M. Schmidt. Herschel space observatory an esa facility for far-infrared and submillimetre astronomy. *Astronomy & Astrophysics*, 518, 2010.

[90] A. Poglitsch, C. Waelkens, N. Geis, H. Feuchtgruber, B. Vandenbussche, L. Rodriguez, O. Krause, E. Renotte, C. van Hoof, P. Saraceno, J. Cepa, F. Kerschbaum, P. Agnese, B. Ali, B. Altieri, P. Andreani, J. L. Augueres, Z. Balog, L. Barl, O. H. Bauer, N. Belbachir, M. Benedettini, N. Billot, O. Boulade, H. Bischof, J. Blommaert, E. Callut, C. Cara, R. Cerulli, D. Cesarsky, A. Contursi, Y. Creten, W. De Meester, V. Doublier, E. Doumayrou, L. Duband, K. Exter, R. Genzel, J. M. Gillis, U. Grozinger, T. Henning, J. Herreros, R. Huygen, M. Inguscio, G. Jakob, C. Jamar, C. Jean, J. de Jong, R. Katterloher, C. Kiss, U. Klaas, D. Lemke, D. Lutz, S. Madden, B. Marquet, J. Martignac, A. Mazy, P. Merken, F. Montfort, L. Morbidelli, T. Muller, M. Nielbock, K. Okumura, R. Orfei, R. Ottensamer, S. Pezzuto, P. Popesso, J. Putzeys, S. Regibo, V. Reveret, P. Royer, M. Sauvage, J. Schreiber, J. Stegmaier, D. Schmitt, J. Schubert, E. Sturm, M. Thiel, G. Tofani, R. Vavrek, M. Wetzstein, E. Wieprecht, and E. Wiezorrek. The photodetector array camera and spectrometer (pacs) on the herschel space observatory. *Astronomy & Astrophysics*, 518, 2010.

[91] A. Karska, G. J. Herczeg, E. F. van Dishoeck, S. F. Wampfler, L. E. Kristensen, J. R. Goicoechea, R. Visser, B. Nisini, I. San Jose-Garcia, S. Bruderer, P. Sniady, S. Doty, D. Fedele, U. A. Yildiz, A. O. Benz, E. Bergin, P. Caselli, F. Herpin, M. R. Hogerheijde, D. Johnstone, J. K. Jorgensen, R. Liseau, M. Tafalla, F. van der Tak, and F. Wyrowski. Water in star-forming regions with herschel (wish) iii. far-infrared cooling lines in low-mass young stellar objects. *Astronomy & Astrophysics*, 552, 2013.

[92] National Aeronautics (NASA) and Space Administration. Origins space telescope: From first light to life. a submission to the 2020 decadal survey. 2019.

[93] C. Battersby, L. Armus, E. Bergin, T. Kataria, M. Meixner, A. Pope, K. B. Stevenson, A. Cooray, D. Leisawitz, D. Scott, J. Bauer, C. M. Bradford, K. Ennico, J. J. Fortney,

L. Kaltenegger, G. J. Melnick, S. N. Milam, D. Narayanan, D. Padgett, K. Pontoppidan, T. Roellig, K. Sandstrom, K. Y. L. Su, J. Vieira, E. Wright, J. Zmuidzinas, J. Staguhn, K. Sheth, D. Benford, E. E. Mamajek, S. G. Neff, S. Carey, D. Burgarella, E. De Beck, M. Gerin, F. P. Helmich, S. H. Moseley, I. Sakon, and M. C. Wiedner. The origins space telescope. *Nature Astronomy*, 2(8):596–599, 2018.

[94] M. C. Wiedner, I. Mehdi, A. Baryshev, V. Belitsky, V. Desmaris, A. M. DiGiorgio, J. D. Gallego, M. Gerin, P. Goldsmith, F. Helmich, W. Jellema, A. Laurens, C. Risacher, A. Cooray, and M. Meixner. A proposed heterodyne receiver for the origins space telescope. *Ieee Transactions on Terahertz Science and Technology*, 8(6):558–571, 2018.

[95] Oleg G. Okhotnikov. *Semiconductor Disk Lasers: Physics and Technology*. John Wiley and Sons, Weinheim, Germany, 2010.

[96] J. G. McInerney, A. Mooradian, A. Lewis, A. Shchegrov, E. M. Strzelecka, D. Lee, J. P. Watson, A. Liebman, G. P. Carey, B. D. Cantos, W. R. Hitchens, and D. Heald. High-power surface emitting semiconductor laser with extended vertical compound cavity. *Electronics Letters*, 39(6):523–525, 2003.

[97] S. Hoogland, S. Dhanjal, A. C. Tropper, J. S. Roberts, R. Haring, R. Paschotta, F. Morier-Genoud, and U. Keller. Passively mode-locked diode-pumped surface-emitting semiconductor laser. *Ieee Photonics Technology Letters*, 12(9):1135–1137, 2000.

[98] A. H. Quarterman, K. G. Wilcox, V. Apostolopoulos, Z. Mihoubi, S. P. Elsmere, I. Farrer, D. A. Ritchie, and A. Tropper. A passively mode-locked external-cavity semiconductor laser emitting 60-fs pulses. *Nature Photonics*, 3(12):729–731, 2009.

[99] J. Chilla, S. Butterworth, A. Zeitschel, J. Charles, A. Caprara, M. Reed, and L. Spinelli. High power optically pumped semiconductor lasers. *Solid State Lasers Xiii: Technology and Devices*, 5332:143–150, 2004.

[100] M. Guina, A. Rantamaki, and A. Harkonen. Optically pumped vecsels: review of technology and progress. *Journal of Physics D-Applied Physics*, 50(38), 2017.

[101] M. Lukowski, C. Hessenius, and M. Fallahi. Widely tunable high-power two-color vecsels for new wavelength generation. *Ieee Journal of Selected Topics in Quantum Electronics*, 21(1):1700208, 2015.

[102] A. A. Tavallaee, P. C. Hon, K. Mehta, T. Itoh, and B. S. Williams. Zero-index terahertz quantum-cascade metamaterial lasers. *Ieee Journal of Quantum Electronics*, 46(7):1091–1098, 2010.

[103] A. A. Tavallaee, B. S. Williams, P. W. C. Hon, T. Itoh, and Q. S. Chen. Terahertz quantum-cascade laser with active leaky-wave antenna. *Applied Physics Letters*, 99(14), 2011.

[104] A. A. Tavallaee, P. W. C. Hon, Q. S. Chen, T. Itoh, and B. S. Williams. Active terahertz quantum-cascade composite right/left-handed metamaterial. *Applied Physics Letters*, 102(2), 2013.

[105] T. Y. Kao, J. L. Reno, and Q. Hu. Phase-locked laser arrays through global antenna mutual coupling. *Nature Photonics*, 10(8):541–+, 2016.

[106] Constantine A. Balanis. *Advanced engineering electromagnetics*. Wiley, New York, 1989.

[107] L. H. Li, L. Chen, J. X. Zhu, J. Freeman, P. Dean, A. Valavanis, A. G. Davies, and E. H. Linfield. Terahertz quantum cascade lasers with ¿ 1 w output powers. *Electronics Letters*, 50(4):309–310, 2014.

[108] V. Jayaraman, J. Jiang, H. Li, P. J. S. Heim, G. D. Cole, B. Potsaid, J. G. Fujimoto, and A. Cable. Oct imaging up to 760 khz axial scan rate using single-mode 1310nm mems-tunable vcsels with ¿ 100nm tuning range. *2011 Conference on Lasers and Electro-Optics (Cleo)*, 2011.

[109] A. W. M. Lee, T. Y. Kao, D. Burghoff, Q. Hu, and J. L. Reno. Terahertz tomography using quantum-cascade lasers. *Optics Letters*, 37(2):217–219, 2012.

[110] L. A. Coldren, G. A. Fish, Y. Akulova, J. S. Barton, L. Johansson, and C. W. Coldren. Tunable semiconductor lasers: A tutorial. *Journal of Lightwave Technology*, 22(1):193–202, 2004.

[111] F. J. Duarte. *Tunable laser optics*. CRC Press : Taylor and Francis Group, Boca Raton, second edition. edition, 2015.

[112] A. Godard. Infrared (2-12 um) solid-state laser sources: a review. *Comptes Rendus Physique*, 8(10):1100–1128, 2007.

[113] V. Jayaraman, Z. M. Chuang, and L. A. Coldren. Theory, design, and performance of extended tuning range semiconductor-lasers with sampled gratings. *Ieee Journal of Quantum Electronics*, 29(6):1824–1834, 1993.

[114] I. Kundu, P. Dean, A. Valavanis, L. Chen, L. H. Li, J. E. Cunningham, E. H. Linfield, and A. G. Davies. Quasi-continuous frequency tunable terahertz quantum cascade lasers with coupled cavity and integrated photonic lattice. *Optics Express*, 25(1):486–496, 2017.

[115] S. Slivken, N. Bandyopadhyay, S. Tsao, S. Nida, Y. Bai, Q. Y. Lu, and M. Razeghi. Sampled grating, distributed feedback quantum cascade lasers with broad tunability and continuous operation at room temperature. *Applied Physics Letters*, 100(26), 2012.

[116] A. Q. Liu and X. M. Zhang. A review of mems external-cavity tunable lasers. *Journal of Micromechanics and Microengineering*, 17(1):R1–R13, 2007.

[117] G. Wysocki, R. F. Curl, F. K. Tittel, R. Maulini, J. M. Bulliard, and J. Faist. Widely tunable mode-hop free external cavity quantum cascade laser for high resolution spectroscopic applications. *Applied Physics B-Lasers and Optics*, 81(6):769–777, 2005.

[118] K. Muro, Y. Shimada, K. Kitahara, T. Endo, Y. Yamagata, Y. Yamada, and T. Fujimoto. High power and widely tunable external cavity diode laser with a single-angled-facet laser chip. *2010 Conference on Lasers and Electro-Optics (Cleo) and Quantum Electronics and Laser Science Conference (Qels)*, 2010.

[119] V. Jayaraman, G. D. Cole, M. Robertson, A. Uddin, and A. Cable. High-sweep-rate 1310 nm mems-vcsel with 150 nm continuous tuning range. *Electronics Letters*, 48(14):867–868, 2012.

[120] A. Hugi, R. Terazzi, Y. Bonetti, A. Wittmann, M. Fischer, M. Beck, J. Faist, and E. Gini. External cavity quantum cascade laser tunable from 7.6 to 11.4 um. *Applied Physics Letters*, 95(6), 2009.

[121] G. Wysocki, R. Lewicki, R. F. Curl, F. K. Tittel, L. Diehl, F. Capasso, M. Troccoli, G. Hofler, D. Bour, S. Corzine, R. Maulini, M. Giovannini, and J. Faist. Widely tunable mode-hop free external cavity quantum cascade lasers for high resolution spectroscopy and chemical sensing. *Applied Physics B-Lasers and Optics*, 92(3):305–311, 2008.

[122] M. Rosch, G. Scalari, M. Beck, and J. Faist. Octave-spanning semiconductor laser. *Nature Photonics*, 9(1):42–47, 2015.

[123] A. W. M. Lee, B. S. Williams, S. Kumar, Q. Hu, and J. L. Reno. Tunable terahertz quantum cascade lasers with external gratings. *Optics Letters*, 35(7):910–912, 2010.

[124] Q. Qin, B. S. Williams, S. Kumar, J. L. Reno, and Q. Hu. Tuning a terahertz wire laser. *Nature Photonics*, 3(12):732–737, 2009.

[125] Q. Qin, J. L. Reno, and Q. Hu. Mems-based tunable terahertz wire-laser over 330ghz. *Optics Letters*, 36(5):692–694, 2011.

[126] L. Mahler, A. Tredicucci, F. Beltram, H. E. Beere, and D. A. Ritchie. Tuning a distributed feedback laser with a coupled microcavity. *Optics Express*, 18(18):19185–19191, 2010.

[127] F. Castellano, V. Bianchi, L. H. Li, J. X. Zhu, A. Tredicucci, E. H. Linfield, A. G. Davies, and M. S. Vitiello. Tuning a microcavity-coupled terahertz laser. *Applied Physics Letters*, 107(26), 2015.

[128] D. D. John, C. B. Burgner, B. Potsaid, M. E. Robertson, B. K. Lee, W. J. Choi, A. E. Cable, J. G. Fujimoto, and V. Jayaraman. Wideband electrically pumped 1050-nm mems-tunable vcsel for ophthalmic imaging. *Journal of Lightwave Technology*, 33(16):3461–3468, 2015.

[129] S. A. Diddams. The evolving optical frequency comb. *Journal of the Optical Society of America B-Optical Physics*, 27(11):B51–B62, 2010.

[130] J. L. Hall. Nobel lecture: Defining and measuring optical frequencies. *Reviews of Modern Physics*, 78(4):1279–1295, 2006.

[131] T. W. Hansch. Nobel lecture: Passion for precision. *Reviews of Modern Physics*, 78(4):1297–1309, 2006.

[132] G. Villares, A. Hugi, S. Blaser, and J. Faist. Dual-comb spectroscopy based on quantum-cascade-laser frequency combs. *Nature Communications*, 5, 2014.

[133] Y. Yang, D. Burghoff, D. J. Hayton, J. R. Gao, J. L. Reno, and Q. Hu. Terahertz multiheterodyne spectroscopy using laser frequency combs. *Optica*, 3(5):499–502, 2016.

[134] M. Rosch, M. Beck, M. J. Suess, D. Bachmann, K. Unterrainer, J. Faist, and G. Scalari. Heterogeneous terahertz quantum cascade lasers exceeding 1.9 thz spectral bandwidth and featuring dual comb operation. *Nanophotonics*, 7(1):237–242, 2018.

[135] P. Gellie, S. Barbieri, J. F. Lampin, P. Filloux, C. Manquest, C. Sirtori, I. Sagnes, S. P. Khanna, E. H. Linfield, A. G. Davies, H. Beere, and D. Ritchie. Injection-locking of terahertz quantum cascade lasers up to 35ghz using rf amplitude modulation. *Optics Express*, 18(20):20799–20816, 2010.

[136] S. Barbieri, M. Ravaro, P. Gellie, G. Santarelli, C. Manquest, C. Sirtori, S. P. Khanna, E. H. Linfield, and A. G. Davies. Coherent sampling of active mode-locked terahertz quantum cascade lasers and frequency synthesis (vol 5, pg 306, 2011). *Nature Photonics*, 5(6):378–378, 2011.

[137] C. Y. Wang, L. Kuznetsova, V. M. Gkortsas, L. Diehl, F. X. Kartner, M. A. Belkin, A. Belyanin, X. Li, D. Ham, H. Schneider, P. Grant, C. Y. Song, S. Haffouz, Z. R. Wasilewski, H. C. Liu, and F. Capasso. Mode-locked pulses from mid-infrared quantum cascade lasers. *Optics Express*, 17(15):12929–12943, 2009.

[138] A. Hugi, G. Villares, S. Blaser, H. C. Liu, and J. Faist. Mid-infrared frequency comb based on a quantum cascade laser. *Nature*, 492(7428):229–233, 2012.

[139] D. Burghoff, T. Y. Kao, N. R. Han, C. W. I. Chan, X. W. Cai, Y. Yang, D. J. Hayton, J. R. Gao, J. L. Reno, and Q. Hu. Terahertz laser frequency combs. *Nature Photonics*, 8(6):462–467, 2014.

[140] P. Del'Haye, A. Schliesser, O. Arcizet, T. Wilken, R. Holzwarth, and T. J. Kippenberg. Optical frequency comb generation from a monolithic microresonator. *Nature*, 450(7173):1214–1217, 2007.

[141] C. Y. Wang, L. Diehl, A. Gordon, C. Jirauschek, F. X. Kartner, A. Belyanin, D. Bour, S. Corzine, G. Hofler, M. Troccoli, J. Faist, and F. Capasso. Coherent instabilities in a semiconductor laser with fast gain recovery. *Physical Review A*, 75(3), 2007.

[142] H. Choi, L. Diehl, Z. K. Wu, M. Giovannini, J. Faist, F. Capasso, and T. B. Norris. Gain recovery dynamics and photon-driven transport in quantum cascade lasers. *Physical Review Letters*, 100(16), 2008.

[143] A. Gordon, C. Y. Wang, L. Diehl, F. X. Kartner, A. Belyanin, D. Bour, S. Corzine, G. Hofler, H. C. Liu, H. Schneider, T. Maier, M. Troccoli, J. Faist, and F. Capasso. Multimode regimes in quantum cascade lasers: From coherent instabilities to spatial hole burning. *Physical Review A*, 77(5), 2008.

[144] J. B. Khurgin, Y. Dikmelik, A. Hugi, and J. Faist. Coherent frequency combs produced by self frequency modulation in quantum cascade lasers. *Applied Physics Letters*, 104(8), 2014.

[145] N. Henry, D. Burghoff, Q. Hu, and J. B. Khurgin. Temporal characteristics of quantum cascade laser frequency modulated combs in long wave infrared and thz regions. *Optics Express*, 26(11):14201–14212, 2018.

[146] N. Henry, D. Burghoff, Y. Yang, Q. Hu, and J. B. Khurgin. Pseudorandom dynamics of frequency combs in free-running quantum cascade lasers. *Optical Engineering*, 57(1), 2018.

[147] G. Villares and J. Faist. Quantum cascade laser combs: effects of modulation and dispersion. *Optics Express*, 23(2):1651–1669, 2015.

[148] G. Villares, S. Riedi, J. Wolf, D. Kazakov, M. J. Suess, P. Jouy, M. Beck, and J. Faist. Dispersion engineering of quantum cascade laser frequency combs. *Optica*, 3(3):252–258, 2016.

[149] J. Hillbrand, P. Jouy, M. Beck, and J. Faist. Tunable dispersion compensation of quantum cascade laser frequency combs. *Optics Letters*, 43(8):1746–1749, 2018.

[150] D. Burghoff, Y. Yang, J. L. Reno, and Q. Hu. Dispersion dynamics of quantum cascade lasers. *Optica*, 3(12):1362–1365, 2016.

[151] D. Bachmann, M. Rosch, G. Scalari, M. Beck, J. Faist, K. Unterrainer, and J. Darmo. Dispersion in a broadband terahertz quantum cascade laser. *Applied Physics Letters*, 109(22), 2016.

[152] M. Wienold, B. Roben, L. Schrottke, R. Sharma, A. Tahraoui, K. Biermann, and H. T. Grahn. High-temperature, continuous-wave operation of terahertz quantum-cascade lasers with metal-metal waveguides and third-order distributed feedback. *Optics Express*, 22(3):3334–3348, 2014.

[153] K. Ohtani, D. Turcinkova, C. Bonzon, I. C. Benea-Chelmus, M. Beck, J. Faist, M. Justen, U. U. Graf, M. Mertens, and J. Stutzki. High performance 4.7 thz gaas quantum cascade lasers based on four quantum wells. *New Journal of Physics*, 18, 2016.

[154] Kai Fong Lee, K. M. Luk, and Hau Wah Lai. *Microstrip patch antennas*. World Scientific Publishing Co. Pte. Ltd., Singapore ; New Jersey, second edition. edition, 2018.

[155] D. Palaferri, Y. Todorov, Y. N. Chen, J. Madeo, A. Vasanelli, L. H. Li, A. G. Davies, E. H. Linfield, and C. Sirtori. Patch antenna terahertz photodetectors. *Applied Physics Letters*, 106(16), 2015.

[156] J. Madeo, Y. Todorov, and C. Sirtori. Antenna-coupled microcavities for terahertz emission. *Applied Physics Letters*, 104(3), 2014.

[157] J. Madeo, Y. Todorov, A. Gilman, G. Frucci, L. H. Li, A. G. Davies, E. H. Linfield, C. Sirtori, and K. M. Dani. Patch antenna microcavity terahertz sources with enhanced emission. *Applied Physics Letters*, 109(14), 2016.

[158] D. Palaferri, Y. Todorov, A. Bigioli, A. Mottaghizadeh, D. Gacemi, A. Calabrese, A. Vasanelli, L. H. Li, A. G. Davies, E. H. Linfield, F. Kapsalidis, M. Beck, J. Faist, and C. Sirtori. Room-temperature nine-mu m-wavelength photodetectors and ghz-frequency heterodyne receivers. *Nature*, 556(7699):85–+, 2018.

[159] T. Y. Kao, J. L. Reno, and Q. Hu. Amplifiers of free-space terahertz radiation. *Optica*, 4(7):713–716, 2017.

[160] D. Heydari, Y. Bai, N. Bandyopadhyay, S. Slivken, and M. Razeghi. High brightness angled cavity quantum cascade lasers. *Applied Physics Letters*, 106(9), 2015.

[161] W. J. Zhou, Q. Y. Lu, D. H. Wu, S. Slivken, and M. Razeghi. High-power, continuous-wave, phase-locked quantum cascade laser arrays emitting at 8 mu m. *Optics Express*, 27(11):15776–15785, 2019.

[162] G. Bloom, C. Larat, E. Lallier, M. Carras, and X. Marcadet. Coherent combining of two quantum-cascade lasers in a michelson cavity. *Optics Letters*, 35(11):1917–1919, 2010.

[163] B. G. Lee, J. Kansky, A. K. Goyal, C. Pflugl, L. Diehl, M. A. Belkin, A. Sanchez, and F. Capasso. Beam combining of quantum cascade laser arrays. *Optics Express*, 17(18):16216–16224, 2009.

[164] A. K. Goyal, M. Spencer, O. Shatrovoy, B. G. Lee, L. Diehl, C. Pfluegl, A. Sanchez, and F. Capasso. Dispersion-compensated wavelength beam combining of quantum-cascade-laser arrays. *Optics Express*, 19(27):26725–26732, 2011.

[165] P. Figueiredo, M. Suttinger, R. Go, A. Todi, H. Shu, E. Tsvid, C. K. N. Patel, and A. Lyakh. Continuous wave quantum cascade lasers with reduced number of stages. *Ieee Photonics Technology Letters*, 29(16):1328–1331, 2017.

[166] M. Suttinger, R. Go, P. Figueiredo, A. Todi, H. Shu, J. Leshin, and A. Lyakh. Power scaling and experimentally fitted model for broad area quantum cascade lasers in continuous wave operation. *Optical Engineering*, 57(1), 2018.

[167] A. Christ, S. G. Tikhodeev, N. A. Gippius, J. Kuhl, and H. Giessen. Waveguide-plasmon polaritons: Strong coupling of photonic and electronic resonances in a metallic photonic crystal slab. *Physical Review Letters*, 91(18), 2003.

[168] M. Carras and A. De Rossi. Photonic modes of metallodielectric periodic waveguides in the midinfrared spectral range. *Physical Review B*, 74(23), 2006.

[169] M. Carras, M. Garcia, X. Marcadet, O. Parillaud, A. De Rossi, and S. Bansropun. Top grating index-coupled distributed feedback quantum cascade lasers. *Applied Physics Letters*, 93(1), 2008.

[170] G. Maisons, M. Carras, M. Garcia, O. Parillaud, B. Simozrag, X. Marcadet, and A. De Rossi. Substrate emitting index coupled quantum cascade lasers using biperiodic top metal grating. *Applied Physics Letters*, 94(15), 2009.

[171] C. Boyle, C. Sigler, J. D. Kirch, D. F. Lindberg, T. Earles, D. Botez, and L. J. Mawst. High-power, surface-emitting quantum cascade laser operating in a symmetric grating mode. *Applied Physics Letters*, 108(12), 2016.

[172] H. Kogelnik and C. V. Shank. Coupled-wave theory of distributed feedback lasers. *Journal of Applied Physics*, 43(5):2327–+, 1972.

[173] M. Sotoodeh, A. H. Khalid, and A. A. Rezazadeh. Empirical low-field mobility model for iii-v compounds applicable in device simulation codes. *Journal of Applied Physics*, 87(6):2890–2900, 2000.

[174] Q. H. Hua, G. P. Li, X. K. He, Q. Wang, and T. N. Sun. Infrared reflectance study of n-type inp grown by the lec method. *Materials Letters*, 3(3):93–97, 1985.

[175] W. J. Moore and R. T. Holm. Infrared dielectric constant of gallium arsenide. *Journal of Applied Physics*, 80(12):6939–6942, 1996.

[176] A. L. Betz, R. T. Boreiko, B. S. Williams, S. Kumar, Q. Hu, and J. L. Reno. Frequency and phase-lock control of a 3 thz quantum cascade laser. *Optics Letters*, 30(14):1837–1839, 2005.

[177] S. Shiba, Y. Irimajiri, T. Yamakura, H. Maezawa, N. Sekine, I. Hosako, and S. Yamamoto. 3.1-thz heterodyne receiver using an nbtin hot-electron bolometer mixer and a quantum cascade laser. *Ieee Transactions on Terahertz Science and Technology*, 2(1):22–28, 2012.

[178] H. W. Hubers, H. Richter, and M. Wienold. High-resolution terahertz spectroscopy with quantum-cascade lasers. *Journal of Applied Physics*, 125(15), 2019.